

Microkinetic Evaluation of the Reforming of Biogas and Biomass Derived Oxygenates for Hydrogen Production.

A thesis presented for the Degree of Doctor of Philosophy at the University of
Aberdeen

By

Ahmed Tijani F. Afolabi,
MSc. University of Manchester
BSc. Izmir Institute of Technology

2021

ABSTRACT

The increased consciousness of the environmental impact of greenhouse gas emissions, as well as the push to meet the ever-increasing global energy demand, has led the chemical industry to source for more sustainable feedstock and prioritise process efficiency. Hydrogen production from biomass derived feedstock as an alternative to the conventional natural gas feedstock, provides an effective solution leaving minimal environmental footprint. Processes like the dry reforming of biogas and steam reforming of biomass derived oxygenates have garnered significant attention as they provide a feasible pathway into a future sustainable hydrogen economy. Improving the performance and efficiency of such processes is therefore an essential goal.

The design of suitable high performance catalyst systems is very important for the optimisation of these processes. Most active noble and transition metal catalysts provide high activity but are handicapped by their susceptibility towards deactivation *via* coke deposition or sintering at high temperatures. Support materials therefore play a vital role as they provide stability for the catalyst by strengthening the metal-support interactions and provide surface area for good metal dispersion which enhances reactivity. Active supports also provide active sites for reactants or intermediate species and participate in the reaction mechanism. This reduces the strain on the metal catalyst leading to higher activity and stability. Thus, it is unequivocally important to obtain an intrinsic mechanistic understanding of the role active metals as well as support materials play in the reforming process. It is also very important to investigate economically favourable support materials capable of performing these duties, as the current range of high-performance support materials in literature are not cost-efficient.

Within this context, this work presents a systematic approach to developing a comprehensive microkinetic model (a great tool for catalyst design and evaluation) that provides consolidated kinetic schemes capable of incorporating the effect of both active metal and active support materials on the reaction mechanism. The developed model is capable of evaluating the microkinetics of ethanol steam reforming (ESR) selected as a model biomass derived oxygenate and biogas dry reforming, over different catalytic systems. A thermodynamically consistent microkinetic model is developed in which all kinetic parameters are either theoretically calculated or correlated to the adsorption enthalpies of participating surface species, using the unity bond index-quadratic exponent potential (UBI-QEP) method. The model performed sensitivity analysis of the parameters, revealing the relative importance of the various reaction steps in the mechanism as well as the adsorption enthalpies of the species.

Initially, the model is used to correctly simulate a wide range of experimental data collected for the ESR over a Nickel metal with an inert silica support catalyst and correctly identified the dominant reaction pathway while also revealing the rate determining step to be the initial dehydrogenation towards 1-hydroxyethyl, occurring in the ethanol dehydrogenation pathway corresponding to a positive partial reaction order for ethanol. The C-C scission is found to occur at the ketyl intermediate. ESR experiments performed with a Ceria containing active support material over the same Nickel metal is then used in validating the developed bifunctional model. The bifunctional model revealed that the activity of the support altered the reaction mechanism by shifting the C-C bond scission further down the dehydrogenation pathway, as a result of the increased contribution of the oxidative dehydrogenation reaction class. The kinetically relevant reactions were determined to be occurring early in the ethanol dehydrogenation pathway and exclusively *via* thermal dehydrogenation, in agreement with the experimentally observed positive partial reaction order of ethanol. The developed model was adapted and used to simulate the dry reforming of biogas over a Rh-based catalyst with industrially relevant CO and H₂ co-feeding. The model was able to describe the experimental trends successfully which ascertained that the developed model was consistent. The dehydrogenation of CH₃* was determined to be the rate determining step and did not change when products were co-fed.

Based on the results observed in the bifunctional model showing the presence of surface oxygen provided by the support (Ceria) as having a positive impact of H₂ yield, an alternative sustainable biomass derived material was experimentally investigated as a support for the ESR process. Biochar was selected as it has shown good activity for tar reforming and contains surface O-containing functional groups. The results and analysis of the data revealed biochar to be catalytically active for the ESR mechanism and the kinetically relevant ethanol dehydrogenation steps appeared to occur on the biochar surface.

The comprehensive microkinetic evaluation studies presented in this work can help clarify the catalytic mechanism of ESR over various metals and support materials as well as the dry reforming of biogas with partial recycle. The model predicts kinetic parameters which can be validated experimentally and helps with predicting the catalytic activity of various metals and supports based on their structure and species binding energies. The model can therefore be expanded to determine the mechanism of the steam reforming of larger biomass derived oxygenates, which will guide the future design of highly catalytic materials for the processes as well as optimise process parameters.

ACKNOWLEDGEMENTS

My utmost praise and gratitude to Allah (SWT), for giving me the strength and guidance to accomplish all my goals through all the challenges life throws my way. I have been blessed with all love and support in the form of people he has surrounded me with and brought into my life.

An infinite amount of my gratitude and thanks go to my supervisor, Dr Panagiotis Kechagiopoulos, for the support, guidance, encouragement and valuable advice he provided me with throughout my study. He was a constant motivator for me and with every meeting we had he gave me the subtle indication that I am capable of achieving whatever I put my mind to and more. My special thanks to Prof. Chun Zhu Li, who was my co-supervisor based in Australia. He was very supportive and never failed to remind me of the potential he saw in me. A very special acknowledgement goes to the Aberdeen-Curtin Alliance board and team, from Cheryl Croydon to Dr Stephen Hill, for awarding me the Scholarship and supporting me through my Joint PhD degree.

Special thanks to Marinela Zhurka and Andrea Navarro for providing me with needed experimental data and doing in their own words “the hard and strenuous lab work, while I sat and modelled all their countless hours of work in minutes”. Thanks to my colleagues, Shakir Mohammed, Yurong Liu, Tunde Lashore here in Aberdeen as well as in Perth, Australia for all the good times and laughs we had as welcomed and much needed distractions.

My heartfelt thanks to my family here in Aberdeen, David, Ashley, Abdullah, Bisola Abdulhamid, Jameel, Jaafar, Jibril, Sabrene (SAAM). You all made this journey easier in your unique ways. Special thanks to Yoana Zdravkova, for supporting me through this journey with your continuous rock-like presence and never say never attitude, you were a bastion for me. Thanks to all my teammates and friends at the Panthers Basketball club and Aberdeen Roughnecks American football club. And how can I forget to mention, Sukhraj Here, David Lanre, Clyde, Hannah-Marie. Through thick and thin, from day one through lockdown and pandemic, you put up with me through it all and stuck by me, even when I’d bore you senseless with always wanting to have intellectual conversations to keep our minds sharp. Sukraj, Clyde, I hope we play basketball till we are 60 but you might have to get used to calling me Dr Teejay now.

This PhD journey has been a family affair and I would not have been successful without the love and support of my family. All my love goes to my mother, Sakeenah Afolabi and my father Fatai Afolabi, for their continuous unconditional love and care. Always reminding me I have a strong

foundation and base and so failure was never even a passing thought. To my lovely older siblings, Rasheedah, Amina, Rafiat, Ruqayyah and Radiyya. You are my 5 other mothers and constantly shower me with all the love anyone could ask for. Your prayers and support were essential to my success. To my cousin, Abdulmalik, my enforced twin, you are and will always be an inspiration to me. To all of my other family here in the UK and everywhere else around the world, your continuous support and love is very much appreciated.

My thesis is dedicated to the memories of my grandfather, Abdulrasheed Afolabi, my great uncle Jimoh Afolabi, my cousins, Olamide Okin and Mariam Ajenifuja. Every one of you believed in me even before I knew I was going to have the desire to pursue this goal. My great uncle said to my father when I was aged 9 years old that I would one day complete a PhD. I only wish you were all here to see that day come. May Allah make our reunion a blissful one.

DECLARATION OF ORIGINALITY

I hereby declare that this thesis and the work reported herein was composed by and originated entirely from me. Information derived from the published and unpublished works of others has been acknowledged in the text and the relevant references are included in this thesis.

Ahmed-Tijani F. Afolabi

University of Aberdeen, January 2021.

TABLE OF CONTENTS

ABSTRACT	1
ACKNOWLEDGEMENTS	3
DECLARATION OF ORIGINALITY	5
TABLE OF CONTENTS	6
LIST OF TABLES	10
LIST OF FIGURES	12
CHAPTER 1: INTRODUCTION	19
1.1. RESEARCH OBJECTIVES	21
1.2. STRUCTURE AND OVERVIEW OF THESIS	22
1.3. REFERENCES	25
CHAPTER 2: LITERATURE REVIEW	27
2.1 HYDROGEN PRODUCTION FROM BIOGAS.....	27
2.1.1 <i>Biogas</i>	27
2.1.2 <i>Biogas Dry Reforming</i>	28
2.1.3 <i>Catalysts for biogas dry reforming</i>	29
2.2 HYDROGEN PRODUCTION FROM OXYGENATED HYDROCARBONS.....	31
2.2.1 <i>Ethanol</i>	31
2.2.2 <i>Ethanol steam reforming</i>	32
2.2.3 <i>Catalysts for ethanol steam reforming</i>	34
2.3 KINETIC MODELLING.....	37
2.3.1 <i>Closed form empirical kinetic models</i>	37
2.3.2 <i>Mean-field Microkinetics</i>	38
2.3.3 <i>Elementary rate constant estimation from semi-empirical methods</i>	40
2.3.4 <i>Thermodynamic consistency in microkinetic modelling</i>	42
2.3.5 <i>Modelling of biogas dry reforming</i>	44
2.3.6 <i>Modelling of ethanol steam reforming</i>	47
REFERENCES	51
CHAPTER 3: METHODOLOGY	61
3.1 MICROKINETIC ANALYSIS	61

3.1.1	<i>Apparent Rate Expressions</i>	61
3.1.2	<i>Reaction Mechanisms</i>	62
3.1.3	<i>Rate Constant Estimation</i>	63
3.1.4	<i>Thermodynamic Consistency</i>	65
3.1.5	<i>Kinetic model parameters calculation</i>	66
3.2	MICROKINETIC ENGINE	70
3.3	EXPERIMENTAL METHODOLOGY FOR THE KINETIC INVESTIGATION OF ESR OVER NI/BIOCHAR CATALYST	72
3.3.1	<i>Catalyst sample preparation</i>	72
3.3.2	<i>Reactor set up</i>	73
3.3.3	<i>Experimental conditions and parameters</i>	74
3.3.4	<i>Biochar characterization</i>	75
3.4	REFERENCES	75
CHAPTER 4: MICROKINETIC MODELLING AND REACTION PATHWAY ANALYSIS OF THE STEAM REFORMING OF ETHANOL OVER NI/SIO₂.....		78
4.1	INTRODUCTION	80
4.2	PROCEDURES.....	82
4.2.1	<i>Experimental details</i>	82
4.2.2	<i>Model formulation and computational details</i>	82
4.2.3	<i>Surface reaction network description</i>	84
4.3	RESULTS	87
4.3.1	<i>Model validation</i>	87
4.3.2	<i>Kinetic relevance of reaction steps</i>	94
4.3.3	<i>Reaction pathway analysis</i>	97
4.3.4	<i>Model parameter sensitivity</i>	100
4.3.5	<i>Estimated model parameters evaluation</i>	104
4.4	CONCLUSIONS	105
	REFERENCES	105
CHAPTER 5: INVESTIGATION OF H₂ AND CO CO-FEEDING ON BIOGAS DRY REFORMING OVER RH/AL₂O₃ CATALYST VIA MICROKINETIC MODELLING ..		111
.....		111
5.1	INTRODUCTION	113
5.2	MATERIALS AND METHODS	116

5.2.1	<i>Catalyst preparation and characterization</i>	116
5.2.2	<i>Catalytic tests</i>	116
5.2.3	<i>Model formulation and computation details</i>	118
5.2.4	<i>Surface reaction network description</i>	119
5.3	RESULTS AND DISCUSSION	120
5.3.1	<i>Catalyst characterization</i>	120
5.3.2	<i>Model validation</i>	121
5.3.3	<i>Influence of operating parameters</i>	122
5.3.4	<i>Model evaluation</i>	128
5.4	CONCLUSIONS	138
	REFERENCES	139
CHAPTER 6: MICROKINETIC EVALUATION OF THE BIFUNCTIONAL MECHANISM OF ETHANOL STEAM REFORMING OVER A NI/CEZRLA.....		149
6.1	INTRODUCTION	151
6.2	PROCEDURES.....	152
6.2.1	<i>Experimental details</i>	152
6.2.2	<i>Model formulation</i>	153
6.2.3	<i>Surface reaction network description</i>	154
6.3	RESULTS	158
6.3.1	<i>Model validation</i>	158
6.3.2	<i>Kinetic relevance of reaction steps</i>	165
6.3.3	<i>Reaction pathway analysis</i>	167
6.3.4	<i>Oxidative dehydrogenation of ethanol derivatives</i>	170
6.3.5	<i>Model parameter sensitivity</i>	175
6.4	CONCLUSIONS	177
	REFERENCES	177
CHAPTER 7: KINETIC FEATURES OF ETHANOL STEAM REFORMING AND DECOMPOSITION USING A BIOCHAR-SUPPORTED NI CATALYST		186
7.1	INTRODUCTION	188
7.2	EXPERIMENTAL.....	190
7.2.1	<i>Sample preparation</i>	190
7.2.2	<i>Reactor set up</i>	190
7.2.3	<i>Experimental conditions and parameters</i>	191

7.2.4	<i>Biochar characterization</i>	192
7.3	RESULTS AND DISCUSSION	192
7.3.1	<i>Ethanol steam reforming catalysed by biochar supported Ni</i>	192
7.3.2	<i>Ethanol steam reforming catalysed by acid-washed biochar</i>	199
7.3.3	<i>Ethanol steam reforming catalysed by biochar</i>	202
7.3.4	<i>Water-gas shift reaction catalysed by Ni/biochar</i>	204
7.3.5	<i>Ethanol decomposition</i>	205
7.3.6	<i>Analysis of kinetic compensation effect</i>	208
7.3.7	<i>Raman spectroscopic characterization of biochar</i>	210
7.4	CONCLUSIONS	212
	REFERENCES	213
	CHAPTER 8: CONCLUSION	218

LIST OF TABLES

- Table 2.1: Proposed LHHW rate expressions for CH₄ dry reforming over Ni-based catalyst
- Table 2.2: Reaction network for dual-site microkinetic model for WGS reaction at Au/MgO interface
- Table 4.1: Experimental operating conditions and catalyst properties.
- Table 4.2: Microkinetic model for ethanol steam reforming on Ni/SiO₂. Activation barriers are calculated using the model parameters shown in Table 4.3 via UBI-QEP and pre-exponential factors calculated via transition state theory as described in Section 4.2.3. Modified Arrhenius equation used of form $R_{i,f} = A_i T^\beta e^{-E_a/RT}$ with the temperature exponents reported below.
- Table 4.3: Estimated model parameters with 95% confidence intervals. Chemisorption enthalpy values without confidence intervals were adopted from the literature sources shown, while those with confidence intervals were regressed using as initial values the respective literature sources shown.
- Table 4.4: Effect of partial pressure of water on partial coverage of surface species at 400°C.
- Table 5.1: Reaction conditions studied.
- Table 5.2: Microkinetic model for dry reforming of biogas.
- Table 5.3: Partial surface coverages for H* and CO* at different locations of the catalyst bed. Conditions: 750°C, CH₄/CO₂ = 1.35, GHSV = 700 NL CH₄/gcat·h.
- Table 5.4: Partial surface coverages for H* and CO* at different locations of the catalyst bed. Conditions: 750°C, CH₄/CO₂ = 1.35, GHSV = 700 NL CH₄/gcat·h.
- Table 5.5: Estimated model parameters.
- Table 6.1: Experimental operating conditions and catalyst properties
- Table 6.2: Microkinetic model for ethanol steam reforming on Ni/CeO₂. Activation barriers are calculated using the model parameters shown in Table 3 via UBI-QEP and pre-exponential factors calculated via transition state theory as described in

Section Model formulation and computational details. Arrhenius equation used of form $\mathbf{R}_{i,f} = \mathbf{A}_i \mathbf{e}^{-Ea/RT}$.

- Table 6.3: Estimated model parameters with 95% confidence intervals. Chemisorption enthalpy values without confidence intervals were adopted from the literature sources shown and kept fixed, while those with confidence intervals were regressed using as initial values the respective literature values from the sources shown.
- Table 6.4: Contributions of thermal and oxidative dehydrogenation reaction classes to the consumption of the first 3 dehydrogenation reactants for three different catalytic scenarios at 400°C.
- Table 6.5: Contributions of thermal and oxidative reaction classes as well as C-C scission to the consumption of the other dehydrogenation reactants for three different catalytic scenarios at 400°C.
- Table 7.1: Summary of ethanol steam reforming/decomposition results over the various catalytic systems studied.
- Table 7.2: Relative change in total Raman peak area (800 - 1800 cm^{-1}) over the 30-60 min reaction interval of biochar samples obtained from experiments varying S/C ratio at 400°C over Ni/biochar and respective products formation.

LIST OF FIGURES

- Figure 3.1: Collision tube
- Figure 3.2: Adsorbed 1-hydroxyethyl species. (grey, white and red balls represent carbon, hydrogen and oxygen respectively)
- Figure 3.3: Schematic of reactor setup.
- Figure 4.1: Parity diagrams for detected liquid and gas components at conditions reported in Table 4.1 and discussed in Zhurka et al. Modelling results have been obtained with the parameter values shown in Table 4.3.
- Figure 4.2: Comparison of model predicted conversions and selectivities over Ni/SiO₂ catalyst (lines) with experimental results (symbols). Operating conditions are indicated on the respective panels.
- Figure 4.3: Reaction orders with respect to ethanol and water partial pressure (operating conditions are that of Figure 4.2 panels b and c respectively).
- Figure 4.4: Ethanol conversion versus products selectivities depicting primary and secondary products at different temperatures (Operating conditions are shown in the respective panels).
- Figure 4.5: Sensitivity analysis of pre-exponential factors of microkinetic model reactions shown in Table 4.2, at 400°C and H₂O/C of 3 for ethanol outlet molar fraction. Base values for pre-exponential factors are calculated as described in Section 4.2.2.
- Figure 4.6: Sensitivity analysis of pre-exponential factors of microkinetic model reactions shown in Table 4.2 at 400°C and H₂O/C of 3 for products and water outlet molar fractions. Base values for pre-exponential factors are calculated as described in Section 4.2.2.
- Figure 4.7: Reaction pathway analysis for ethanol steam reforming over Ni/SiO₂ at 400°C and H₂O/C of 3 at an ethanol conversion of 25%. Net production rates are considered in calculating contribution percentages of carbon containing species towards other species. Colour mapping from blue to red indicate increasing contribution

percentages. Line thickness indicates the relative magnitude of the rates of the reaction.

Figure 4.8: Sensitivity analysis of adsorption enthalpies for liquid and gaseous compounds outlet molar fractions for Ni/SiO₂ at 400°C and H₂O/C of 3. Base values for model parameters are shown in Table 3.

Figure 5.1: Parity diagrams for (a) CH₄, (b) CO₂, (c) H₂ and (d) CO. Experimental conditions are reported in Table 5.1, while modelling results have been obtained with parameter values presented in Table 5.5.

Figure 5.2: Effect of GHSV in the dry reforming of biogas at (a) 750°C, (b) 725°C and (c) 700°C on biogas conversion, hydrogen yield and CO selectivity. Comparison of model CH₄ and CO₂ conversion, H₂ yield and CO selectivity (lines) with experimental results (symbols).

Figure 5.3: Effect of CH₄/CO₂ feed molar ratio in the dry reforming of biogas at (a) 750°C, (b) 725°C and (c) 700°C and 350 N L CH₄/gcat·h. Comparison of model CH₄ and CO₂ conversion, CO selectivity and H₂ yield (lines) with experimental results (symbols).

Figure 5.4: Effect of H₂ content in the feed in the dry reforming of biogas at (a) 750°C, (b) 725°C and (c) 700°C, at 700 N L CH₄/gcat·h. Comparison of model CH₄ and CO₂ conversion, CO selectivity and H₂ yield (lines) with experimental results (symbols).

Figure 5.5: Effect of the CO content in the feed over reaction temperature in the dry reforming of biogas at 700 N L CH₄/gcat·h. Comparison of model CH₄ and CO₂ conversion, H₂ selectivity and CO yield (lines) with experimental results (symbols).

Figure 5.6: Sensitivity analysis of pre-exponential factors of the microkinetic model reactions shown in Table 5.2, for both pure DRM and 20% H₂ co-feeding DRM. Base values of pre-exponential factors are calculated using transition state theory as described previously. Conditions: 750°C, CH₄/CO₂ = 1.35, GHSV = 700 NL CH₄/gcat·h.

Figure 5.7: Contribution analysis at the end of the catalyst bed for pure DRM (regular black fonts) and for 20 % H₂ co-feeding DRM (underlined purple italics). Net production rates are considered in calculating contribution percentages of carbon containing species towards other species. Colour mapping from blue to red on lines indicates increasing contribution percentages. Line thickness indicates relative magnitude of

the reaction rates. Conditions: 750°C, CH₄/CO₂ = 1.35, GHSV = 700 NL CH₄/gcat·h.

Figure 5.8: Model parameters sensitivity analysis for reactants outlet fractions. Base values for the parameters are shown in Table 5.5. Operating conditions: 750°C, CH₄/CO₂ = 1.35, GHSV = 700 NL CH₄/gcat·h.

Figure 5.9: Parity diagram for CH₄, H₂O, H₂, CO and CO₂. Experimental conditions of steam reforming of methane are reported in previous work, while modelling results have been obtained with parameter values presented in Table 5.5.

Figure 6.0: Top view of assumed geometry of catalyst

Figure 6.1: Parity plot comparing experimental product molar flow over Ni/CeO₂ with values obtained from model based on a single type of active site.

Figure 6.2: Parity plot comparing experimental outlet molar flow over Ni/CeO₂ (top) and Ni/SiO₂ (bottom) with values calculated from the bifunctional microkinetic model.

Figure 6.3: Comparison of model predicted conversions and selectivities over Ni/CeO₂ catalyst (lines) with experimental results (symbols). Operating conditions are indicated on the respective panels.

Figure 6.4: Sensitivity analysis of pre-exponential factors of microkinetic model reactions shown in Table 6.2, at 400°C & 450°C and H₂O/C = 3 for ethanol outlet molar fraction. Base values for pre-exponential factors are calculated as described in Section Model formulation and computational details.

Figure 6.5: Reaction pathway analysis for ethanol steam reforming over Ni/CeO₂ at 400°C and H₂O/C = 3. Net production rates are considered in calculating contribution percentages of carbon containing species towards other species. Colour mapping from blue to red indicates increasing contribution percentages. Line thickness indicates the relative magnitude of the rates of the reaction. The respective contributions of the thermal and oxidative dehydrogenation reaction classes to the dehydrogenation pathway are presented as underlined values in green (top) and orange (bottom), respectively, for instances where the contribution is split.

Figure 6.6: Surface coverage of specific species for three different catalytic scenarios at 400°C.

- Figure 6.7: Model parameter sensitivity analysis for ethanol and CH₄ outlet molar flow at 400°C and H₂O/C = 3. Base values for the parameters are shown in Table 7.3.
- Figure 6.8: Parity plot comparing experimental outlet molar flow over Ni/SiO₂ with values calculated from the bifunctional microkinetic model.
- Figure 6.9: Sensitivity analysis of pre-exponential factors of Ni/SiO₂ microkinetic shown in Table 6.2 excluding support site reactions, at 400°C & 450°C (H₂O/C = 3) for ethanol outlet molar fraction and model parameters sensitivity analysis for ethanol and CH₄ outlet molar flow at 400°C (H₂O/C = 3).
- Figure 6.10: Sensitivity analysis of pre-exponential factors of microkinetic model reactions shown in Table 6.2, at 450°C and H₂O/C = 3 for gas product outlet molar fraction. Base values for pre-exponential factors are calculated as described in Section Model formulation and computational details.
- Figure 7.1: Effect of temperature on conversion and H₂ yield (a), carbon selectivities of CO & CO₂ (b) and CH₄ & CH₃CHO (c) during ESR catalysed by Ni/biochar compared with equilibrium (Exp = experimental, Eq = equilibrium) (S/C = 3, W/F_{Eth} = 90.9 g_{cat} s⁻¹ g_{Eth}⁻¹).
- Figure 7.2: Arrhenius plot of ESR catalysed by Ni/biochar (S/C = 3, W/F_{Eth} = 90.9 g_{cat} s⁻¹ g_{Eth}⁻¹).
- Figure 7.3: Effect of partial pressure of water on ethanol conversion and H₂ yield (a), carbon selectivities of CO & CO₂ (b), CH₄ & CH₃CHO (c) during ESR catalysed by Ni/biochar compared with equilibrium at 400°C.
- Figure 7.4: Effect of W/F on ethanol conversion and H₂ yield (a) and carbon selectivities of CO, CO₂, CH₄ and CH₃CHO (b) during ESR catalysed by Ni/biochar at 400°C (S/C = 3).
- Figure 7.5: Effect of temperature on conversion, H₂ yield (a) and carbon selectivities of CO, CO₂, CH₄ & CH₃CHO (b) during ESR catalysed by acid-washed biochar (S/C = 3, W/F_{Eth} = 90.9 g_{cat} s⁻¹ g_{Eth}⁻¹).
- Figure 7.6: Arrhenius plot of ESR catalysed by acid-washed biochar (S/C = 3, W/F_{Eth} = 90.9 g_{cat} s⁻¹ g_{Eth}⁻¹).

Figure 7.7: Effect of temperature on conversion and H₂ yield (top) and carbon selectivities of CO, CO₂, CH₄ & CH₃CHO (bottom) during ESR catalysed by biochar (S/C = 3, W/F_{Eth} = 90.9 g_{cat} s⁻¹ g_{Eth}⁻¹).

Figure 7.8: Arrhenius plot of ESR catalysed by biochar (S/C = 3, W/F_{Eth} = 90.9 g_{cat} s⁻¹ g_{Eth}⁻¹).

Figure 7.9: Effect of temperature on the conversion of CO during WGS reaction catalysed by Ni/biochar (S/C = 3, W/F_{CO} = 45.6 g_{cat} s⁻¹ g_{CO}⁻¹).

Figure 7.10: Ethanol decomposition conversion and H₂ yield over Ni/biochar (a), carbon selectivities of CO, C₂H₆, CH₄ and CH₃CHO over Ni/biochar (b), ethanol decomposition conversion and H₂ yield over biochar (c), carbon selectivities of CO, C₂H₆ and CH₄ over biochar (d) (S/C = 0, W/F_{Eth} = 90.9 g_{cat} s⁻¹ g_{Eth}⁻¹).

Figure 7.11: Arrhenius plots of ethanol decomposition catalysed by Ni/biochar (a) and biochar (b) (S/C = 0, W/F_{Eth} = 90.9 g_{cat} s⁻¹ g_{Eth}⁻¹).

Figure 7.12: Reaction barriers vs pre-exponential factors for ethanol consumption and product formation in the experiments over the different catalysts showing the presence of a kinetic compensation effect. Ni/SiO₂ data obtained from.

Figure 7.13: Schematic view of postulated distribution of ethanol and steam derived species on various active sites on Ni/biochar during the reforming reaction.

Figure 7.14: Raman spectroscopic data showing total Raman peak area (800 - 1800 cm⁻¹) of biochar samples obtained from ESR (ethanol steam reforming) and ED (ethanol decomposition) experiments at 450°C at different reaction times, in comparison to that of raw biochar and fresh reduced Ni/biochar.

Figure 7.15: Normalised Raman spectra of biochar samples obtained from ESR (ethanol steam reforming) and ED (ethanol decomposition) experiments at different reaction times, in comparison to that of raw biochar and fresh reduced Ni/biochar.

Figure 7.16: Deconvolution example of a Raman spectrum using 10 bands for a biochar sample.

Nomenclature

Roman Symbols

A_i	:	pre-exponential factor of reaction i , unit reaction dependent
E_i	:	activation energy of reaction i , J mol ⁻¹
h	:	Planck constant, 6.62607×10 ⁻³⁴ J s
H_i	:	enthalpy of species i , J mol ⁻¹
I_i	:	moment of inertia of i , kg m ²
k_B	:	Boltzmann constant, 1.38065×10 ⁻²³ J K ⁻¹
k_i	:	rate coefficient of reaction i , (Pa ⁻¹) s ⁻¹
L_t	:	density of active sites, mol _{surf-metal} m _{cat} ⁻²
M_i	:	molar mass of component i , kg mol ⁻¹
n	:	reaction order
P	:	total pressure, Pa
Q_i	:	heat of chemisorption of species i , J mol ⁻¹
R	:	ideal gas constant, 8.31446 J mol ⁻¹ K ⁻¹
r_i	:	rate of reaction i , mol m ⁻³ s ⁻¹
S_i	:	entropy of species i , J mol ⁻¹ K ⁻¹
S_p	:	catalyst specific surface area, m ² kg _{cat} ⁻¹
T	:	temperature, K

Greek Symbols

ΔH_i : enthalpy of reaction i , J mol⁻¹

ΔS_i : entropy of reaction i , J mol⁻¹ K⁻¹

σ : symmetry number

Superscripts

b : backward reaction step

f : forward reaction step

Subscripts

g : gas phase

s : surface

CHAPTER 1: INTRODUCTION

Growing concerns over greenhouse gas emissions from the combustion of fossil fuels for the generation of consumer energy, has driven mankind to develop better sustainable energy solutions. The establishment of renewable energy sources such as solar, wind and biomass, serve as an effective solution to the problem of fossil fuel dependency. The low cost of these renewables coupled with the increasing carbon pricing regulations as well as increasing fossil fuel price, is predicted to ultimately increase the share of primary energy used from renewable sources in the future [1]. One of the most promising alternative energy carriers is hydrogen, which is the most abundant element on earth. Naturally, hydrogen is not found in its atomic form but is found as part of organic materials, hydrocarbons and water molecules, with the processes required to extract hydrogen needing some external energy input. Having a specific high energy density, hydrogen has been recognized as an ideal, sustainable energy carrier [2]. Traditionally, hydrogen is produced from the reforming of natural gas and the gasification of coal to a lesser extent. These processes are still fossil fuel dependent and do little to hinder the production of greenhouse gas emissions. Alternatively, hydrogen produced from bio-renewable sources are more carbon-neutral in the sense that the emissions produced during combustion are offset by those utilised during the feedstock growth cycle [3]. Currently, biomass processing is divided into two categories: thermochemical and biological processes, yielding fuels in solid, liquid and gas forms. Thermochemical processes involve pyrolysis, liquefaction, reforming and gasification, whereas biological processes focus on direct bio-photolysis, indirect bio-photolysis, biological water-gas shift reaction, photo-fermentation and dark-fermentation.

Biogas produced *via* anaerobic digestion of renewable biodegradable organic materials and the oxygen containing hydrocarbons (oxygenates) produced from biomass processing can undergo similar reforming technologies as natural gas for hydrogen production. Reforming is a thermochemical process in which hydrogen is formed as a main product with carbon dioxide and carbon monoxide. Thermodynamics of reactions as well as the catalyst selected affect the yield of hydrogen obtained during reforming. Biogas and biomass-derived oxygenated hydrocarbons can undergo various reforming processes including dry reforming, steam reforming and autothermal reforming [4]. Reforming of biogas and biomass-derived oxygenates like monohydric alcohols, phenolics and polyhydric alcohols has garnered large interest due to their abundance.

Biogas is generally composed of CH₄ (55-70%) and CO₂ (30-45%). The methane content of biogas has similar commercial value to that of fossil fuel based natural gas and has almost a zero

net CO₂ contribution [5]. Reforming of biogas produces synthesis gas which serves a key intermediate in the petrochemicals industry and is source for pure hydrogen. Steam reforming is the most popular technology for biogas of the possible reforming technologies, however, dry reforming of biogas has the added benefit of converting two greenhouse gases concurrently. Dry reforming of biogas is an endothermic reaction and requires high temperatures (700-900°C) for high conversion towards syngas. Noble and non-noble metal catalysts have been studied for the dry reforming of biogas. The two most commonly used metal catalysts are Rh-based [6] and Ni-based [7] catalysts. Dry reforming has a higher coke deposition rate than steam reforming owing to the lower H/C and O/C ratio. Deactivation of catalyst is hence a hinderance. Acidic oxide (Al₂O₃) and basic oxide (MgO) supports are commonly used to improve the activity and stability of the catalyst. The best practice involves using mixed acidic and basic oxide supports and bimetallic catalysts (Co-Ni/Al₂O₃-La₂O₃)[8]. Conventional methane reforming in industry involves partial recycling of product stream to optimise reaction efficiency. Co-feeding during biogas dry reforming on a large scale would therefore be highly likely. Co-feeding hydrogen is also being studied for the reduction of coke deposition in industrial biogas dry reforming reactors [9].

Bio-ethanol is very attractive due to its relatively high hydrogen content, non-toxicity and availability, also as a liquid its storage and transportation are of relative ease. More importantly bio-ethanol can be produced from various renewable sources, such as energy crops, forestry or agro-industry waste, the organic fraction of municipal solid waste, etc., via hydrolysis and fermentation processes [10,11].

Of the different types of reforming processes, the steam reforming of the oxygenates like bio-ethanol has received more attention due to its relatively higher hydrogen yield [4]. Steam reforming of ethanol (ESR) is an endothermic reaction, therefore the reformat produced has a higher heating value making it more efficient for energy production. Above 478 K the reaction Gibbs free energy becomes negative, however at low temperatures it is difficult to achieve high conversions and reduce catalyst deactivation by coke deposition. Therefore, catalytic ESR is usually performed at temperatures between 573-873 K. In order to increase the energy efficiency, various approaches have been investigated using different reactor types and catalysts. For example, a reactor-separator combined system has proven effective in increasing the purity of hydrogen produced as well as the equilibrium conversion [12–14]. The development of highly active and selective catalyst for ESR has been rigorously pursued. Noble metal catalysts like Rh, Pt, Pd, Ir, and Ru have all exhibited high activity and stability for ESR [15–21]. However, these

catalysts are not suitable for industrial level hydrogen production due to their cost. Therefore, non-noble metal catalysts particularly Ni, Co and Cu have been widely used for ESR [15,22–27]. These catalysts are prone to deactivation and significant methane formation which leads to difficulties in product separation. To suppress this, various costly, high performing acidic oxide, basic oxide and complex mixed oxide support materials have been proposed. The supports help to improve catalyst stability and metal dispersion. Some supports take active roles in the reaction mechanism which could improve catalytic activity.

The aim of this research work is to develop a comprehensive and consistent microkinetic model which would serve as a tool for the future design of high-performance catalyst systems for hydrogen production *via* the steam reforming of ethanol and larger biomass derived oxygenates.

1.1. Research Objectives

The specific objectives of this work are as follows:

- i. Initially a monofunctional microkinetic model is developed and validated using ESR experiments over a metal dominated catalysts (inert support), to form a baseline and reference point.
- ii. The consistency of the developed model is examined by adapting the model to simulate the dry reforming of biogas and investigate the effect of industrially relevant co-feeding of products to biogas dry reforming process.
- iii. The effect of active support materials is then incorporated into the microkinetic model making it a bifunctional model capable of simulating single or multiple active sites. The model is then validated using ESR experiments over a metal and active support catalyst system.
- iv. Information obtained from the bifunctional model developed is then used to suggest a possible alternative cost-effective active support material which is experimentally investigated.

In all cases above, suitable case study systems are selected, and validation data are used.

1.1.1 Novelty and contribution of work

The most significant contribution of this work is the development of a fully parametrised bifunctional microkinetic model which incorporates the effect of active support materials, for the ethanol steam reforming process. This model is the first of its kind in literature and provides a good baseline for modelling the steam reforming of larger biomass derived oxygenates. Another contribution is the clarification and elucidation of the reaction pathway of ESR over a

Nickel metal dominated catalyst. This work identified the difference between the decomposition pathway of ethanol over Ni as was postulated in literature and the actual dehydrogenation pathway followed over Ni during steam reforming. This work also provides an explanation for the experimentally observed partial negative reaction order for steam. It is found to be as a result of surface saturation.

1.2. Structure and overview of thesis

This PhD thesis is structured in the *Journal Format* as specified in the University of Aberdeen Presentation of Theses policy. The journal format allows sections of the doctoral thesis to be written in a format suitable for publication in a peer-reviewed journal. A brief summary of the content of the thesis chapters follows.

Chapter 1 provides background information and the objectives of the study.

Chapter 2 presents a review of relevant literature pertinent to the subject matter not covered elsewhere in the thesis. It presents an overview of hydrogen production from biogas, hydrogen production from ethanol, microkinetic modelling, modelling of biogas dry reforming, and modelling of ethanol steam reforming.

Chapter 3 presents the overview of the methodology followed in tackling the first objective of this study. It includes a brief summary of microkinetic analysis and the approach followed in formulating and developing the initial single-site microkinetic model presented in Chapter 4.

Chapter 4 presents the development and validation of a comprehensive microkinetic model for the ethanol steam reforming over a Ni/SiO₂ catalyst. The work presented in Chapter 4 has been published in the International journal of Hydrogen Energy. The details of the publication are:

A.T.F. Afolabi, C.Z. Li, P.N. Kechagiopoulos, Microkinetic modelling and reaction pathway analysis of the steam reforming of ethanol over Ni/SiO₂, Int. J. Hydrogen Energy. 44 (2019) 22816–22830. <https://doi.org/10.1016/j.ijhydene.2019.07.040>.

The chapter presents a model that successfully describes the overall reaction pathway, decomposition pathway, product formation pathways, kinetically relevant intermediate species and rate determining step for the ESR process over the Ni metal with inert support.

Chapter 5 presents the development and validation of a microkinetic model capable of simulating biogas dry reforming experiments over a Rh/Al₂O₃ catalyst. The work presented in Chapter 5 has been submitted to the Chemical Engineering Journal. The details of the publication are:

A Navarro-Puyuelo, A.T.F. Afolabi, P.N. Kechagiopoulos, F. Bimbela, L.M. Gandia, Investigation of H₂ and CO co-feeding on biogas dry reforming over Rh/Al₂O₃ catalyst *via* microkinetic modelling.

The model presented correctly predicts the reaction mechanism and pathway for biogas dry reforming and successfully reproduces the effect of co-feeding hydrogen and carbon monoxide alongside biogas. The model clearly demonstrates the effects the recycled products co-fed to the reactor has on the reaction pathway and surface reaction mechanism.

Chapter 6 presents the development and validation of a consolidated bifunctional microkinetic model for the steam reforming of ethanol over a Ni catalyst with a ceria containing support. The work presented in Chapter 6 is under review for submission.

A.T.F. Afolabi, P.N. Kechagiopoulos, Microkinetic evaluation of the bifunctional mechanism of ethanol steam reforming over Ni/CeZrLa.

The presented model provides the first intrinsic microkinetic analysis that incorporates the effect of support materials on the reaction pathway and mechanism of ethanol steam reforming process. The model correctly describes the support activity alterations to the decomposition pathway and product formation pathways.

Chapter 7 presents a kinetic study of ethanol steam reforming and ethanol decomposition over a wide range of experimental conditions in a fixed-bed reactor aimed at elucidating the reaction mechanism over a biochar supported Ni catalyst. The work presented in Chapter 7 has been published in the Fuel Processing Technology journal. The details of the publication are:

A.T.F. Afolabi, P.N. Kechagiopoulos, Y. Liu, C.Z. Li, Kinetic features of ethanol steam reforming and decomposition using a biochar-supported Ni catalyst, Fuel Processing Technology. 212 (2021) 106622. <https://doi.org/10.1016/j.fuproc.2020.106622>.

Biochar which is obtained from biomass sources has surface O-containing functional groups and intrinsic alkali and alkaline earth metals, and it has proven to be catalytically active for tar destruction and steam reforming as well as steam reforming of acetic acid.

Chapter 8 presents a summary and critical evaluation of this work. Recommendations on the future direction for research are also made in this chapter.

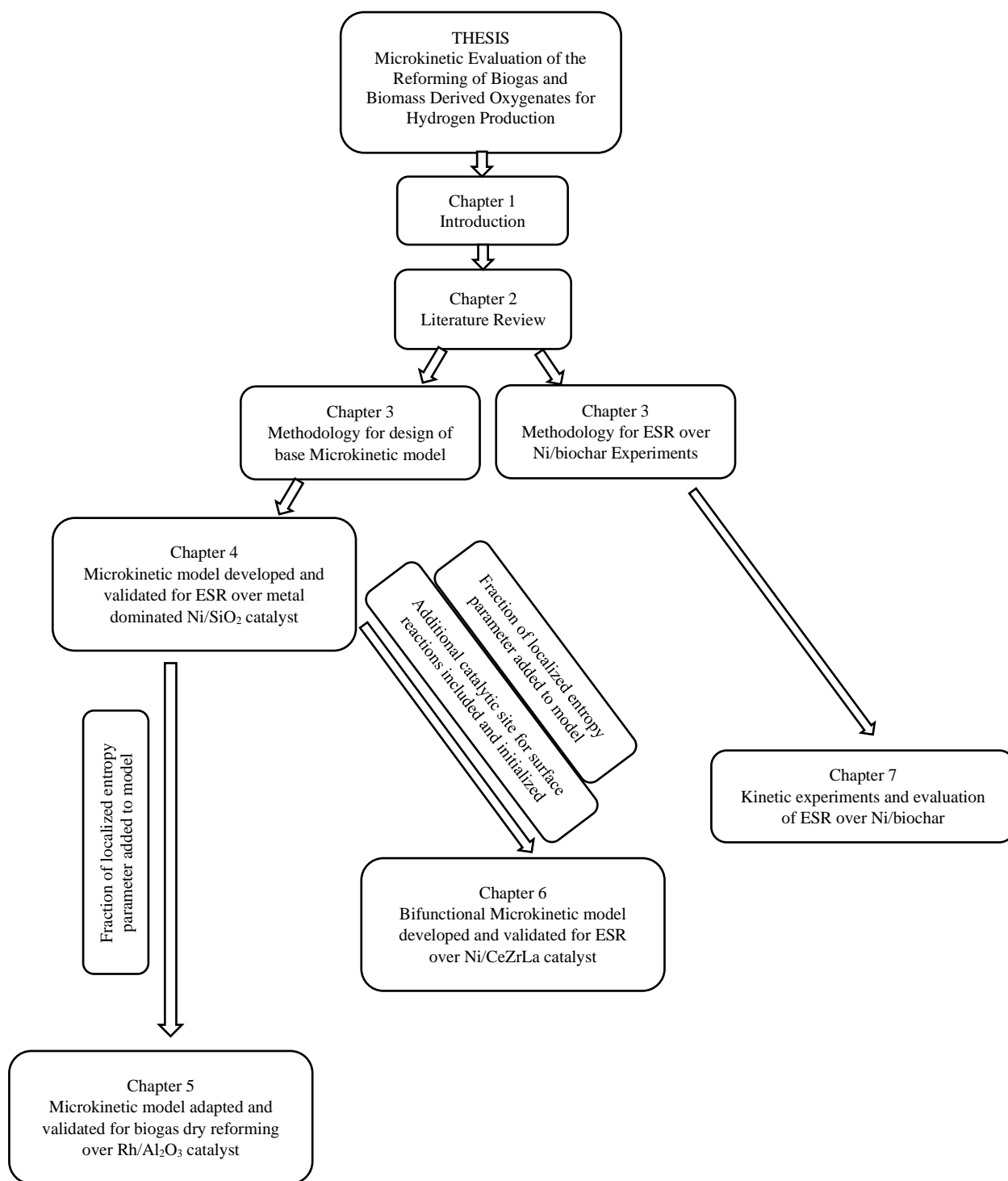


Figure 1-1: A hierarchical flow chart providing some insight as to the connection between chapters.

1.3. References

- [1] IEA, World Energy Outlook 2012: OECD Publishing, 2012.
- [2] M. Zerta, P.R. Schmidt, C. Stiller, H. Landinger, Alternative World Energy Outlook (AWEO) and the role of hydrogen in a changing energy landscape, *Int. J. Hydrogen Energy*. 33 (2008) 3021–3025. <https://doi.org/10.1016/j.ijhydene.2008.01.044>.
- [3] Y. Zhang, T.R. Brown, G. Hu, R.C. Brown, Comparative techno-economic analysis of biohydrogen production via bio-oil gasification and bio-oil reforming, *Biomass and Bioenergy*. 51 (2013) 99–108. <https://doi.org/10.1016/j.biombioe.2013.01.013>.
- [4] M. Ni, D.Y.C. Leung, M.K.H. Leung, A review on reforming bio-ethanol for hydrogen production, *Int. J. Hydrogen Energy*. 32 (2007) 3238–3247. <https://doi.org/10.1016/j.ijhydene.2007.04.038>.
- [5] H. Katuwal, A.K. Bohara, Biogas: A promising renewable technology and its impact on rural households in Nepal, *Renew. Sustain. Energy Rev.* 13 (2009) 2668–2674. <https://doi.org/10.1016/j.rser.2009.05.002>.
- [6] Z. Hou, P. Chen, H. Fang, X. Zheng, T. Yashima, Production of synthesis gas *via* methane reforming with CO₂ on noble metals and small amount of noble-(Rh-) promoted Ni catalysts, *Int. J. Hydrogen Energy*. 31 (2006) 555–561. <https://doi.org/10.1016/j.ijhydene.2005.06.010>.
- [7] O. Omoregbe, H.T. Danh, C. Nguyen-Huy, H.D. Setiabudi, S.Z. Abidin, Q.D. Truong, D.V.N. Vo, Syngas production from methane dry reforming over Ni/SBA-15 catalyst: Effect of operating parameters, *Int. J. Hydrogen Energy*. 42 (2017) 11283–11294. <https://doi.org/10.1016/j.ijhydene.2017.03.146>.
- [8] C. Wang, Y. Zhang, Y. Wang, Y. Zhao, Comparative Studies of Non-noble Metal Modified Mesoporous M-Ni-CaO-ZrO₂ (M = Fe, Co, Cu) Catalysts for Simulated Biogas Dry Reforming, *Chinese J. Chem.* 35 (2017) 113–120. <https://doi.org/10.1002/cjoc.201600609>.
- [9] L.C.S. Kahle, T. Roussière, L. Maier, K. Herrera Delgado, G. Wasserschaff, S.A. Schunk, O. Deutschmann, Methane dry reforming at high temperature and elevated pressure: Impact of gas-phase reactions, *Ind. Eng. Chem. Res.* 52 (2013) 11920–11930. <https://doi.org/10.1021/ie401048w>.
- [10] M. Galbe, G. Zacchi, A review of the production of ethanol from softwood, *Appl. Microbiol. Biotechnol.* 59 (2002) 618–628. <https://doi.org/10.1007/s00253-002-1058-9>.
- [11] Y. Sun, J. Cheng, Hydrolysis of lignocellulosic materials for ethanol production: A review, *Bioresour. Technol.* 83 (2002) 1–11. [https://doi.org/10.1016/S0960-8524\(01\)00212-7](https://doi.org/10.1016/S0960-8524(01)00212-7).
- [12] T.P.K. Sidhu, A. Govil, S. Roy, Optimal monolithic configuration for heat integrated ethanol steam reformer, *Int. J. Hydrogen Energy*. 42 (2017) 7770–7785. <https://doi.org/10.1016/j.ijhydene.2017.01.008>.
- [13] M. Serra, C. Ocampo-Martinez, M. Li, J. Llorca, Model predictive control for ethanol steam reformers with membrane separation, *Int. J. Hydrogen Energy*. 42 (2017) 1949–1961. <https://doi.org/10.1016/j.ijhydene.2016.10.110>.
- [14] A. Iulianelli, V. Palma, G. Bagnato, C. Ruocco, Y. Huang, N.T. Veziroğlu, A. Basile, From bioethanol exploitation to high grade hydrogen generation: Steam reforming

- promoted by a Co-Pt catalyst in a Pd-based membrane reactor, *Renew. Energy*. 119 (2018) 834–843. <https://doi.org/10.1016/j.renene.2017.10.050>.
- [15] D. Zanchet, J.B.O. Santos, S. Damyanova, J.M.R. Gallo, J.M.C. Bueno, Toward understanding metal-catalyzed ethanol reforming, *ACS Catal.* 5 (2015) 3841–3863. <https://doi.org/10.1021/cs5020755>.
- [16] L. V Mattos, G. Jacobs, B.H. Davis, F.B. Noronha, Production of hydrogen from ethanol: Review of reaction mechanism and catalyst deactivation, *Chem. Rev.* 112 (2012) 4094–4123. <https://doi.org/10.1021/cr2000114>.
- [17] R. Baruah, M. Dixit, A. Parejiya, P. Basarkar, A. Bhargav, S. Sharma, Oxidative steam reforming of ethanol on rhodium catalyst – I: Spatially resolved steady-state experiments and microkinetic modeling, *Int. J. Hydrogen Energy*. 42 (2017) 10184–10198. <https://doi.org/10.1016/j.ijhydene.2017.03.168>.
- [18] W. Cai, F. Wang, E. Zhan, A.C. Van Veen, C. Mirodatos, W. Shen, Hydrogen production from ethanol over Ir/CeO₂ catalysts: A comparative study of steam reforming, partial oxidation and oxidative steam reforming, *J. Catal.* 257 (2008) 96–107. <https://doi.org/10.1016/j.jcat.2008.04.009>.
- [19] A.C. Basagiannis, P. Panagiotopoulou, X.E. Verykios, Low temperature steam reforming of ethanol over supported noble metal catalysts, *Top. Catal.* 51 (2008) 2–12. <https://doi.org/10.1007/s11244-008-9130-z>.
- [20] D.K. Liguras, D.I. Kondarides, X.E. Verykios, Production of hydrogen for fuel cells by steam reforming of ethanol over supported noble metal catalysts, *Appl. Catal. B Environ.* 43 (2003) 345–354. [https://doi.org/10.1016/S0926-3373\(02\)00327-2](https://doi.org/10.1016/S0926-3373(02)00327-2).
- [21] F. Wang, W. Cai, Tana, H. Provendier, Y. Schuurman, C. Descorme, C. Mirodatos, W. Shen, Ageing analysis of a model Ir/CeO₂ catalyst in ethanol steam reforming, *Appl. Catal. B Environ.* 125 (2012) 546–555. <https://doi.org/10.1016/j.apcatb.2012.06.023>.
- [22] D.R. Sahoo, S. Vajpai, S. Patel, K.K. Pant, Kinetic modeling of steam reforming of ethanol for the production of hydrogen over Co/Al₂O₃ catalyst, *Chem. Eng. J.* 125 (2007) 139–147. <https://doi.org/10.1016/j.cej.2006.08.011>.
- [23] I. Llera, V. Mas, M.L. Bergamini, M. Laborde, N. Amadeo, Bio-ethanol steam reforming on Ni based catalyst. Kinetic study, *Chem. Eng. Sci.* 71 (2012) 356–366. <https://doi.org/10.1016/j.ces.2011.12.018>.
- [24] P. Biswas, D. Kunzru, Steam reforming of ethanol for production of hydrogen over Ni/CeO₂ - ZrO₂, *Int. J. Hydrogen Energy*. 32 (2007) 969–980. <https://doi.org/10.1016/j.ijhydene.2006.09.031>.
- [25] Y.J. Wu, J.C. Santos, P. Li, J.G. Yu, A.F. Cunha, A.E. Rodrigues, Simplified kinetic model for steam reforming of ethanol on a Ni/Al₂O₃ catalyst, *Can. J. Chem. Eng.* 92 (2014) 116–130. <https://doi.org/10.1002/cjce.21773>.
- [26] A.N. Fatsikostas, X.E. Verykios, Reaction network of steam reforming of ethanol over Ni-based catalysts, *J. Catal.* 225 (2004) 439–452. <https://doi.org/10.1016/j.jcat.2004.04.034>.
- [27] J.W.C. Liberatori, R.U. Ribeiro, D. Zanchet, F.B. Noronha, J.M.C. Bueno, Steam reforming of ethanol on supported nickel catalysts, *Appl. Catal. A Gen.* 327 (2007) 197–204. <https://doi.org/10.1016/j.apcata.2007.05.010>.

CHAPTER 2: LITERATURE REVIEW

This chapter will provide a broad review of works previously carried out by other researchers focusing on hydrogen production from biogas, biogas dry reforming, hydrogen production from ethanol, ethanol steam reforming, kinetic modelling, modelling of biogas dry reforming and modelling of ethanol steam reforming. In addition, the key gaps and challenges identified in all the topics and tackled in the course of this research will be highlighted in the text.

2.1 Hydrogen Production from Biogas

2.1.1 Biogas

Biogas is a valuable renewable energy carrier produced from biodegradable organic materials *via* anaerobic digestion. The organic materials could be obtained from sources such as sewage sludge, landfills, animal farm manure, energy crops, commercial composting sites and agro-food industry wastes. The methane content of biogas depends on the nature of the substrate used. Biogas obtained *via* the anaerobic digestion of sewage sludge, energy crop waste and animal manure are generally composed of methane (CH₄) (55-70%), carbon dioxide (CO₂) (30-45%) and impurities like nitrogen (N₂), oxygen (O₂), water vapour (H₂O), hydrogen sulphide (H₂S), carbon monoxide (CO), ammonia (NH₃), siloxanes and aromatics [1]. The methane produced from these sources has similar commercial and heating value to that of natural gas with the added advantage of having an almost zero net CO₂ contribution [2]. Increasing amount of research has gone into studying biogas utilization pathways, including the traditional pathways of heat and energy generation and other upgrading technologies. The production of synthesis gas (a mixture of hydrogen (H₂) and CO) *via* reforming of biogas has garnered substantial attention as the produced synthesis gas serves as a key intermediate in the chemical industry for the production of biofuels, petrochemicals and most importantly pure hydrogen [3–6].

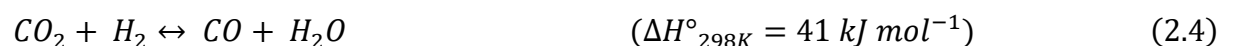
Of the reforming technologies, steam reforming is the most popularly used in industry for hydrogen production. An estimated 80-85% of the worlds produced H₂ is obtained *via* methane steam reforming [7]. Traditionally in industrial hydrogen production *via* methane steam reforming process usually involves the implementation of product gas recycling to improve process efficiency and also help improve process heat energy efficiency. The main biogas steam reforming reaction is usually accompanied by a water-gas shift reaction as seen in equations 2.1 and 2.2.



Ni-based catalyst are the most used during biogas (methane) steam reforming as they assure high activity and lower cost compared to precious metal-based catalysts. However, improved catalyst performance in terms of yield and carbon capture have been the object of continuous study in recent years. For example, recently Phromprasit et al. [8] developed a Ni catalyst with Ce and Zr doped over CaO for sorption enhanced steam reforming to improve hydrogen purity. In the study they found that Zr and Ce doped CaO provided stable CO₂ capture activity for 10 sorption/desorption cycles mainly due to their oxygen storage capacity at low temperatures which promotes the diffusion of CO₂ between the bulk and surface. High purity hydrogen (90% and 85%) was produced when Ni was loaded onto the sorption capable catalysts. Conversion of CH₄ was found to decrease significantly over 5 sorption/desorption cycles as a result of Ni active site loss due to pore closure *via* CaCO₃ formation. Similarly, Daneshmand-Jahromi et al. [9] performed the steam reforming of methane using a Ni/SBA-16 oxygen carrier with a yttrium promoter. They found that the yttrium promoter enhanced the formation of smaller NiO species and led to a better distribution of the metal particles. Ultimately the coke deposition was greatly reduced with the presence of the promoter on the oxygen carrier surface and high CH₄ conversion and hydrogen yield of 99.83 and 85.34% were attained at 650°C and S/C ratio of 2.

2.1.2 Biogas Dry Reforming

Among the existing biogas utilization technologies, dry reforming of biogas offers the added incentive of converting two major greenhouse gases methane and carbon dioxide simultaneously into syngas. The main reaction in biogas dry reforming can be seen in equation 2.3. It is an endothermic reaction with high temperatures in the range of 700-900°C typically needed to promote high conversions towards synthesis gas. Another reaction which typically accompanies the dry reforming reaction is the reverse water-gas shift (RWGS), presented in equation 2.4. This reaction negatively affects the hydrogen yield in the syngas product. However, it provides a proper adjustment of the H₂/CO ratio for the production of higher hydrocarbons [10]. As in steam reforming, the selection and activity of catalyst plays a vital role in the conversion to syngas.



The most common problem facing biogas dry reforming is the deposition of coke which significantly impacts the activity of catalysts by blocking pores, reducing the number of active sites or prompting the collapse of the support [11]. Some of the side reactions which may occur during biogas dry reforming that could lead to coke deposition include the decomposition of CH₄ (equation 2.5), the Boudouard reaction (CO disproportionation) (equation 2.6) and the hydrogenation of CO and CO₂ (equations 2.7 and 2.8).



Based on thermodynamic Gibbs free energy calculations, CH₄ decomposition mainly occurs at temperatures above 553°C, while the Boudouard reaction occurs at temperatures below 700°C. Hence, during biogas dry reforming coke deposition is mainly likely to occur within the temperature range of 553-700°C [12]. The ratio of carbon, hydrogen and oxygen in the biogas feed also affect the tendency for coke deposition. Lower H/C ratio as well as lower O/C ratio will increase the coke formation tendency, therefore, coke deposition is more likely to occur during dry reforming than in steam reforming.

2.1.3 Catalysts for biogas dry reforming.

2.1.3.1 Metals

Noble metals such as Pt, Pd, Ir, Rh and Ru as well as non-noble metals such as Ni, Co and Fe have been widely studied in catalysis for the dry reforming of biogas. Non-noble metal catalysts have gained interest mainly due to their relatively low cost. Amongst the non-noble metals, the most frequently studied and used in industry is Ni [10].

Charisiou et al. [13] performed biogas dry reforming over an 8.0 wt.% Ni/Al₂O₃ catalyst with a CH₄/CO₂ ratio of 1.5:1 at 850°C and obtained reactant conversions of 72 and 92% for CH₄ and CO₂, respectively. Omoregbe et al. [14] obtained high conversions of 91 and 94% for CH₄ and CO₂ respectively whilst performing biogas dry reforming over a 10 wt.% Ni/SBA-15 catalyst at 750°C. Akbari et al. [15] investigated the effect of Ni loading on reactant conversion during biogas dry reforming over a Ni-MgO-Al₂O₃ catalyst by varying the Ni content between 2.5-15.0 wt.%, they observed an increase in reactant conversions as the Ni loading was increased.

The biggest setback in the application of Ni (as well as other non-noble metals) single-metal based catalysts is the apparent carbon deposition usually observed [14,16,17]. In order to resolve this issue, recent studies have explored the performance of Ni-based bimetallic catalysts, modified with noble or other non-noble transition metals. Hou et al. [18] investigated the effects of modifying Ni/Yas3-8 catalyst with small amounts of Rh on the catalytic performance during biogas dry reforming. They observed no carbon deposition occurring when the ratio of Rh/Ni was above 0.1. They also found the reforming activity was improved with CH₄ and CO₂ conversions increasing to approximately 80% when 5 wt.% Rh was added, from respective values of 62 and 68.4% when pure Ni/Yas3-8 was used. Similarly, Luisetto et al. [19] investigated a Ru-promoted Ni/ γ -Al₂O₃ catalyst and found improved catalytic activity and stability when compared with the Ni/ γ -Al₂O₃ catalyst. Wang et al. [20] also investigated biogas dry reforming with a CH₄/CO₂ ratio of 1:1 over a Ni/CaO-ZrO₂ modified with non-noble metals Cu, Co and Fe. The catalytic activity was improved with the addition of all three metals individually compared to the pure Ni catalyst. The Co-Ni bimetallic catalyst proved to be the most stable and suitable due to the electron interactions between the metals which help suppress the formation of coke deposition species. Xu et al. [21] similarly found that the addition of Co to Ni based catalyst Ni/ γ -Al₂O₃-La₂O₃ increased the stability of the catalyst as the Co was found to improve CO₂ adsorption due to strong Co-O interactions, thereby reducing the carbon deposition.

Noble metal catalysts on the other hand are very attractive as single-metal based catalysts due to their high catalytic activity and resistance to carbon deposition and deactivation. Hou et al. [18] performed a systematic evaluation of different noble metal catalysts for biogas dry reforming. 5 wt.% of Rh, Ru, Pd, Pt and Ir were loaded onto α -Al₂O₃ supports and used for dry reforming biogas with a CH₄/CO₂ ratio of 1:1. The results showed Rh as having the highest catalytic activity and stability over the other four noble metals.

2.1.3.2 Supports

The main role of support materials is to provide large surface areas to allow for better dispersion of metal active sites. It is also believed that biogas dry reforming could possibly follow a bifunctional mechanism where CH₄ is activated on the metal whilst the acidic or basic support is responsible for activating the CO₂ [22,23]. The most commonly studied supports include SiO₂, Al₂O₃, MgO, ZrO₂, TiO₂, La₂O₃ and CeO₂. SiO₂ is a relatively inert support material as it has quite weak interactions with metal and is therefore less active than the other

supports. It is however very stable and relatively cheap and is therefore commonly applied in catalysts.

Al₂O₃ is a mildly acidic support material used in catalysts. The most common crystal structures used in industry are α -Al₂O₃ and γ -Al₂O₃. Bychkov et al. [24] evaluated the behaviour of α -Al₂O₃, θ -Al₂O₃ and γ -Al₂O₃ as a support for Ni in biogas dry reforming. It was found that the catalytic activity and coke deposition resistance of γ -Al₂O₃ supported Ni catalyst was the best whilst the α -Al₂O₃ had the worst performance. Sokolov et al. [25] performed low-temperature biogas dry reforming with a CH₄/CO₂ ratio of 1:1 over a Ni based catalyst using different support materials (Al₂O₃, MgO, TiO₂, SiO₂ and ZrO₂). The results showed that the basic supports (ZrO₂ > TiO₂ > MgO) performed better in terms of hydrogen yield than the mildly acidic Al₂O₃ which in turn performed better than the inert SiO₂. Min et al. [26] systematically evaluated the performance of a mixed support 15 wt.% Ni-based catalyst for dry reforming. Different ratios of Mg/Al were tested, and they found higher catalytic activity and stability at Mg/Al ratios of 0.78-6.2. The basic MgO enhanced the adsorption of CO₂ which would react with C and reduce the carbon deposition.

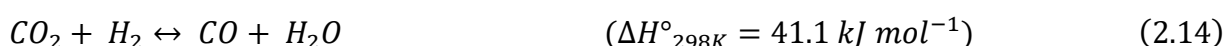
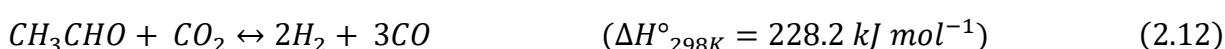
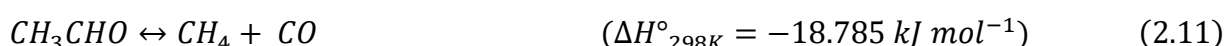
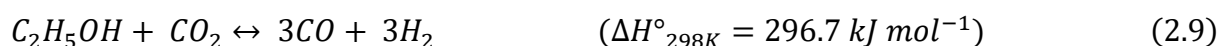
2.2 Hydrogen Production from Oxygenated hydrocarbons

2.2.1 Ethanol

Oxygenated hydrocarbons serve as a good fuel source for endothermic reforming processes which require high temperatures, as they complement the amount of heating required and therefore could save costs. Amongst the various renewable feedstocks for oxygenated hydrocarbons, ethanol is a very alluring option as it has a relatively high hydrogen content, it is widely available, non-toxic and easy to store and handle safely. Ethanol can be produced from a renewable biomass sources such as energy crops, municipal solid waste, agricultural wastes and forestry residues. The utilisation of bio-ethanol therefore has no net contribution to greenhouse gases. Processes such as pyrolysis, gasification and reforming have been developed to utilize bio-ethanol. The reforming of bio-ethanol to produce hydrogen has however garnered the most attention as it is one of the processes likely to drive a future hydrogen economy.

Dry reforming of ethanol is a process with higher risk of coke deposition and lower hydrogen yields it is therefore not as tenable as steam reforming. It is however gaining renewed interest in the catalysis community due to its CO₂ emission reduction potential. The main reaction in the dry reforming of ethanol produces equal amounts of H₂ and CO (equation 2.9). Thermodynamic analysis predicts that CH₄, CO₂, H₂O, H₂, C and CO are all possible products formed during ethanol dry reforming. Ethanol may dehydrogenate towards acetaldehyde (CH₃CHO) (equation

2.10), which further decomposes to form CH₄ and CO (equation 2.11). CH₃CHO can also be reformed into syngas (equation 2.12). Methane reforming and reverse water-gas shift reactions are also observable (equations 2.13 and 2.14). Thermodynamic analysis showed that reaction temperatures in the range of 927-1027°C and CO₂/ethanol ratios of 1.2-1.3 are the ideal conditions where complete conversion of ethanol can be achieved with an acceptable amount of carbon formation [27].

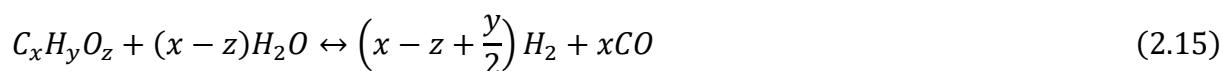


Various noble and non-noble metal-based catalysts are synthesized and used for the dry reforming of ethanol. Ni based catalysts are the most studied in literature. Bej et al. [28] synthesized an Al₂O₃ supported nano NiO-SiO₂ catalyst for dry reforming of ethanol. With 10 wt.% Ni loading demonstrating the best activity, optimal conditions were found at 750°C and a CO₂/ethanol ratio of 1.4. At this condition nearly complete conversion of ethanol was achieved with an accompanying 75% conversion of CO₂. The catalyst did however promote the dehydrogenation of ethanol towards CH₄ and water-gas shift reaction thereby reducing the CO yield. Zawadzki et al. [29] evaluated the performance of Al₂O₃, CeO₂, MgO and ZrO₂ supported Ni-based catalyst for dry reforming of ethanol. Ni-CeO₂ was found to have the best performance at 750°C with high conversion and inhibited carbon deposition. The reducibility of Ni which was affected by the support, as well as the redox properties and oxygen vacancies of the CeO₂, promoted the H₂ selectivity and inhibited unwanted side reactions. This process is however of lesser interest to this study as the hydrogen yield potential pales in comparison to steam reforming.

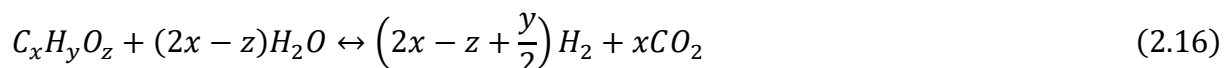
2.2.2 Ethanol steam reforming

Steam reforming is the most popular and established reforming technology for hydrogen production in the industry. A substantial amount of research has gone into optimising the performance of this technology for a variety of hydrocarbon fuel sources including oxygenated hydrocarbons and heavy hydrocarbons.

The general reaction scheme for the steam reforming of oxygenated hydrocarbons is;

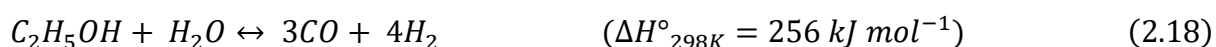


Combining this reaction with WGS at temperatures and pressures favouring the reaction shift to the right we get:

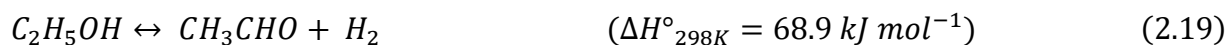


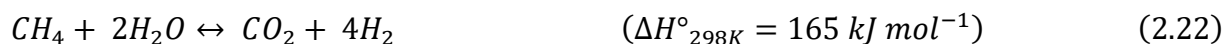
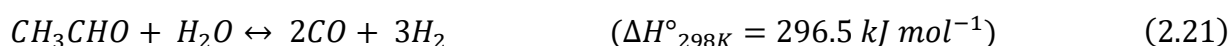
The reforming reaction of oxygenates like conventional reforming is also endothermic and therefore favours high temperatures and low-pressure operating conditions. At high temperatures however CO will be present in substantial amount as the WGS reaction equilibrium will shift to the left. Methanation, as well as thermal decomposition, will also influence the product distribution, the latter however should be minimised as it will lead to coke formation and catalyst degradation. Theoretically, thermodynamics proposes a possible full conversion of oxygenates whilst equilibrium regulates the product distribution. For high yields of H₂ a catalyst that promotes WGS is required. The ratio of CO/H₂ depends on the operating temperature as well as the steam to carbon ratio of the feed. For high amounts of hydrogen, meaning a lower CO/H₂ ratio, increasing the steam to carbon ratio is prescribed. The main challenge this technology faces is the deactivation of catalysts due to coke formation as well as metal sintering at high operating temperatures.

For ethanol steam reforming the main reaction with and without excess supply of steam can be written as follows:



Ethanol is highly likely to dehydrogenate towards acetaldehyde (equation 2.19) which serves a reaction intermediate and decomposes to form CH₄ and CO (equation 2.20) [30,31]. The formation of acetaldehyde is an endothermic reaction of lower magnitude in comparison with the steam reforming reaction. The steam reforming of acetaldehyde may also occur (equation 2.21). At ideal conditions, the formed CH₄ may undergo steam reforming to produce hydrogen and CO or CO₂ (equation 2.22 and 2.23). CO will undergo water-gas shift to produce CO₂ and H₂ (equation 2.24).





Ethanol steam reforming has a wide range of operating temperature, ranging from 300-650°C [32–34]. At temperatures as low as 350°C and at atmospheric pressure, total conversion of ethanol is achievable in the presence of a catalyst. The selection of catalyst and support material also affects the formation of coke, as some supports could either promote the dehydration of ethanol to ethylene or inhibit the dehydration and promote the dehydrogenation to acetaldehyde.

2.2.3 Catalysts for ethanol steam reforming

2.2.3.1 Metals

Catalyst play an important role in the reactivity towards complete ethanol conversion, however, the pathways induced by catalysts vary, therefore it is crucial to select active catalysts able to maximize hydrogen production by pushing the water-gas shift and inhibiting coke formation. Various noble metal-based (Rh, Ru, Pt, Pd) and non-noble metal-based (Ni, Co, Cu and Fe) [21,35–40] catalysts have been widely studied for this purpose.

Noble metal catalysts are more resistant to coke deactivation and are known for their high catalytic activities. Liguras et al. [41] evaluated the performance of Rh, Ru, Pt and Pd catalysts supported by Al₂O₃ for ethanol steam reforming in the temperature range of 600-850°C. The metal loading was varied in the range of 0-5 wt.%. Rh displayed the highest activity through the range of loadings, however, at 5 wt% loading the Ru/Al₂O₃ showed comparable activity to Rh. Complete conversion of ethanol was achieved by both catalysts with hydrogen selectivity of above 95%. In terms of the stability and coke deposition, the selection of mildly acidic Al₂O₃ support promoted the dehydration of ethanol forming ethylene, which is known as a coke precursor. With the same catalyst and support, Cavallaro et al. [42] was able to inhibit the formation of coke by increasing the steam/ethanol ratio. Similarly, Frusteri et al. [43] also investigated the catalytic performance of Pd, Rh, Ni and Co-based catalysts supported by MgO for hydrogen production during ethanol steam reforming. The Rh/MgO catalyst was found to be the most active with the highest conversion and least coke deposition. Ni/MgO however, had the

highest hydrogen selectivity. Of the noble metal catalysts, the consensus that can be extracted from literature is that Rh-based catalyst are the most efficient for the reforming process.

Non-noble transition metal catalysts like Ni and Co are widely studied owing to their high activity and relatively cheap cost. Co attracts interest due to its high activity and lower formation of side products CH₄ and coke compared to Ni [44,45]. However, Ni has high C-C cleavage activity and is therefore highly attractive for the steam reforming of ethanol. Comas et al. [46] investigated the steam reforming of bio-ethanol over a Ni/Al₂O₃ catalyst operating in the temperature range of 300-500°C, with a Ni loading of 35 wt.%. At 500°C and high steam to ethanol ratio (6:1), 91% hydrogen selectivity was achieved. However, they observed low CO₂ selectivity (<80%) and therefore surmised that the pathway involved ethanol dehydrogenating to acetaldehyde and dehydrating to ethylene. Both intermediates would then be converted into the final products. The high CO₂ selectivity observed by Auprete et al. [47] whilst performing ethanol steam reforming using the same catalyst with a lower Ni wt.% loading, and operating in the same temperature range, provide a contradiction. This may, however, be as a result of the different Ni wt.% loading used. Zhang et al. [32] performed the steam reforming of ethanol over a Ni/Al₂O₃ catalyst and investigated the effect of modifying the catalyst with the addition of a second metal (Co and La) and second support SiO₂. The selectivity of hydrogen was significantly improved with the addition of Co (72.7%) and La (68.6%). In summary, Ni exhibits excellent catalytic activity for ethanol steam reforming at high temperatures, however coke deposition is an issue which requires the use of a basic or redox support material and high steam to ethanol ratios.

2.2.3.2 Supports

Various types of oxides have been extensively studied as support materials for Ni, in order to guarantee thermal stability as well as optimum metal dispersion and also participate in the catalytic process [39,48–52]. Acidic oxides like Al₂O₃, TiO₂, SiO₂ have been employed to improve the ethanol conversion during reforming. Of the acidic oxides, Al₂O₃ is the most intensively used for ethanol steam reforming process due to its strong mechanical and thermal stability. However, acidic oxide supports induce the dehydration of ethanol towards ethylene and at high temperatures will decompose ethylene and produce coke. Basic oxides such as La₂O₃, MgO and ZnO on the other hand strengthen the interactions between metal and support and reduce the surface acidity of the catalyst and consequently reduce carbon deposition. The catalytic performance over these basic oxide supports is dependent on the operating conditions as well as metal wt.% loading. Yang et al. [53] evaluated the performance of 10 wt.% Ni

supported by La_2O_3 , MgO , ZnO and Al_2O_3 for the steam reforming of ethanol at 650°C . Complete conversion of ethanol was achieved in all cases however the hydrogen selectivities of the basic oxide supported catalysts were better than that of $\text{Ni}/\gamma\text{-Al}_2\text{O}_3$. While acidic oxides generally provide better ethanol conversion than the basic oxides [54], the basic oxides provide better hydrogen selectivity as they inhibit coke deposition. To neutralize this effect, acid oxide supports are modified with a basic oxide promoter in order to neutralize the acid sites and inhibit ethanol dehydration. Sanchez et al. [55] observed that $\text{Ni}/\text{MgO-Al}_2\text{O}_3$ exhibited better catalytic performance than $\text{Ni}/\text{Al}_2\text{O}_3$.

The redox property and strong metal-support interaction proffered by CeO_2 has made it widely studied as an ideal support material for ethanol steam reforming. CeO_2 has the ability to store and release active oxygen due to its high oxygen storage capacity, it is therefore able to perform water and/or oxygen activation. It can also serve as an anchor with the ability to disperse and stabilise active materials.

To summarise, the choice of support material plays a vital role in catalytic activity, product distribution and stability. The support materials are able to participate in the reaction mechanism and can provide acidic sites to promote dehydration, basic sites that push dehydrogenation or provide sites for activation of reactants.

2.2.3.3 *Biochar as a support material*

Reviews on the progress and advances in ethanol steam reforming over non-noble transition metals [56] and Ni specifically [57], highlight as summarised above the importance of support materials on enhancing catalyst stability and performance. However, to achieve optimal performance, intricate design of catalysts with supported mixed oxides or modifications using a variety of materials are required [58]. This inevitably increases the cost of catalyst production and the process in a commercial context.

Biochar is the solid product of biomass pyrolysis and/or partial gasification. It is a cheap, highly porous material and has recently began receiving significant attention as a possible catalyst or support material for several reaction including hydrolysis, (trans)esterification and reforming [59]. Recently, the catalytic cracking and steam reforming of tar and its model compounds by biochar-based catalysts have become emphasised in literature [60], with various studies emphasising the high reforming and tar destruction activity of biochar-based catalysts [61–64]. Additionally, through gasification or combustion the energy value of spent biochar can be recovered, hence reducing the energy loss during the process and disposal costs [65–67]. The properties of intrinsic alkali and alkaline earth metallic (AAEM) species in biochar have been

shown to contribute to its catalytic activity [67–69]. Biochar produced from pyrolysis and subsequent gasification usually has a high concentration of O-containing functional groups [70]. The importance of the O-containing functional groups to the activity of biochar have been demonstrated in previous studies [67,71].

Therefore, utilising biochar as a support material for Ni in the reforming process would help reduce the overall cost and enhance its sustainability. The inherent content of surface oxygen containing groups and alkali and alkaline earth metals could provide additional available sites and functionalities, which could potentially improve the stability of the catalyst. **There is an evident scarcity in literature regarding the use of biochar as a catalyst or support for the steam reforming of small, non-aromatic biomass derived oxygenates and the investigation of kinetics for such reaction processes. The steam reforming of acetic acid has been studied recently on Ni/biochar [61,72], however no similar works exist for ethanol. The intrinsic kinetic effect a biochar support would possibly have on the adsorption and reaction pathway in the ethanol reforming process remains unclear.**

2.3 Kinetic modelling

The kinetic modelling of reforming in literature is usually executed in form of macrokinetics or microkinetics.

2.3.1 Closed form empirical kinetic models

Macrokinetic models or closed-form empirical kinetic models are mainly of two types: Power-law kinetics and Langmuir-Hinshelwood-Hougen-Watson (LHHW) models.

2.3.1.1 Power-law kinetics

During the earlier periods of kinetic modelling and limited computational power, the power-law was the most popular and utilised rate expression. This type of model involves the use of a known activation barrier, effective rate constant and reaction orders of the reactants to estimate the reaction rate as shown in equation 2.25 below,

$$r = k_{eff} C_A^a C_B^b, \quad k_{eff} = A_{eff} e^{-E_{eff}/RT} \quad (2.25)$$

This type of model is frequently used in reactor modelling as well as process design due to its computational ease and small number of parameters. It is able to model very limited range of experimental data and does not have any genuine predictive power. It is therefore not of much importance to this study.

2.3.1.2 *Langmuir-Hinshelwood-Hougen-Watson models*

LHHW models are the more popular of the two macrokinetic models for heterogeneous catalytic reactions. They can be used for reaction mechanisms where an adsorption step of a reactant is present. Developing a LHHW model begins with defining a detailed surface reaction mechanism. Essential to developing this model type is the *a priori* determination of the rate determining step (RDS). Typically, the RDS is selected as a reaction involving exclusively surface species, whilst the adsorption and desorption reaction steps are usually assumed to be in some state of partial equilibrium (PE). A rate expression is then formed based on the choice of RDS and the equilibrium constants of other steps. The validity of this rate expression is tested against experimental data and a qualitative fit of data is desired. If the rate expression does not fit data, then different assumptions are made on selecting the RDS until a qualitative fit is achieved. Once qualitative fit is achieved the rate constants and equilibrium constants are regressed using select experimental data from a particular type of experiment.

One drawback of this type of models is the rate expression and rate constant multiplicity described in the assessment of overall rate expressions performed by Prasad et al. [74]. The empirical nature of the rate expressions in this method makes it possible that multiple rate expressions can describe the same data with similar accuracy. Also, it is possible that different values of the rate constants will make the same rate expression fit selected experimental data. Additionally, the selected rate expression may be based on wrong assumptions, or the regressed parameters may prove to be unrealistic values. If this is the case, the model predictions of the fundamental properties of the reaction mechanism (i.e., reaction orders or most abundant surface intermediate), would be unreliable and inaccurate. Also noteworthy, is that these rate expressions are unable to describe any changes in RDS when operating conditions vary and are therefore limited to specific range of operating conditions where the rate steadily changes with a change in parameter.

Examples of LHHW models developed for the reforming reactions, which are of particular interest in this study, are given in subsequent sections to highlight these limitations and drawbacks.

2.3.2 *Mean-field Microkinetics*

Microkinetic modelling entails the use of comprehensive reaction mechanisms depicting elementary reaction steps taking place on catalyst surfaces. The need for these comprehensive mechanisms is made clear when considering the aforementioned limitations of closed form empirical kinetic models. The main framework for microkinetic modelling used today was first

properly laid out in the book of Dumesic et al. [73] All relevant elementary steps capturing the essential surface chemistry of the process are presented in these models. No assumptions on the RDS and most abundant surface intermediate are made when solving the system of mathematical equations. These detailed kinetic models offer better accuracy and predictive power over a wider range of experimental conditions, when compared to LHHW and power-law expressions which can only be regressed over limited data ranges [74]. Microkinetic models give fundamental insight into the reaction rates of surface intermediate species and the sensitivity of the reaction rate to operation-based or catalyst-based model parameters. Thus, they are a very useful process optimisation tool.

The key first step in microkinetic modelling is the construction of detailed reaction mechanisms. Kinetic codes designed for the study of detailed reaction mechanisms, such as CHEMKIN [75,76], are a useful tool in the microkinetic modelling for the generation of reaction mechanisms. Elementary reaction steps are not unique to any specific chemical process and can be applied to numerous mechanisms involving similar reactants and intermediates [77]. Steam reforming and dry reforming of methane for example, will share a number of elementary reaction steps in common. Also, reaction mechanisms for a process involving larger species could be built from those of smaller species.

In the past there was a lack of extensive parameter estimation methods and the rate constants in microkinetic models were fit to experimental data directly, hence reducing the predictive power of these models. In the past two decades, however, several approaches for accurate parameter estimation have been put to use. First-principles methods like density functional theory (DFT), which require abundant computational power, are widely applied in microkinetic modelling. Semi-empirical methods, which offer relatively inexpensive and reasonably accurate estimation for parameters like activation energy of adsorbates, are also quite popular.

Mean-field microkinetic models are based on the assumption that there is a consistent distribution of catalyst active sites and adsorbate species. The rate constants of surface reactions are therefore taken to be independent of the local environment in which the reaction occurs. These models combine energetics with reaction rates and concentration of species. The elementary reaction steps follow the law of mass action and the reaction rates are written as equation 2.26 below:

$$r_i = k_i \prod_j C_j = A_i \exp\left(-\frac{\Delta E_i}{k_b T}\right) \prod_j C_j \quad (2.26)$$

k_i represents the reaction rate constant, A_i is the pre-exponential factor, ΔE_i is the activation energy, T is the absolute temperature, k_b is the Boltzmann constant, and C_j is the concentration of the reactant.

2.3.3 *Elementary rate constant estimation from semi-empirical methods*

Even though semi-empirical methods are not always as accurate as quantum mechanical methods of rate constant determination (i.e., DFT), their ability to predict kinetic parameters from thermochemistry with high accuracy makes them a relatively inexpensive method for the estimation of kinetic parameters. Hence, they are more suitable when considering mechanisms with a large number of species and reaction steps. These methods relate thermochemical properties of surface species either to atomic properties or to properties of smaller units that make up the species. The thermochemical properties of surface species are also correlated with properties of corresponding gas phase molecules and kinetic parameters.

2.3.3.1 *Unity bond index-quadratic exponential potential (UBI-QEP) or bond order conservation (BOC) method*

The UBI-QEP, or BOC, method is a semi-empirical technique used to estimate the binding energies of molecules from binding energies of atoms and gas-phase dissociation energies [78]. The activation barriers of reactions are estimated by minimizing the energy of a two-body adsorbate specie configuration modelled through a Morse potential. Vlachos and his group were the first to introduce UBI-QEP/BOC based microkinetic models in 1999 [79]. By estimating the activation energies of elementary reaction steps, the UBI-QEP technique-based microkinetic model was able to predict the possible reaction pathways and rate determining step. With reasonable parameter adjustment, they found that microkinetic models using this method are able to provide quantitative fit to wide range of experimental data. The correlation of atomic binding energies to molecular binding energies in this method allows for the estimation of microkinetic model parameters from just atomic binding energies, making this a very useful and powerful tool [80–83].

One of the main advantages of this method is that it allows for easier implementation of enthalpic thermodynamic consistency which will be elaborated in a later section. This method has been found to be very accurate when compared to experimentally determined binding and activation energies [82,84]. It is also able to reasonably describe the effects of surface coverages on activation energies [79]. One limitation, however, is that this method requires experimental data validation to ensure the predicted values of energies are reliable.

2.3.3.2 Estimation of entropic parameters

The pre-exponential factors and sticking coefficients are factors of a reaction rate constant in which entropy plays a role. For activated processes, transition state theory (TST) and vibrational analysis are the common methods of obtaining pre-exponential factors and sticking coefficients, while molecular dynamics (MD) is used for non-activated or low barrier reactions. The determination of partition functions of adsorbed species through first-principles methods (DFT) can prove difficult, therefore, empirical approximation methods are preferred. Reasonable estimations of properties of adsorbed species that are contingent on temperature have been found to be achievable by the simple analysis of the change in degrees of freedom of the corresponding gas phase molecule upon adsorption [85]. The entropy of a surface adsorbed species is therefore relatable to that of the corresponding gas phase species by the simple deduction of the translational degrees of freedom upon adsorption [86–88].

$$S_{i,surf}(T) = F_{loc}(S_{i,gas}(T) - S_{i,trans}(T)) \quad (2.27)$$

The F_{loc} multiplier in equation 2.27, represents the fraction of local entropy that will be retained by the species upon adsorption. This fraction is usually a value close to unity and is mostly used as an adjustable parameter during microkinetic modelling [86].

2.3.3.3 Brønsted-Evans-Polanyi (BEP) relations

The BEP relations is another method that enables the estimation of kinetic parameters from thermochemical properties of adsorbed species [89,90]. It is a more attractive method when considering large reaction systems. Its validity for the estimation of surface reaction properties was only recently proved in the past two decades [91–93]. A fundamental relationship proposed in BEP is:

$$\delta\Delta E_i = \alpha\delta\Delta E_{i,rxn} \quad (2.28)$$

Where the $\delta\Delta E_i$ represents a change in the activation energy, $\delta\Delta E_{i,rxn}$ represents a change in the energy of reaction, and α is a constant related to the reaction classification. In essence, BEP relations enable prediction of activation energies using the energy of reactions (enthalpies or free energies) derived by correlating reaction energies of similar reactions belonging to the same homologous series. Reactions involving species belonging to the same homologous series will have transition states with similar chemical properties. Therefore, if a number of transition state searches are done for reactions having similar transition states (i.e., dehydrogenation or C-C scission) for species within a homologous series, then an estimation of parameters of the rest of

the reactions in the homologous series can be obtained using thermochemistry. Such relationships have been developed in recent literature for different reaction on different metals.

2.3.4 Thermodynamic consistency in microkinetic modelling

Thermodynamic consistency is an important facet of microkinetic modelling that must be considered when the thermodynamic and kinetic parameters of species and elementary reactions are merged during the formulation of kinetic mechanisms. There are two key reasons why thermodynamic consistency is crucial during model development. Firstly, for reaction mechanisms that involve reversible and therefore equilibrium limited processes, the equilibrium constants of reactions are directly linked to thermodynamic properties. Hence if the thermodynamics of the process are not consistent and equilibrium constants are wrong, the predictions of the microkinetic model would be grossly misleading. Secondly, for reactions occurring under non-isothermal conditions, discrepancies in the thermodynamic properties and kinetic parameters would lead to wrong energy balance calculations and therefore, wrong values of composition and temperature.

The equilibrium constant of a reaction step is represented as:

$$K_i = k_{i,f}/k_{i,b} \quad (2.29)$$

here $k_{i,f}$ and $k_{i,b}$ represent the forward and backward kinetic rate constants, respectively. Dumesic et al. [73] provided a comprehensive description of thermodynamic constraints in microkinetic modelling in the 1993 book. Ensuring the thermodynamic consistency for elementary reaction steps implies that:

$$\Delta E_{i,b} = \Delta E_{i,f} - \Delta H_i \quad (2.30)$$

$$A_{i,b} = A_{i,f} \exp(\Delta S_i / R) = A_{i,f} \exp((\Delta G_i - \Delta H_i) / RT) \quad (2.31)$$

$\Delta E_{i,b}$ is the activation energy of the reverse reaction step, $\Delta E_{i,f}$ is the forwards activation energy, and the ΔH_i is the enthalpy of change of the reaction. Likewise, $A_{i,b}$ is the reverse reaction step pre-exponential, $A_{i,f}$ is the pre-exponential for forward reaction, and ΔS_i and ΔG_i represent the standard entropy change for the reaction and Gibbs free energy of reaction, respectively.

For heterogeneous catalytic reaction processes, a net reaction starting and ending with gas phase species, can be written as a linear combination of several reaction steps. The thermodynamic consistency constraints can therefore also be written as:

$$\sum \sigma_i(\Delta E_{i,f}) - \sum \sigma_i(\Delta E_{i,b}) = \Delta H_{net} \quad (2.32)$$

$$\prod \left(\frac{A_{i,f}}{A_{i,b}} \right)^{\sigma_i} = \exp \left(\frac{\Delta S_{net}}{R} \right) \quad (2.33)$$

The subscript “net” in equations 2.32 and 2.33, represent the total change in thermodynamic property from the net reactants to net products. σ_i represents the coefficient of elementary reactions in the linear combination of the net reaction. If we consider a simple reaction of gas-phase molecule A converting to gas-phase B *via* the steps:



A thermodynamic cycle is formed along which the gas-phase change in thermodynamic property must be equal to the net change in thermodynamic properties of the elementary reactions (Hess’s law).

Thermodynamic consistency in microkinetic models is usually conserved either through the adjustment of surface reaction properties or the adjustment of adsorption properties.

2.3.4.1 Thermodynamic consistency via surface reaction properties adjustment

When dealing with first-principle or semi-empirical microkinetic models, the main impediment to conserving thermodynamic consistency is finding a way to merge the gas-phase properties to surface properties. This proves more difficult when multiple parameter estimation methods are employed in the model. Gas-phase thermodynamic properties are calculated using *ab initio*, high level theory and are considered, very accurate.

The most straightforward way of constraining surface reaction mechanism to gas-phase properties is through the use of adsorption properties as a basis set. This method is beneficial when utilising semi-empirical rate constant estimation methods like UBI-QEP. All thermodynamic properties of surface species are correlated to the corresponding gas-phase species and the change in property upon adsorption.

$$\zeta_{i,surf}(T, \theta_j) = \zeta_{i,gas}(T) - \zeta_{i,ads}(T, \theta_j) \quad (2.35)$$

Subsequently, the change in thermodynamic function of a surface reaction ($\Delta\zeta_{i,surf}$) is directly correlated to that of the corresponding gas-phase species reactions ($\Delta\zeta_{i,gas}$) and the adsorption properties of the species. This implicitly places a thermodynamic constraint on each elementary reaction in the mechanism. Therefore, if a thermodynamic cycle is formed between the overall gas-phase reaction and the kinetically relevant surface reaction pathway, the free energies, enthalpies and entropies would be conserved.

Another method of ensuring thermodynamic consistency involves using a linearly independent basis set of elementary reactions to constrain the kinetic parameters or surface reactions. This basis set of reactions is selected such that the rest of the elementary reactions are linear combinations of the basis set. This method was presented by Mhadeshwar et al. [85]. The thermodynamic properties of the linearly dependent reactions in the network are calculated as linear combinations of those of the linearly independent basis set. Therefore, the activation energies and pre-exponential factors calculated from these thermodynamic properties are constrained. Usually the adsorption/desorption reactions of all possible gas phase species are selected as the basis set of linearly independent reactions because all surface reactions can be written as linear combinations of these adsorption/desorption reactions.

2.3.4.2 Thermodynamic consistency via adsorption properties adjustment

While the surface reaction properties adjustment method uses the adjustment of surface reaction energies by constraining the thermodynamics using gas-phase and adsorption thermodynamics, Thermodynamic consistency via adsorption properties adjustment method involves the adjustment of adsorption/desorption reaction energetics. This method is feasible when the mechanism and energetics of surface reactions are entirely defined from first-principle DFT calculations. This is because when first-principle methods of kinetic parameter estimation are used, the accuracy of estimated surface reaction energies is higher than that of estimated adsorption/desorption energies [94]. As the microkinetic model methodology used in this study mainly focuses of semi-empirical kinetic parameter estimation methods, this thermodynamic constraining method used in tandem with first-principle DFT is not expanded upon further.

2.3.5 Modelling of biogas dry reforming

2.3.5.1 Macrokinetic models

Macrokinetic models for dry reforming are usually based on a Power law model, Eley Rideal (ER) type models or a Langmuir Hinshelwood-Hougen Watson (LHHW) type models. Of these three types, the LHHW models are widely used due to the conformity of the mechanistic steps proposed to experimental techniques for validation [95]. The LHHW mechanisms and models proposed in literature for simulated biogas dry reforming have a varying description of the rate determining step (RDS) and the order of reactions for different catalytic systems.

Wei et al. [96] performed a kinetic study of dry reforming of methane over a Ni/MgO catalyst and obtained a good fit of experimental data with the rate determining step being the activation of CH₄. They also found a first-order dependence of the reaction rate on the concentration of CH₄ whilst the rate was not influenced by the co-reactant or products. Similarly, Zhang et al.

[97] observed a fit with experimental data when CH₄ activation was selected as the rate determining step over a Ni/Al₂O₃ catalyst. Wang et al. [98], on the other hand, obtained desirable fit with dry reforming of methane over Ni/Al₂O₃ catalyst experimental data, with a reaction mechanism in which the oxidation of C is the rate determining step. Over a Ni/La₂O₃ catalyst, Verykios et al. [99] proposed a reaction mechanism establishing the RDS as the cracking of CH₄ and the reaction of carbon and oxycarbonate species formed by the interaction between CO₂ and La₂O₃. Munera et al. [100] proposed an identical mechanism on a Rh/La₂O₃ catalyst. Wei et al. [101] proposed a mechanism establishing the activation of CH₄ as the RDS for dry reforming of methane over a Rh/Al₂O₃ catalyst. Donazzi et al. [102] performed the dry reforming of methane kinetic experiments over a 4% Rh/Al₂O₃ catalyst and proposed a reaction mechanism in which the RDS varied based on the CO₂/CH₄ ratio. At CO₂/CH₄ ratio of 1, the RDS was identified as the reverse water-gas shift reaction (RWGS) and at CO₂/CH₄ ratio > 1, the RDS was steam reforming.

Table 2.1: Proposed LHHW rate expressions for CH₄ dry reforming over Ni-based catalyst

Catalyst	Rate expression	Rate determining step (RDS)	Reference
Ni/SiO ₂ , Ni/MgO	$r = \frac{aP_{CH_4}P_{CO_2}}{bP_{CO}P_{H_2}^{\frac{4-x}{2}} + (1 + cP_{CH_4})P_{CO_2}}$	Decomposition of CH _x O	[103]
Ni/Al ₂ O ₃	$r = \frac{kP_{CH_4}P_{CO_2}}{(1 + K_{CH_4}P_{CH_4})(1 + K_{CO_2}P_{CO_2})}$	Oxidation of C	[98]
Ni/La ₂ O ₃	$r = \frac{aP_{CH_4}P_{CO_2}}{bP_{CH_4}P_{CO_2} + cP_{CH_4} + dP_{CO}}$	Cracking of CH ₄ and the reaction of carbon and oxycarbonate species	[104]

As is evident, there has been considerable amount of macrokinetic modelling research carried out on dry reforming of methane, however, based on the different proposed LHHW models on similar metal-based catalysts, a consensus on a ubiquitous reaction mechanism for biogas dry reforming and rate determining step *via* LHHW modelling is not feasible. A more intrinsic kinetic look is therefore required.

2.3.5.2 Microkinetic models

Microkinetic models examine catalytic reactions in terms of elementary steps occurring on the catalyst surface and involves the theoretical or experimental estimation of kinetic parameters in the rate expression of these steps. An *a priori* determination of the RDS is not required and the model is able to suggest the kinetically relevant reaction steps and surface intermediates.

Delgado et al. [105] developed a comprehensive microkinetic model for the dry reforming of methane as well as partial oxidation over a Ni based catalyst. The thermodynamically consistent model included 26 reversible reaction steps (6 adsorption and 20 surface reactions) and involved 14 surface species and 6 gas-phase species. The adsorption of methane was identified as the most sensitive reaction in the overall reaction mechanism. Dehimi et al. [106] also developed a microkinetic model for the dry reforming of methane in a temperature range of 450-600°C. The model involving 17 reversible reactions and 12 surface species proposed a mechanism in which the main oxidizer is OH* obtained from the oxidation of surface H*. Xie et al. [107] applied the model developed by Delgado et al. [105] for the dry reforming of methane over a Ni catalyst and found the kinetic relevant steps and dominant reaction pathway to be varied based on the reaction conditions.

Maestri et al. [81] performed a microkinetic investigation of steam and dry reforming of methane over a 4 wt.% Rh/Al₂O₃ catalyst. The developed microkinetic model established the dehydrogenation of CH₃* as the RDS and the OH* surface intermediate as the main oxidizer for surface C*. In a similar model developed by Karakaya et al. [108] for dry reforming of methane over 5 wt.% Rh/Al₂O₃ catalyst, the RDS was found to be the initial dehydrogenation of adsorbed CH₄* surface species. They also found that the dominant pathway for CO formation proceeded *via* the formation of COOH* surface intermediate.

The general accepted consensus in literature on microkinetic models is that the relevant reaction step in dry reforming of methane reaction mechanism occurs in the CH₄ activation and dehydrogenation pathway.

2.3.5.3 *Co-feeding and recycle*

Currently in industry, the most commonly used hydrogen production process is the steam reforming of methane. On the large industry scale this process involves the partial recycling of the product gas stream in order to optimise reaction and energy efficiency. It is therefore inevitable that the dry reforming of methane process when scaled up will include a partial recycling and co-feeding of products, CO and H₂ with reactor feed stream. Additionally, hydrogen co-feeding has been studied recently as a way of inhibiting coke formation and deposition in industrial reactors during dry reforming of methane at higher temperatures and pressures [109]. Kinetic studies that investigate co-feeding streams on the overall mechanism are therefore vital. A number of macrokinetic models incorporate the effect of a H₂ and/or CO co-feeding stream on the dry reforming of methane mechanism over Ni and Rh based catalysts

[96,99–102,110]. However as discussed earlier, these LHHW models do little in discerning a prevalent reaction mechanism and rate determining step.

Regarding microkinetic models, however, only two studies that consider the co-feeding of products can be found in literature to our knowledge.

Delgado et al. [105] observed that the addition of H₂ to the feed stream during dry reforming of methane over a Ni-based catalyst led to an increase in the formation of surface H₂O*. At high temperatures the formed H₂O* will participate and be consumed in the methane steam reforming pathway, thereby improving the methane conversion.

On the contrary, Behroozsarand et al. [110] found that their developed microkinetic model for dry reforming of methane over a Rh-based catalyst predicted hydrogen co-feeding to have a negative impact on the conversion of methane. **This contradiction indicates a gap in research that warrants clarification. Therefore, a comprehensive microkinetic study of dry reforming of biogas over a Rh-based catalyst and an investigation into the effect of co-feeding H₂ and CO in the feed stream is necessary in order to ascertain if the contradiction is only as a result of the different metal catalysts used.**

2.3.6 Modelling of ethanol steam reforming

2.3.6.1 Macrokinetic models

The macrokinetic models for ethanol steam reforming found in literature are developed using either the ER mechanism or the LHHW mechanism. In the ER mechanism the ethanol is adsorbed on the catalyst surface and dissociates by reacting with adjacent vacant sites on the surface to form intermediate carbon surface species. These surface species then readily react with steam molecules in the gas phase to form CO₂ and H₂. The LHHW mechanism has all reactants adsorbed on the catalyst surface wherein they undergo surface reactions and desorption.

Akande et al. [111] developed a kinetic model for steam reforming of crude ethanol over a Ni/Al₂O₃ catalyst using ER mechanism. The dissociation of adsorbed ethanol to form the oxygenated hydrocarbon fraction was considered to be the RDS. This model however does not account for the formation of well-established primary products or intermediates like acetaldehyde. Using LHHW mechanism Akpan et al. [112] developed a kinetic model for the steam reforming of ethanol over a Ni based commercial catalyst. With both reactants adsorbing and dissociating on the catalyst surface, the best fit to experimental data was attained when the RDS was taken to be the molecular adsorption of ethanol. Wu et al. [113] developed a simplified

kinetic model for ethanol steam reforming over Ni/Al₂O₃ catalyst using LHHW mechanism. In the model the formation of adsorbed carbon species is excluded due to the presence of excess water and assumption that OH species stick better to Ni active sites. The surface decomposition of methane is regarded as the RDS however the reverse reaction is assumed to be equilibrated with all other reactions. Gracchinsky et al. [114] conducted a kinetic study of ethanol steam reforming over Rh catalyst supported on a spinel structure MgAl₂O₄/Al₂O₃. Through their initial rate method analysis, they found that the rate determining step was a surface reaction involving two active sites of the same type. Nonetheless, the specific nature of the active sites was not identified. Sahoo et al. [115] developed a LHHW mechanism for Co/Al₂O₃ catalysed ethanol steam reforming. The dehydrogenation of adsorbed ethoxy species was considered the RDS. In the kinetic analysis of ethanol steam reforming over Ir/CeO₂ performed by Wang et al. [116], it was found that a model based solely on the metal sites did not provide good agreement with the experimental results. A bifunctional model, using a LHHW mechanism including only reactions that involve both metal and support active sites provided satisfactory agreement with the experimental results. It was assumed that both reactants were initially adsorbed on the support surface and the Ir active sites were required for the formation and desorption of CO and H₂.

All proposed macrokinetic models present differing insight into the reaction mechanism by postulating varying RDS, even for similar systems with the same metal catalyst and same conditions. Again, justifying the need for more intrinsic kinetic models to be developed.

Additionally, only one study could be found in with a bifunctional mechanism in which the support materials participation in the reaction mechanism is included.

2.3.6.2 *Microkinetic models*

Sutton et al. [117] developed a comprehensive microkinetic model for the steam reforming of ethanol over a Pt/ γ -Al₂O₃ catalyst. The model was almost exclusively parametrised using DFT values from Pt(111). A comprehensive list of 160 elementary reaction was assembled including the thermal decomposition pathway and complete water-gas shift mechanism and involved 67 gas and surface species. The rate determining step was identified as the initial dehydrogenation of ethanol step, whilst the Carbon selectivity was C₁ products was controlled by the C-C cracking of CHCO surface species. The oxidative dehydrogenation reaction pathway was investigated by DFT but found to be negligible from the mechanism due to the low surface concentrations of O and OH species.

In the work of Baruah et al. [118], a microkinetic model is adapted from literature and validated against oxidative steam reforming of ethanol experiments carried out over a Rh/CeO₂ catalyst.

The adopted and adjusted microkinetic model consists of 56 renewable reactions. The model showed good agreement with experimental results and suggested a linear activation pathway for ethanol over Rh forming ethoxide, acetyl and acetate intermediates. The molecular adsorption of ethanol was determined to be the rate determining step.

Based on the observations from microkinetic models in conjunction with literature density functional theory (DFT) studies carried out on the decomposition of ethanol over various metals which are reviewed in chapter 4, the accepted consensus is that the kinetically relevant reaction steps during ethanol steam reforming occur in the ethanol activation and dehydrogenation pathway.

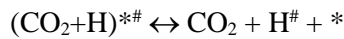
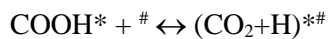
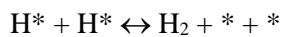
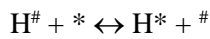
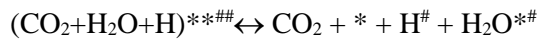
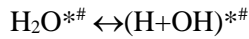
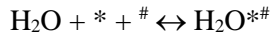
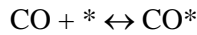
In addition, the two studies reviewed above are the only previously reported microkinetic models on steam reforming of ethanol and they are both over noble metal catalysts. Developing a microkinetic model for a non-noble metal catalyst, specifically Ni, is therefore important.

2.3.6.3 *Bifunctional microkinetic models*

Regarding microkinetic models that account for bifunctional mechanisms of processes catalysed by bimetallic catalysts or metal catalysts with active supports, there have been a few studies in literature that investigate the effect of the support material or the second metal on the reaction mechanism and overall activity of catalyst.

Zhao et al. [119] investigated the effect of metal-oxide interface in catalysis by performing a combined DFT, microkinetic and experimental study of water-gas shift (WGS) over Au/MgO catalyst. A first-principle DFT parametrised dual-site mean-field microkinetic model was developed. Only the Au/MgO interface sites (*) and the top sites of O atoms of the MgO close to the interface (#) were considered. The interaction between species on different sites was accounted for by allowing simultaneous occupation of both sites by a few adsorbates. Diffusion of adsorbates from the Au metal or the MgO support to the interface was not included. The only transfer reaction that was included was the possible case of atomic hydrogen moving from the # interface sites to the * interface sites. The DFT energetics results demonstrated that the activation of water on the interface was barrierless compared to a value of 192 kJ/mol on the Au metal surface. The microkinetic analysis showed that the RDS at the interface was the formation of COOH and that the competitive adsorption of CO and H has a strong influence. Overall, the activation barriers and partial orders agree well with the kinetic experiments done and the analysis found that when compared to just Au metal site, the activity of the supported catalyst is higher and specifically the activity at the metal-support interface is higher than at any other types of site. The reaction mechanism used in this model is as shown in Table 2.2.

Table 2.2: Reaction network for dual-site microkinetic model for WGS reaction at Au/MgO interface



Similarly, Kauppinen et al. [120] developed a microkinetic model parametrised using first-principle DFT kinetic values, to study the role of the metal-support interface for WGS reaction over Rh/ZrO₂. Separate single site microkinetic analysis were carried out to determine the individual activities and mechanisms on the Rh sites, ZrO₂ sites and Rh-ZrO₂ interface, respectively. No transfer reactions were included in the networks on each site. They found that Rh-ZrO₂ interface demonstrated the highest activity towards WGS. For each of the sites geometric calculations are done to determine the number of active sites to be used in the model. Starting with a known number of zirconia particles obtained using BET experiments, hemispheric geometry is assumed for Rh atoms and an assumption of optimal packing is also taken.

Baz et al. [121] built a microkinetic model for the electro-oxidation reaction of CO over a bimetallic Pt-Ru catalyst using first-principle DFT calculations and BEP scaling relations. The model was used to investigate whether the bifunctional or electronic effects of using the bimetallic catalyst are most operative. A single-site model is initially designed and then extended

to two-site type. They found that for metal alloys the electronic effects usually remain dominant over bifunctional effect, with the electronically modified Pt sites acting as the sole active sites.

Through the review of literature, we have found that there exists no work that provides a comprehensive microkinetic model capable of incorporating the effect of support materials on the reaction mechanism for the steam reforming of ethanol or any other biomass derived oxygenate. As we have already established that for these processes knowledge of the functionality of support materials is of crucial importance, it is therefore, vital that we develop a consolidated microkinetic model that can simulate single or multiple active sites and will serve as a tenable tool for the design of high performance catalyst systems for the steam reforming of ethanol or larger biomass derived oxygenates.

References

- [1] M. Persson, O. Jonsson, A. Wellinger, Biogas Upgrading To Vehicle Fuel Standards and Grid, IEA Bioenergy. (2007) 1–32.
- [2] H. Katuwal, A.K. Bohara, Biogas: A promising renewable technology and its impact on rural households in Nepal, *Renew. Sustain. Energy Rev.* 13 (2009) 2668–2674. <https://doi.org/10.1016/j.rser.2009.05.002>.
- [3] Y. Wang, L. Yao, S. Wang, D. Mao, C. Hu, Low-temperature catalytic CO₂ dry reforming of methane on Ni-based catalysts: A review, *Fuel Process. Technol.* 169 (2018) 199–206. <https://doi.org/10.1016/j.fuproc.2017.10.007>.
- [4] N.A.K. Aramouni, J.G. Touma, B.A. Tarboush, J. Zeaiter, M.N. Ahmad, Catalyst design for dry reforming of methane: Analysis review, *Renew. Sustain. Energy Rev.* 82 (2018) 2570–2585. <https://doi.org/10.1016/j.rser.2017.09.076>.
- [5] A. Navarro-Puyuelo, I. Reyero, A. Moral, F. Bimbela, L.M. Gandía, Rutas y retos para la valorización de biogás, *Av. Investig. En Ing.* 14 (2017) 211–224.
- [6] W.M. Budzianowski, A review of potential innovations for production, conditioning and utilization of biogas with multiple-criteria assessment, *Renew. Sustain. Energy Rev.* 54 (2016) 1148–1171. <https://doi.org/10.1016/j.rser.2015.10.054>.
- [7] L. Yang, X. Ge, C. Wan, F. Yu, Y. Li, Progress and perspectives in converting biogas to transportation fuels, *Renew. Sustain. Energy Rev.* 40 (2014) 1133–1152. <https://doi.org/10.1016/j.rser.2014.08.008>.
- [8] J. Phromprasit, J. Powell, S. Wongsakulphasatch, W. Kiatkittipong, P. Bumroongsakulsawat, S. Assabumrungrat, H₂ production from sorption enhanced steam reforming of biogas using multifunctional catalysts of Ni over Zr-, Ce- and La-modified CaO sorbents, *Chem. Eng. J.* 313 (2017) 1415–1425. <https://doi.org/10.1016/j.cej.2016.11.051>.
- [9] S. Daneshmand-Jahromi, M.R. Rahimpour, M. Meshksar, A. Hafizi, Hydrogen production from cyclic chemical looping steam methane reforming over yttrium promoted Ni/SBA-16 oxygen carrier, *Catalysts.* 7 (2017) 64–75.

<https://doi.org/10.3390/catal7100286>.

- [10] B. Abdullah, N.A. Abd Ghani, D.V.N. Vo, Recent advances in dry reforming of methane over Ni-based catalysts, *J. Clean. Prod.* 162 (2017) 170–185. <https://doi.org/10.1016/j.jclepro.2017.05.176>.
- [11] J.R. Rostrup-Nielsen, Industrial relevance of coking, *Catal. Today.* 37 (1997) 225–232. [https://doi.org/10.1016/S0920-5861\(97\)00016-3](https://doi.org/10.1016/S0920-5861(97)00016-3).
- [12] S. Wang, G.Q. Lu, G.J. Millar, Carbon dioxide reforming of methane to produce synthesis gas over metal-supported catalysts: State of the art, *Energy and Fuels.* 10 (1996) 896–904. <https://doi.org/10.1021/ef950227t>.
- [13] N.D. Charisiou, A. Baklavaridis, V.G. Papadakis, M.A. Goula, Synthesis Gas Production via the Biogas Reforming Reaction Over Ni/MgO–Al₂O₃ and Ni/CaO–Al₂O₃ Catalysts, *Waste and Biomass Valorization.* 7 (2016) 725–736. <https://doi.org/10.1007/s12649-016-9627-9>.
- [14] O. Omoregbe, H.T. Danh, C. Nguyen-Huy, H.D. Setiabudi, S.Z. Abidin, Q.D. Truong, D.V.N. Vo, Syngas production from methane dry reforming over Ni/SBA-15 catalyst: Effect of operating parameters, *Int. J. Hydrogen Energy.* 42 (2017) 11283–11294. <https://doi.org/10.1016/j.ijhydene.2017.03.146>.
- [15] E. Akbari, S.M. Alavi, M. Rezaei, Synthesis gas production over highly active and stable nanostructured Ni[sbnd]MgO[sbnd]Al₂O₃ catalysts in dry reforming of methane: Effects of Ni contents, *Fuel.* 194 (2017) 171–179. <https://doi.org/10.1016/j.fuel.2017.01.018>.
- [16] M. Usman, W.M.A. Wan Daud, H.F. Abbas, Dry reforming of methane: Influence of process parameters - A review, *Renew. Sustain. Energy Rev.* 45 (2015) 710–744. <https://doi.org/10.1016/j.rser.2015.02.026>.
- [17] Y. Khani, Z. Shariatnia, F. Bahadoran, High catalytic activity and stability of ZnLaAlO₄ supported Ni, Pt and Ru nanocatalysts applied in the dry, steam and combined dry-steam reforming of methane, *Chem. Eng. J.* 299 (2016) 353–366. <https://doi.org/10.1016/j.cej.2016.04.108>.
- [18] Z. Hou, P. Chen, H. Fang, X. Zheng, T. Yashima, Production of synthesis gas via methane reforming with CO₂ on noble metals and small amount of noble-(Rh-) promoted Ni catalysts, *Int. J. Hydrogen Energy.* 31 (2006) 555–561. <https://doi.org/10.1016/j.ijhydene.2005.06.010>.
- [19] I. Luisetto, C. Sarno, D. De Felicis, F. Basoli, C. Battocchio, S. Tuti, S. Licocchia, E. Di Bartolomeo, Ni supported on γ -Al₂O₃ promoted by Ru for the dry reforming of methane in packed and monolithic reactors, *Fuel Process. Technol.* 158 (2017) 130–140. <https://doi.org/10.1016/j.fuproc.2016.12.015>.
- [20] C. Wang, Y. Zhang, Y. Wang, Y. Zhao, Comparative Studies of Non-noble Metal Modified Mesoporous M-Ni-CaO-ZrO₂ (M = Fe, Co, Cu) Catalysts for Simulated Biogas Dry Reforming, *Chinese J. Chem.* 35 (2017) 113–120. <https://doi.org/10.1002/cjoc.201600609>.
- [21] J. Xu, W. Zhou, Z. Li, J. Wang, J. Ma, Biogas reforming for hydrogen production over nickel and cobalt bimetallic catalysts, *Int. J. Hydrogen Energy.* 34 (2009) 6646–6654. <https://doi.org/10.1016/j.ijhydene.2009.06.038>.
- [22] D. Pakhare, J. Spivey, A review of dry (CO₂) reforming of methane over noble metal catalysts, *Chem. Soc. Rev.* 43 (2014) 7813–7837. <https://doi.org/10.1039/c3cs60395d>.

- [23] P. Ferreira-Aparicio, I. Rodriguez-Ramos, J.A. Anderson, A.R. Guerrero-Ruiz, Mechanistic aspects of the dry reforming of methane over ruthenium catalysts, *Appl. Catal. A, Gen.* 202 (2000) 183–196. https://doi.org/10.1007/978-3-319-99441-3_91.
- [24] V.Y. Bychkov, Y.P. Tyulenin, A.A. Firsova, E.A. Shafranovsky, A.Y. Gorenberg, V.N. Korchak, Carbonization of nickel catalysts and its effect on methane dry reforming, *Appl. Catal. A Gen.* 453 (2013) 71–79. <https://doi.org/10.1016/j.apcata.2012.12.006>.
- [25] S. Sokolov, E. V. Kondratenko, M.M. Pohl, A. Barkschat, U. Rodemerck, Stable low-temperature dry reforming of methane over mesoporous La₂O₃-ZrO₂ supported Ni catalyst, *Appl. Catal. B Environ.* 113–114 (2012) 19–30. <https://doi.org/10.1016/j.apcatb.2011.09.035>.
- [26] J.E. Min, Y.J. Lee, H.G. Park, C. Zhang, K.W. Jun, Carbon dioxide reforming of methane on Ni-MgO-Al₂O₃ catalysts prepared by sol-gel method: Effects of Mg/Al ratios, *J. Ind. Eng. Chem.* 26 (2015) 375–383. <https://doi.org/10.1016/j.jiec.2014.12.012>.
- [27] W. Wang, Y. Wang, Dry reforming of ethanol for hydrogen production: Thermodynamic investigation, *Int. J. Hydrogen Energy.* 34 (2009) 5382–5389. <https://doi.org/10.1016/j.ijhydene.2009.04.054>.
- [28] B. Bej, S. Bepari, N.C. Pradhan, S. Neogi, Production of hydrogen by dry reforming of ethanol over alumina supported nano-NiO/SiO₂ catalyst, *Catal. Today.* 291 (2017) 58–66. <https://doi.org/10.1016/j.cattod.2016.12.010>.
- [29] A. Zawadzki, J.D.A. Bellido, A.F. Lucrédio, E.M. Assaf, Dry reforming of ethanol over supported Ni catalysts prepared by impregnation with methanolic solution, *Fuel Process. Technol.* 128 (2014) 432–440. <https://doi.org/10.1016/j.fuproc.2014.08.006>.
- [30] A. Casanovas, M. Saint-Gerons, F. Griffon, J. Llorca, Autothermal generation of hydrogen from ethanol in a microreactor, *Int. J. Hydrogen Energy.* 33 (2008) 1827–1833. <https://doi.org/10.1016/j.ijhydene.2008.01.018>.
- [31] B. Zhang, W. Cai, Y. Li, Y. Xu, W. Shen, Hydrogen production by steam reforming of ethanol over an Ir/CeO₂ catalyst: Reaction mechanism and stability of the catalyst, *Int. J. Hydrogen Energy.* 33 (2008) 4377–4386. <https://doi.org/10.1016/j.ijhydene.2008.05.022>.
- [32] L. Zhang, W. Li, J. Liu, C. Guo, Y. Wang, J. Zhang, Ethanol steam reforming reactions over Al₂O₃ · SiO₂-supported Ni-La catalysts, *Fuel.* 88 (2009) 511–518. <https://doi.org/10.1016/j.fuel.2008.09.030>.
- [33] C.Y. Yu, D.W. Lee, S.J. Park, K.Y. Lee, K.H. Lee, Study on a catalytic membrane reactor for hydrogen production from ethanol steam reforming, *Int. J. Hydrogen Energy.* 34 (2009) 2947–2954. <https://doi.org/10.1016/j.ijhydene.2009.01.039>.
- [34] W. Cai, F. Wang, A. van Veen, C. Descorme, Y. Schuurman, W. Shen, C. Mirodatos, Hydrogen production from ethanol steam reforming in a micro-channel reactor, *Int. J. Hydrogen Energy.* 35 (2010) 1152–1159. <https://doi.org/10.1016/j.ijhydene.2009.11.104>.
- [35] H. Song, L. Zhang, R.B. Watson, D. Braden, U.S. Ozkan, Investigation of bio-ethanol steam reforming over cobalt-based catalysts, 129 (2007) 346–354. <https://doi.org/10.1016/j.cattod.2006.11.028>.
- [36] R.U. Ribeiro, J.W.C. Liberatori, H. Winnishofer, J.M.C. Bueno, D. Zanchet, Colloidal Co nanoparticles supported on SiO₂: Synthesis, characterization and catalytic properties for steam reforming of ethanol, *Appl. Catal. B Environ.* 91 (2009) 670–678. <https://doi.org/10.1016/j.apcatb.2009.07.009>.

- [37] J.W.C. Liberatori, R.U. Ribeiro, D. Zanchet, F.B. Noronha, J.M.C. Bueno, Steam reforming of ethanol on supported nickel catalysts, *Appl. Catal. A Gen.* 327 (2007) 197–204. <https://doi.org/10.1016/j.apcata.2007.05.010>.
- [38] I. Llera, V. Mas, M.L. Bergamini, M. Laborde, N. Amadeo, Bio-ethanol steam reforming on Ni based catalyst. Kinetic study, *Chem. Eng. Sci.* 71 (2012) 356–366. <https://doi.org/10.1016/j.ces.2011.12.018>.
- [39] J. Sun, X.P. Qiu, F. Wu, W.T. Zhu, H₂ from steam reforming of ethanol at low temperature over Ni/Y₂O₃ and Ni/La₂O₃ catalysts for fuel-cell application, *Int. J. Hydrogen Energy.* 30 (2005) 437–445. <https://doi.org/10.1016/j.ijhydene.2004.11.005>.
- [40] A.J. Vizcaíno, A. Carrero, J.A. Calles, Hydrogen production by ethanol steam reforming over Cu-Ni supported catalysts, *Int. J. Hydrogen Energy.* 32 (2007) 1450–1461. <https://doi.org/10.1016/j.ijhydene.2006.10.024>.
- [41] D.K. Liguras, D.I. Kondarides, X.E. Verykios, Production of hydrogen for fuel cells by steam reforming of ethanol over supported noble metal catalysts, *Appl. Catal. B Environ.* 43 (2003) 345–354. [https://doi.org/10.1016/S0926-3373\(02\)00327-2](https://doi.org/10.1016/S0926-3373(02)00327-2).
- [42] S. Cavallaro, Ethanol Steam Reforming on Rh/Al₂O₃ Catalysts, *Energy and Fuels.* 14 (2000) 1195–1199. <https://doi.org/10.1021/ef0000779>.
- [43] F. Frusteri, S. Freni, L. Spadaro, V. Chiodo, G. Bonura, S. Donato, S. Cavallaro, H₂ production for MC fuel cell by steam reforming of ethanol over MgO supported Pd, Rh, Ni and Co catalysts, *Catal. Commun.* 5 (2004) 611–615. <https://doi.org/10.1016/j.catcom.2004.07.015>.
- [44] A. Haryanto, S. Fernando, N. Murali, S. Adhikari, Current status of hydrogen production techniques by steam reforming of ethanol: A review, *Energy and Fuels.* 19 (2005) 2098–2106. <https://doi.org/10.1021/ef0500538>.
- [45] D. Zanchet, J.B.O. Santos, S. Damyanova, J.M.R. Gallo, J.M.C. Bueno, Toward understanding metal-catalyzed ethanol reforming, *ACS Catal.* 5 (2015) 3841–3863. <https://doi.org/10.1021/cs5020755>.
- [46] J. Comas, F. Marino, M. Laborde, N. Amadeo, Bio-ethanol steam reforming on Ni/Al₂O₃ catalyst, *Chem. Eng. J.* 98 (2004) 61–68. [https://doi.org/10.1016/S1385-8947\(03\)00186-4](https://doi.org/10.1016/S1385-8947(03)00186-4).
- [47] F. Auprêtre, C. Descorme, D. Duprez, Bio-ethanol catalytic steam reforming over supported metal catalysts, *Catal. Commun.* 3 (2002) 263–267. [https://doi.org/10.1016/S1566-7367\(02\)00118-8](https://doi.org/10.1016/S1566-7367(02)00118-8).
- [48] A.J. Akande, R.O. Idem, A.K. Dalai, Synthesis, characterization and performance evaluation of Ni/Al₂O₃ catalysts for reforming of crude ethanol for hydrogen production, *Appl. Catal. A Gen.* 287 (2005) 159–175. <https://doi.org/10.1016/j.apcata.2005.03.046>.
- [49] A.N. Fatsikostas, X.E. Verykios, Reaction network of steam reforming of ethanol over Ni-based catalysts, *J. Catal.* 225 (2004) 439–452. <https://doi.org/10.1016/j.jcat.2004.04.034>.
- [50] G.T. Wurzler, R.C. Rabelo-Neto, L. V. Mattos, M.A. Fraga, F.B. Noronha, Steam reforming of ethanol for hydrogen production over MgO - Supported Ni-based catalysts, *Appl. Catal. A Gen.* 518 (2016) 115–128. <https://doi.org/10.1016/j.apcata.2015.11.020>.
- [51] C. Wu, V. Dupont, M.A. Nahil, B. Dou, H. Chen, P.T. Williams, Investigation of Ni/SiO₂

- catalysts prepared at different conditions for hydrogen production from ethanol steam reforming, *J. Energy Inst.* 90 (2017) 276–284. <https://doi.org/10.1016/j.joei.2016.01.002>.
- [52] A. Rodriguez-Gomez, A. Caballero, Bimetallic Ni-Co/SBA-15 catalysts for reforming of ethanol: How cobalt modifies the nickel metal phase and product distribution, *Mol. Catal.* 449 (2018) 122–130. <https://doi.org/10.1016/j.mcat.2018.02.011>.
- [53] Y. Yang, J. Ma, F. Wu, Production of hydrogen by steam reforming of ethanol over a Ni/ZnO catalyst, *Int. J. Hydrogen Energy.* 31 (2006) 877–882. <https://doi.org/10.1016/j.ijhydene.2005.06.029>.
- [54] T. Hou, S. Zhang, Y. Chen, D. Wang, W. Cai, Hydrogen production from ethanol reforming: Catalysts and reaction mechanism, *Renew. Sustain. Energy Rev.* 44 (2015) 132–148. <https://doi.org/10.1016/j.rser.2014.12.023>.
- [55] M.C. Sánchez-Sánchez, R.M. Navarro, J.L.G. Fierro, Ethanol steam reforming over Ni / Mx Oy-Al₂ O₃ (M = Ce, La, Zr and Mg) catalysts: Influence of support on the hydrogen production, *Int. J. Hydrogen Energy.* 32 (2007) 1462–1471. <https://doi.org/10.1016/j.ijhydene.2006.10.025>.
- [56] S. Ogo, Y. Sekine, Recent progress in ethanol steam reforming using non-noble transition metal catalysts: A review, *Fuel Process. Technol.* 199 (2020) 106238. <https://doi.org/10.1016/j.fuproc.2019.106238>.
- [57] T.K. Phung, T.L.M. Pham, A.N.T. Nguyen, K.B. Vu, H.N. Giang, T.A. Nguyen, T.C. Huynh, H.D. Pham, Effect of Supports and Promoters on the Performance of Ni-Based Catalysts in Ethanol Steam Reforming, *Chem. Eng. Technol.* 43 (2020) 672–688. <https://doi.org/10.1002/ceat.201900445>.
- [58] V. Palma, C. Ruocco, M. Cortese, M. Martino, Bioalcohol Reforming: An Overview of the Recent Advances for the Enhancement of Catalyst Stability, *Catalysts.* 10 (2020). <https://doi.org/10.3390/catal10060665>.
- [59] R. Shan, J. Han, J. Gu, H. Yuan, B. Luo, Y. Chen, A review of recent developments in catalytic applications of biochar-based materials, *Resour. Conserv. Recycl.* 162 (2020) 105036. <https://doi.org/10.1016/j.resconrec.2020.105036>.
- [60] J. Ashok, N. Dewangan, S. Das, P. Hongmanorom, M.H. Wai, K. Tomishige, S. Kawi, Recent progress in the development of catalysts for steam reforming of biomass tar model reaction, *Fuel Process. Technol.* 199 (2020) 106252. <https://doi.org/10.1016/j.fuproc.2019.106252>.
- [61] J. Chen, M. Wang, S. Wang, X. Li, Hydrogen production via steam reforming of acetic acid over biochar-supported nickel catalysts, *Int. J. Hydrogen Energy.* 43 (2018) 18160–18168. <https://doi.org/10.1016/j.ijhydene.2018.08.048>.
- [62] D. Buentello-Montoya, X. Zhang, J. Li, V. Ranade, S. Marques, M. Geron, Performance of biochar as a catalyst for tar steam reforming: Effect of the porous structure, *Appl. Energy.* 259 (2020) 114176. <https://doi.org/10.1016/j.apenergy.2019.114176>.
- [63] L. Ren, L.J. Yan, Y.H. Bai, Y. Liu, P. Lv, Y.X. Wang, F. Li, Effects of loading methods and oxidation degree of support on the tar reforming activity of char-supported Ni catalyst using toluene as a model compound, *Fuel Process. Technol.* 201 (2020) 106347. <https://doi.org/10.1016/j.fuproc.2020.106347>.
- [64] C. Quan, H. Wang, N. Gao, Development of activated biochar supported Ni catalyst for enhancing toluene steam reforming, *Int. J. Energy Res.* 44 (2020) 5749–5764.

<https://doi.org/10.1002/er.5335>.

- [65] Z. Min, P. Yimsiri, M. Asadullah, S. Zhang, C.Z. Li, Catalytic reforming of tar during gasification. Part II. Char as a catalyst or as a catalyst support for tar reforming, *Fuel*. 90 (2011) 2545–2552. <https://doi.org/10.1016/j.fuel.2011.03.027>.
- [66] Y. Song, Y. Zhao, X. Hu, L. Zhang, S. Sun, C.Z. Li, Destruction of tar during volatile-char interactions at low temperature, *Fuel Process. Technol.* 171 (2018) 215–222. <https://doi.org/10.1016/j.fuproc.2017.11.023>.
- [67] Y. Song, Y. Wang, X. Hu, S. Hu, J. Xiang, L. Zhang, S. Zhang, Z. Min, C.Z. Li, Effects of volatile-char interactions on in situ destruction of nascent tar during the pyrolysis and gasification of biomass. Part I. Roles of nascent char, *Fuel*. 122 (2014) 60–66. <https://doi.org/10.1016/j.fuel.2014.01.002>.
- [68] S. Zhang, Y. Song, Y.C. Song, Q. Yi, L. Dong, T.T. Li, L. Zhang, J. Feng, W.Y. Li, C.Z. Li, An advanced biomass gasification technology with integrated catalytic hot gas cleaning. Part III: Effects of inorganic species in char on the reforming of tars from wood and agricultural wastes, *Fuel*. 183 (2016) 177–184. <https://doi.org/10.1016/j.fuel.2016.06.078>.
- [69] C. Xu, Z.-Y. Du, S.-Q. Yang, H.-D. Ma, J. Feng, Effects of Inherent Potassium on the Catalytic Performance of Ni/Biochar for Steam Reforming of Toluene as a Tar Model Compound, *Chinese J. Chem. Eng.* (2020) 108653. <https://doi.org/https://doi.org/10.1016/j.cjche.2020.06.010>.
- [70] Y. Liu, M. Paskevicius, H. Wang, G. Parkinson, J.P. Veder, X. Hu, C.Z. Li, Role of O-containing functional groups in biochar during the catalytic steam reforming of tar using the biochar as a catalyst, *Fuel*. 253 (2019) 441–448. <https://doi.org/10.1016/j.fuel.2019.05.037>.
- [71] Z. Min, S. Zhang, P. Yimsiri, Y. Wang, M. Asadullah, C.Z. Li, Catalytic reforming of tar during gasification. Part IV. Changes in the structure of char in the char-supported iron catalyst during reforming, *Fuel*. 106 (2013) 858–863. <https://doi.org/10.1016/j.fuel.2012.11.063>.
- [72] Y. Wang, Z. Zhang, S. Zhang, Y. Wang, S. Hu, J. Xiang, X. Hu, Steam reforming of acetic acid over Ni/biochar catalyst treated with HNO₃: Impacts of the treatment on surface properties and catalytic behaviors, *Fuel*. 278 (2020) 118341. <https://doi.org/10.1016/j.fuel.2020.118341>.
- [73] J.A. Dumesic, D.F. Rudd, L.M. Aparicio, J.E. Rekoske, A.A. Treviño, *The Microkinetics of Heterogeneous Catalysis*, 1993.
- [74] V. Prasad, A.M. Karim, A. Arya, D.G. Vlachos, Assessment of overall rate expressions and multiscale, microkinetic model uniqueness via experimental data injection: Ammonia decomposition on Ru/ γ -Al₂O₃ for hydrogen production, *Ind. Eng. Chem. Res.* 48 (2009) 5255–5265. <https://doi.org/10.1021/ie900144x>.
- [75] M.E. Coltrin, R.J. Kee, F.M. Rupley, *Surface chemkin (version 4.0): A FORTRAN package for analyzing heterogeneous chemical kinetics at a solidsurface-gas phase interface*, 1991.
- [76] R.J. Kee, F.M. Rupley, J.A. Miller, *Chemkin-II: a FORTRAN chemical kinetics package for the analysis of gas phase chemical kinetics*, n.d.
- [77] A.A. Gokhale, S. Kandoi, J.P. Greeley, M. Mavrikakis, J.A. Dumesic, *Molecular-level*

- descriptions of surface chemistry in kinetic models using density functional theory, *Chem. Eng. Sci.* 59 (2004) 4679–4691. <https://doi.org/10.1016/j.ces.2004.09.038>.
- [78] E. Shustorovich, H. Sellers, The UBI-QEP method: A practical theoretical approach to understanding chemistry on transition metal surfaces, *Surf. Sci. Rep.* 31 (1998) 1–119. [https://doi.org/10.1016/s0167-5729\(97\)00016-2](https://doi.org/10.1016/s0167-5729(97)00016-2).
- [79] Y.K. Park, P. Aghalayam, D.G. Vlachos, A Generalized Approach for Predicting Coverage-Dependent Reaction Parameters of Complex Surface Reactions: Application to H₂ Oxidation over Platinum, *J. Phys. Chem. A.* 103 (1999) 8101–8107. <https://doi.org/10.1021/jp9916485>.
- [80] I. V. Kuz'min, A. V. Zeigarnik, Microkinetic modeling of ethane hydrogenolysis on metals, *Kinet. Catal.* 45 (2004) 561–569. <https://doi.org/10.1023/B:KICA.0000038086.87163.6e>.
- [81] M. Maestri, D.G. Vlachos, A. Beretta, G. Groppi, E. Tronconi, Steam and dry reforming of methane on Rh: Microkinetic analysis and hierarchy of kinetic models, *J. Catal.* 259 (2008) 211–222. <https://doi.org/10.1016/j.jcat.2008.08.008>.
- [82] S. Raimondeau, D.G. Vlachos, Recent developments on multiscale, hierarchical modeling of chemical reactors, *Chem. Eng. J.* 90 (2002) 3–23. [https://doi.org/10.1016/S1385-8947\(02\)00065-7](https://doi.org/10.1016/S1385-8947(02)00065-7).
- [83] A.B. Mhadeshwar, D.G. Vlachos, A thermodynamically consistent surface reaction mechanism for CO oxidation on Pt, *Combust. Flame.* 142 (2005) 289–298. <https://doi.org/10.1016/j.combustflame.2005.01.019>.
- [84] M. Maestri, K. Reuter, Semiempirical rate constants for complex chemical kinetics: First-principles assessment and rational refinement, *Angew. Chemie - Int. Ed.* 50 (2011) 1194–1197. <https://doi.org/10.1002/anie.201006488>.
- [85] A.B. Mhadeshwar, H. Wang, D.G. Vlachos, Thermodynamic Consistency in Microkinetic Development of Surface Reaction Mechanisms, *J. Phys. Chem. B.* 107 (2003) 12721–12733. <https://doi.org/10.1021/jp034954y>.
- [86] L.C. Grabow, A.A. Gokhale, S.T. Evans, J.A. Dumesic, M. Mavrikakis, Mechanism of the water gas shift reaction on Pt: First principles, experiments, and microkinetic modeling, *J. Phys. Chem. C.* 112 (2008) 4608–4617. <https://doi.org/10.1021/jp7099702>.
- [87] S. Kandoi, J. Greeley, M.A. Sanchez-castillo, S.T. Evans, A.A. Gokhale, J.A. Dumesic, M. Mavrikakis, Prediction of experimental methanol decomposition rates on platinum from first principles, 37 (2006). <https://doi.org/10.1007/s11244-006-0001-1>.
- [88] M. Saliccioli, M. Stamatakis, S. Caratzoulas, D.G. Vlachos, A review of multiscale modeling of metal-catalyzed reactions: Mechanism development for complexity and emergent behavior, *Chem. Eng. Sci.* 66 (2011) 4319–4355. <https://doi.org/10.1016/j.ces.2011.05.050>.
- [89] J.N. Brønsted, Acid and basic catalysis, *Chem. Rev.* 5 (1928) 231–338. <https://doi.org/10.1021/cr60019a001>.
- [90] M. G. Evans, M. Polanyi, Further considerations on the thermodynamics of chemical equilibria and reaction rates, *Trans. Faraday Soc.* 32 (1936) 1333–1360.
- [91] R. Alcalá, M. Mavrikakis, J.A. Dumesic, DFT studies for cleavage of C-C and C-O bonds in surface species derived from ethanol on Pt(111), *J. Catal.* 218 (2003) 178–190.

[https://doi.org/10.1016/S0021-9517\(03\)00090-3](https://doi.org/10.1016/S0021-9517(03)00090-3).

- [92] T. Bligaard, J.K. Nørskov, S. Dahl, J. Matthiesen, C.H. Christensen, J. Sehested, The Brønsted-Evans-Polanyi relation and the volcano curve in heterogeneous catalysis, *J. Catal.* 224 (2004) 206–217. <https://doi.org/10.1016/j.jcat.2004.02.034>.
- [93] J.K. Nørskov, T. Bligaard, A. Logadottir, S. Bahn, L.B. Hansen, M. Bollinger, H. Bengaard, B. Hammer, Z. Sljivancanin, M. Mavrikakis, Y. Xu, S. Dahl, C.J.H. Jacobsen, Universality in heterogeneous catalysis, *J. Catal.* 209 (2002) 275–278. <https://doi.org/10.1006/jcat.2002.3615>.
- [94] D.W. Blaylock, Teppei Ogura, H.G. William, J.O.B. Gregory, Computational investigation of thermochemistry and kinetics of steam methane reforming on Ni(111) under realistic conditions, *J. Phys. Chem. C.* 113 (2009) 4898–4908. <https://doi.org/10.1021/jp806527q>.
- [95] Y. Kathiraser, U. Oemar, E.T. Saw, Z. Li, S. Kawi, Kinetic and mechanistic aspects for CO₂ reforming of methane over Ni based catalysts, *Chem. Eng. J.* 278 (2015) 62–78. <https://doi.org/10.1016/j.cej.2014.11.143>.
- [96] J. Wei, E. Iglesia, Isotopic and kinetic assessment of the mechanism of reactions of CH₄ with CO₂ or H₂O to form synthesis gas and carbon on nickel catalysts, *J. Catal.* 224 (2004) 370–383. <https://doi.org/10.1016/j.jcat.2004.02.032>.
- [97] Z.L. Zhang, X.E. Verykios, Carbon dioxide reforming of methane to synthesis gas over supported Ni catalysts, *Catal. Today.* 21 (1994) 589–595. [https://doi.org/10.1016/0920-5861\(94\)80183-5](https://doi.org/10.1016/0920-5861(94)80183-5).
- [98] S. Wang, G.Q. (Max) Lu, Reaction kinetics and deactivation of Ni-based catalysts in CO₂ reforming of methane, *React. Eng. Pollut. Prev.* (2000) 75–84. <https://doi.org/10.1016/b978-044450215-5/50080-9>.
- [99] X.E. Verykios, Catalytic dry reforming of natural gas for the production of chemicals and hydrogen, *Chem. Ind. Chem. Eng. Q.* 8 (2002) 238–255. <https://doi.org/10.2298/hemind0206238v>.
- [100] J.F. Múnera, S. Irusta, L.M. Cornaglia, E.A. Lombardo, D. Vargas Cesar, M. Schmal, Kinetics and reaction pathway of the CO₂ reforming of methane on Rh supported on lanthanum-based solid, *J. Catal.* 245 (2007) 25–34. <https://doi.org/10.1016/j.jcat.2006.09.008>.
- [101] J. Wei, E. Iglesia, Structural requirements and reaction pathways in methane activation and chemical conversion catalyzed by rhodium, *J. Catal.* 225 (2004) 116–127. <https://doi.org/10.1016/j.jcat.2003.09.030>.
- [102] A. Donazzi, A. Beretta, G. Groppi, P. Forzatti, Catalytic partial oxidation of methane over a 4% Rh/ α -Al₂O₃ catalyst Part II: Role of CO₂ reforming, *J. Catal.* 255 (2008) 259–268. <https://doi.org/10.1016/j.jcat.2008.02.010>.
- [103] M.C.J. Bradford, M.A. Vannice, Catalytic reforming of methane with carbon dioxide over nickel catalysts II. Reaction kinetics, *Appl. Catal. A Gen.* 142 (1996) 97–122. [https://doi.org/10.1016/0926-860X\(96\)00066-X](https://doi.org/10.1016/0926-860X(96)00066-X).
- [104] V.A. Tspouriari, X.E. Verykios, Kinetic study of the catalytic reforming of methane with carbon dioxide to synthesis gas over Ni/La₂O₃ catalyst, *Catal. Today.* 64 (2001) 83–90. [https://doi.org/10.1016/S0920-5861\(00\)00511-3](https://doi.org/10.1016/S0920-5861(00)00511-3).

- [105] K. Herrera Delgado, L. Maier, S. Tischer, A. Zellner, H. Stotz, O. Deutschmann, Surface reaction kinetics of steam- and CO₂-reforming as well as oxidation of methane over nickel-based catalysts, *Catalysts*. 5 (2015) 871–904. <https://doi.org/10.3390/catal5020871>.
- [106] L. Dehimi, Y. Benguerba, M. Virginie, H. Hijazi, Microkinetic modelling of methane dry reforming over Ni/Al₂O₃ catalyst, *Int. J. Hydrogen Energy*. 42 (2017) 18930–18940. <https://doi.org/10.1016/j.ijhydene.2017.05.231>.
- [107] Z. Xie, Q. Liao, M. Liu, Z. Yang, L. Zhang, Micro-kinetic modeling study of dry reforming of methane over the Ni-based catalyst, *Energy Convers. Manag.* 153 (2017) 526–537. <https://doi.org/10.1016/j.enconman.2017.10.022>.
- [108] C. Karakaya, L. Maier, O. Deutschmann, Surface Reaction Kinetics of the Oxidation and Reforming of CH₄ over Rh/Al₂O₃ Catalysts, *Int. J. Chem. Kinet.* 48 (2016) 144–160. <https://doi.org/10.1002/kin.20980>.
- [109] L.C.S. Kahle, T. Roussi re, L. Maier, K. Herrera Delgado, G. Wasserschaff, S.A. Schunk, O. Deutschmann, Methane dry reforming at high temperature and elevated pressure: Impact of gas-phase reactions, *Ind. Eng. Chem. Res.* 52 (2013) 11920–11930. <https://doi.org/10.1021/ie401048w>.
- [110] A. Behroozsarand, A.N. Pour, Modeling of microreactor for methane dry reforming: Comparison of Langmuir-Hinshelwood kinetic and microkinetic models, *J. Nat. Gas Sci. Eng.* 20 (2014) 99–108. <https://doi.org/10.1016/j.jngse.2014.06.011>.
- [111] A. Akande, A. Aboudheir, R. Idem, A. Dalai, Kinetic modeling of hydrogen production by the catalytic reforming of crude ethanol over a co-precipitated Ni-Al₂O₃ catalyst in a packed bed tubular reactor, *Int. J. Hydrogen Energy*. 31 (2006) 1707–1715. <https://doi.org/10.1016/j.ijhydene.2006.01.001>.
- [112] E. Akpan, A. Akande, A. Aboudheir, H. Ibrahim, R. Idem, Experimental, kinetic and 2-D reactor modeling for simulation of the production of hydrogen by the catalytic reforming of concentrated crude ethanol (CRCCE) over a Ni-based commercial catalyst in a packed-bed tubular reactor, *Chem. Eng. Sci.* 62 (2007) 3112–3126. <https://doi.org/10.1016/j.ces.2007.03.006>.
- [113] Y.J. Wu, J.C. Santos, P. Li, J.G. Yu, A.F. Cunha, A.E. Rodrigues, Simplified kinetic model for steam reforming of ethanol on a Ni/Al₂O₃ catalyst, *Can. J. Chem. Eng.* 92 (2014) 116–130. <https://doi.org/10.1002/cjce.21773>.
- [114] C. Graschinsky, M. Laborde, N. Amadeo, A. Le Valant, N. Bion, F. Epron, D. Duprez, Ethanol steam reforming over Rh(1%)MgAl₂O₄/Al₂O₃: A kinetic study, *Ind. Eng. Chem. Res.* 49 (2010) 12383–12389. <https://doi.org/10.1021/ie101284k>.
- [115] D.R. Sahoo, S. Vajpai, S. Patel, K.K. Pant, Kinetic modeling of steam reforming of ethanol for the production of hydrogen over Co/Al₂O₃ catalyst, *Chem. Eng. J.* 125 (2007) 139–147. <https://doi.org/10.1016/j.cej.2006.08.011>.
- [116] F. Wang, W. Cai, C. Descorme, H. Provendier, W. Shen, C. Mirodatos, Y. Schuurman, From mechanistic to kinetic analyses of ethanol steam reforming over Ir/CeO₂ catalyst, *Int. J. Hydrogen Energy*. 39 (2014) 18005–18015. <https://doi.org/10.1016/j.ijhydene.2014.06.121>.
- [117] J.E. Sutton, P. Panagiotopoulou, X.E. Verykios, D.G. Vlachos, Combined DFT, microkinetic, and experimental study of ethanol steam reforming on Pt, *J. Phys. Chem. C*.

117 (2013) 4691–4706. <https://doi.org/10.1021/jp312593u>.

- [118] R. Baruah, M. Dixit, A. Parejiya, P. Basarkar, A. Bhargav, S. Sharma, Oxidative steam reforming of ethanol on rhodium catalyst – I: Spatially resolved steady-state experiments and microkinetic modeling, *Int. J. Hydrogen Energy*. 42 (2017) 10184–10198. <https://doi.org/10.1016/j.ijhydene.2017.03.168>.
- [119] Z.J. Zhao, Z. Li, Y. Cui, H. Zhu, W.F. Schneider, W.N. Delgass, F. Ribeiro, J. Greeley, Importance of metal-oxide interfaces in heterogeneous catalysis: A combined DFT, microkinetic, and experimental study of water-gas shift on Au/MgO, *J. Catal.* 345 (2017) 157–169. <https://doi.org/10.1016/j.jcat.2016.11.008>.
- [120] M.M. Kauppinen, M.M. Melander, A.S. Bazhenov, K. Honkala, Unraveling the Role of the Rh-ZrO₂ Interface in the Water-Gas-Shift Reaction via a First-Principles Microkinetic Study, *ACS Catal.* 8 (2018) 11633–11647. <https://doi.org/10.1021/acscatal.8b02596>.
- [121] A. Baz, A. Holewinski, Understanding the interplay of bifunctional and electronic effects: Microkinetic modeling of the CO electro-oxidation reaction, *J. Catal.* 384 (2020) 1–13. <https://doi.org/10.1016/j.jcat.2020.02.003>.

CHAPTER 3: METHODOLOGY

This chapter will give a brief summary of microkinetic analysis and the approach followed in formulating and developing the initial single-site microkinetic model developed for the steam reforming of ethanol over a Ni/SiO₂ catalyst. The alterations and improvements to the model performed in order to achieve the other set objectives will be discussed in the relevant chapters. The inclusion of the fraction of local entropy (F_{loc}) of an adsorbed species as a model parameter was integrated into the initially developed model and will be described in Chapter 5. The addition of a second defined active site with a separate set of differential and algebraic equations will be described in Chapter 6. Finally, the experimental methodology is discussed in this chapter.

3.1 Microkinetic analysis

Microkinetic analysis is an examination of catalytic reactions in terms of elementary chemical reaction steps that occur on the surface of a catalyst, and their relation with each other and the catalyst surface. The first step in a microkinetic analysis is to develop a rigorous network of elementary reactions that capture the essential surface chemistry involved in the process. A fundamental principle of microkinetic analysis is the use of chemical reaction kinetic parameters in the rate expressions which can be estimated theoretically or experimentally.

With reasonably accurate estimates of preexponential factors, enthalpies and entropies of adsorption, sticking coefficients, surface bond energies, activation energies active site densities etc., a microkinetic analysis suggests which steps in the network/mechanism are likely to be kinetically significant and which surface species is/are most abundant, which are all important information for the prediction of how different reaction steps affect catalyst performance and are consequentially important in the catalyst selection process [1].

3.1.1 Apparent Rate Expressions

The Power law is the most utilised rate expression in kinetic analysis, as it captures the temperature and concentration dependence of the process. Generally, any rate expression can be reduced to a power law form, that is the power law becomes a limiting approximation of the more complicated rate expression, with its reaction order and activation energy becoming functions of the reaction conditions. The power law is therefore valid over a rather narrow range of conditions and is a simple expression convenient for reactor design for non-catalytic gas phase reactions.

However, for catalytic reactions the power law rate expression is not valid over a very wide range of conditions, owing in part to the fact that the expression does not account for saturation or

inhibition effect, of certain surface species, which could cause a zero-reaction rate when there is increase in their concentration. Langmuir-Hinshelwood and Hougen-Watson rate expressions are more appropriate for heterogeneous catalytic reactions.

3.1.2 Reaction Mechanisms

Different reaction mechanism schemes for the same process can lead to the same apparent rate expression, so even if kinetic data is accurately collected the correct reaction mechanism cannot be predicted by fitting the collected data to a rate expression, in other words the rate expression for a process can be determined from the reaction mechanism but the reaction mechanism cannot be determined from the rate expression (unidirectional mapping between rate and mechanism). This is the reason as to why research into chemical reactions is not focused solely on the rates of the reaction but also on the collection of other information, like spectroscopy, to provide information about important species occurring and important elementary steps in the reaction mechanism. Catalytic reaction mechanisms are a sequence of elementary reaction steps that describe on a molecular level, which reactions take place and how they occur.

As stated previously the strategy in microkinetics is to formulate a rigorous and serviceable mechanism that captures the essential surface chemistry occurring on the surface of the catalyst. This formulated mechanism is based on a series of speculations that must be validated with experimental data and revised when necessary. A feasible reaction mechanism must contain all reactants, products and a number of proposed reaction intermediates formed and consumed during the process.

The validity of an elementary step in a reaction mechanism is usually assessed by counting the number of chemical bonds broken and formed, with steps involving the transformation of more than a few chemical bonds being somewhat unrealistic. The formulation of reaction mechanism in terms of elementary steps on catalyst surface must be balanced with the need for expressing said mechanism in terms of kinetic parameters relatable to experimental measurements and theoretical predictions. This compromise between mechanistic detail of mechanism and kinetic parameter estimation plays a key role in microkinetic analysis.

The strategy in kinetic analysis is to examine the reaction mechanism by analysing available kinetic data using realistic values of kinetic rate constants. Collision theory and Transition state theory are used to complement available experimental data for kinetically significant kinetic parameters and provide accurate estimates of rate constants.

3.1.3 Rate Constant Estimation

Collision Theory

Collision theory provides a simple description of kinetic processes. It explains that reactions occur when molecules collide with sufficient kinetic energy. It therefore uses the probability of molecules colliding to determine a rate expression.

Imagine a gas phase bimolecular reaction, $A + B = C + D$. The number of collisions per unit time, Z_A , a molecule of A will undergo with B molecules is equal to the volume swept by molecule A per unit time, V_A , multiplied by the concentration of molecule B in the collision volume.

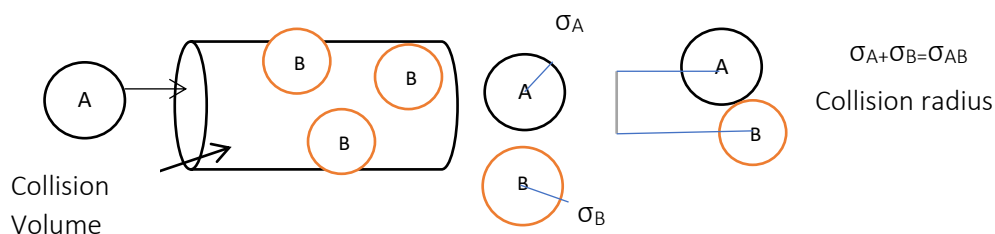


Figure 3-1: Collision tube

$$Z_A = V_A n_B = \pi \sigma_{AB}^2 v_{AB} n_B \quad (3.1)$$

$$v_{AB} = \text{Average relative velocity of A with respect to B} = \sqrt{\frac{8k_b T}{\pi \mu_{AB}}} \quad (3.2)$$

$$\mu_{AB} = \text{Reduced mass of A B pair} \quad (3.3)$$

The reaction rate is the total number of AB collisions multiplied by the probability of collision leading to a reaction:

$$r_{AB} = Z_{AB} * P_{rxn} = Z_A n_A P_{rxn} \quad (3.4)$$

$$r_{AB} = \pi \sigma_{AB}^2 \sqrt{\frac{8k_b T}{\pi \mu_{AB}}} \exp\left(-\frac{E_a}{k_b T}\right) n_A n_B \quad (3.5)$$

Rate Constant is therefore:

$$k_{AB} = \pi \sigma_{AB}^2 \sqrt{\frac{8k_b T}{\pi \mu_{AB}}} \exp\left(-\frac{E_a}{k_b T}\right) \quad (3.6)$$

For a Surface reaction however the relative velocity of the molecule differs:

$$v_{AB} = \sqrt{\frac{\pi k_b T}{2\mu_{AB}}} \quad (3.7)$$

And the rate constant for surface reaction according to collision theory is:

$$k_{AB} = 2\sigma_{AB} \sqrt{\frac{\pi k_b T}{2\mu_{AB}}} \exp\left(-\frac{E_a}{k_b T}\right) \quad (3.8)$$

Transition State Theory

Although Collision theory provides a convenient basis for initial rate constant estimation, it does not allow for details of the structure of the molecules to be incorporated into the rate constant estimation. Transition state theory however does account for molecular structure.

The transition state theory assumption is that between the reactant species and an activated complex equilibrium is established. The activated complex is a species in transition between reactant and product.

For a reaction $A+B = C+D$, the ideal equilibrium constant is written as a function of the product concentrations and reactant concentrations, however between the reactant and an activated complex it is written as;

$$K = \frac{n_{AB}}{n_A n_B} \quad (3.9)$$

The rate of the reaction is equal to the concentration of the activated complex multiplied by frequency factor

$$r_{AB} = (k_b T/h) K n_A n_B \quad (3.10)$$

The macroscopic formulation of transition state theory is obtained when the equilibrium constant is written in terms of standard entropy and enthalpy changes.

$$r_{AB} = (k_b T/h) \exp(\Delta S^0/k_b) \exp(\Delta S^0/k_b T) n_A n_B \quad (3.11)$$

The Microscopic formulation is obtained when the equilibrium constant between activated complex and reactants is written in terms of molecular partition functions per unit volume, Q_i''' .

The molecular partition function for a species is a product of its translational, rotational and vibrational degrees of freedom, $q_{it}''', q_{ir}, q_{vib}$.

$$Q_i''' = q_{it}''' q_{ir} q_{vib} \quad (3.12)$$

$$q_{it}''' = \frac{(2\pi m_i k_b T)^{3/2}}{h^3} \quad (3.13)$$

$$q_{ir} = \frac{8\pi^2 I_i k_b T}{\sigma h^2} \quad (3.14)$$

$$q_{vib} = \prod \frac{1}{1 - \exp\left(-\frac{h\nu_{ij}}{k_b T}\right)} \quad (3.15)$$

I_i , is the moment of inertia about the molecular axis, σ is the rotational symmetry, ν_{ij} are the frequencies of the modes of vibration.

The rate constant using microscopic formulation of transition state theory is written as;

$$k_{AB} = (k_b T/h) Q_{AB}''' / Q_A''' Q_B''' \exp\left(-\frac{\Delta E_a}{k_b T}\right) \quad (3.16)$$

3.1.4 Thermodynamic Consistency

During the development of the microkinetic model it is necessary to ensure thermodynamic consistency at both enthalpic and entropic level [1,2]. Kinetic parameters of forward and backward elementary surface reaction steps are selected under *thermochemical constraints at individual reaction*, but also, more importantly, at reaction mechanism level. For every elementary step i considered in the model, the following relations hold between the respective forward and backward pre-exponential factors and activation energies:

$$e^{\Delta S_{s,i}/R} = A_i^f / A_i^b \quad (3.17)$$

$$E_i^f - E_i^b = \Delta H_{s,i} \quad (3.18)$$

Thermodynamic relationships are further established between surface reaction enthalpies and entropies and analogous gas-phase reactions, wherein the thermodynamic data of involved

surface intermediates are either explicitly obtained through appropriate correlations or are defined as adjustable parameters.

The entropy of each surface species j at the average experimental temperature is calculated through the subtraction of the gaseous translational entropy from the entropy of the equivalent gas species, leaving the entropy contributions from vibrational and rotational degrees of freedom, hence the following equation is applied:

$$S_{s,j} = S_{g,j} - S_{trans_{3D},j} \quad (3.19)$$

The equation above suggests that all surface species are essentially immobile on the surface losing three degrees of freedom upon adsorption. The translational entropy contribution in equation (19) is calculated according to [3]:

$$S_{trans_{3D},j} = R \left[\ln \left(\frac{(2\pi M_j k_B T)^{3/2}}{h^3} \right) + \ln \left[\frac{k_B T}{P} \right] + \frac{5}{2} \right] \quad (3.20)$$

Equivalently, the enthalpy of each surface species j at the average experimental temperature is correlated to the gaseous enthalpy through the chemisorption enthalpy of the respective species:

$$H_{s,j} = H_{g,j} - Q_j \quad (3.21)$$

In the current work, these chemisorption enthalpies of all surface species have been defined as model parameters and are obtained through regression of the experimental data or fixed at DFT calculated values if found to possess low sensitivity coefficients. Standard-state thermodynamic properties of all gaseous species are assumed to be functions of temperature and are expressed in the form of polynomial fits, namely in the NASA chemical equilibrium code format.

3.1.5 Kinetic model parameters calculation

Arrhenius equations are used in calculating the rate coefficients of the elementary reaction steps in the network, whilst the rate of the elementary step itself is related to the concentrations of the reacting species and calculated *via* the law of mass action.

For the adsorption reactions, collision theory is used to determine the maximum possible pre-exponential factor. The calculated maximum value of pre-exponential factor is further adjusted using a factor called the sticking coefficient, denoting the probability of a collision of a molecule or radical leading to an adsorption.

The pre-exponential factor for a reaction i involving the adsorption of species j is given by:

$$A_i^f = k_i = \frac{S_p}{L_t^n} \frac{1}{\sqrt{2\pi M_j RT}} \quad (3.22)$$

The temperature used is the average experimental temperature.

The pre-exponential factor for the desorption reactions is calculated based on that of the adsorption reaction by preserving entropic level thermodynamic consistency according to equation (3.17).

Pre-exponential factors for the forward step for all reactions involving surface species are calculated using the microscopic formulation of transition state theory obtained when the equilibrium constant for the production of an activated complex from reactants is written in terms of molecular partition functions, as seen equation (3.23) [1]. Entropic thermodynamic consistency is again used to determine the backward pre-exponential factor according to equation (3.17).

$$A_i^f = k_i = \left(\frac{k_b T}{h}\right) * \frac{Q_{AB}'''}{Q_A''' Q_B'''} \quad Q_i''' = q_{it}''' q_{ir} q_{iv} \quad (3.23)$$

where Q_i''' depicts the overall partition function for a species, with q_{it}''' , q_{ir} and q_{iv} depicting the translational, rotational and vibrational partition functions respectively. In this work, it is assumed that the translational partition function degrees of freedom are negligible as the values of the transition state and the reactants will only vary based on the minute difference in the mass of the molecules considered, and it therefore can be said that the ratio of the translational partition functions will yield approximately unity. The vibrational partition function for surface reaction is also assumed to be unity. The molecular partition function ratio is therefore just a ratio of the rotational partition functions of the transition state and the reactants.

The rotational partition function is calculated from the moment of inertia of the molecule I_i as well as the temperature T , as shown in equation (24):

$$q_{ir} = \frac{8\pi^2 I_i k_b T}{\sigma h^2} \quad (3.24)$$

It is assumed that the molecule upon adsorption rotates around the vertical axis of the atom attached to the surface of the catalyst. The moment of inertia of functional groups or molecules attached to the absorbed atom can be calculated given their bond lengths and angles. The overall moment of inertia can then be calculated by taking the attached groups as reduced masses rotating around the absorbed atom's vertical axis.

As an example, CH₃CHOH is depicted as being attached to the surface of the catalyst through its carbon atom. This was derived from the DFT analysis conducted by Sutton et al. [4] on ethanol decomposition. The attached carbon atom has a CH₃, OH and H groups attached to it and the moment of inertia of these can be calculated knowing the respective bond lengths and angles. The overall moment of inertia can then be found by the calculation of the sum of moments of inertia of the attached functional groups internal rotation and the external rotation around the attached carbon. In essence, the moment of inertia is the sum all moments of inertia of the compounds rotating around the attached atom.

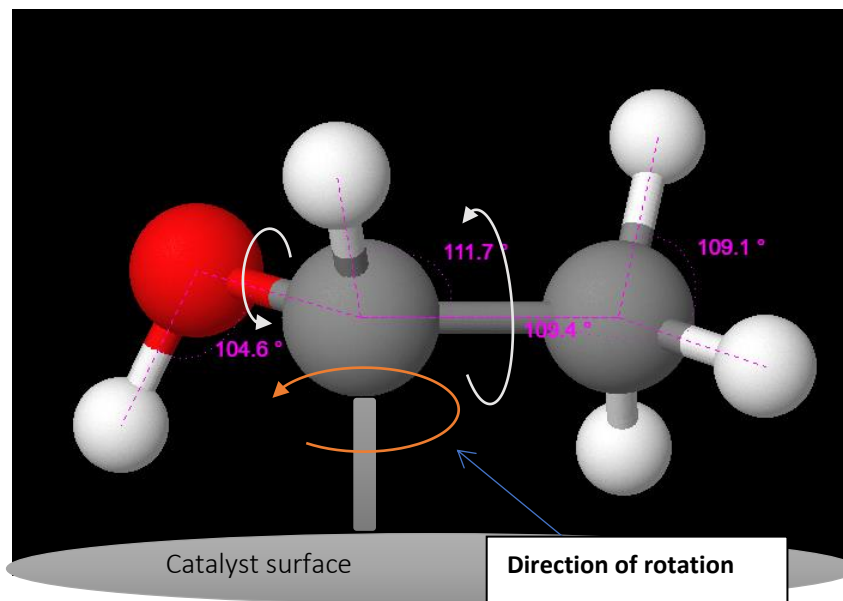


Figure 3-2: Adsorbed 1-hydroxyethyl species. (grey, white and red balls represent carbon, hydrogen and oxygen respectively)

For this case the following can be determined:

Bond Lengths; C-H = 1.09 Å, C-C = 1.487 Å, C-O = 1.38 Å, O-H = 0.971 Å.

Bond Angles; H-C-H = 109.1°, C-C-O = 120°, C-C-H = 111.7°

Temperature = 723.15 K, $\sigma = 1$

Moreover, to simplify calculations it is assumed that the β carbon, oxygen and hydrogen atoms attached to the α carbon are all on a same plane that is horizontal to the metal surface. Based on this, the following moments of inertia can be calculated:

Hydrogens rotating around β C atom:

$$I_{\text{beta H}} = 3 * m_{\text{hydrogen}} * (1.09 \times 10^{-10} \cos(109.4 - 90))^2 = 5.35 \times 10^{-47} \text{ kg m}^2$$

Hydrogen rotating around α carbon atom:

$$I_{\alpha H} = m_{hydrogen} * (1.09 \times 10^{-10})^2 = 1.988 \times 10^{-47} \text{ kg m}^2$$

Oxygen rotating around α carbon atom:

$$I_O = m_O * (1.38 \times 10^{-10})^2 = 5.06 \times 10^{-46} \text{ kg m}^2$$

Hydrogen rotating around oxygen atom:

$$I_H = m_H * (0.971 \times 10^{-10} \cos(104.6 - 90))^2 = 9.11 \times 10^{-48} \text{ kg m}^2$$

Total moment of inertia of CH₃ group:

$$I_{CH_3} = m_{carbon} * (1.487 \times 10^{-10})^2 + I_{\beta H} = 4.95 \times 10^{-46} \text{ kg m}^2$$

These calculations give the rotation of the reduced masses around the attached C atom and the summation therefore gives the total moment of inertia of the species.

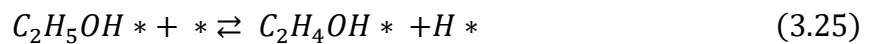
$$I_{total} = 1.029 \times 10^{-45} \text{ kg m}^2 \text{ and } q_{rot} = 8\pi^2 I_i k_b T / \sigma h^2 = 1848.35$$

To calculate the pre-exponential factors of all forward steps the assumption was made that all transition states look like the products and therefore the moment of inertia of the latter can be used as that of the former. However, in the event that the reaction entropy change is a negative value, the pre-exponential of the reverse reaction is calculated using the transition state theory with thermodynamic consistency now being used to calculate the forward pre-exponential factor.

The activation energies of the molecular adsorption reactions are set as zero, assuming the latter non-activated. The desorption reaction activation energies are therefore equivalent to the surface reaction enthalpy change $\Delta H_{s,i}$, which in an adsorption reaction is obtained directly from the chemisorption enthalpy of the species.

For surface reactions, the UBI-QEP method was used to determine the activation energies of forward steps, with enthalpic thermodynamic consistency used to determine that of the reverse step according to equation (2).

As an example, the activation energy of the following surface reaction:



is calculated *via* the UBI-QEP theory using the adsorption enthalpies of the species involved and the overall reaction enthalpy:

$$E_i^f = \frac{1}{2} \cdot \left(\Delta H_{s,i} + \frac{Q_{C_2H_4OH} Q_H}{Q_{C_2H_4OH} + Q_H} \right) \quad (3.26)$$

where Q_i , represents the chemisorption enthalpy of the species i .

The surface reaction enthalpy $\Delta H_{s,i}$, can be calculated directly from the surface enthalpies of the product and reactant species or based on the chemisorption enthalpies of the involved species as:

$$\Delta H_{s,i} = \Delta H_{g,i} + Q_{C_2H_5OH} - Q_{C_2H_4OH} - Q_H \quad (3.27)$$

3.2 Microkinetic engine

The microkinetic engine is a FORTRAN code designed to perform parameter estimation for chemical reaction networks. It uses reactions with parameterised Arrhenius rate equations in conjunction with a reactor model to calculate the outlet conditions of the reactor. It numerically solves systems of differential equations. The numeric integration of the set of equation simulates the reactor, and then the resulting outlet flow rates are used in the approximation of the minimum sum of squared differences coupled with given weights with the aid of Rosenbrock and Levenberg-Marquardt optimisation algorithms. The objective function used is the weighted residual sum of squares of the molar flow rates of the components and is minimized with respect to the unknown model parameter b :

$$S(b) = \sum_{i=1}^{N_{resp}} \sum_{j=1}^{N_{exp}} w_p (F_{j,i} - \dot{F}_{i,j})^2 \xrightarrow{b} \min \quad (3.28)$$

where N_{resp} equals the number of responses, N_{exp} equals the number of experiments, \dot{F} represents the model calculated outlet molar flow rates, and w_p are elements of the inverse of the error variance-covariance matrix, calculated from replicate experiments or estimated from the observed and calculated molar fractions at the reactor outlet, and represent the weights for each response.

The model for the reactor could either be a mixed flow reactor or an ideal plug flow reactor. The reactants and products in our case are modelled using ideal plug flow reactor mass balance with reaction. The following set of differential and algebraic equations are integrated for each gas phase component i :

$$\frac{dF_i}{dW} = R_i \quad (3.29)$$

Where F_i is the molar flow rate of the component i (mol s⁻¹), W is the catalyst mass (kg), and R_i is the net production rate of component i (mol kg⁻¹ s⁻¹). The net rate of formation of species i is the sum of the rates of the elementary steps, in which i is produced minus the rates of the elementary steps in which i is consumed:

$$R_i = \sum_j v_{ij} k_j C_{obs}^n \theta_{int}^m \quad (3.30)$$

where k_j is the rate coefficient of elementary step j , v_{ij} the stoichiometric coefficient, C_{obs} is the concentration of the observable (mol kg^{-1}), θ_{int} is the concentration of the surface intermediate (mol kg^{-1}), and n, m are the reaction orders. In a microkinetic reaction network, the reaction orders are all equal to stoichiometry.

Pseudo-steady state approximation is used to model intermediates. Thus, their net production rate is zero:

$$R_{intermediate} = 0 \quad (3.31)$$

The catalyst free active sites are modelled using the mole balance over all the active sites.

$$\theta_{tot} = \theta_* + \sum \theta_{int} \quad (3.32)$$

Thus, providing us with a system of both differential and algebraic equations.

The system is numerically integrated by the DDASPK solver, initial values are given to the products and reactants which are modelled as differential equations. The intermediates and free sites are algebraic equations. Good initial values for the coverage of the sites by the intermediates are required for the solver to initialise successfully. To obtain these initial values, the clean catalyst surface is evolved to steady state. The solver integrates the differential equations using the finite difference approximation thus converting the entire system into algebraic equation to be solved *via* Newton method.

The net reaction rate is calculated based on stoichiometric coefficients supplied in the reaction mechanism. Each reaction is characterised by Arrhenius rate equation using the pre-exponential factors, activation energy and reaction order as parameters.

The engine output consists of parameter estimation represented graphically through parity and residual plots. For the parity plots the simulated result is plotted as a function of the experimental result.

For further information on the Microkinetic engine refer to Metaxas et al. [5]

3.2.1 Alterations to the Microkinetic engine

A large subroutine was written in which the reaction kinetics and kinetic parameters are calculated from input data. The gas phase thermochemical properties are calculated using the NASA polynomials equations with input data gotten from available databases. The surface

thermochemical properties are calculated as previously described and the elementary reaction rates are obtained within this subroutine, which are then used by the microkinetic engine in the plug flow reactor model as the R_i .

Additionally, a subroutine was written to initialise the system of differential and algebraic equations and give good initial values for the surface coverages of intermediate species. This was done by integrating and evolving a clean catalyst surface to steady state with the initial input of all reaction rates.

Compared to a previous version in which the rate data was manually input after simple estimation of barriers and approximation of pre-exponential factors from experimental data. These alterations have had minimal impact on the computational speed of the engine but have improved significantly the accuracy of the model developed.

3.3 Experimental methodology for the kinetic investigation of ESR over Ni/biochar catalyst

3.3.1 Catalyst sample preparation

The samples of biochar utilised were acquired from the Renergi gasification demonstration plant at Curtin University, Australia [6]. The sample was prepared from the pyrolysis and subsequent partial gasification of Mallee wood biomass. The gasification of the sample took place for a duration of 5-10 minutes at temperature of 750-850°C, ensuring increased O-containing functional group concentration and in turn increased catalytic activity [7,8]. The presence of surface O-containing functional groups on these samples, specifically of aromatic C – O and C = O structures, was confirmed *via* X-Ray Photoelectron Spectroscopy and mentioned in literature [9]. The biochar sample was sieved to obtain two samples of particle size, range 106-250 μm and 55-106 μm , respectively. The elemental composition of the biochar (dry and ash-free basis) was 91.5% carbon, 1.0% hydrogen, 0.7% nitrogen and 6.8% oxygen.

The Ni/biochar catalyst with 10 wt.% Ni was prepared by the commonly applied incipient wetness impregnation method [10–12] using $\text{Ni}(\text{NO}_3)_2 \cdot 6\text{H}_2\text{O}$ obtained from Merck as the precursor. The water saturation volume of biochar was determined and then an aqueous solution of precursor was prepared with the same volume of water. The aqueous solution was added to the biochar sample and stirred for 4 hours before being dried in an oven at 105°C overnight. The collected catalyst sample was calcined in Ar flow (100 ml min^{-1}) with a ramp rate of 15°C min^{-1} to 600°C for 3 hours.

3.3.2 Reactor set up

A quartz tubular fixed-bed reactor of internal diameter 10 mm was used for the catalytic reforming and decomposition of ethanol. The catalyst bed was made up of two layers supported on a porous plate, including a layer of quartz wool to support the bed and then the Ni/biochar catalyst bed mixed with quartz sand to maintain bed height and smooth gas flow through the bed. A thermocouple was placed directly above the catalyst bed to ensure accurate temperature readings. The reactant mixture was fed by an HPLC pump. The feed was preheated using a heating tape set at 150°C prior to reactor inlet. Mass flow controllers (MFC) were used to control the flowrates of nitrogen and hydrogen gas, the former used as the carrier gas and the latter used for catalyst reduction prior to the experimental run. Connected pressure gauges were used to monitor the pressures of the gas flows.

The outlet of the reactor is connected to a three-way valve. The first outlet was connected to a HP Agilent 6890 capillary column GC equipped with pre-column backflush, a flame ionization detector (FID) and a thermal conductivity detector (TCD) for the analysis of total gaseous product range at regular intervals. The second outlet was connected to three cold traps filled with 50, 40 and 30ml of HPLC-grade $\text{CHCl}_3/\text{CH}_3\text{OH}$ mixture (4:1 volume ratio) in series [13]. The traps are cooled by an ice-water bath (0°C) and two dry-ice baths (-78°C) respectively to collect liquid effluent, which was then analysed in a [Agilent 6850 GC/5975B MS](#).

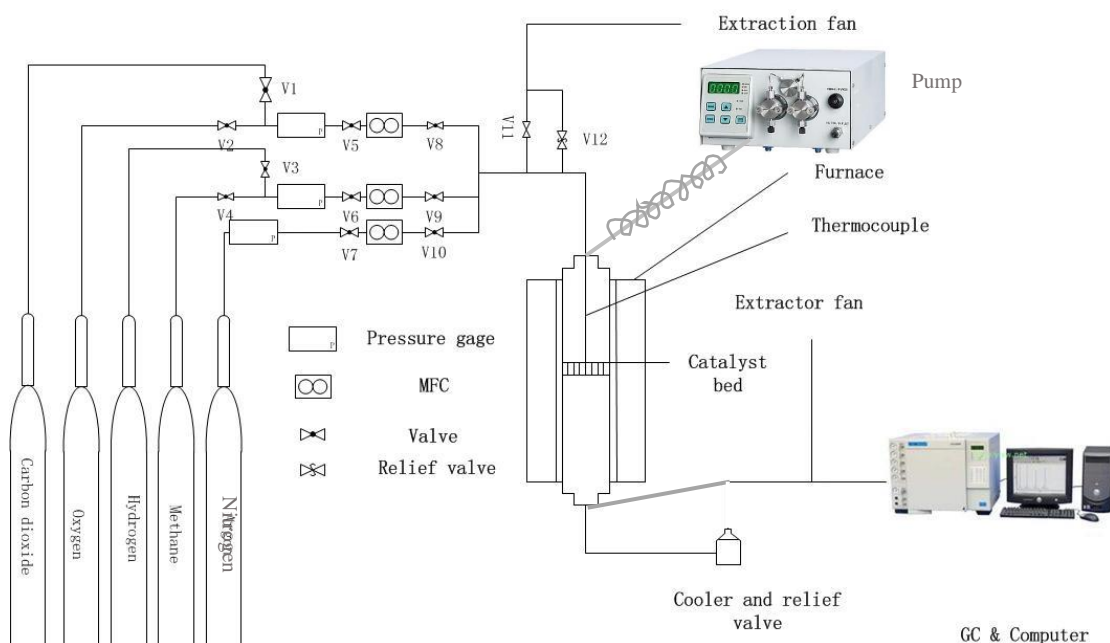


Figure 3-3: Schematic of reactor setup.

3.3.3 Experimental conditions and parameters

Prior to experiments the catalyst was reduced at 500°C with a stream of 5% H₂ in N₂ flow of 1 L min⁻¹ for 1 h. To ensure explicit kinetic control, external mass transfer was investigated by varying the carrier gas flow rate from 0.1 to 2.5 L min⁻¹ of N₂ (at 450°C and atmospheric pressure) and observing the changes in the observed reaction rate. Internal mass transfer was investigated by varying the catalyst particle size range of the catalyst and likewise observing the changes in reaction rate. Reaction conditions were chosen to ensure that the observed reaction rates were under explicit kinetic control. This necessitated conversion to be low (typically below 20%) and the operating temperature to be limited up to 450°C.

Reaction temperature was varied in the range of 300-450°C with a fixed reactant H₂O/C (C in feed) of 3 mol_{H₂O}/mol_C and N₂ flow of 2 L min⁻¹ at atmospheric pressure. It is important to note that initial runs were performed with no catalyst in the bed, in order to ascertain the impact of the gas phase reactions. Negligible conversion and no discernible peaks were observed from the gas phase reactions in the temperature range of 300°C to 450°C at H₂O/C ratio of 3.

The partial pressure of water was varied from 15.94 to 88.59 mbar with the partial pressure of ethanol kept at 7.91 mbar. The partial pressure variation experiments were performed at 400°C. The contact time effect was investigated by varying the reactant feed flow from 0.5 to 3.0 ml min⁻¹, corresponding to a catalyst wt./flowrate of ethanol (W/F_{0,ethanol}) of 58 to 349 g_{cat} s g_{eth}⁻¹ (fixed catalyst weight) at 400°C with a fixed H₂O/C ratio of 3 and at atmospheric pressure. All experiments were carried out with a catalyst mass of approximately 0.1000 g.

Thermodynamic equilibrium data were obtained *via* the simulation of a Gibbs reactor (Gibbs free energy minimisation) in Aspen Plus software using the Peng-Robinson equation of state. The data were collected in terms of the parameters: conversion, selectivity and yield. The experimental equivalents of these parameters were calculated as shown below:

$$\text{Conversion: } X_C = \frac{F_{Eth}^{In} - F_{Eth}^{Out}}{F_{Eth}^{In}} \times 100\%$$

$$\text{Carbon selectivity of } y \text{ compound: } S_c(y) = \frac{F_y^{out}}{\sum F_{Carbon products}^{out}} \times 100\%$$

$$\text{Hydrogen yield: } Y_{H_2} = \frac{F_{H_2}^{Out}}{n \times F_{Eth}^{In}} \times 100\%$$

where F^{in} and F^{out} represent inlet and outlet flowrates, respectively. n equals 6 and 3 for steam reforming and decomposition experiments, respectively.

Measured ethanol consumption rates were used to construct Arrhenius plots through the assumption of a pseudo-first-order reaction rate in ethanol partial pressure for both reforming and decomposition experiments:

$$r = kP_{Eth}; k = Ae^{\frac{-E_a}{RT}}$$

3.3.4 Biochar characterization

Raman spectroscopy has been extensively implemented in characterising the chemical structure of biochar [14–17]. The structural features of the aromatic ring systems as well as the O-containing functional groups of the biochar samples obtained in this study were analysed using a Perkin-Elmer Spectrum GX FT-IR/Raman spectrometer. The procedure was adopted from the work of Li et al. [14] and has been described in detail in a previous study [15]. Briefly, 0.25 wt.% biochar sample was mixed with KBr and then ground and scanned. A baseline-corrected Raman spectrum in the range of 800-1800 cm^{-1} was fitted with 10 Gaussian bands [14]. Large aromatic ring systems with 6 or more fused benzene rings were represented by the assigned D band at 1300 cm^{-1} , while the G_R (1540 cm^{-1}), V_L (1465 cm^{-1}) and V_R (1380 cm^{-1}) bands represented the smaller aromatic ring systems containing 3-5 fused benzene rings. The total Raman peak area in the spectral range of 800-1800 cm^{-1} was used to reflect the relative content of O-containing functional groups that generate a resonance effect together with their attached aromatic ring systems.

3.4 References

- [1] J.A. Dumesic, D.F. Rudd, L.M. Aparicio, J.E. Rekoske, A.A. Treviño, *The Microkinetics of Heterogeneous Catalysis*, 1993.
- [2] A.B. Mhadeshwar, H. Wang, D.G. Vlachos, Thermodynamic Consistency in Microkinetic Development of Surface Reaction Mechanisms, *J. Phys. Chem. B.* 107 (2003) 12721–12733.
- [3] S. Kandoi, J. Greeley, M.A. Sanchez-castillo, S.T. Evans, A.A. Gokhale, J.A. Dumesic, M. Mavrikakis, Prediction of experimental methanol decomposition rates on platinum from first principles, 37 (2006).
- [4] J.E. Sutton, P. Panagiotopoulou, X.E. Verykios, D.G. Vlachos, Combined DFT, microkinetic, and experimental study of ethanol steam reforming on Pt, *J. Phys. Chem. C.* 117 (2013) 4691–4706.
- [5] K. Metaxas, J.W. Thybaut, G. Morra, D. Farrusseng, C. Mirodatos, G.B. Marin, A microkinetic vision on high-throughput catalyst formulation and optimization: Development of an appropriate software tool, in: *Top. Catal.*, 2010: pp. 64–76.
- [6] Advanced biomass gasification technology, Australian Renewable Energy Agency. <https://arena.gov.au/projects/advanced-biomass-gasification-technology/>. (accessed

October 28, 2019), (2018) 1–13.

- [7] Z. Min, P. Yimsiri, M. Asadullah, S. Zhang, C.Z. Li, Catalytic reforming of tar during gasification. Part II. Char as a catalyst or as a catalyst support for tar reforming, *Fuel*. 90 (2011) 2545–2552.
- [8] Z. Min, S. Zhang, P. Yimsiri, Y. Wang, M. Asadullah, C.Z. Li, Catalytic reforming of tar during gasification. Part IV. Changes in the structure of char in the char-supported iron catalyst during reforming, *Fuel*. 106 (2013) 858–863.
- [9] Y. Liu, M. Paskevicius, H. Wang, G. Parkinson, J.P. Veder, X. Hu, C.Z. Li, Role of O-containing functional groups in biochar during the catalytic steam reforming of tar using the biochar as a catalyst, *Fuel*. 253 (2019) 441–448.
- [10] Y. Wang, Z. Zhang, S. Zhang, Y. Wang, S. Hu, J. Xiang, X. Hu, Steam reforming of acetic acid over Ni/biochar catalyst treated with HNO₃: Impacts of the treatment on surface properties and catalytic behaviors, *Fuel*. 278 (2020) 118341.
- [11] J. Chen, M. Wang, S. Wang, X. Li, Hydrogen production via steam reforming of acetic acid over biochar-supported nickel catalysts, *Int. J. Hydrogen Energy*. 43 (2018) 18160–18168.
- [12] J. Ashok, N. Dewangan, S. Das, P. Hongmanorom, M.H. Wai, K. Tomishige, S. Kawi, Recent progress in the development of catalysts for steam reforming of biomass tar model reaction, *Fuel Process. Technol.* 199 (2020) 106252.
- [13] Z. Min, M. Asadullah, P. Yimsiri, S. Zhang, H. Wu, C.Z. Li, Catalytic reforming of tar during gasification. Part I. Steam reforming of biomass tar using ilmenite as a catalyst, *Fuel*. 90 (2011) 1847–1854.
- [14] X. Li, J. Hayashi, C.Z. Li, FT-Raman spectroscopic study of the evolution of char structure during the pyrolysis of a Victorian brown coal, *Fuel*. 85 (2006) 1700–1707.
- [15] X. Li, J. Hayashi, C.Z. Li, Volatilisation and catalytic effects of alkali and alkaline earth metallic species during the pyrolysis and gasification of Victorian brown coal. Part VII. Raman spectroscopic study on the changes in char structure during the catalytic gasification in air, *Fuel*. 85 (2006) 1509–1517.
- [16] H.L. Tay, S. Kajitani, S. Zhang, C.Z. Li, Inhibiting and other effects of hydrogen during gasification: Further insights from FT-Raman spectroscopy, *Fuel*. 116 (2014) 1–6.
- [17] H.L. Tay, S. Kajitani, S. Zhang, C.Z. Li, Effects of gasifying agent on the evolution of char structure during the gasification of Victorian brown coal, in: *Fuel*, Elsevier Ltd, 2013: pp. 22–28.

Preface to Chapter 4

A version of this chapter has been published in the International Journal of Hydrogen Energy (A.T.F. Afolabi, C.Z. Li, P.N. Kechagiopoulos, Microkinetic modelling and reaction pathway analysis of the steam reforming of ethanol over Ni/SiO₂, Int. J. Hydrogen Energy. 44 (2019) 22816–22830. <https://doi.org/10.1016/j.ijhydene.2019.07.040>). I was the lead investigator, responsible for all major areas of concept formation, data collection and analysis, as well as manuscript composition. Li C.Z. was the secondary supervisory author and was mainly involved in the manuscript review. Kechagiopoulos P.N. was the main supervisory author on this project and was involved throughout the project in concept formation and manuscript composition.

The aim of this study was to investigate the microkinetics of the ethanol steam reforming process over a metal dominated (inert support) catalyst, in order to form a baseline and reference point for future works on support effects. The mean-field microkinetic modelling approach used in this work is described in Chapter 3, with the semi-empirical rate parameter estimation method used previously reviewed in Chapter 2.

CHAPTER 4: MICROKINETIC MODELLING AND REACTION PATHWAY ANALYSIS OF THE STEAM REFORMING OF ETHANOL OVER Ni/SiO₂.

Ahmed Tijani F. Afolabi,^{1,2} Chun-Zhu Li,² Panagiotis N. Kechagiopoulos^{1*}

¹Chemical and Materials Engineering Group, School of Engineering, University of Aberdeen, Aberdeen, AB24 3UE, UK

²Fuels and Energy Technology Institute, Curtin University, GPO Box U1987, Perth, WA 6845, Australia

* Corresponding author: p.kechagiopoulos@abdn.ac.uk, +44 (0) 1224 272205

Abstract

Hydrogen production *via* the steam reforming of biomass-derived ethanol is a promising environmental alternative to the use of fossil fuels and a means of clean power generation. A microkinetic modelling study of ethanol steam reforming (ESR) on Nickel is presented for the first time and validated with minimal parameter fitting against experimental data collected over a Ni/SiO₂ catalyst. The thermodynamically consistent model utilises transition state theory and the UBI-QEP method for the determination of kinetic parameters and is able to describe correctly experimental trends across a wide range of conditions. The kinetically controlling reaction steps are predicted to occur in the dehydrogenation pathway of ethanol, with the latter found to proceed primarily *via* the formation of 1-hydroxyethyl. C-C bond cleavage is predicted to take place at the ketene intermediate leading to the formation of CH₂ and CO surface species. The latter intermediates proceed to react according to methane steam reforming and water gas shift pathways that are enhanced by the presence of water derived OH species. The experimentally observed negative reaction order for water is explained by the model predictions *via* surface saturation effects of adsorbed water species. The model results highlight a possible distinction between ethanol decomposition pathways as predicted by DFT calculations on Ni close-packed surfaces and ethanol steam reforming pathways at the broad range of experimental conditions considered.

Keywords: Ethanol steam reforming; Nickel catalyst; Microkinetic modelling

4.1 Introduction

Hydrogen production *via* steam reforming is of significant research interest due to the potential of hydrogen as an alternative, efficient and environmentally benign energy carrier. Conventional steam reforming of natural gas, however, is accompanied by high CO₂ emissions, both generated as by-product in the reaction stage and follow-up purification, and due to the high heat supply requirements of the process. The utilisation of renewable, biomass-derived, feeds provides the possibility to lower significantly the environmental impact of hydrogen production *via* steam reforming.

Ethanol steam reforming has been researched extensively, due to its obtainability from the fermentation process of various renewable sources [1–3] and also as a model compound for the lumped alcohol class of the aqueous phase of bio-oil (the liquid product of biomass pyrolysis) [4–6]. The general consensus is that the reaction mechanism primarily depends on the metal catalyst, which facilitates the scission of C-C and C-H bonds [3,7,8]. The support, if active, may participate in the water-gas shift reaction or dehydration of ethanol to ethylene [8], the latter recognised as an important coke precursor, although bifunctional mechanisms with sites at the metal-support interface determining the reaction rate have also been postulated [9]. An extensive understanding of the underlying chemical kinetics as well as the exact role of the metal catalyst is a key to enhancing catalyst performance, as the overall process comprises various sub-mechanisms. The most relevant of these are ethanol dehydrogenation and decomposition, water-gas shift and methane steam reforming/methanation, with maximum hydrogen yield being achieved *via* the overall ethanol steam reforming reaction, shown Previously in equations 2.19 – 2.24.

Various theoretical and experimental methods have been applied with the aim of obtaining information on the intrinsic kinetics of the process and clarifying the dominant pathways on various catalysts, including Ni [10–13], Pt [14,15], Rh [10] and Pd [16]. Early on, the isotopic work by Gates et al. [17] proposed that on Ni(111) ethanol decomposition proceeds initially *via* a O-H bond cleavage leading to the formation of ethoxy species. Following a C-H bond scission the latter species were suggested to dehydrogenate to acetaldehyde, eventually leading to the formation of CH₄ and CO through C-C bond cleavage, with the C-O bond remaining intact. More recently, Wang et al. [10] proposed *via* DFT calculations a similar pathway for a variety of (111) metal surfaces, including Ni, however ethanol decomposition was primarily identified to occur *via* CH₂CH₂OH and CH₂CH₂O doubly adsorbed surface intermediates. Ferrin et al. [18] mapped the entire potential energy surface for ethanol decomposition on Pt, Ru, Rh, Pd and Ir using DFT

calculations, Brønsted-Evans-Polyani correlations and scaling relations, finding that C-C cleavage in all active surfaces takes place at the ketyl intermediate. The combined DFT and microkinetics study of ethanol steam reforming on Pt by Sutton et al. [19] agreed with the latter finding, but revealed the first dehydrogenation step to 1-hydroxyethyl as rate limiting. *Via* periodic DFT calculations Ming Li et al. proposed a similar pathway over Pd [16], however the same authors found an ethoxy based decomposition route to be more probable over Rh [20] with the dehydrogenation of that species being rate-determining. Jia Zhang et al. [21] similarly suggested a pathway *via* ethoxy on Rh in their DFT study, however C-C scission was predicted to occur at the acetyl intermediate and the water gas shift reaction was identified as rate-controlling. Over Co(0001), the periodic DFT study of Ma et al. [22] attempted to probe the experimental observations and mechanism proposed by Sahoo et al. [23] finding H-abstraction from ethoxy to acetaldehyde to be the rate determining step. The above findings were consolidated in the DFT work on close-packed transition-metal surfaces of Sutton et al. [24] and the review by Zanchet et al. [25]. A dominant finding of these works was that the initial dehydrogenation of ethanol preferentially proceeds *via* O-H abstraction leading to ethoxy and, eventually, acetaldehyde on Ni, Co and Ru, *via* α C-H scission on Pt and Pd, and through both pathways on Rh.

It is evident that theoretical studies have focused on the decomposition pathways of ethanol, while all previously reported microkinetic models on ethanol conversion towards syngas are over noble metals, namely Pt [19,26] and Rh [27]. It is recognised though that the high cost of the latter poses significant economic difficulties to the commercial implementation of the process. Ni based catalysts exhibit good activity and are relatively cheap compared to noble metal ones, hence it is particularly important to obtain a mechanistic understanding of ESR on this metal. To this end, in this work a comprehensive microkinetic model for ethanol steam reforming that considers multiple pathways to describe the primary ethanol decomposition and dehydrogenation reactions and the follow-up pathways of their products is proposed and validated using a kinetic dataset collected over a Ni/SiO₂ catalyst at a broad range of experimental conditions [13]. The inert support used aims specifically at the elucidation of the metal-driven reaction pathways, so that support effects can be discerned at a follow-up stage and a unified kinetic view on the ESR mechanism can be obtained.

4.2 Procedures

4.2.1 Experimental details

The experimental data used in this study have been obtained from the work of Zhurka et al. [13]. Experiments were carried out in a fixed bed reactor setup over a Ni/SiO₂ catalyst under explicit kinetic control. The kinetic dataset obtained covers the effect of temperature, space velocity and partial pressure of reactants across a wide range. A summary of the operating conditions and catalyst properties is provided in Table 4.1, with more details being available in the original publication.

Table 4.1: Experimental operating conditions and catalyst properties.

Catalyst	Ni/SiO ₂
Ni loading (wt %)	10
Ni dispersion (%)	38.6
Surface area (m ² g ⁻¹)	105.32
Catalyst weight per experiment (g)	0.08
Temperature (°C)	300 – 550
H ₂ O/C (mol mol ⁻¹)	1 – 6
Partial pressure of ethanol (bar)	0.03 – 0.18
Partial pressure of water (bar)	0.12 – 0.74
W/F _{Eth,t0} (g _{cat} S g _{Eth} ⁻¹)	58.2 – 349.4

4.2.2 Model formulation and computational details

The microkinetic model for ethanol stream reforming on Ni catalysts proposed in this work is developed using a FORTRAN based modelling platform, the microkinetic engine (MKE), described in more details previously [28–30]. The experimental data are simulated using a plug flow reactor model, while the pseudo steady state approximation and a mass balance for the active sites are applied to determine the partial coverage of the surface intermediates. Entropic and enthalpic thermodynamic consistency is upheld by correlating the surface reaction entropies and enthalpies to those of the corresponding gas phase reactions in line with the work of Kechagiopoulos et al. [30]. Surface species entropies are obtained from the equivalent gas species entropies, assuming that upon adsorption all species lose their translational degrees of

freedom. Similarly, surface species enthalpies are obtained from the equivalent gas species enthalpies subtracting their chemisorption enthalpies. The temperature dependence of the latter is linked to the degrees of freedom lost or gained upon adsorption or desorption as described in Mhadeshwar et al. [31] and is implemented according to the equation below:

$$Q(T) = Q(T_0) - \gamma R(T - T_0) \quad (4.5)$$

where γ is the temperature dependence coefficient, R is the universal gas constant and T_0 is taken as 300 K in this study. Modified Arrhenius-type equations and the law of mass action are used to calculate the rates of elementary reactions. For adsorption steps collision theory is used to calculate the maximum values of pre-exponential factors, the latter further adjusted *via* sticking coefficients. Pre-exponential factors for forward steps of all reactions involving only surface species are obtained *via* transition state theory [32] as was shown in equation 3.23.

It is assumed that the ratios of the translational and vibrational partition functions of the transition state and the reactants are approximately unity [19,33], so the molecular partition function ratio is obtained in this work as the ratio of the rotational partition functions of the transition state and the reactants. These are calculated from the moments of inertia of species I_i as well as the temperature T , as shown in equation 3.24.

It is further assumed that all species upon adsorption rotate around the vertical axis of the atom attached to the surface of the catalyst. Literature DFT studies are used to discern the most likely adsorption mode for each species [19], while product-like transition states are assumed. The moment of inertia of functional groups with internal rotation or molecules attached to the surface bound atom is calculated based on their bond lengths and angles, while the overall moment of inertia is estimated as the sum of the moment of inertia of all attached groups or atoms rotating around the absorbed atom's vertical axis. The pre-exponential factors of reverse reactions for both adsorption and surface reactions are calculated through the preservation of entropic consistency. Adsorption reaction steps are considered non-activated, while the activation barrier for reactions involving surface species are calculated using the UBI-QEP method [34,35]. Activation barriers of reverse reactions are calculated through enthalpic consistency [30].

The active site density and catalyst surface area were determined experimentally, as reported by Zhurka et al. [13]. The resulting differential and algebraic equations (DAE) system is numerically integrated with the DDASPK solver [36], while to obtain the surface partial coverage at the reactor's inlet and initialise this DAE system a clean catalyst surface is evolved towards the steady state. Rosenbrock [37] and Levenberg–Marquardt [38,39] optimization

methods are used for the estimation of the model's parameters, namely chemisorption enthalpies, temperature exponents of modified Arrhenius equations and sticking coefficients, through regression of the experimental data, with the objective function being the weighed sum of the squared residuals between the observed and calculated outlet molar flowrates.

4.2.3 Surface reaction network description

A comprehensive network of 64 elementary reaction steps involving 7 gaseous molecules and 22 surface species is considered to account for the various possible reaction pathways during ESR over Ni (Table 4.2). The proposed network describes the molecular adsorption of the ethanol and water reactants (R1-4), with the absorbed water further dissociating towards hydroxyl (OH*) and oxygen (O*) surface species (R15-18). Absorbed ethanol dehydrogenation proceeds *via* two possible routes, leading to the formation of 1-hydroxyethyl (R19-20) and ethoxy (R21-22) species. Subsequent dehydrogenation steps of these intermediates (R23-26) lead to adsorbed acetaldehyde, the latter recognized to be a key intermediate in ESR [40]. Dehydrogenation of 1-hydroxyethyl can also proceed *via* 1-hydroxyethylidene to acetyl (R27-30), at which point three possible C-C cleavage steps are proposed: The C-C bond scission can occur directly after acetyl is formed to produce methyl species and carbon monoxide (R37-38) or after further dehydrogenation to CH₂CO* (R39-42) or CHCO* (R43-46). Acetaldehyde can similarly dehydrogenate to acetyl (R31-32) or decompose according to R33-36. Water-gas shift occurs *via* the reaction of carbon monoxide with either hydroxyl or oxygen surface species accounted for in reactions R47-52. Reactions R53-56 describe the (de)hydrogenation of CH_x* species, whilst methane steam reforming is accounted for in reactions R57-64. Carbon oxides and acetaldehyde are assumed to adsorb molecularly (R9-14) whereas methane and hydrogen adsorption proceeds dissociatively (R5-9).

Table 4.2: Microkinetic model for ethanol steam reforming on Ni/SiO₂. Activation barriers are calculated using the model parameters shown in Table 4.3 *via* UBI-QEP and pre-exponential factors calculated *via* transition state theory as described in Section 4.2.3. Modified Arrhenius equation used of form $R_i^f = A_i \cdot T^\beta \cdot e^{-E_a/RT}$ with the temperature exponents reported below.

No.	Reaction	E_a (kJ mol ⁻¹)	A (s ⁻¹)	Temperature exponent, β
R1	CH ₃ CH ₂ OH + * → CH ₃ CH ₂ OH*	0.00	3.33 × 10 ⁺⁰⁴	0.0
R2	CH ₃ CH ₂ OH* → CH ₃ CH ₂ OH + *	43.49	3.51 × 10 ⁺¹³	0.0
R3	H ₂ O + * → H ₂ O*	0.00	5.32 × 10 ⁺⁰⁴	0.0
R4	H ₂ O* → H ₂ O + *	53.07	1.37 × 10 ⁺¹³	0.0
R5	H ₂ + 2* → H* + H*	30.92	1.59 × 10 ⁺⁰⁵	0.0
R6	H* + H* → H ₂ + 2*	97.58	4.19 × 10 ⁺¹²	0.0

R7	$\text{CH}_4 + 2^* \rightarrow \text{CH}_3^* + \text{H}^*$	55.53	$5.64 \times 10^{+04}$	0.0
R8	$\text{CH}_3^* + \text{H}^* \rightarrow \text{CH}_4 + 2^*$	57.10	$2.26 \times 10^{+12}$	-2.0±0.035
R9	$\text{CO} + ^* \rightarrow \text{CO}^*$	0.00	$4.27 \times 10^{+04}$	0.0
R10	$\text{CO}^* \rightarrow \text{CO} + ^*$	98.74	$2.14 \times 10^{+13}$	1.5±0.0436
R11	$\text{CO}_2 + ^* \rightarrow \text{CO}_2^*$	0.00	$3.40 \times 10^{+04}$	0.0
R12	$\text{CO}_2^* \rightarrow \text{CO}_2 + ^*$	20.97	$3.36 \times 10^{+13}$	0.0
R13	$\text{CH}_3\text{CHO} + ^* \rightarrow \text{CH}_3\text{CHO}^*$	0.00	$3.40 \times 10^{+04}$	0.0
R14	$\text{CH}_3\text{CHO}^* \rightarrow \text{CH}_3\text{CHO} + ^*$	74.52	$3.36 \times 10^{+13}$	2.0±0.0091
R15	$\text{H}_2\text{O}^* + ^* \rightarrow \text{OH}^* + \text{H}^*$	93.59	$1.44 \times 10^{+13}$	0.0
R16	$\text{OH}^* + \text{H}^* \rightarrow \text{H}_2\text{O}^* + ^*$	29.02	$2.00 \times 10^{+13}$	0.0
R17	$\text{OH}^* + ^* \rightarrow \text{O}^* + \text{H}^*$	63.92	$3.19 \times 10^{+13}$	0.0
R18	$\text{O}^* + \text{H}^* \rightarrow \text{OH}^* + ^*$	98.61	$4.90 \times 10^{+13}$	0.0
R19	$\text{CH}_3\text{CH}_2\text{OH}^* + ^* \rightarrow \text{CH}_3\text{CHOH}^* + \text{H}^*$	58.92	$7.83 \times 10^{+12}$	0.0
R20	$\text{CH}_3\text{CHOH}^* + \text{H}^* \rightarrow \text{CH}_3\text{CH}_2\text{OH}^* + ^*$	42.61	$1.51 \times 10^{+13}$	0.0
R21	$\text{CH}_3\text{CH}_2\text{OH}^* + ^* \rightarrow \text{CH}_3\text{CH}_2\text{O}^* + \text{H}^*$	74.72	$1.00 \times 10^{+12}$	0.0
R22	$\text{CH}_3\text{CH}_2\text{O}^* + \text{H}^* \rightarrow \text{CH}_3\text{CH}_2\text{OH}^* + ^*$	36.81	$1.93 \times 10^{+13}$	0.0
R23	$\text{CH}_3\text{CHOH}^* + ^* \rightarrow \text{CH}_3\text{CHO}^* + \text{H}^*$	53.73	$1.91 \times 10^{+11}$	0.0
R24	$\text{CH}_3\text{CHO}^* + \text{H}^* \rightarrow \text{CH}_3\text{CHOH}^* + ^*$	3.86	$1.42 \times 10^{+13}$	0.0
R25	$\text{CH}_3\text{CH}_2\text{O}^* + ^* \rightarrow \text{CH}_3\text{CHO}^* + \text{H}^*$	45.63	$1.91 \times 10^{+11}$	0.0
R26	$\text{CH}_3\text{CHO}^* + \text{H}^* \rightarrow \text{CH}_3\text{CH}_2\text{O}^* + ^*$	17.28	$1.42 \times 10^{+13}$	0.0
R27	$\text{CH}_3\text{CHOH}^* + ^* \rightarrow \text{CH}_3\text{COH}^* + \text{H}^*$	46.07	$1.91 \times 10^{+11}$	0.0
R28	$\text{CH}_3\text{COH}^* + \text{H}^* \rightarrow \text{CH}_3\text{CHOH}^* + ^*$	29.65	$1.42 \times 10^{+13}$	0.0
R29	$\text{CH}_3\text{COH}^* + ^* \rightarrow \text{CH}_3\text{CO}^* + \text{H}^*$	20.14	$1.51 \times 10^{+13}$	0.0
R30	$\text{CH}_3\text{CO}^* + \text{H}^* \rightarrow \text{CH}_3\text{COH}^* + ^*$	87.78	$5.64 \times 10^{+11}$	0.0
R31	$\text{CH}_3\text{CHO}^* + ^* \rightarrow \text{CH}_3\text{CO}^* + \text{H}^*$	3.41	$1.10 \times 10^{+12}$	0.0
R32	$\text{CH}_3\text{CO}^* + \text{H}^* \rightarrow \text{CH}_3\text{CHO}^* + ^*$	104.50	$3.38 \times 10^{+13}$	0.0
R33	$\text{CH}_3\text{CHO}^* + ^* \rightarrow \text{CH}_3^* + \text{CHO}^*$	11.82	$1.00 \times 10^{+11}$	0.0
R34	$\text{CH}_3^* + \text{CHO}^* \rightarrow \text{CH}_3\text{CHO}^* + ^*$	87.01	$2.10 \times 10^{+09}$	0.0
R35	$\text{CHO}^* + ^* \rightarrow \text{CO}^* + \text{H}^*$	0.00	$6.60 \times 10^{+11}$	0.0
R36	$\text{CO}^* + \text{H}^* \rightarrow \text{CHO}^* + ^*$	81.97	$1.67 \times 10^{+13}$	0.0
R37	$\text{CH}_3\text{CO}^* + ^* \rightarrow \text{CH}_3^* + \text{CO}^*$	4.71	$2.08 \times 10^{+12}$	0.0
R38	$\text{CH}_3^* + \text{CO}^* \rightarrow \text{CH}_3\text{CO}^* + ^*$	60.79	$1.34 \times 10^{+13}$	0.0
R39	$\text{CH}_3\text{CO}^* + ^* \rightarrow \text{CH}_2\text{CO}^* + \text{H}^*$	50.90	$4.24 \times 10^{+12}$	0.0
R40	$\text{CH}_2\text{CO}^* + \text{H}^* \rightarrow \text{CH}_3\text{CO}^* + ^*$	9.47	$1.66 \times 10^{+13}$	0.0
R41	$\text{CH}_2\text{CO}^* + ^* \rightarrow \text{CH}_2^* + \text{CO}^*$	2.07	$7.43 \times 10^{+11}$	0.0
R42	$\text{CH}_2^* + \text{CO}^* \rightarrow \text{CH}_2\text{CO}^* + ^*$	76.55	$1.93 \times 10^{+12}$	0.0
R43	$\text{CH}_2\text{CO}^* + ^* \rightarrow \text{CHCO}^* + \text{H}^*$	81.57	$1.15 \times 10^{+13}$	0.0
R44	$\text{CHCO}^* + \text{H}^* \rightarrow \text{CH}_2\text{CO}^* + ^*$	40.29	$1.65 \times 10^{+13}$	0.0

R45	$\text{CHCO}^* + * \rightarrow \text{CH}^* + \text{CO}^*$	0.00	$5.18 \times 10^{+11}$	0.0
R46	$\text{CH}^* + \text{CO}^* \rightarrow \text{CHCO}^* + *$	107.61	$3.74 \times 10^{+12}$	0.0
R47	$\text{COOH}^* + * \rightarrow \text{CO}^* + \text{OH}^*$	44.88	$7.56 \times 10^{+10}$	0.0
R48	$\text{CO}^* + *\text{OH} \rightarrow \text{COOH}^* + *$	24.87	$1.10 \times 10^{+12}$	0.0
R49	$\text{COOH}^* + * \rightarrow \text{CO}_2^* + \text{H}^*$	0.79	$1.42 \times 10^{+11}$	0.0
R50	$\text{CO}_2^* + \text{H}^* \rightarrow \text{COOH}^* + *$	18.58	$1.54 \times 10^{+13}$	0.0
R51	$\text{CO}_2^* + * \rightarrow \text{CO}^* + \text{O}^*$	40.24	$1.93 \times 10^{+12}$	0.0
R52	$\text{CO}^* + \text{O}^* \rightarrow \text{CO}_2^* + *$	55.93	$1.15 \times 10^{+13}$	0.0
R53	$\text{CH}_3^* + * \rightarrow \text{CH}_2^* + \text{H}^*$	88.00	$1.03 \times 10^{+13}$	0.0
R54	$\text{CH}_2^* + \text{H}^* \rightarrow \text{CH}_3^* + *$	64.97	$7.38 \times 10^{+12}$	0.0
R55	$\text{CH}_2^* + * \rightarrow \text{CH}^* + \text{H}^*$	90.89	$8.03 \times 10^{+12}$	0.0
R56	$\text{CH}^* + \text{H}^* \rightarrow \text{CH}_2^* + *$	82.75	$3.19 \times 10^{+13}$	0.0
R57	$\text{CH}_2^* + \text{OH}^* \rightarrow \text{HCHO}^* + \text{H}^*$	22.27	$2.35 \times 10^{+10}$	0.0
R58	$\text{HCHO}^* + \text{H}^* \rightarrow \text{CH}_2^* + \text{OH}^*$	7.80	$3.77 \times 10^{+11}$	0.0
R59	$\text{HCHO}^* + \text{OH}^* \rightarrow \text{HCOOH}^* + \text{H}^*$	0.00	$2.89 \times 10^{+12}$	0.0
R60	$\text{HCOOH}^* + \text{H}^* \rightarrow \text{HCHO}^* + \text{OH}^*$	94.28	$9.75 \times 10^{+12}$	0.0
R61	$\text{HCOOH}^* + * \rightarrow \text{COOH}^* + \text{H}^*$	36.01	$1.70 \times 10^{+13}$	0.0
R62	$\text{COOH}^* + \text{H}^* \rightarrow \text{HCOOH}^* + *$	88.65	$3.10 \times 10^{+12}$	0.0
R63	$\text{CH}_2^* + *\text{O} \rightarrow \text{CHO}^* + \text{H}^*$	58.14	$1.42 \times 10^{+13}$	0.0
R64	$\text{CHO}^* + \text{H}^* \rightarrow \text{CH}_2^* + \text{O}^*$	53.91	$1.51 \times 10^{+13}$	0.0

Table 4.3: Estimated model parameters with 95% confidence intervals. Chemisorption enthalpy values without confidence intervals were adopted from the literature sources shown, while those with confidence intervals were regressed using as initial values the respective literature sources shown.

Species	Chemisorption enthalpy, Q (kJ mol ⁻¹)	Sources for initial or used value	Temperature dependence coefficient γ in equation (5) [31]
CH₃CH₂OH	45.84	[41]	2.5
H₂O	58.95±0. 69	[42]	2.5
CO₂	25.68	[30,42]	2.0
CH₃CH₂O	171.54	[41]	2.5
CH₃CHO	71.04	[42]	2.5
OH	242.2±0. 87	[42,43]	2.0
H	257.0±0. 66	[42,44]	1.5

CH₃	200.48±0.59	[30,42]	2.5
CH₂	391.73	[30]	2.5
CH	556.07	[30]	2.0
CO	113.44	[30]	2.0
CHO	206.69	[30]	2.5
HCHO	23.68±0.38	[43]	2.5
HCOOH	65.01	[44]	2.5
CH₃CO	191.39±0.91	[42]	2.0
CH₂CO	83.61±0.18	[42]	2.0
CHCO	283.94	[42]	2.0
COOH	250.01	[30]	2.0
O	453.0	[30]	1.0
CH₃CHOH	180±2.21	[41]	2.5
CH₃COH	213.8	[42]	2.5

4.3 Results

4.3.1 Model validation

The microkinetic model presented in the current work is fully parameterised on the basis of three sets of parameters: sticking coefficients, Arrhenius temperature exponents and chemisorption enthalpies (see Table 4.2 and Table 4.3). Initial values for chemisorption enthalpies were collected from experimental and DFT studies on Ni catalysts [30,42], while Arrhenius temperature exponents were initialised with values of 0. Sticking coefficients were kept equal at a value of 1 due to their low impact on modelled outputs, while the coefficients γ used in equation (5) for the temperature dependence of chemisorption enthalpies were fixed at values obtained from previous studies [26,31]. Table 4.3 shows the final estimated values of the chemisorption enthalpies of species as well as γ coefficients, while the final values of the Arrhenius temperature exponents are reported in Table 4.2. The obtained values will be discussed in more detail in Section 4.3.5 pertaining to the evaluation of model parameters.

In order to evaluate the overall agreement between the model predicted and experimental results, parity plots for all gas molecules are presented in Figure 4-1. A satisfactory agreement over the entire experimental range for all detected molecules is visible. The parity plots for the reactants ethanol and water provide proof that the model is correctly describing the main activation pathways, while conversion pathways appear to be captured appropriately for all major products. Acetaldehyde shows the highest variance, most likely attributed to the lower order of magnitude

of its molar flowrate values, as well as the comparatively higher difficulty of liquid products sampling and analysis. Nonetheless, acetaldehyde's detection is in line with the theoretical predictions of the Ni metal's affinity towards forming the species from ethanol [24] and the equivalent well established experimental observations of other groups on similar catalysts [40,45].

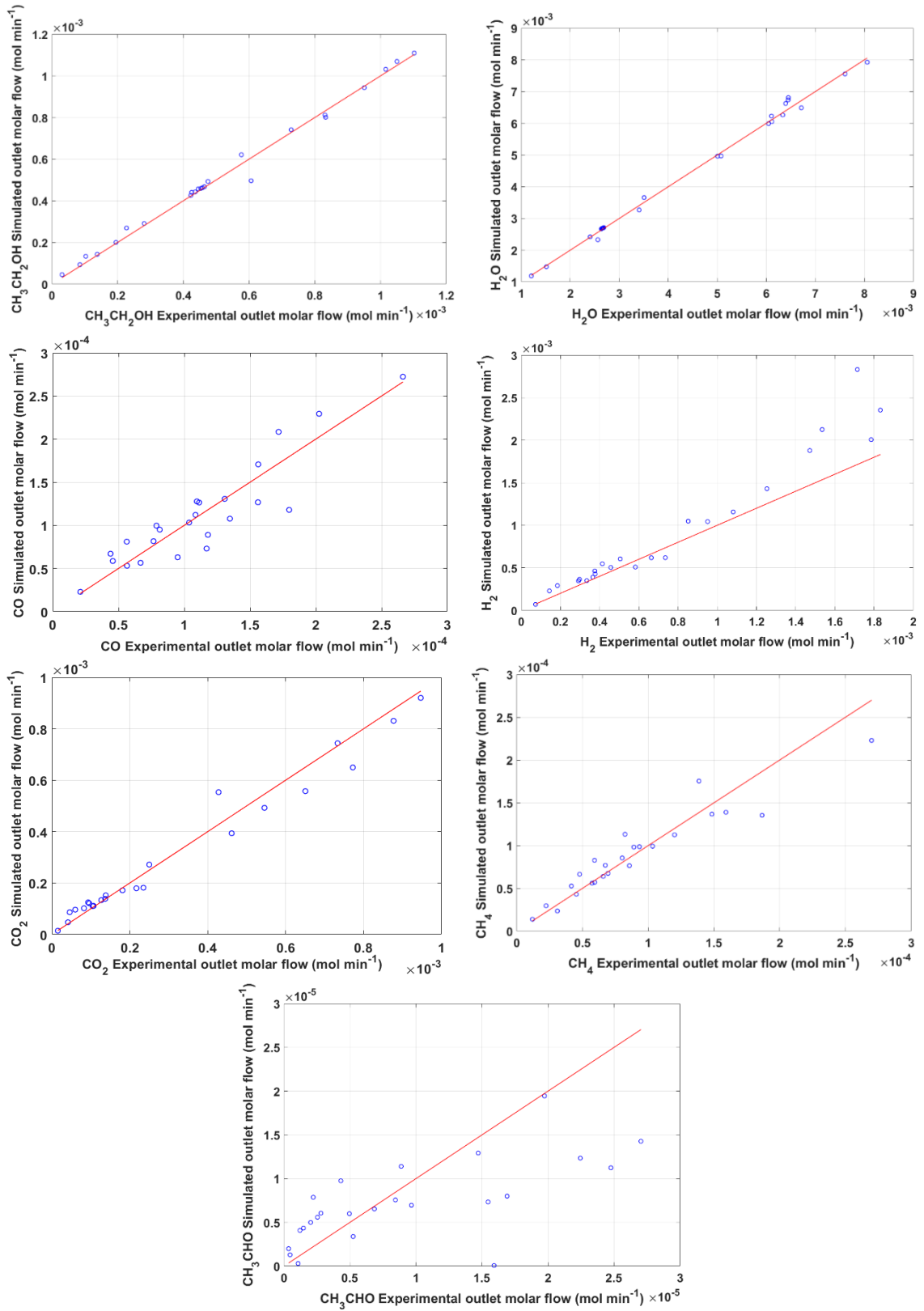


Figure 4-1: Parity diagrams for detected liquid and gas components at conditions reported in Table 4.1 and discussed in Zhurka et al. [13]. Modelling results have been obtained with the parameter values shown in Table 4.3.

Performance curves are shown in Figure 4-2, presenting the effect of temperature, partial pressure of ethanol and water and space time on the conversion of ethanol and water as well as the carbon selectivities towards CO, CO₂, CH₄ and CH₃CHO. As indicated also from the parity plots, the model can reproduce to a good degree the experimental trends based on the reported parameter values in Table 4.2. As expected, the conversion of reactants increases with temperature (panel (a)). In line with our experimental observations [13], at low temperatures ethanol dehydrogenation leads to the production of acetaldehyde, while the carbon selectivity towards CO and CH₄ outweighs that of CO₂. As the temperature rises, the CO₂ selectivity increases and is accompanied by an equivalent decrease in the selectivities of CO, CH₄ and CH₃CHO, indicative of the promotion of secondary reaction pathways. Results are specifically consistent with a rising contribution of the water gas shift reaction and the progressive promotion of the decomposition and oxidation of surface CH_x species, in equivalence to methane steam reforming mechanisms [46].

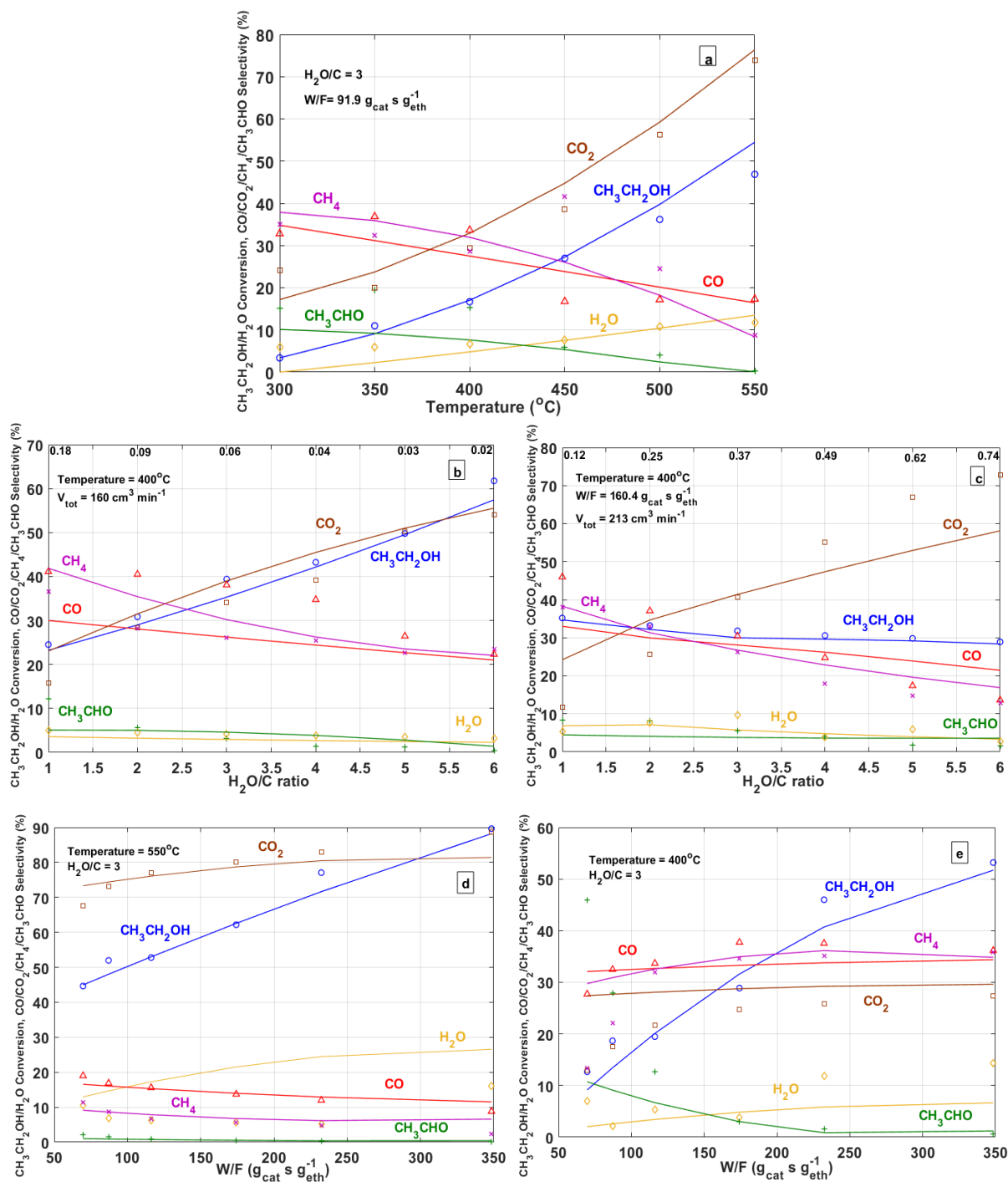


Figure 4-2: Comparison of model predicted conversions and selectivities over Ni/SiO₂ catalyst (lines) with experimental results (symbols). Operating conditions are indicated on the respective panels.

In order to elucidate the effect of reactants' partial pressures on the order of the reaction, two sets of experimental data obtained from the work of Zhurka et al. [13] were modelled. Results are presented in Figure 4-2 as H₂O/C variation, since these relate better to the observed selectivity trends, however the corresponding inlet partial pressures of the reactants are also indicated. Panel (b) shows the effect of ethanol partial pressure, maintaining the water partial

pressure and total pressure constant, while panel (c) shows the inverse with water partial pressure varied and ethanol kept constant. Varying ethanol partial pressure, the model predicts that the conversion of ethanol and selectivity towards CO_2 are positively affected, while CH_4 and CO selectivities are negatively affected. The results on varying H_2O partial pressure show that ethanol conversion displays a mild decrease, however a positive influence is still observed for CO_2 selectivity accompanied by a negative effect for CH_4 and CO selectivity. For both partial pressure variation data sets, the above trends are well in line with the experimental observations of Zhurka et al. [13]. Selectivity trends are consistent with a promotion of secondary reactions by the increase of water derived surface species due to the rising $\text{H}_2\text{O}/\text{C}$ ratio. Conversion profiles are better explained looking at Figure 4-3, where the model predicted and experimental partial reaction orders for ethanol and water are compared. A clearly positive order for ethanol (approximately equal to 0.5 as indicated by the square root of the partial pressure in the left panel) and a slightly negative order for water are visible, with the model reproducing the experimental trends very well, affirming that the kinetically relevant processes have been accurately captured.

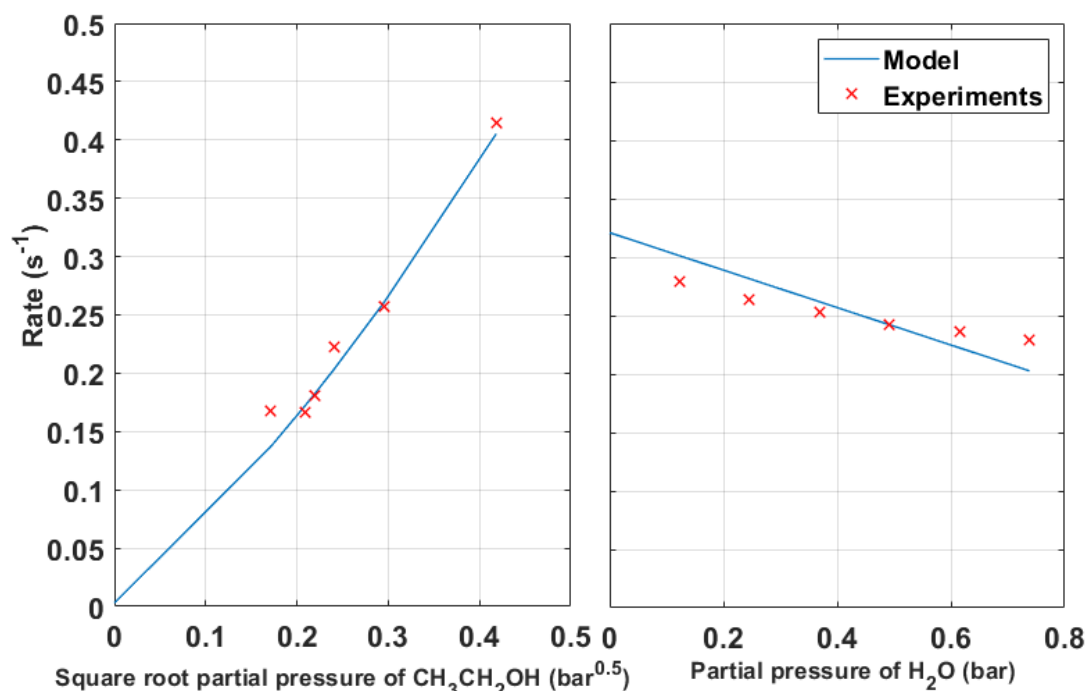


Figure 4-3: Reaction orders with respect to ethanol and water partial pressure (operating conditions are that of Figure 4-2 panels b and c respectively).

The positive order for ethanol is evidence of the participation of an ethanol-derived surface intermediate in the rate determining step, as stipulated in the analysis of the experimental work [13] and further elaborated with the microkinetic model in the following section. For the negative

water reaction order, the partial coverages across this range of simulated conditions, shown in Table 4.4, reveal that the increase in the partial pressure of water leads to a progressive catalyst surface saturation by adsorbed H₂O species, leading to a decreasing availability of active sites. Even though a rise in water-derived surface species, such as OH*, is indeed observed and explains the selectivity trends, overall a decrease in the coverage by adsorbed ethanol is predicted by the model that ultimately results in the observed decrease in conversion and supports the experimental findings. It is worth commenting that a similar negative order for water was observed in the experiments modelled by Sutton et al. [19], whereas the microkinetic model presented in that work predicted a zero order. That experimental negative order was attributed to support effects, namely excess water limiting ethanol activation on the Al₂O₃ support. In the present work, though, the SiO₂ support used was overall inert [13], hence the competitive adsorption of ethanol and water on the Ni metal is considered as the most probable reason for the experimental trends, which the model correctly describes.

Table 4.4: Effect of partial pressure of water on partial coverage of surface species at 400°C.

Partial pressure (bar)		Partial coverage of catalyst surface (-)				
C ₂ H ₅ OH	H ₂ O	C ₂ H ₅ OH*	H ₂ O*	H*	OH*	Vacant site
0.06	0.12	8.86×10 ⁻³	0.41	8.94×10 ⁻²	1.49×10 ⁻³	0.31
0.06	0.25	5.35×10 ⁻³	0.50	5.92×10 ⁻²	1.89×10 ⁻³	0.21
0.06	0.37	3.87×10 ⁻³	0.52	4.69×10 ⁻²	2.06×10 ⁻³	0.18
0.06	0.49	2.94×10 ⁻³	0.53	3.86×10 ⁻²	2.18×10 ⁻³	0.15
0.06	0.61	2.45×10 ⁻³	0.55	3.24×10 ⁻²	2.27×10 ⁻³	0.13
0.06	0.74	2.10×10 ⁻³	0.57	2.75×10 ⁻²	2.33×10 ⁻³	0.11

With respect to the space time effect, the model is again able to predict sufficiently the experimental trends as is seen in panels (d) and (e) of Figure 4-2, but with some discrepancies in relation to acetaldehyde. Experimentally [13], results at low conversions (below 15-20%), indicated that temperature affects strongly the main reactive pathway of ethanol, the latter not involving acetaldehyde as an intermediate, at least at high temperatures. At 400°C, acetaldehyde did appear as the sole primary product, as indicated also by its very high selectivity at the lowest space velocities studied, however at 550°C CH₄ and CO also appeared as such. Qualitatively, the model predicts similar differences in the temperature dependence of the main reaction pathways, although milder to the experimentally observed and evident at relatively lower conversions (below 5%), as shown also from the suboptimal description of acetaldehyde's selectivity in panel

(e) of Figure 4-2. Figure 4-4 shows the model predicted product selectivities as a function of ethanol conversion at different temperatures. At 400°C, as conversion approaches zero, acetaldehyde is indeed predicted to be the only product whose selectivity is increasing substantially, while at 550°C, CO, CH₄ and acetaldehyde selectivities are all clearly tending towards finite values at a zero conversion. More importantly, the model indeed predicts that the main pathway of ethanol conversion towards CH₄ and CO is not linked to adsorbed acetaldehyde and proceeds *via* another surface intermediate. The quantitative differences could potentially indicate that the assumptions made in relation to the mobility of the surface species during the development of the model are in need of revision or that the surface reaction energetics, as predicted by the semi-empirical UBI-QEP, require further refinement. Nonetheless, the overall very good agreement of the model-derived results with the experimental ones across a range of conditions, as highlighted in this section, allows using the model further in the following to obtain information on the kinetic importance of reaction steps.

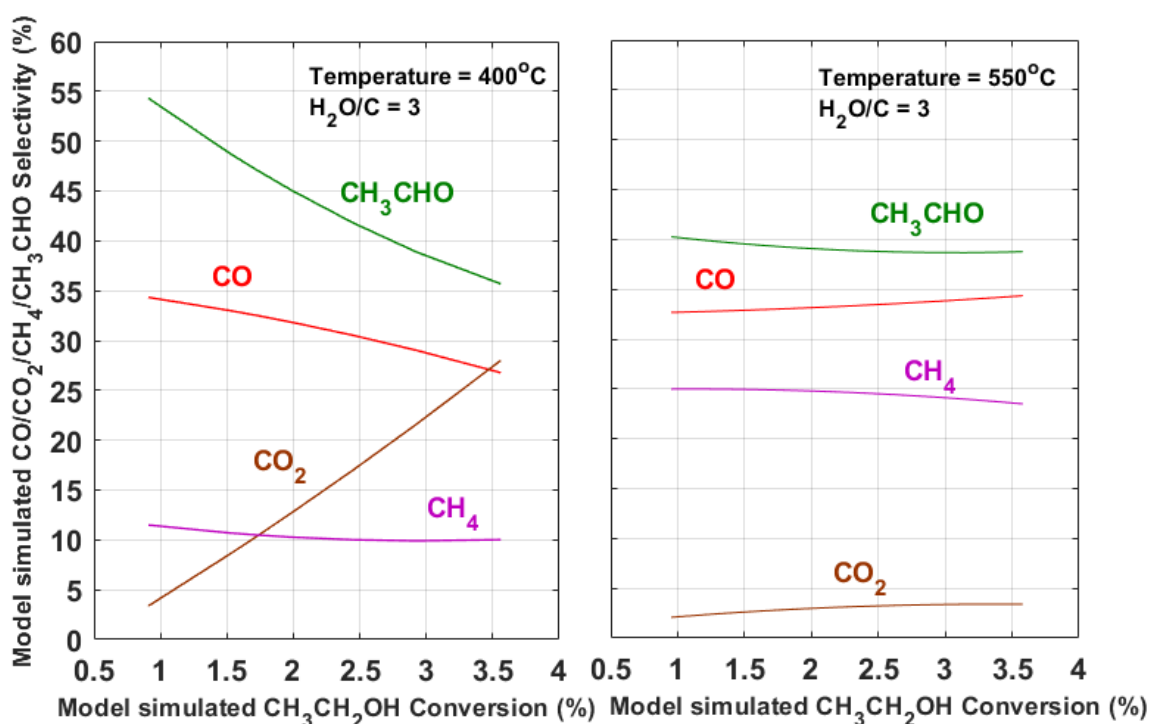


Figure 4-4: Ethanol conversion versus products selectivities depicting primary and secondary products at different temperatures (Operating conditions are shown in the respective panels).

4.3.2 Kinetic relevance of reaction steps

A sensitivity analysis of the model's parameters was carried out in order to investigate the kinetic relevance of the elementary surface reaction steps. A temperature of 400°C and a H₂O/C of 3 are

selected to align with the conditions of the partial pressure variation runs. The pre-exponential factors of each reversible reaction pair were perturbed by a small fraction of their base value, the latter calculated by transition state theory as described in Section 4.2.2. The effect of this perturbation on the outlet molar fractions of reactants and products was quantified by the calculation of normalised sensitivity coefficients. Figure 4-5 shows the relevant results for ethanol. As discussed in the Introduction, previous studies [19,20,26] have identified the dehydrogenation pathways of ethanol as the kinetically relevant surface reactions, with the initial abstraction of H from the α -C, β -C or O of surface ethanol being in many cases the rate determining step. As seen in Figure 4-5, the most important steps identified in the current model *via* the sensitivity analysis are indeed along ethanol's dehydrogenation pathway and specifically are the secondary dehydrogenation of CH_3CHOH^* to CH_3COH^* and the further dehydrogenation of the latter to CH_3CO^* , according to reactions R27-28 and R29-30, respectively. These findings are further in line with the experimental observations and the discussion in Section 4.3.1, as both of these steps are consistent with an overall reaction mechanism with a positive order in ethanol (Figure 4-3). Nonetheless, it bears notice and will be discussed further in the following section that these steps do not involve the ethoxy intermediate that is commonly accepted to be participating in the conversion of ethanol on Ni following an initial O-H bond cleavage [17,24,47]. On the other hand, steam derived intermediates do not participate in these kinetically relevant steps and would suggest a zero order in water for the conversion of ethanol. As discussed previously though, the experimentally observed slightly negative order in water across a $\text{H}_2\text{O}/\text{C}$ ratio that spans from sub-stoichiometric to large excess values is predicted by the model to be on account of surface saturation effects.

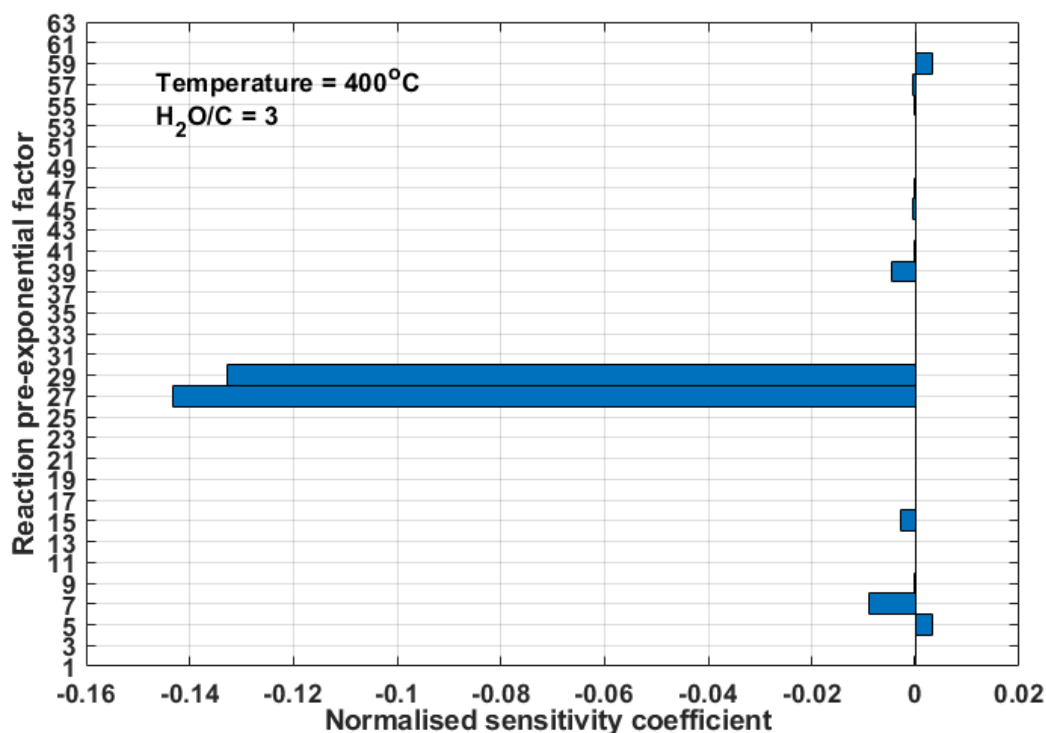


Figure 4-5: Sensitivity analysis of pre-exponential factors of microkinetic model reactions shown in Table 4.2, at 400°C and H₂O/C of 3 for ethanol outlet molar fraction. Base values for pre-exponential factors are calculated as described in Section 4.2.2.

Figure 4-6 shows the results of the sensitivity analysis for the molar fractions of H₂O and products CO, CO₂, H₂, CH₄ and CH₃CHO. In line with the ethanol sensitivity analysis, R27-28 and R29-30 are the major kinetically relevant steps identified for all the gaseous products, having a positive effect to their production. A negative effect for the same reaction steps to the outlet molar fraction of H₂O is also identified and is consistent with the above results, as an increase in ethanol conversion and its decomposition products leads to a further consumption of water *via* secondary reactions. Nonetheless, reaction pair R59-60 is found to have the largest effect on H₂O, which, linked with the similar negative sensitivity for CH₄ and the positive one for CO, CO₂ and H₂, leads to the identification of these steps as the kinetically relevant ones for the methane steam reforming or CH_x oxidation sub-mechanism. For CH₃CHO, the effect of the same steps is the opposite to the gas products, meaning that the main ethanol consuming reactions lead to a decrease in the production of acetaldehyde. The latter fact, which will be discussed in more detail in the following, further suggests that the primary formation pathway of the acetaldehyde is not linked to the dominant conversion pathway of ethanol, as observed experimentally. This follows on the previous discussion of not identifying ethoxy as a key species, as the latter is the widely considered precursor to acetaldehyde [25]. In summary, the sensitivity analysis revealed

R27-28 and R29-30 as the kinetically important steps under these conditions, a conclusion that will be elaborated in the next section, where the reaction steps involved in the overall reaction pathways are probed through a contribution analysis.

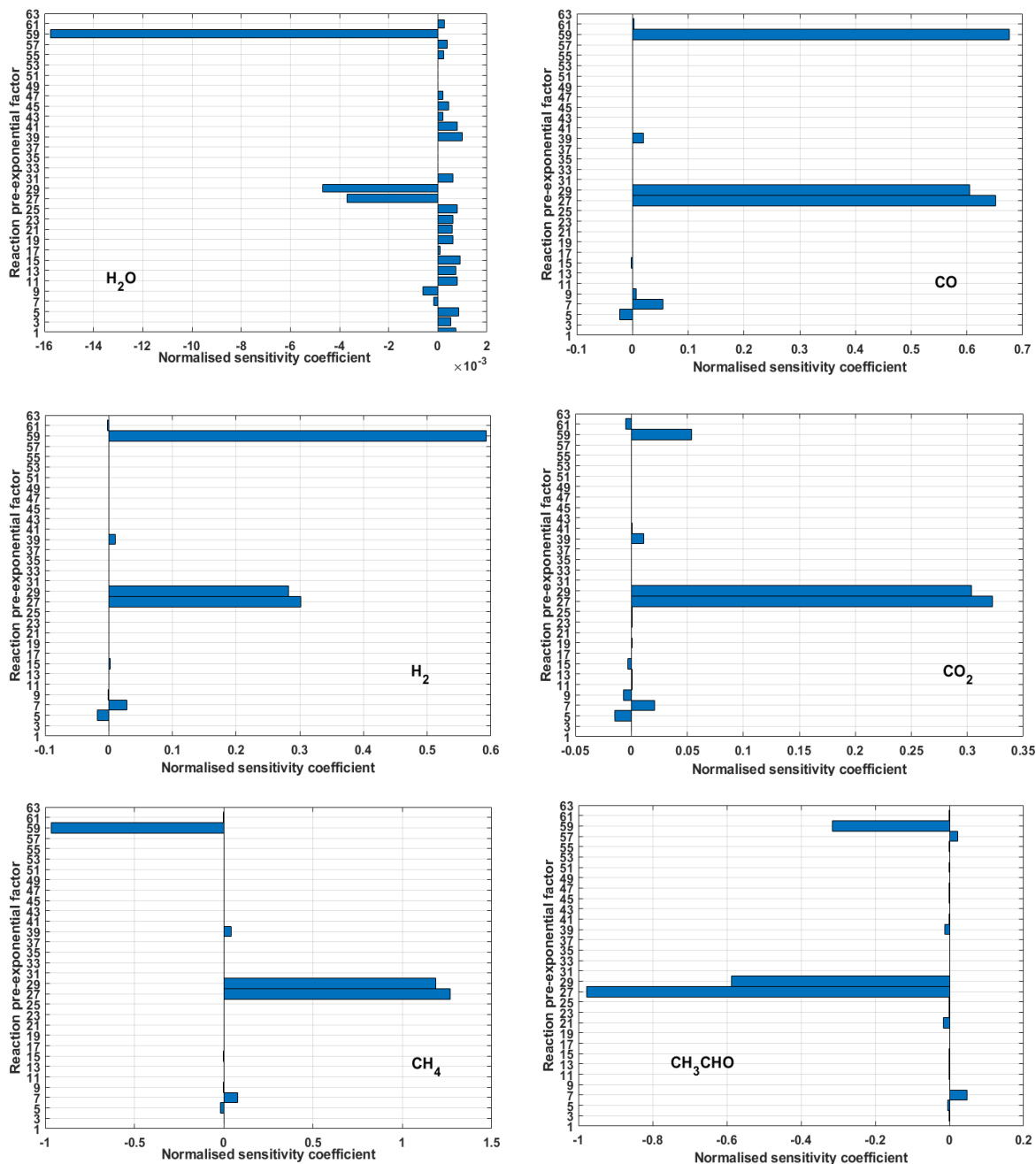


Figure 4-6: Sensitivity analysis of pre-exponential factors of microkinetic model reactions shown in Table 4.2 at 400°C and H₂O/C of 3 for products and water outlet molar fractions. Base values for pre-exponential factors are calculated as described in Section 4.2.2.

4.3.3 Reaction pathway analysis

A differential contribution analysis at the outlet of the catalyst bed at the same conditions as the previous section is further carried out to clarify the significance of the various reaction pathways

considered in the network. Specifically, the net production rates of all carbon containing species are considered in order to estimate their conversion percentages towards all other compounds. Results of this analysis are presented in Figure 4-7 and are further discussed below.

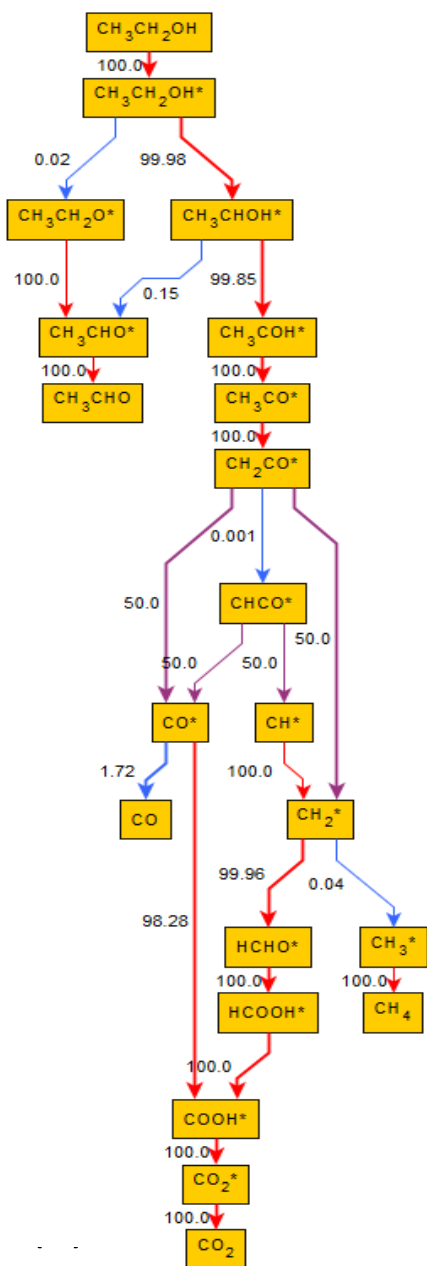


Figure 4-7: Reaction pathway analysis for ethanol steam reforming over Ni/SiO₂ at 400°C and H₂O/C of 3 at an ethanol conversion of 25%. Net production rates are considered in calculating contribution percentages of carbon containing species towards other species. Colour mapping from blue to red indicate increasing contribution percentages. Line thickness indicates the relative magnitude of the rates of the reaction.

According to the model predictions, ethanol adsorbs on the catalyst surface *via* reaction R1, and then dehydrogenates *via* two main pathways. The dominant route proceeds *via* an α -

dehydrogenation (R19) producing CH_3CHOH^* with a high contribution of over 99% of the converted ethanol. Similar findings were reported in the work of Sutton et al. [19] which is one of the very few published works to have presented a comprehensive microkinetic model for ethanol steam reforming, although as commented earlier on a Pt metal catalyst. In the work of Koehle et al. [26], again a Pt catalyst was studied, but for ethanol partial oxidation, so understandably the high temperature oxidative conditions led to the surface pathways being substantially different to those discussed above, with ethanol activation proceeding primarily through dehydration. Similarly, the work of Baruah et al. [27], focusing on the oxidative steam reforming of ethanol on Rh, proposed dehydroxylation (C-O cleavage) as the initial ethanol activation step, although again for a different reaction and conditions. In the current work, in parallel to the main pathway to CH_3CHOH^* , ethanol is predicted to also dehydrogenate successively first towards $\text{CH}_3\text{CH}_2\text{O}^*$ and then CH_3CHO^* *via* reactions R21 and R25, which is well in line with the expected paths on Ni discussed previously [10,17,24,47]. Considering that these works, either experimental [17,47] or theoretical [10,24] referred to decomposition of ethanol on the close-packed Ni(111) surface, it cannot be excluded that the presence of low-coordinated sites and steam-derived O^* and OH^* species in our experiments promotes alternate dehydrogenation pathways [25].

Following the initial favoured α -dehydrogenation, the formed CH_3CHOH^* continues dehydrogenating towards CH_3CHO^* and CH_3COH^* *via* R23 and R27, with the latter accounting for over 99% of conversion contribution, in line also with R27 having been identified as a key rate controlling step in Section 4.3.2. The formed CH_3COH^* species further dehydrogenate exclusively towards CH_3CO^* and CH_2CO^* *via* reactions R29 and R39, the former of which was also identified as an important rate controlling step in Section 4.3.2. The model reports CH_2CO^* as a key surface intermediate for the production of CO^* , which aligns well with various works on the kinetics of ethanol steam reforming [19–21,48] all suggesting C-C bond scission to occur at CH_xCO^* species of varying degrees of dehydrogenation. The current work predicts that the C-C bond cleavage takes place predominantly at the CH_2CO^* intermediate leading to the formation of CH_2^* and CO^* *via* reaction R41.

CO^* is predicted to follow two pathways, the less important of which contributes to surface CO^* desorption and production of gas phase CO at an approximately 2% contribution. CO^* follows primarily a water gas shift pathway, reacting with steam-derived OH^* species to produce COOH^* *via* reaction R48. CO^* can, in principle, also react with O^* to produce CO_2^* directly *via* R52, however this pathway is not predicted to occur at the simulated conditions. COOH^* is

a primary species in the CO_2^* production pathway, with the latter exclusively desorbing to the gas phase as CO_2 . CH_2^* species formed upon the C-C bond cleavage follow multiple pathways. The dominant one can be described as methane steam reforming with CH_2^* reacting successively with 2 OH^* species *via* reactions R57 and R59 to form COOH^* , ultimately leading to gas phase CO_2 . On the other hand, all CH_x^* species, including CH_2^* , can also hydrogenate up to CH_3^* , the latter associatively desorbing as CH_4 *via* reaction R8. As such, the reaction pathway analysis further supports the discussion of previous sections and the experimental observations, suggesting the dominant ethanol conversion pathway on Ni to be that of decomposition, not involving dehydrogenation to acetaldehyde, the latter revealed to be a parallel and less important reaction path.

Concerning the non-carbon containing surface species, water, following its molecular adsorption, decomposes towards H^* and OH^* . The participation of OH^* in various reactions and particularly R57, R59 and R48, accounts largely for the consumption of steam, whereas surface O^* are predicted to participate to a much lesser extent. Surface hydrogen H^* formed *via* multiple processes desorbs associatively for the production of gas phase hydrogen.

Based on the results of the space-velocity effect experiments, an additional case was considered to investigate the occurring changes in the reaction pathways at a low ethanol conversion of 3%. The pathways among species remain at these conditions overall similar, so the relevant plot is not shown, however the respective contributions of the initial ethanol conversion steps shift noticeably. The reactions producing acetaldehyde are comparatively promoted, with the dominant dehydrogenation pathway of adsorbed ethanol towards CH_3CHOH^* now also contributing by a measureable 25.5% to the formation of CH_3CHO^* *via* reaction R23 instead of only 0.15% seen in Figure 4-7. The secondary path to $\text{CH}_3\text{CH}_2\text{O}^*$, leading exclusively to CH_3CHO^* *via* reaction R25, also rises substantially in its contribution from 0.02% to as high as 17.6%. The above trends become more pronounced as conversion tends to zero values, and, given the lower adsorption enthalpy of CH_3CHO in comparison to CH_3 and CO (see Table 4.3), result in CH_3CHO appearing as a dominant product at low temperatures. At higher temperatures, the desorption of CH_4 and CO is enhanced leading to all three products appearing as primary ones.

4.3.4 Model parameter sensitivity

A sensitivity analysis was also performed to discern the relevance of the model parameters of the microkinetic model, namely the adsorption enthalpies of considered species. Figure 4-8 shows results of the analysis in which normalised sensitivity coefficients were calculated for the

outlet molar fractions of ethanol, CO, CO₂, CH₄, CH₃CHO and H₂ with a 1% perturbation of the model parameter values shown in Table 4.3. The adsorption enthalpy of CH₃CHOH is identified as having the highest positive effect on ethanol conversion, which, as expected, leads also to positively influencing the production of CO, CO₂, CH₄ and H₂. UBI-QEP stipulates that an increase in the adsorption enthalpy of a compound will in turn lead to a higher or lower activation barrier for any reactions in which this compound participates as a reactant or product, respectively. Therefore, increasing the CH₃CHOH adsorption enthalpy causes the initial ethanol dehydrogenation to have a lower barrier, however it also increases the barrier of the follow-up dehydrogenations towards key intermediates CH₃CO* and CH₂CO*. At the same time, though, the stronger binding of CH₃CHOH to the surface enhances its partial coverage and, as such, the overall rate of reaction R27, leading to the simulated overall acceleration of the reaction pathway.

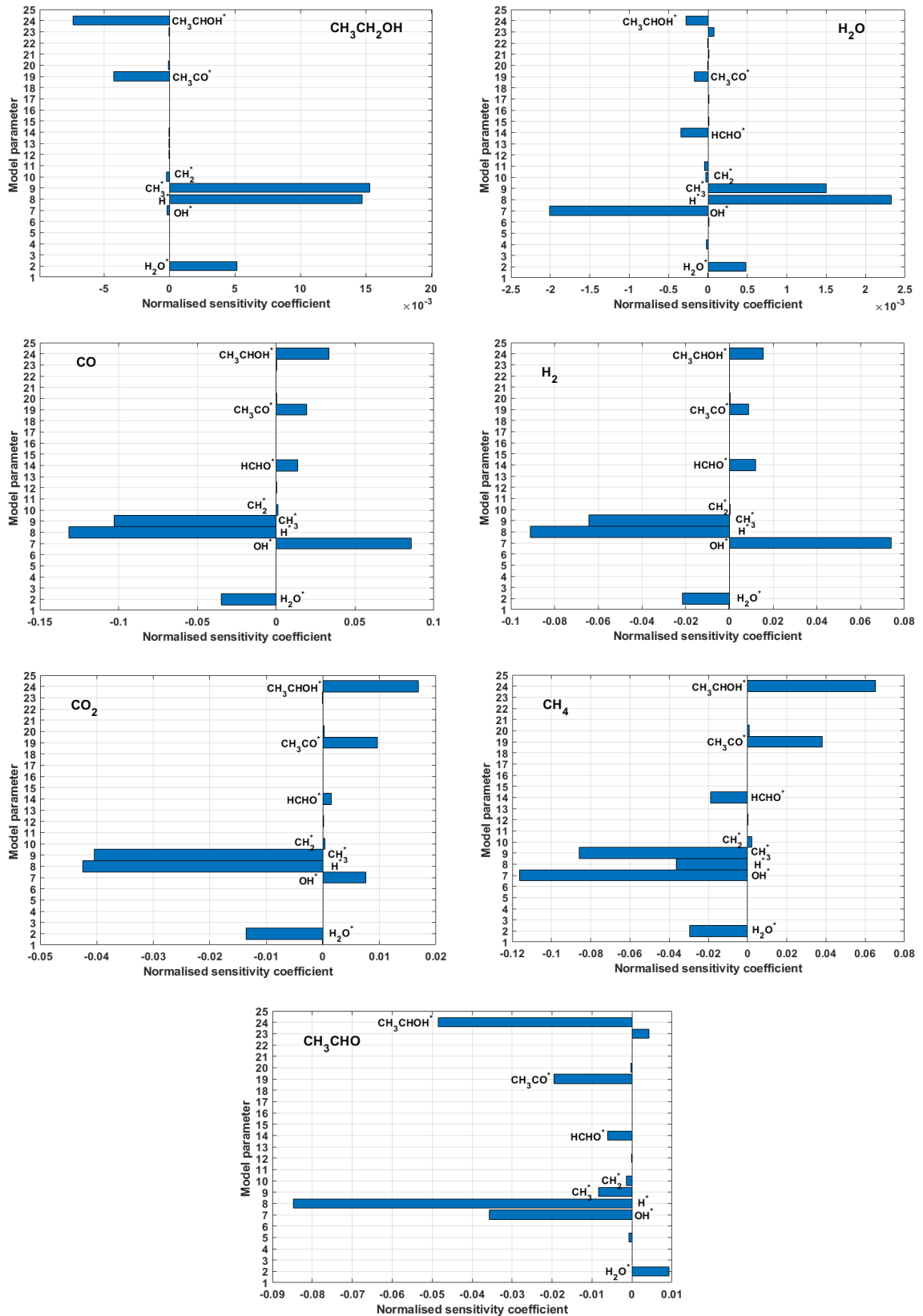


Figure 4-8: Sensitivity analysis of adsorption enthalpies for liquid and gaseous compounds outlet molar fractions for Ni/SiO₂ at 400°C and H₂O/C of 3. Base values for model parameters are shown in Table 3.

The second model parameter with an important positive effect on ethanol conversion is the chemisorption enthalpy of CH_3CO , which, as above, through partial coverage effects leads to a higher rate of production of key intermediate for C-C scission CH_2CO^* , enhancing the dominant reaction pathway. The only other model parameter with a significant effect on the formation of products is the chemisorption enthalpy of OH, which, as also discussed in the previous section, is a co-reactant in most selectivity controlling reactions. The increased activation barrier for the reactions R48, R57, R59 should reduce the formation of key products, however OH^* derives from water, which is the most abundant reactant. A higher OH chemisorption enthalpy, therefore, has a positive effect on H_2O^* dissociation, which in turn leads to a rise in the partial coverage of OH^* , thus leading to a much faster reaction rate for the production of gas phase products CO and CO_2 . For example, at 400°C and $\text{H}_2\text{O}/\text{C}$ of 3 with an inlet water partial pressure of 0.37 bar, the partial coverages of H_2O^* and OH^* are predicted to be 0.52 and 0.002 respectively, with an OH chemisorption enthalpy of 242 kJ mol^{-1} . An increase of the OH chemisorption enthalpy to 245 kJ mol^{-1} at the same conditions changes the coverages of H_2O^* and OH^* to 0.516 and 0.037, respectively, hence a substantially higher hydroxyl coverage is achieved. CH_4 formation as expected is negatively affected by the stronger binding of OH, as CH_2^* , the main precursor to its production, is a reactant in the methane steam reforming pathway.

The sensitivity analysis also identifies strong negative influences on the conversion of ethanol from the chemisorption enthalpies of CH_3 , H and H_2O . As the C-C bond cleavage in reaction R41 leads to an even production of CH_2^* and CO^* it follows that at the point of scission these products are equally abundant on the surface. Therefore, whilst CO^* further participates in the water-gas shift sub-mechanism, an increase in the adsorption enthalpy of CH_3 leads to the methane steam reforming pathway becoming less prominent, thus explaining the negative effect on the production of CO and CO_2 . The increase in the CH_3 binding strength also causes the desorption rate of methane to be reduced explaining the negative effect on CH_4 production. The drop in the conversion of ethanol is propagated by the gradual saturation of the catalyst active sites by surface CH_3^* , with this saturation leading to a reduced rate of reaction in the main ethanol dehydrogenation pathway. H^* is a product of all dehydrogenation reactions and, therefore, an increase in its adsorption enthalpy leads to the surface being saturated easily by this species, explaining again the negative effect of the parameter on conversion and product formation. Similarly, and as discussed in relation to the partial pressure variation experiments, a stronger H_2O binding leads to a progressively more saturated surface.

4.3.5 Estimated model parameters evaluation

Table 4.3 shows the final estimated values, following regression, for the adsorption enthalpies of the microkinetic model, while the temperature exponent values can be seen in Table 4.2. As described in Section 4.2.1, the initial values for chemisorption enthalpies of all species during model development were obtained from literature DFT and prior experimental studies. After model parameter sensitivity analysis was conducted (Figure 4-8), parameters with little or no sensitivity were fixed at the literature obtained values in order to allow for higher confidence in the regression of the more sensitive ones. Estimated parameters shown in Table 4.3 have narrow confidence intervals evidencing a low standard error. The maximum value for the correlation coefficient between two parameters occurs between Q_{H_2O} and Q_{CH_3CHOH} and has a value of -0.86 most likely related to the negative relationship between the surface coverages of both species, as discussed in the previous section. The squared multiple correlation coefficient value obtained for the regression was sufficiently close to unity ($R^2=0.886$), which, coupled with the high F-value of 215.61 (tabulated value = 3.01) for the significance of the regression, affirms the model's good performance.

All chemisorption enthalpies estimated conform to physically realistic values and show adequate agreement with theoretical and experimentally reported ones. The presently estimated value for CH_3 , $200.48 \text{ kJ mol}^{-1}$, is only slightly higher than various reported values. In particular, a DFT study for the steam reforming of acetic acid on the Ni (111) [42] surface reports a CH_3 chemisorption enthalpy value of $191.97 \text{ kJ mol}^{-1}$. With respect to H, a very good agreement for the estimated value of 257 kJ mol^{-1} in this work can be seen in literature with different reported values usually ranging from 240 to 270 kJ mol^{-1} [30,42,43]. Similarly, the estimated values of OH and H_2O ($242.2 \text{ kJ mol}^{-1}$ and $58.95 \text{ kJ mol}^{-1}$ respectively) both fall within the range of reported DFT or experimental values (see references above). The weak binding of HCHO on Ni (111) as reported by Remediakis et al. [43] is qualitatively well reproduced with an estimated adsorption enthalpy in this work of $23.68 \text{ kJ mol}^{-1}$. For ethanol decomposition derived surface species, the estimated values of chemisorption enthalpies presented in Table 4.3 all lie within the range of observed literature published values [41,42,48,49]. Values of $191.39 \text{ kJ mol}^{-1}$ and $83.61 \text{ kJ mol}^{-1}$ were estimated for CH_3CO and CH_2CO , respectively, comparing very well with the equivalent $202.62 \text{ kJ mol}^{-1}$ and $83.94 \text{ kJ mol}^{-1}$ reported by Ran et al. [42]. In summary, the parameterisation of the model based on the above adsorption enthalpies was demonstrated to describe successfully the experimental data and provided insight on the mechanistic trends of the ethanol steam reforming process over Ni catalysts when support effects are not dominant.

4.4 Conclusions

In the current work a microkinetic model is presented for ethanol steam reforming over a Ni/SiO₂ catalyst, the later metal selected on account of its favourable economics in comparison to noble metals. The model is used to simulate an experimental data set that spans a wide range of conditions. All kinetic parameters are either a priori determined or correlated with the adsorption enthalpies of participating species. This allows carrying out a sensitivity analysis that reveals the relative importance of adsorption enthalpies in the kinetic mechanism. Experimental observations relating to a positive reaction order for ethanol were able to be linked to its kinetically relevant dehydrogenation of 1-hydroxyethyl, while the negative order for steam was shown to be due to a progressive saturation of the surface of the catalyst by water. The consideration of secondary surface reactions of ethanol decomposition products, describing methane steam reforming and water gas shift, was revealed necessary for the explanation of the experimentally observed selectivities across the broad range of conditions simulated. The predicted decomposition pathways share similarities to previously reported by other microkinetic studies on noble metals, however differences with DFT calculations on Ni(111) are identified and suggest that under reforming conditions and over “real” catalysts different surface steps might be preferred. This model’s results serve as a basis for and prompt the development of consolidated kinetic schemes that incorporate the effect of supports on the ethanol steam reforming mechanism.

References

- [1] N. Sanchez, R.Y. Ruiz, B. Cifuentes, M. Cobo, Hydrogen from glucose: A combined study of glucose fermentation, bioethanol purification, and catalytic steam reforming, *Int. J. Hydrogen Energy*. 41 (2016) 5640–5651. <https://doi.org/10.1016/j.ijhydene.2016.01.155>.
- [2] H. Song, L. Zhang, R.B. Watson, D. Braden, U.S. Ozkan, Investigation of bio-ethanol steam reforming over cobalt-based catalysts, 129 (2007) 346–354. <https://doi.org/10.1016/j.cattod.2006.11.028>.
- [3] M. Ni, D.Y.C. Leung, M.K.H. Leung, A review on reforming bio-ethanol for hydrogen production, *Int. J. Hydrogen Energy*. 32 (2007) 3238–3247. <https://doi.org/10.1016/j.ijhydene.2007.04.038>.
- [4] C.. Rioche, S.. Kulkarni, M.. Meunier, J.. Breen, R.. Burch, Steam reforming of model compounds and fast pyrolysis bio-oil on supported noble metal catalysts, *Appl. Catal. B Environ.* 61 (2005) 130–139.
- [5] R. González-Gil, I. Chamorro-Burgos, C. Herrera, M.A. Larrubia, M. Laborde, F. Mariño, L.J. Alemany, Production of hydrogen by catalytic steam reforming of oxygenated model compounds on Ni-modified supported catalysts. Simulation and experimental study, *Int. J. Hydrogen Energy*. 40 (2015) 11217–11227.

<https://doi.org/10.1016/j.ijhydene.2015.05.167>.

- [6] R. Trane, S. Dahl, M.S. Skjøth-Rasmussen, A.D. Jensen, Catalytic steam reforming of bio-oil, *Int. J. Hydrogen Energy*. 37 (2012) 6447–6472. <https://doi.org/10.1016/j.ijhydene.2012.01.023>.
- [7] P.D. Vaidya, A.E. Rodrigues, Insight into steam reforming of ethanol to produce hydrogen for fuel cells, *Chem. Eng. J.* 117 (2006) 39–49. <https://doi.org/10.1016/j.cej.2005.12.008>.
- [8] L. V Mattos, G. Jacobs, B.H. Davis, F.B. Noronha, Production of hydrogen from ethanol: Review of reaction mechanism and catalyst deactivation, *Chem. Rev.* 112 (2012) 4094–4123. <https://doi.org/10.1021/cr2000114>.
- [9] F. Wang, W. Cai, C. Descorme, H. Provendier, W. Shen, C. Mirodatos, Y. Schuurman, From mechanistic to kinetic analyses of ethanol steam reforming over Ir/CeO₂ catalyst, *Int. J. Hydrogen Energy*. 39 (2014) 18005–18015. <https://doi.org/10.1016/j.ijhydene.2014.06.121>.
- [10] J.H. Wang, C.S. Lee, M.C. Lin, Mechanism of ethanol reforming: Theoretical foundations, *J. Phys. Chem. C*. 113 (2009) 6681–6688. <https://doi.org/10.1021/jp810307h>.
- [11] I. Llera, V. Mas, M.L. Bergamini, M. Laborde, N. Amadeo, Bio-ethanol steam reforming on Ni based catalyst. Kinetic study, *Chem. Eng. Sci.* 71 (2012) 356–366. <https://doi.org/10.1016/j.ces.2011.12.018>.
- [12] A. Akande, A. Aboudheir, R. Idem, A. Dalai, Kinetic modeling of hydrogen production by the catalytic reforming of crude ethanol over a co-precipitated Ni-Al₂O₃ catalyst in a packed bed tubular reactor, *Int. J. Hydrogen Energy*. 31 (2006) 1707–1715. <https://doi.org/10.1016/j.ijhydene.2006.01.001>.
- [13] M.D. Zhurka, A.A. Lemonidou, J.A. Anderson, P.N. Kechagiopoulos, Kinetic analysis of the steam reforming of ethanol over Ni/SiO₂ for the elucidation of metal-dominated reaction pathways, *React. Chem. Eng.* 3 (2018) 883–897. <https://doi.org/10.1039/c8re00145f>.
- [14] R. Alcalá, M. Mavrikakis, J.A. Dumesic, DFT studies for cleavage of C-C and C-O bonds in surface species derived from ethanol on Pt(111), *J. Catal.* 218 (2003) 178–190. [https://doi.org/10.1016/S0021-9517\(03\)00090-3](https://doi.org/10.1016/S0021-9517(03)00090-3).
- [15] F. Soybal-Baltacioğlu, A.E. Aksoylu, Z.I. Önsan, Steam reforming of ethanol over Pt-Ni Catalysts, *Catal. Today*. 138 (2008) 183–186. <https://doi.org/10.1016/j.cattod.2008.05.035>.
- [16] M. Li, W. Guo, R. Jiang, L. Zhao, H. Shan, Decomposition of ethanol on Pd(111): A density functional theory study, *Langmuir*. 26 (2010) 1879–1888. <https://doi.org/10.1021/la902641t>.
- [17] S.M. Gates, J.N. Russell Jr., J.T. Yates Jr., Bond activation sequence observed in the chemisorption and surface reaction of ethanol on Ni(111), *Surf. Sci.* 171 (1986) 111–134.
- [18] P. Ferrin, D. Simonetti, S. Kandoi, E. Kunkes, J.A. Dumesic, J.K. Nørskov, M. Mavrikakis, Modeling ethanol decomposition on transition metals: A combined application of scaling and brønsted-evans-polanyi relations, *J. Am. Chem. Soc.* 131 (2009) 5809–5815. <https://doi.org/10.1021/ja8099322>.

- [19] J.E. Sutton, P. Panagiotopoulou, X.E. Verykios, D.G. Vlachos, Combined DFT, microkinetic, and experimental study of ethanol steam reforming on Pt, *J. Phys. Chem. C.* 117 (2013) 4691–4706. <https://doi.org/10.1021/jp312593u>.
- [20] M. Li, W. Guo, R. Jiang, L. Zhao, X. Lu, H. Zhu, D. Fu, H. Shan, Density functional study of ethanol decomposition on Rh(111), *J. Phys. Chem. C.* 114 (2010) 21493–21503. <https://doi.org/10.1021/jp106856n>.
- [21] J. Zhang, Z. Zhong, X.M. Cao, P. Hu, M.B. Sullivan, L. Chen, Ethanol steam reforming on rh catalysts: Theoretical and experimental understanding, *ACS Catal.* 4 (2014) 448–456. <https://doi.org/10.1021/cs400725k>.
- [22] Y. Ma, L. Hernández, C. Guadarrama-Pérez, P.B. Balbuena, Ethanol reforming on Co(0001) surfaces: A density functional theory study, *J. Phys. Chem. A.* 116 (2012) 1409–1416. <https://doi.org/10.1021/jp208179e>.
- [23] D.R. Sahoo, S. Vajpai, S. Patel, K.K. Pant, Kinetic modeling of steam reforming of ethanol for the production of hydrogen over Co/Al₂O₃ catalyst, *Chem. Eng. J.* 125 (2007) 139–147. <https://doi.org/10.1016/j.cej.2006.08.011>.
- [24] J.E. Sutton, D.G. Vlachos, Ethanol activation on closed-packed surfaces, *Ind. Eng. Chem. Res.* 54 (2015) 4213–4225. <https://doi.org/10.1021/ie5043374>.
- [25] D. Zanchet, J.B.O. Santos, S. Damyanova, J.M.R. Gallo, J.M.C. Bueno, Toward understanding metal-catalyzed ethanol reforming, *ACS Catal.* 5 (2015) 3841–3863. <https://doi.org/10.1021/cs5020755>.
- [26] M. Koehle, A. Mhadeshwar, Microkinetic modeling and analysis of ethanol partial oxidation and reforming reaction pathways on platinum at short contact times, *Chem. Eng. Sci.* 78 (2012) 209–225. <https://doi.org/10.1016/j.ces.2012.05.017>.
- [27] R. Baruah, M. Dixit, A. Parejiya, P. Basarkar, A. Bhargav, S. Sharma, Oxidative steam reforming of ethanol on rhodium catalyst – I: Spatially resolved steady-state experiments and microkinetic modeling, *Int. J. Hydrogen Energy.* 42 (2017) 10184–10198. <https://doi.org/10.1016/j.ijhydene.2017.03.168>.
- [28] K. Metaxas, J.W. Thybaut, C. Mirodatos, G.B. Marin, A Microkinetic Vision on High-Throughput Catalyst Formulation and Optimization : Development of an Appropriate Software Tool, (2010) 64–76. <https://doi.org/10.1007/s11244-009-9432-9>.
- [29] C. Sprung, P.N. Kechagiopoulos, J.W. Thybaut, B. Arstad, U. Olsbye, G.B. Marin, Microkinetic evaluation of normal and inverse kinetic isotope effects during methane steam reforming to synthesis gas over a Ni/NiAl₂O₄ model catalyst, *Appl. Catal. A Gen.* 492 (2015) 231–242. <https://doi.org/10.1016/j.apcata.2014.10.062>.
- [30] P.N. Kechagiopoulos, S.D. Angeli, A.A. Lemonidou, Low temperature steam reforming of methane: A combined isotopic and microkinetic study, *Appl. Catal. B Environ.* 205 (2017) 238–253. <https://doi.org/10.1016/j.apcatb.2016.12.033>.
- [31] A.B. Mhadeshwar, H. Wang, D.G. Vlachos, Thermodynamic Consistency in Microkinetic Development of Surface Reaction Mechanisms, *J. Phys. Chem. B.* 107 (2003) 12721–12733. <https://doi.org/10.1021/jp034954y>.
- [32] J.A. Dumesic, D.F. Rudd, L.M. Aparicio, J.E. Rekoske, A.A. Treviño, *The Microkinetics of Heterogeneous Catalysis*, 1993.

- [33] M. Faheem, M. Saleheen, J. Lu, A. Heyden, *Catalysis Science & Technology* aqueous phases †, 2 (2016) 8242–8256. <https://doi.org/10.1039/c6cy02111e>.
- [34] E. Shustorovich, The Bond-Order Conservation Approach to Chemisorption and Heterogeneous Catalysis: Applications and Implications, *Adv. Catal.* 37 (1990) 101–163. [https://doi.org/10.1016/S0360-0564\(08\)60364-8](https://doi.org/10.1016/S0360-0564(08)60364-8).
- [35] E. Shustorovich, H. Sellers, The UBI-QEP method: A practical theoretical approach to understanding chemistry on transition metal surfaces, *Surf. Sci. Rep.* 31 (1998) 1–119. [https://doi.org/http://dx.doi.org/10.1016/S0167-5729\(97\)00016-2](https://doi.org/http://dx.doi.org/10.1016/S0167-5729(97)00016-2).
- [36] P.N. Brown, A.C. Hindmarsh, L.R. Petzold, Using Krylov methods in the solution of large-scale differential-algebraic systems, *SIAM J. Sci. Comput.* 15 (1994) 1467–1488.
- [37] H.H. Rosenbrock, An Automatic Method for Finding the Greatest or Least Value of a Function, *Comput. J.* 3 (1960) 175–184. <https://doi.org/10.1093/comjnl/3.3.175>.
- [38] D.W. Marquardt, An algorithm for least-squares estimation of nonlinear parameters, *J. Soc. Ind. Appl. Math.* 11 (1963) 431–441.
- [39] P.T. Boggs, J.R. Donaldson, R. h. Byrd, R.B. Schnabel, Algorithm 676: ODRPACK: software for weighted orthogonal distance regression, *ACM Trans. Math. Softw.* 15 (1989) 348–364. <https://doi.org/10.1145/76909.76913>.
- [40] A.N. Fatsikostas, X.E. Verykios, Reaction network of steam reforming of ethanol over Ni-based catalysts, *J. Catal.* 225 (2004) 439–452. <https://doi.org/10.1016/j.jcat.2004.04.034>.
- [41] O. Skoplyak, M.A. Barteau, J.G. Chen, Ethanol and ethylene glycol on Ni/Pt(1 1 1) bimetallic surfaces: A DFT and HREELS study, *Surf. Sci.* 602 (2008) 3578–3587. <https://doi.org/10.1016/j.susc.2008.09.040>.
- [42] Y.X. Ran, Z.Y. Du, Y.P. Guo, J. Feng, W.Y. Li, Density functional theory study of acetic acid steam reforming on Ni(111), *Appl. Surf. Sci.* 400 (2017) 97–109. <https://doi.org/10.1016/j.apsusc.2016.12.148>.
- [43] I.N. Remediakis, F. Abild-Pedersen, J.K. Nørskov, DFT study of formaldehyde and methanol synthesis from CO and H₂ on Ni(111), *J. Phys. Chem. B.* 108 (2004) 14535–14540. <https://doi.org/10.1021/jp0493374>.
- [44] W. Zhao, S.J. Carey, S.E. Morgan, C.T. Campbell, Energetics of adsorbed formate and formic acid on Ni(111) by calorimetry, *J. Catal.* 352 (2017) 300–304. <https://doi.org/10.1016/j.jcat.2017.05.023>.
- [45] J. Vicente, J. Ereña, C. Montero, M.J. Azkoiti, J. Bilbao, A.G. Gayubo, Reaction pathway for ethanol steam reforming on a Ni/SiO₂ catalyst including coke formation, *Int. J. Hydrogen Energy.* 39 (2014) 18820–18834. <https://doi.org/10.1016/j.ijhydene.2014.09.073>.
- [46] J.W.C. Liberatori, R.U. Ribeiro, D. Zanchet, F.B. Noronha, J.M.C. Bueno, Steam reforming of ethanol on supported nickel catalysts, *Appl. Catal. A Gen.* 327 (2007) 197–204. <https://doi.org/10.1016/j.apcata.2007.05.010>.
- [47] J. Xu, X. Zhang, R. Zenobi, J. Yoshinobu, Z. Xu, J.T. Yates, Ethanol decomposition on Ni(111): observation of ethoxy formation by IRAS and other methods, *Surf. Sci.* 256

(1991) 288–300. [https://doi.org/10.1016/0039-6028\(91\)90872-P](https://doi.org/10.1016/0039-6028(91)90872-P).

- [48] I. Llera, V. Mas, M.L. Bergamini, M. Laborde, N. Amadeo, Bio-ethanol steam reforming on Ni based catalyst. Kinetic study, *Chem. Eng. Sci.* 71 (2012) 356–366. <https://doi.org/10.1016/j.ces.2011.12.018>.
- [49] I.N. Remediakis, F. Abild-Pedersen, J.K. Nørskov, DFT study of formaldehyde and methanol synthesis from CO and H₂ on Ni(111), *J. Phys. Chem. B.* 108 (2004) 14535–14540. <https://doi.org/10.1021/jp0493374>.

Preface to Chapter 5

A version of this chapter has been submitted for publication to the *Chemical Engineering Journal* (A Navarro-Puyuelo, A.T.F. Afolabi, P.N. Kechagiopoulos, F. Bimbela, L.M. Gandia,

Investigation of H₂ and CO co-feeding on biogas dry reforming over Rh/Al₂O₃). This was a collaborative study with all of the experimental work carried out in the Institute of Advanced Materials and Mathematics at the Universidad Publica de Navarra. The modelling aspects of the study were carried out in the Chemicals and Materials Engineering group at the University of Aberdeen. I was the co-lead investigator, responsible for the major areas of concept formation, data collection and analysis, as well as manuscript composition pertaining to the microkinetic modelling parts of the study. A Navarro-Puyuelo was the co-lead investigator responsible for the major experimental concept formation, data collection and analysis, as well as manuscript composition. In addition, A. Navarro-Puyuelo was also involved in the early stages of modelling concept formation. Kechagiopoulos P.N. was the secondary supervisory author and was involved concept formation and manuscript composition of the modelling. F. Bimbela was the main supervisory author on this project and was involved throughout the project in concept formation and manuscript composition.

The aim of this study was to investigate the effect of the co-feeding of H₂ and CO on the kinetics and mechanism of biogas dry reforming. This is done to account for the possible requirement of a recycle stream during dry reforming on industrial scale as is the case in the conventional steam reforming of methane (biogas).

The mean-field microkinetic model developed in Chapter 4, provided the ideal foundation for the development of the biogas dry reforming model. The biogas model consists of fewer surface intermediates, increasing the ease of model formulation. Most of the surface intermediates were also already present in the developed ethanol steam reforming model. The same semi-empirical methods of rate constant estimation are utilised. Initial values for the adsorption energy of surface species were obtained as in the previous model from DFT and experimental studies. An additional model parameter F_{loc} , which represents the fraction of localised entropy retained by the adsorbed species was implemented into the existing model and its use is discussed in more detail in the paper.

CHAPTER 5: INVESTIGATION OF H₂ AND CO CO-FEEDING ON BIOGAS DRY REFORMING OVER Rh/Al₂O₃ CATALYST VIA MICROKINETIC MODELLING

Andrea Navarro-Puyuelo^a, Ahmed Tijani F. Afolabi^b, Inés Reyero^a, Fernando Bimbela^{a*}, Panagiotis N. Kechagiopoulos^{b*}, Luis M. Gandía^a

^a Grupo de Reactores Químicos y Procesos para la Valorización de Recursos Renovables, Institute for Advanced Materials and Mathematics (InaMat²), Departamento de Ciencias, Edificio de los Acebos, Universidad Pública de Navarra, Campus de Arrosadía, E-31006 Pamplona, Spain

^b Chemical and Materials Engineering Group, School of Engineering, University of Aberdeen, Aberdeen, AB24 3UE, UK

* Corresponding authors. E-mail addresses: fernando.bimbela@unavarra.es; p.kechagiopoulos@abdn.ac.uk

Highlights:

Microkinetic model developed for dry reforming of biogas over a Rh/Al₂O₃ catalyst

H₂ co-feeding had a positive effect on biogas conversion and syngas yield

Negative effect of CO co-feeding on CO₂ conversion and H₂ and CO yields

Dehydrogenation of CH₃* identified as rate-determining step

Model valid for methane steam reforming on Rh/Al₂O₃ with minor changes

Abstract

The effect of co-feeding biogas dry reforming reaction products (H_2 or CO) on biogas conversion and selectivity to syngas over a 0.5 wt. % $\text{Rh}/\text{Al}_2\text{O}_3$ catalyst was studied by means of microkinetic modelling. The experimental dataset was collected by conducting kinetic experiments in which different gas feeding compositions and flow rates of CH_4 , CO_2 , H_2 and CO were used, at various reaction temperatures (700 – 750 °C) and spatial velocities (350 – 1134 N L $\text{CH}_4/(\text{g}_{\text{cat}}\cdot\text{h})$). The microkinetic model developed consisted of 86 elementary reaction steps and was defined based on the estimation of heats of chemisorption and fractions of local entropy upon adsorption. The model described satisfactorily the experimental trends found for CH_4 and CO_2 conversions, H_2 and CO yields and selectivities. A sensitivity analysis of pre-exponential factors was carried out to check the model's robustness. Dehydrogenation of CH_3^* was identified as the rate reaction controlling step. A differential contribution analysis at the outlet of the catalyst bed clarified the kinetic relevance of reaction pathways, which was not altered by H_2 co-feeding. Increasing the H_2 concentration in the reactor feed resulted in increased biogas conversions and syngas yields, due to augmented partial coverage of H^* and CO^* species, thus causing promoting effects on the reverse Water-Gas shift (rWGS) and methane steam reforming reactions. In contrast, CO co-feeding had negative effects on CO_2 conversion, H_2 and CO yields, due to the high partial coverage of CO^* , which saturates the catalyst surface and negatively affects the rWGS reaction.

Keywords: Biogas dry reforming, CO co-feeding, H_2 co-feeding, Rh catalyst, Microkinetic modelling

5.1 Introduction

Efforts on biogas valorisation have risen in the last years due to a global increase in the implementation of waste management technologies, which has augmented the amount of biogas produced, reaching a world production of 60.8 billion Nm³ in 2016 [1]. Biogas transformation into synthesis gas *via* reforming reactions catalysed over a variety of materials has attracted the attention of many research groups, as evidenced by the numerous reviews that can be found in the literature [2–7]. Synthesis gas or syngas is a gas mixture of H₂ and CO that constitutes a key intermediate in the production of biofuels by means of Gas-to-Liquids (GtL) technologies, as well as various chemicals of industrial relevance, including the production of hydrogen [8,9].

Different biogas conversion processes have been investigated, including catalytic partial oxidation [10,11], steam reforming [12–15], dry reforming [16,17], and combinations of these that result in the autothermal reforming (ATR) of biogas [18,19].

Amidst the different biogas reforming reactions, dry reforming is particularly interesting because it allows the simultaneous conversion of both main biogas constituents in a simple and straightforward manner. The use of Ni-based catalysts has been extensively researched in biogas reforming [13,16,17,19–25], because of their high catalytic activity and relative low cost [26,27], though they suffer from deactivation mainly by coke deposition and sintering [28] and by loss of Ni active sites upon regeneration [29]. For this reason, noble metal catalysts, such as Rh, have been studied as an alternative, obtaining superior performance and resistance to deactivation [10,30–33]. In previous works, dry reforming combined with partial oxidation of methane was studied over Rh catalysts, finding that 0.5 % Rh/Al₂O₃ presented the best activity and stability results. It could be concluded that the thermal treatments of the catalysts are an important factor to take into account in order to improve their catalytic activity. Furthermore, by combining dry reforming of biogas with partial oxidation, simultaneous CH₄ and CO₂ conversion is enhanced, the H₂/CO molar ratio among the reaction products is increased and the catalyst stability is improved [10,31]. Most of the studies cited above investigate the influence of reaction conditions and other process parameters on the catalytic performance, focusing on reforming activity and selectivity to syngas, as well as on catalyst stability and causes for deactivation. In this sense, kinetic studies are needed to elucidate reaction mechanisms, improve catalyst formulations and performing reactor modelling and simulation.

The development of dry reforming kinetic studies in the literature has basically followed two distinct approaches: macrokinetic and microkinetic. Regarding the macrokinetic approach, most of the models proposed are of the Langmuir-Hinshelwood-Hougen-Watson (LHHW) type,

whereas Ni [22,34–39], Co [40,41] and noble metals as Rh [33,42–48] have been considered as catalytic active phases. Wei *et al.* studied the steam and dry reforming of methane on Ni/MgO [35], Rh/Al₂O₃ and Rh/ZrO₂ [46] catalysts and found that the reaction rates had a first-order dependence on CH₄ concentration, whereas they were not influenced by the co-reactants (H₂O or CO₂) nor by the main reaction products (H₂ and CO), in accordance with the fact that the rate determining step (RDS) was the activation of CH₄. Niu *et al.* [37] came to the same conclusions in their study of the dry reforming reaction on Ni hydrotalcites with CeO₂, ZrO₂ and ZnO as promoters. Verykios [38] proposed the cracking of methane as the RDS on Ni as well as the reaction of carbon and oxycarbonate species, formed by the interaction of CO₂ and La₂O₃. Múnera *et al.* also proposed this mechanism on Rh/La₂O₃ [45] and Rh/La₂O₃-SiO₂ [47] catalysts. A combined LHHW and microkinetic model was developed by Sawatmongkhon *et al.* for a monolithic Pt-Rh alumina catalyst [42], finding that the RDS changed from CH₄ adsorption at low temperatures to dry reforming surface reaction at high temperatures. Donazzi *et al.* [44] concluded that dry reforming on a 4 % Rh/Al₂O₃ catalyst consisted of a combination of methane steam reforming (SRM) and reverse water-gas shift (rWGS) reactions, varying the controlling process from rWGS at CO₂/CH₄=1 to SRM for CO₂/CH₄>1. These studies reflect the lack of consensus on the prevalent reaction mechanism by which biogas dry reforming takes place and on the rate determining step. This is somewhat logical though, since the reaction mechanism may vary depending on the type of metal, support, additives and even reaction conditions.

The microkinetic approach does not require to assume *a priori* a RDS and allows to identify the dominant reaction paths and to model the process under different operating conditions [49]. Some works on the microkinetic modelling of dry reforming of methane using Ni [50–54] and Rh [42,48,49,55–59] based catalysts can be found in the existing literature. In a study conducted by Prof. Deutschmann's group [50], a microkinetic model was developed for several catalytic processes on a Ni-based catalyst, including partial oxidation, steam and dry reforming of methane. Concerning the latter reaction, the authors identified methane adsorption and desorption as well as methane dehydrogenation as the most relevant processes in the overall reaction mechanism. This model was applied by Xie *et al.* [51] in the dry reforming of methane on a Ni catalyst, where they found that the kinetic relevant steps varied under different reaction conditions. Maestri *et al.* [49] adapted Mahdeshwar and Vlachos' model [55] in order to describe several reactions, such as steam and dry reforming, partial oxidation of methane, WGS or rWGS, using a 4 % Rh/Al₂O₃ catalyst in an annular reactor. In other work with the same catalyst and reactor configuration, Maestri *et al.* [56] studied only steam and dry reforming reactions, developing a reduced microkinetic model which established, in both cases, CH₃*

dehydrogenation as the RDS, and OH^* , provided by H_2O or CO_2 , as the main C^* oxidizer. Karakaya *et al.* [58] formulated a model for dry reforming of methane, among other reactions, on a 5 % Rh/ Al_2O_3 catalyst. It was found that CO was formed *via* a COOH^* intermediate and that the RDS was related to CH_4 dehydrogenation. In conclusion, there is some agreement in the literature about the importance of CH_4 adsorption and dehydrogenation on the dry reforming mechanism.

However, it must be borne in mind that scaling up of biogas dry reforming technologies to larger scales will probably be based on partial recycling of the product gas stream, as occurs in current methane steam reforming technologies. Such approach, will inevitably result in a gas feeding stream into the catalytic reforming unit that may contain H_2 and/or CO, owing to the above mentioned recycle stream derived from the product gas outlet.

For this reason, it is interesting to carry out kinetic studies in which synthesis gas products are taken into account. Some macrokinetic models have been reported that studied the effect of H_2 and/or CO co-feeding in the reaction [35,38,44–46,48] on Ni and Rh catalysts. However, as for the microkinetic approach, only two studies can be found to date. Herrera Delgado *et al.* [50] observed that adding H_2 to the feeding stream leads to an increment in H_2O production that promoted the steam reforming reaction at high temperatures. Behroozsarand and Pour [48] simulated H_2 or CO addition to the dry reforming reaction on a Rh monolith using Langmuir-Hinshelwood (LH) and microkinetic models, finding different effects depending on the model used, thus evidencing the need for kinetic studies to help gain further insight on the actual mechanism for biogas dry reforming on Rh catalysts, and on the effect of co-feeding H_2 and or CO in the biogas feed stream.

Therefore, the general objective of this work is to develop a microkinetic model for biogas dry reforming on a Rh/ Al_2O_3 catalyst to evaluate the effects of H_2 and CO addition on the biogas feeding stream. The influence of the gas hourly space velocity (GHSV), the CH_4/CO_2 molar ratio and H_2 and CO co-feeding on the biogas reforming activity of the catalyst and selectivity to syngas have been experimentally studied to validate the kinetic model developed.

5.2 Materials and methods

5.2.1 Catalyst preparation and characterization

A 0.5 wt. % Rh/Al₂O₃ catalyst was prepared by the incipient wetness impregnation technique. Before impregnation, the γ -Al₂O₃ support (Alfa Aesar) was ground and sieved to get a particle size distribution ranged between 100 and 200 μm and calcined at 750 °C for 6 h under flowing air. A Rh (III) nitrate solution (10 % (w/v) Rh in 20-25 wt. % HNO₃) (Across Organics) was used as the Rh precursor. The solid obtained after impregnation was dried overnight at 105 °C.

The fresh catalyst was characterized by means of different techniques. N₂ adsorption-desorption isotherms were determined in a Micromeritics Gemini V 2380 static volumetric analyser at 77 K. The specific surface area was determined by the Brunauer-Emmett-Teller (BET) method, whereas the specific pore volume and the average pore size were calculated by the Barrett-Joyner-Halenda (BJH) method. Temperature-programmed reduction (TPR) and CO pulse chemisorption analyses were carried out using a Micromeritics AUTOCHEM II 2920 equipped with a thermal conductivity detector (TCD). Further details on catalyst preparation procedure and characterization can be found in a previous work [31].

5.2.2 Catalytic tests

All catalytic tests were performed in a fixed-bed quartz tubular reactor (8 mm of internal diameter) at atmospheric pressure. Online gas analysis system consisted of a gas chromatograph (GC) (Agilent 6890N) equipped with two columns connected in series, a HPINNOWAX and a MolSieve 5A, and a thermal conductivity detector (TCD). The analyses were carried out at 85 °C every 5 min using N₂ as internal standard. The catalytic bed was constituted by 10 mg of 0.5 wt. % Rh/Al₂O₃ catalyst in powder form (100-200 μm particle size fraction) mixed with 1 g of high-purity α -Al₂O₃ (99.5 %, Strem Chemicals), used as inert filler.

The catalytic tests were carried out at gas hourly space velocities (GHSV) within the 350 – 1134 N L CH₄/(g_{cat}·h) range, and reaction temperatures between 700 and 750 °C. The reaction temperature was reached following a 10 °C/min temperature ramp under He flow, with a dwell time of 30 min before allowing the feed stream into the reactor. A biogas synthetic mixture composed of 54 mol % of CH₄, 40 mol % of CO₂ and 6 mol % of N₂ was used as reference biogas feed. Other gas feeding compositions were also tested by adding high purity CH₄, CO₂, H₂ or CO to the gas feeding line. Table 5.1 presents a summary of all the reaction conditions considered in this work, thus obtaining a dataset comprising a total of 39 experimental

points. All high purity gases and gas mixtures were supplied by Nippon Gases Spain. Further information about the experimental setup and procedures can be found in a previous work [31].

Table 5.1: Reaction conditions studied.

Experiment	GHSV (N L CH ₄ /(g _{cat} ·h))	CH ₄ (mol %)	CO ₂ (mol %)	N ₂ (mol %)	H ₂ (mol %)	CO (mol %)	Temperature range (°C)
Biogas	350 - 1134	54	40	6	-	-	700-750
Biogas + CH ₄	350 - 700	66	28	6	-	-	700-750
Biogas + CO ₂	350 - 700	39	55	6	-	-	700-750
Biogas + H ₂	700	50	37	6	7	-	700-750
	700	48	36	6	10	-	700-750
	700	43	32	6	19	-	700-750
	700	37	24	6	33	-	700-750
Biogas + CO	700	49	36	5	-	9	700-750
	700	43	32	6	-	19	700-750

CH₄ and CO₂ conversions, as well as H₂ and CO yields and selectivities have been calculated from the GC analyses according to the following expressions:

$$CH_4 \text{ conversion (\%)} = \frac{CH_{4,in} - CH_{4,out}}{CH_{4,in}} \cdot 100 \quad (5.1)$$

$$CO_2 \text{ conversion (\%)} = \frac{CO_{2,in} - CO_{2,out}}{CO_{2,in}} \cdot 100 \quad (5.2)$$

$$H_2 \text{ yield (\%)} = \frac{H_{2,out} - H_{2,in}}{2 \cdot CH_{4,in}} \cdot 100 \quad (5.3)$$

$$CO \text{ yield (\%)} = \frac{CO_{in} - CO_{out}}{2 \cdot CO_{2,in}} \cdot 100 \quad (5.4)$$

$$H_2 \text{ selectivity (\%)} = \frac{H_{2,in} - H_{2,out}}{2 \cdot (CH_{4,in} - CH_{4,out})} \cdot 100 \quad (5.5)$$

$$CO \text{ selectivity (\%)} = \frac{CO_{in} - CO_{out}}{2 \cdot (CO_{2,in} - CO_{2,out})} \cdot 100 \quad (5.6)$$

In these equations, CH_4 , CO_2 , H_2 and CO are the corresponding molar flow rates, whereas subscripts *in* and *out* refer to the reactor inlet and exit, respectively.

5.2.3 Model formulation and computation details

The microkinetic model for biogas dry reforming over Rh/Al₂O₃ catalyst implemented in this work closely follows the procedure described in the work of Kechagiopoulos *et al.* [13], with only the main features and improvements highlighted here.

For all surface reactions, the reaction entropy and enthalpy are correlated to the corresponding gas phase reaction entropy and enthalpy in order to maintain thermodynamic consistency. The enthalpy of surface species is obtained by deducting the chemisorption enthalpy of the species from the equivalent gas phase enthalpy. The chemisorption enthalpies are temperature dependent based on the degrees of freedom lost or gained during adsorption or desorption as described in Mhadeshwar *et al.* [60] and implemented according to equation 4.5.

The entropies for adsorbed species are estimated by deducting their standard three-dimensional translational entropy $S_{trans,3D}$ from the gas phase entropy. A fitting factor F_{loc} , which is used to represent the fraction of rotational and vibrational entropy of the gas phase molecule that remains after adsorption, as described in Grabow *et al.* [61], is included in the determination of surface species entropy. The fitting factor is added to the list of model parameters and implemented according to the equation below:

$$S_{surf} = F_{loc}(S_{gas} - S_{trans,3D}) \quad (5.8)$$

The rates of elementary reaction steps are calculated using the law of mass action and the Arrhenius rate equation. Collision theory is used for the estimation of the pre-exponential factors values of forward adsorption steps, while the pre-exponential factors for forward reaction steps involving adsorbed species are estimated *via* transition state theory as described in detail in Afolabi *et al.* [62]. The reverse reaction pre-exponential factors are calculated by the preservation of entropic thermodynamic consistency. The activation barriers for forward surface reactions are calculated using the unity bond index-quadratic exponential potential (UBI-QEP) method [63,64], while the reverse values are calculated through enthalpic thermodynamic consistency. Adsorption reaction steps are considered non-activated, while sticking coefficients for adsorption reactions are taken equal to 1.

5.2.4 Surface reaction network description

The previously developed microkinetic model by Kechagiopoulos *et al.* for steam reforming of methane [13] has served as basis and has been modified in this work in order to describe the dry reforming of methane. A comprehensive set of 86 elementary reaction steps involving 5 molecules and 15 surface species is considered to describe the various possible reaction pathways during the dry reforming of biogas on the Rh catalyst (Table 5.2). The proposed network describes the dissociative adsorption of methane on the catalyst surface (R1-2). Obtained CH_3^* species dehydrogenate up to bare carbon atoms through direct (R17-22) or oxidative pathways, either with O^* (R23-28) or OH^* (R29-34) species. Additionally, H-transfer can take place among CH_x^* species (R35-40). Carbon oxides adsorb molecularly (R13-16) with their further decomposition described in reactions (R57-68). CHO^* and COOH^* species dissociate and interact with other surface species in reactions (R41-56) and (R69-78), respectively. The dissociation of HCOO^* (R79-82) and HCHO^* (R83-86) species has been included in the model in order to improve the dry reforming of methane modelling [49]. Water absorbs molecularly (R3-4) and dissociates to OH^* (R5-6) and O^* (R7-8) species, as well as to H^* . OH^* species can also interact with themselves (R9-10). Hydrogen formed is assumed to desorb associatively (R11-12).

Table 5.2: Microkinetic model for dry reforming of biogas.

No.	Reaction	E_a (kJ/mol)	No.	Reaction	E_a (kJ/mol)
1	$\text{CH}_4 + 2^* \rightarrow \text{CH}_3^* + \text{H}^*$	53.69	44	$\text{CO}^* + \text{H}^* \rightarrow \text{CHO}^* + ^*$	149.62
2	$\text{CH}_3^* + \text{H}^* \rightarrow \text{CH}_4 + 2^*$	46.43	45	$\text{CHO}^* + \text{O}^* \rightarrow \text{CO}_2^* + \text{H}^*$	0.00
3	$\text{H}_2\text{O} + ^* \rightarrow \text{H}_2\text{O}^*$	0.00	46	$\text{CO}_2^* + \text{H}^* \rightarrow \text{CHO}^* + \text{O}^*$	208.81
4	$\text{H}_2\text{O}^* \rightarrow \text{H}_2\text{O} + ^*$	67.22	47	$\text{CHO}^* + \text{O}^* \rightarrow \text{CO}^* + \text{OH}^*$	0.00
5	$\text{H}_2\text{O}^* + ^* \rightarrow \text{OH}^* + \text{H}^*$	88.13	48	$\text{CO}^* + \text{OH}^* \rightarrow \text{CHO}^* + \text{O}^*$	165.26
6	$\text{OH}^* + \text{H}^* \rightarrow \text{H}_2\text{O}^* + ^*$	41.57	49	$\text{CHO}^* + \text{CH}_2^* \rightarrow \text{CO}^* + \text{CH}_3^*$	0.00
7	$\text{OH}^* + ^* \rightarrow \text{H}^* + \text{O}^*$	80.16	50	$\text{CO}^* + \text{CH}_3^* \rightarrow \text{CHO}^* + \text{CH}_2^*$	186.17
8	$\text{H}^* + \text{O}^* \rightarrow \text{OH}^* + ^*$	94.53	51	$\text{CHO}^* + \text{CH}^* \rightarrow \text{CO}^* + \text{CH}_2^*$	0.00
9	$\text{OH}^* + \text{OH}^* \rightarrow \text{H}_2\text{O}^* + \text{O}^*$	0.00	52	$\text{CO}^* + \text{CH}_2^* \rightarrow \text{CHO}^* + \text{CH}^*$	135.89
10	$\text{H}_2\text{O}^* + \text{O}^* \rightarrow \text{OH}^* + \text{OH}^*$	94.49	53	$\text{CO}_2^* + \text{CH}^* \rightarrow \text{CO}^* + \text{CHO}^*$	61.30
11	$\text{H}_2 + 2^* \rightarrow \text{H}^* + \text{H}^*$	28.76	54	$\text{CO}^* + \text{CHO}^* \rightarrow \text{CO}_2^* + \text{CH}^*$	4.87
12	$\text{H}^* + \text{H}^* \rightarrow \text{H}_2 + 2^*$	75.81	55	$\text{CH}_2^* + \text{O}^* \rightarrow \text{CHO}^* + \text{H}^*$	36.47
13	$\text{CO} + ^* \rightarrow \text{CO}^*$	0.00	56	$\text{CHO}^* + \text{H}^* \rightarrow \text{CH}_2^* + \text{O}^*$	52.96
14	$\text{CO}^* \rightarrow \text{CO} + ^*$	123.44	57	$\text{CO}_2^* + ^* \rightarrow \text{CO}^* + \text{O}^*$	75.72
15	$\text{CO}_2 + ^* \rightarrow \text{CO}_2^*$	0.00	58	$\text{CO}^* + \text{O}^* \rightarrow \text{CO}_2^* + ^*$	16.53
16	$\text{CO}_2^* \rightarrow \text{CO}_2 + ^*$	18.72	59	$\text{CO}^* + ^* \rightarrow \text{C}^* + \text{O}^*$	167.07
17	$\text{CH}_3^* + ^* \rightarrow \text{CH}_2^* + \text{H}^*$	91.26	60	$\text{C}^* + \text{O}^* \rightarrow \text{CO}^* + ^*$	79.06

18	$\text{CH}_2^* + \text{H}^* \rightarrow \text{CH}_3^* + ^*$	54.71	61	$\text{CO}_2^* + \text{H}^* \rightarrow \text{CO}^* + \text{OH}^*$	58.74
19	$\text{CH}_2^* + ^* \rightarrow \text{CH}^* + \text{H}^*$	80.93	62	$\text{CO}^* + \text{OH}^* \rightarrow \text{CO}_2^* + \text{H}^*$	15.19
20	$\text{CH}^* + \text{H}^* \rightarrow \text{CH}_2^* + ^*$	91.66	63	$\text{CO}^* + \text{H}^* \rightarrow \text{CH}^* + \text{O}^*$	188.35
21	$\text{CH}^* + ^* \rightarrow \text{C}^* + \text{H}^*$	56.69	64	$\text{CH}^* + \text{O}^* \rightarrow \text{CO}^* + \text{H}^*$	35.97
22	$\text{C}^* + \text{H}^* \rightarrow \text{CH}^* + ^*$	128.07	65	$\text{CO}^* + \text{H}^* \rightarrow \text{C}^* + \text{OH}^*$	209.91
23	$\text{CH}_3^* + \text{O}^* \rightarrow \text{CH}_2^* + \text{OH}^*$	82.20	66	$\text{C}^* + \text{OH}^* \rightarrow \text{CO}^* + \text{H}^*$	137.54
24	$\text{CH}_2^* + \text{OH}^* \rightarrow \text{CH}_3^* + \text{O}^*$	51.29	67	$\text{CO}^* + \text{CO}^* \rightarrow \text{C}^* + \text{CO}_2^*$	28.82
25	$\text{CH}_2^* + \text{O}^* \rightarrow \text{CH}^* + \text{OH}^*$	55.30	68	$\text{C}^* + \text{CO}_2^* \rightarrow \text{CO}^* + \text{CO}^*$	0.00
26	$\text{CH}^* + \text{OH}^* \rightarrow \text{CH}_2^* + \text{O}^*$	84.68	69	$\text{COOH}^* + ^* \rightarrow \text{CO}^* + \text{OH}^*$	27.38
27	$\text{CH}^* + \text{O}^* \rightarrow \text{C}^* + \text{OH}^*$	34.08	70	$\text{CO}^* + \text{OH}^* \rightarrow \text{COOH}^* + ^*$	46.56
28	$\text{C}^* + \text{OH}^* \rightarrow \text{CH}^* + \text{O}^*$	114.09	71	$\text{COOH}^* + ^* \rightarrow \text{CO}_2^* + \text{H}^*$	0.00
29	$\text{CH}_3^* + \text{OH}^* \rightarrow \text{CH}_2^* + \text{H}_2\text{O}^*$	0.00	72	$\text{CO}_2^* + \text{H}^* \rightarrow \text{COOH}^* + ^*$	62.74
30	$\text{CH}_2^* + \text{H}_2\text{O}^* \rightarrow \text{CH}_3^* + \text{OH}^*$	123.59	73	$\text{CO}^* + \text{H}_2\text{O}^* \rightarrow \text{COOH}^* + \text{H}^*$	179.32
31	$\text{CH}_2^* + \text{OH}^* \rightarrow \text{CH}^* + \text{H}_2\text{O}^*$	0.00	74	$\text{COOH}^* + \text{H}^* \rightarrow \text{CO}^* + \text{H}_2\text{O}^*$	0.00
32	$\text{CH}^* + \text{H}_2\text{O}^* \rightarrow \text{CH}_2^* + \text{OH}^*$	173.87	75	$\text{CO}_2^* + \text{OH}^* \rightarrow \text{COOH}^* + \text{O}^*$	98.98
33	$\text{CH}^* + \text{OH}^* \rightarrow \text{C}^* + \text{H}_2\text{O}^*$	0.00	76	$\text{COOH}^* + \text{O}^* \rightarrow \text{CO}_2^* + \text{OH}^*$	20.61
34	$\text{C}^* + \text{H}_2\text{O}^* \rightarrow \text{CH}^* + \text{OH}^*$	224.51	77	$\text{CO}_2^* + \text{H}_2\text{O}^* \rightarrow \text{COOH}^* + \text{OH}^*$	222.87
35	$\text{CH}^* + \text{CH}^* \rightarrow \text{CH}_2^* + \text{C}^*$	99.60	78	$\text{COOH}^* + \text{OH}^* \rightarrow \text{CO}_2^* + \text{H}_2\text{O}^*$	0.00
36	$\text{CH}_2^* + \text{C}^* \rightarrow \text{CH}^* + \text{CH}^*$	150.24	79	$\text{HCOO}^* + ^* \rightarrow \text{CO}_2^* + \text{H}^*$	4.82
37	$\text{CH}_2^* + \text{CH}^* \rightarrow \text{C}^* + \text{CH}_3^*$	23.26	80	$\text{CO}_2^* + \text{H}^* \rightarrow \text{HCOO}^* + ^*$	7.26
38	$\text{C}^* + \text{CH}_3^* \rightarrow \text{CH}_2^* + \text{CH}^*$	124.18	81	$\text{HCOO}^* + ^* \rightarrow \text{CHO}^* + \text{O}^*$	206.37
39	$\text{CH}_2^* + \text{CH}_2^* \rightarrow \text{CH}_3^* + \text{CH}^*$	44.53	82	$\text{CHO}^* + \text{O}^* \rightarrow \text{HCOO}^* + ^*$	0.00
40	$\text{CH}_3^* + \text{CH}^* \rightarrow \text{CH}_2^* + \text{CH}_2^*$	94.81	83	$\text{CH}_2^* + \text{OH}^* \rightarrow \text{HCHO}^* + \text{H}^*$	0.00
41	$\text{CHO}^* + ^* \rightarrow \text{CH}^* + \text{O}^*$	113.54	84	$\text{HCHO}^* + \text{H}^* \rightarrow \text{CH}_2^* + \text{OH}^*$	38.07
42	$\text{CH}^* + \text{O}^* \rightarrow \text{CHO}^* + ^*$	110.78	85	$\text{HCHO}^* + ^* \rightarrow \text{CHO}^* + \text{H}^*$	63.32
43	$\text{CHO}^* + ^* \rightarrow \text{CO}^* + \text{H}^*$	0.00	86	$\text{CHO}^* + \text{H}^* \rightarrow \text{HCHO}^* + ^*$	26.10

5.3 Results and discussion

5.3.1 Catalyst characterization

The 0.5 % Rh/Al₂O₃ catalyst presented values of specific surface area (200 m²/g), pore volume (0.59 cm³/g) and average pore size of (8.1 nm) very similar to those of the calcined Al₂O₃ support. Regarding CO chemisorption analysis, the fresh catalyst presented a metal dispersion of 51.9 % and a metallic surface area of 228.5 m²/g_{metal}. The TPR profile did not reveal any H₂ consumption peak that could be attributed to the reduction of Rh species, probably due to the low Rh loading on the catalyst [31].

5.3.2 Model validation

The microkinetic model developed in this work is fully defined on the basis of two sets of parameters: heats of chemisorption, Q_i , and fractions of local entropy upon adsorption, $F_{loc,i}$. Table 5.5 shows the estimated values for the model parameters.

Parity diagrams for all gaseous species are depicted in Figure 5.1. An overall satisfactory agreement between the model predicted results and experimental results across the entire data range is observed. The good parity plots of the reactants CH_4 and CO_2 indicate that the model has correctly described the main activation and conversion pathways. The effect of temperature, GHSV, CH_4/CO_2 molar ratio and H_2 and CO co-feeding at selected conditions on the biogas conversion and on the syngas yield and selectivity, as well as their comparison with the model predicted results, will be discussed in Section 5.3.3.

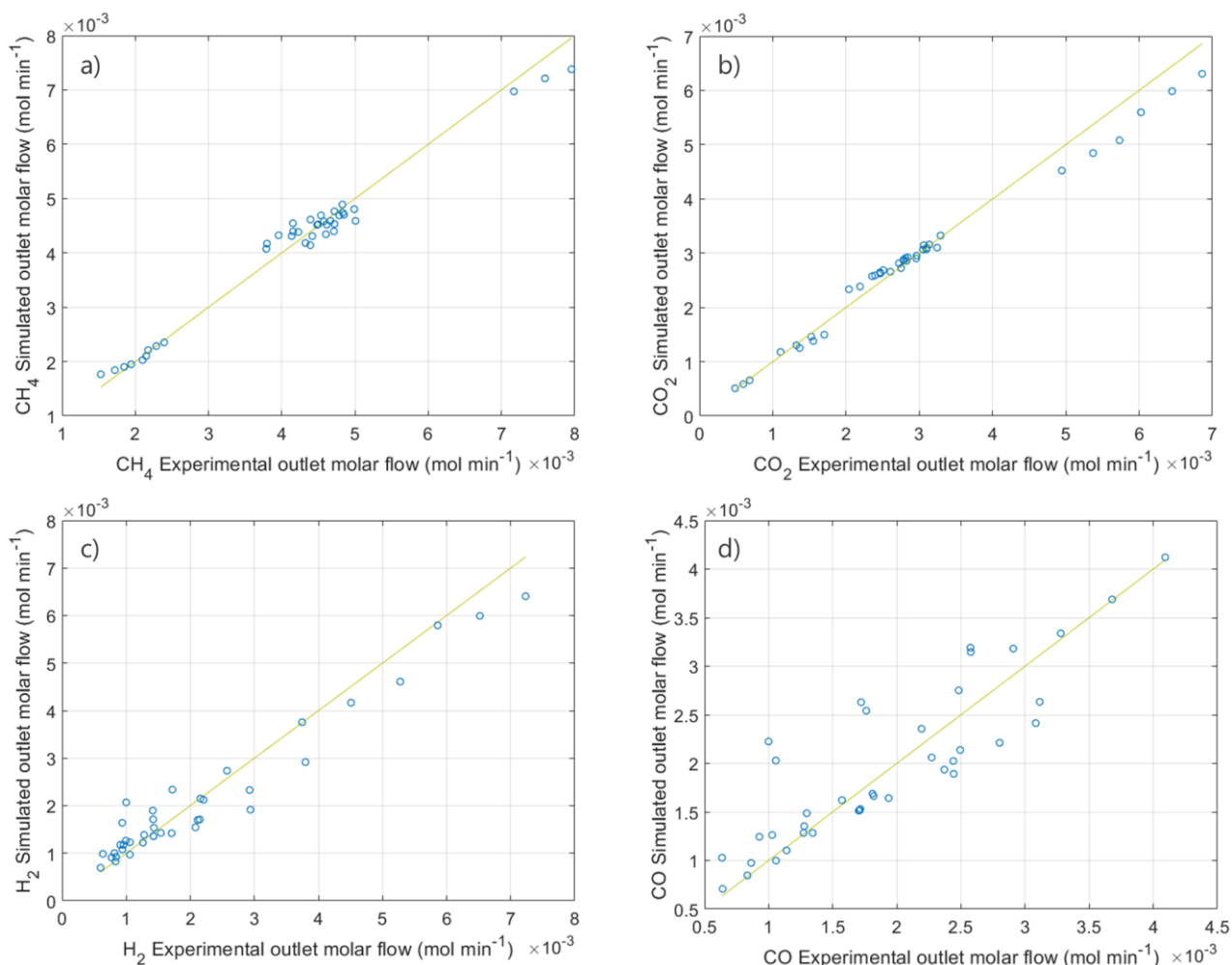


Figure 5-1: Parity diagrams for (a) CH_4 , (b) CO_2 , (c) H_2 and (d) CO . Experimental conditions are reported in Table 5.1, while modelling results have been obtained with parameter values presented in Table 5.5.

5.3.3 Influence of operating parameters

5.3.3.1 Influence of the GHSV

The influence of the GHSV on the dry reforming of biogas was studied at a reaction temperature range between 700 and 750 °C and a CH₄/CO₂ ratio of 1.35 (pristine biogas). Figure 5.2 shows the model and experimental CH₄ and CO₂ conversions and H₂ and CO selectivities at the three GHSV studied. As seen in the figure, the experimental trends are accurately reproduced by the microkinetic model, with only small deviations being observable for CO₂ at the highest GHSV tested.

Increasing GHSV resulted in a decrease in CH₄ and CO₂ conversions and H₂ and CO yields, while H₂ and CO selectivities between 95 and 100 % were obtained in all cases. These results are in agreement with others previously reported in the literature [10,38,43]. Furthermore, these trends were also observed at different reaction temperatures, even though an enhancement of conversions and yields was obtained by increasing the temperature [31,42,57]. At the three GHSV and temperatures studied, the H₂/CO molar ratio obtained was around a value of 0.95. This ratio slightly lower than 1 could be explained by the occurrence of the reverse water-gas shift reaction (rWGS).

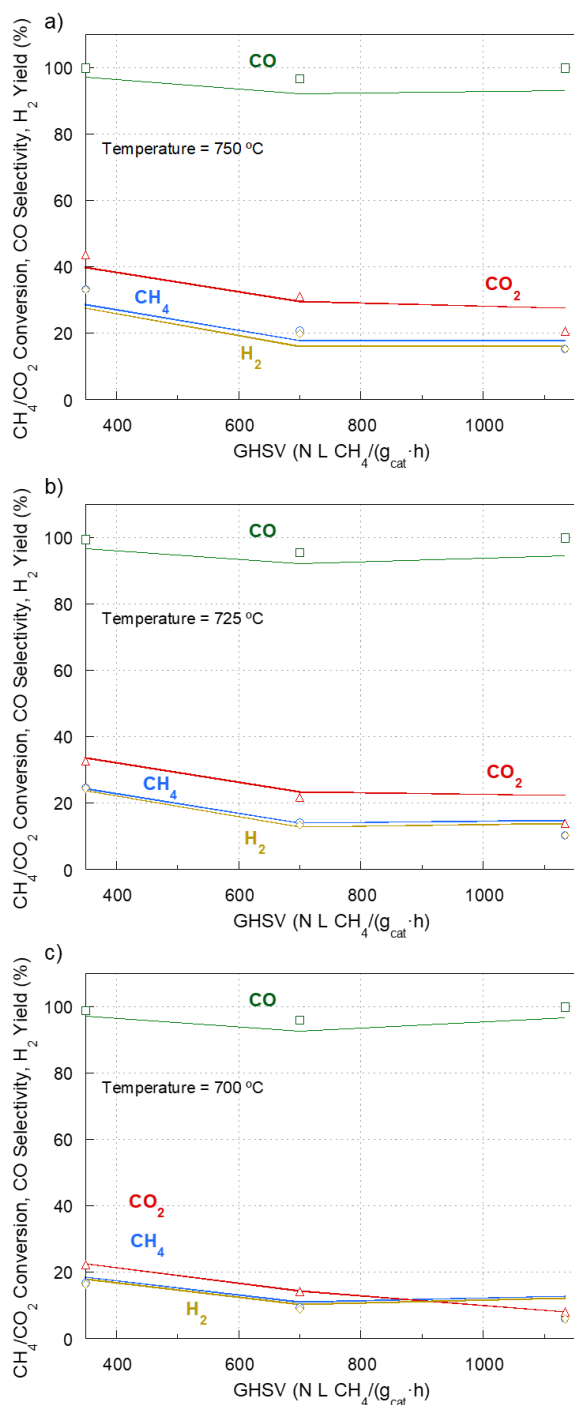


Figure 5-2: Effect of GHSV in the dry reforming of biogas at (a) 750, (b) 725 and (c) 700°C on biogas conversion, hydrogen yield and CO selectivity. Comparison of model CH₄ and CO₂ conversion, H₂ yield and CO selectivity (lines) with experimental results (symbols).

5.3.3.2 Effect of CH₄/CO₂ molar ratio

The effect of feeding biogas with different CH₄/CO₂ molar ratios was studied between 700 and 750 °C and GHSV values of 350 and 700 N L CH₄/(g_{cat}·h). Figure 5.3 presents the comparison of model and experimental results for CH₄ and CO₂ conversion, CO selectivity and H₂ yield at

the three studied temperatures and $350 \text{ N L CH}_4/(\text{g}_{\text{cat}}\cdot\text{h})$. For the sake of clarity, the results at $700 \text{ N L CH}_4/(\text{g}_{\text{cat}}\cdot\text{h})$ have not been depicted since similar tendencies were found in both cases.

Increasing the CH_4/CO_2 molar ratio resulted in an increase in the CO_2 conversion and CO yield, at the expense of a decay in CH_4 conversion, as well as in H_2 yield. This is due to the fact that CO_2 consumption is proportionally increased due to its reduced availability, consequently the CH_4 does not have enough co-reactant to aid its conversion. As for the H_2/CO ratio in the syngas typically had values around 1, though these decreased to 0.8 when the CH_4/CO_2 ratio was diminished to 0.7. Overall, these results are in agreement with most of the previous kinetic studies of dry reforming of methane on Rh based catalysts [42–44]. The decay in H_2 and CO selectivity from 100 % to values around 90 % observed when the CH_4/CO_2 ratio was decreased can be explained by the augmented influence of the rWGS at low CH_4/CO_2 ratios, also in agreement with previous studies [44,57]. Again, the experimental trends across the range of conditions studied are accurately described by the kinetic model, which is indicative of its ability to correctly capture the conversion pathways of both reactants and the contribution of secondary reactions to products selectivities.

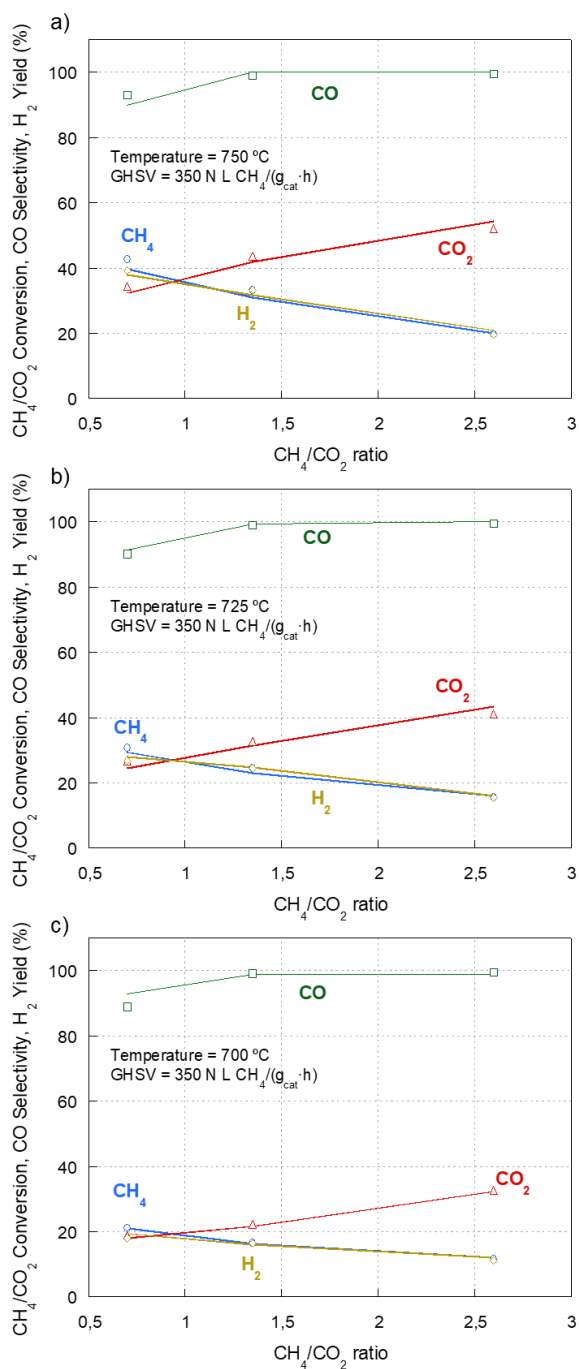


Figure 5-3: Effect of CH_4/CO_2 feed molar ratio in the dry reforming of biogas at (a) 750, (b) 725 and (c) 700°C and 350 N L $\text{CH}_4/\text{g}_{\text{cat}} \cdot \text{h}$. Comparison of model CH_4 and CO_2 conversion, CO selectivity and H_2 yield (lines) with experimental results (symbols).

5.3.3.3 Effect of H_2 co-feeding

The effect of H_2 addition to reaction feed was studied at GHSV of 700 N L $\text{CH}_4/(\text{g}_{\text{cat}} \cdot \text{h})$ and temperatures between 700 and 750 °C. Figure 5.4 shows the experimental and model CH_4 and CO_2 conversions, CO selectivity and H_2 yield for all three studied temperatures.

When the H₂ content in the reaction feed was augmented, there was an increase in CH₄ and CO₂ conversions, H₂ and CO yields and in H₂/CO molar ratio. H₂ (not depicted) and CO selectivity also increased slightly, though the very high selectivity values obtained in pure dry reforming conditions (close to 100 %) are not reached in the studied interval. The results can be explained by the major influence exerted by the rWGS on the selectivity of CO and on the biogas conversion, especially on CO₂ conversion. Adding H₂ in the feed results in the production of CO and H₂O by rWGS, leading to an increased CO₂ conversion. Furthermore, the H₂O generated is consumed *via* the steam reforming of methane (SRM), thus leading also to an increase in CH₄ conversion and, in turn, increasing the yield to syngas. The microkinetic model reproduces accurately these trends further suggesting that surface pathways are correctly described by the proposed mechanism.

The results are in agreement with the observations by Deutschmann's group in their microkinetic study validated with experimental results obtained using a commercial Ni-based catalyst [50], by Múnera *et al.* in their macrokinetic study using a Rh/La₂O₃ catalyst [45], and by Prof. Verykios, in his mechanistic study in which experiments were conducted using a Ni/La₂O₃ catalyst [38]. In contrast, Forzatti's group [44], in their microkinetic study on a 4 % Rh/Al₂O₃ catalyst, did not observe an effect of H₂ addition on CH₄ and CO₂ conversion or on products distribution, though the very distinct conditions compared to those in the present study could explain the differences. It could be possible that the low Rh loading in the present work (0.5 % Rh), which resulted in a relatively high metallic dispersion (~52 %) and metallic surface area (282.5 m²/g_{metal}), and the much higher concentrations of reactants in the reactor feed stream (in comparison to the diluted mixtures in the work by Donatti *et al.* [44]), could result in competitive adsorption of CH₄ and H₂ for Rh active sites, which could have an influence on the relative impact of the rWGS in the overall reaction scheme. Wei and Iglesia proposed that low metal dispersions in Rh/Al₂O₃ catalysts result in low CH₄ turnover rates [35], which might be the reason why Forzatti and co-workers did not observe a significant effect of co-feeding H₂ in their methane dry reforming tests.

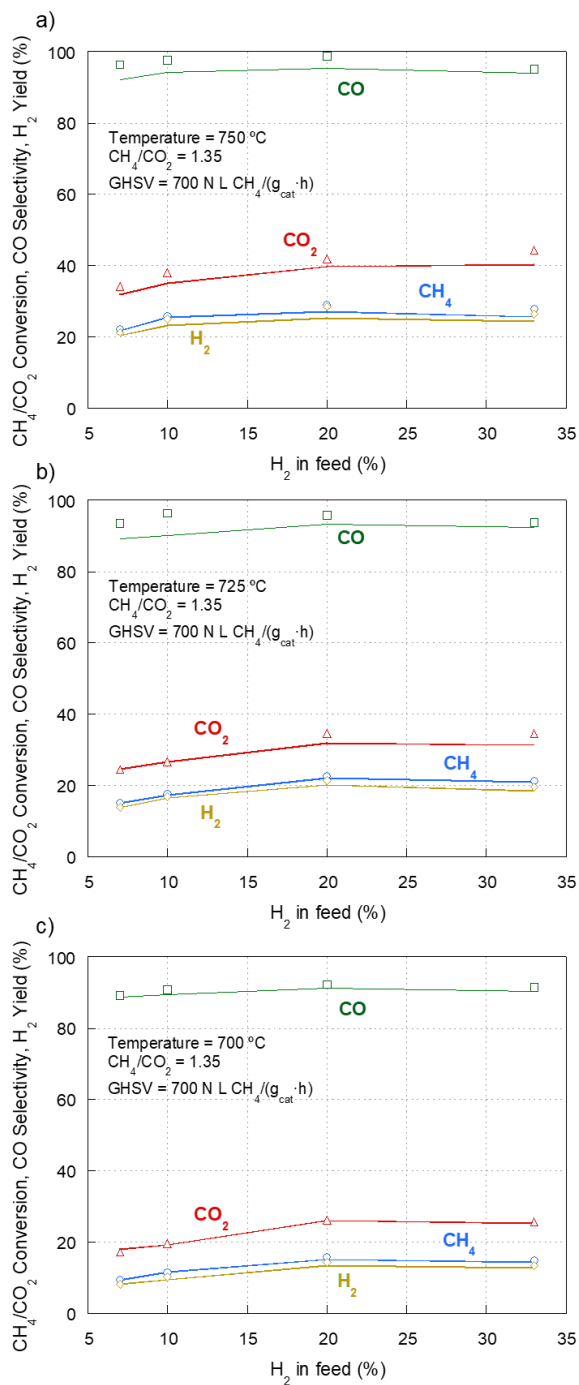


Figure 5-4: Effect of H₂ content in the feed in the dry reforming of biogas at (a) 750, (b) 725 and (c) 700°C, at 700 N L CH₄/gcat·h. Comparison of model CH₄ and CO₂ conversion, CO selectivity and H₂ yield (lines) with experimental results (symbols).

5.3.3.4 Effect of CO co-feeding

The CO co-feeding effect on biogas conversion and syngas selectivity was studied at GHSV of 700 N L CH₄/(g_{cat}·h) and temperatures between 700 and 750 °C. Figure 5.5 presents the experimental and model CH₄ and CO₂ conversions, CO yield and H₂ selectivity for all three temperatures studied.

Nearly doubling the CO content in the feeding stream (from 9 to 19 %) resulted in a decay in CO₂ conversion as well as decreased H₂ and CO yields, whereas CH₄ conversion presented a very slight decrease. Furthermore, adding CO resulted in a decay in CO selectivity from around 100 % (no CO co-fed) to values between 90 and 80 %. In contrast, increasing the CO content in the feed did increase H₂ selectivity. This, together with the decay in CO₂ conversion could be a consequence of hindering the rWGS. As for CH₄ conversion, adding CO to the feed did not have any significant effect, which is in agreement with previous studies [35,48].

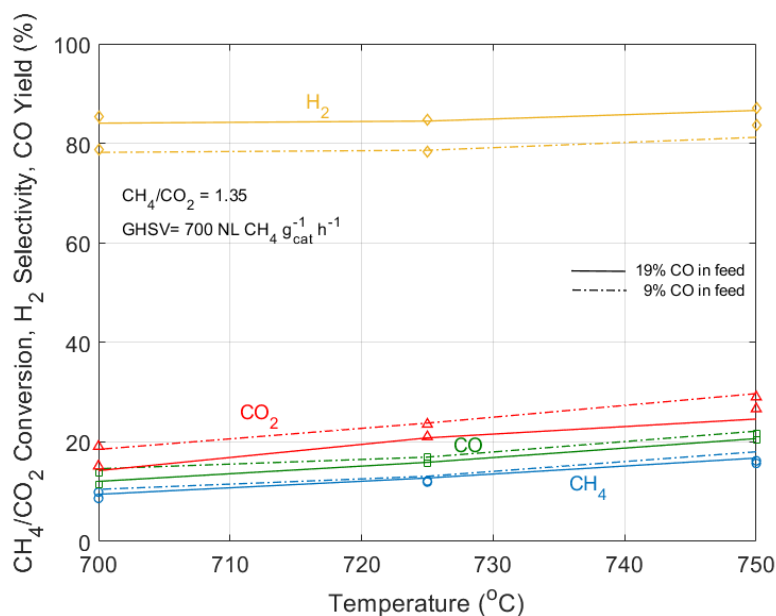


Figure 5-5: Effect of the CO content in the feed over reaction temperature in the dry reforming of biogas at 700 N L CH₄/gcat·h. Comparison of model CH₄ and CO₂ conversion, H₂ selectivity and CO yield (lines) with experimental results (symbols).

5.3.4 Model evaluation

5.3.4.1 Kinetic relevance of reaction steps

In order to determine the kinetic relevance of elementary steps, the pre-exponential factors of each individual surface reaction pair, calculated by transition state theory, were varied by a small fraction of their base value. The effect of the variation on the conversion of the reactants was quantified by calculating normalised sensitivity coefficients. Figure 5.6 shows the sensitivity analysis results for both CH₄ and CO₂ conversion. For CH₄, the sensitivity analysis recognizes the dehydrogenation of CH₃* (R17) as the most important reaction step with all others not exhibiting significant kinetic relevance at the conditions modelled. Similar observations were reported in previous studies, e.g. of the microkinetic model by Maestri *et al.* [49] for methane conversion to syngas over Rh/Al₂O₃, and the density functional theory (DFT) analysis of dry

reforming of methane (DRM) over Ni performed by Wang *et al.* [65]. For CO₂, three main paths of activation are considered in the model, namely its direct decomposition to CO (R57), and two H-mediated pathways leading to the formation of COOH* (R72) and HCOO* (R80). The sensitivity analysis clearly identifies the former of the three (R57) as the most kinetically important; however, interestingly, CH₃* dehydrogenation is revealed as the overall most sensitive step even in the case of CO₂ conversion. This finding is explained considering that the dissociation of CO₂ produces CO* and O* and OH* species. Whilst CO* can proceed to desorb, forming gas phase CO, the O* and OH* with strong adsorption enthalpies of 453.68 and 252.10 kJ/mol, respectively, accrue on the surface and negatively affect the equilibrium of the dissociation reactions. The reforming pathway involving the products of the CH₄ dehydrogenation provides a route for the consumption of surface O* and OH*. Similarly, the H* species required for the H-mediated CO₂ dissociation are obtained solely from the CH₄ dehydrogenation pathway.

H₂ co-feeding had little impact on the sensitivity analysis results, with the CH₃* dehydrogenation still being identified as the most kinetically important step. Nonetheless, the H-mediated CO₂ decomposition reaction steps showed a slightly increased relevance, in line with the discussion in Section 5.3.3.3 on the promotion of the rWGS. The enhanced COOH* and HCOO* formation and their subsequent dissociation in turn leads to increased availability of O* and OH* species which react with CH₄ derived species to enhance the production of CO in agreement with the experimentally observed increased conversion of CH₄ and CO₂ during H₂ co-feeding. These observations are further elaborated in the next section.

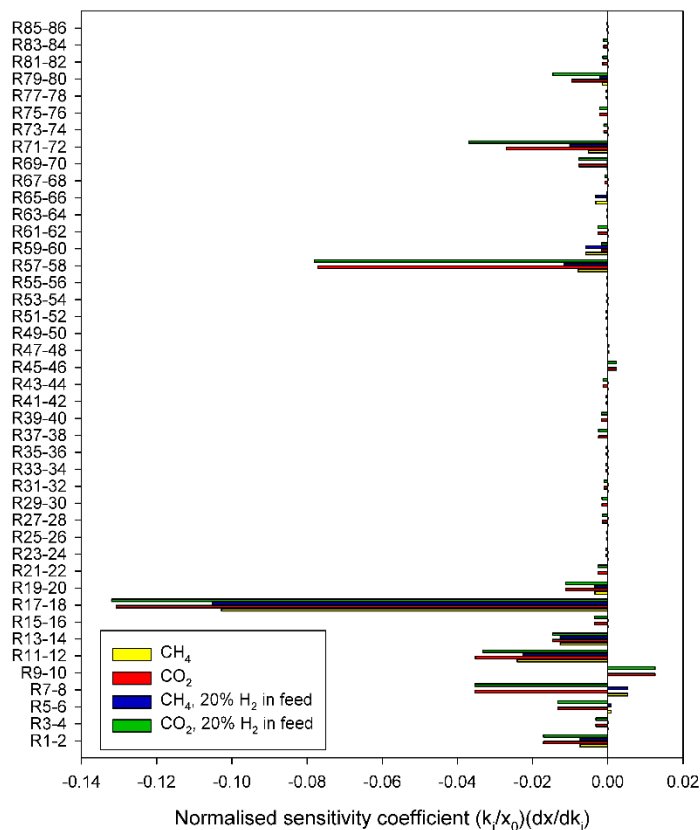


Figure 5-6: Sensitivity analysis of pre-exponential factors of the microkinetic model reactions shown in Table 5.2, for both pure DRM and 20% H₂ co-feeding DRM. Base values of pre-exponential factors are calculated using transition state theory as described previously [62]. Conditions: 750°C, CH₄/CO₂ = 1.35, GHSV = 700 NL CH₄/gcat·h.

5.3.4.2 Reaction pathway analysis

In order to elucidate the importance and kinetic relevance of reaction pathways, a differential contribution analysis at the outlet of the catalyst bed was conducted. The net formation rates of all carbon containing species are utilised in estimating their conversion percentages to other compounds. Results of the analysis are presented in Figure 5.7 and are discussed below.

According to the model predictions, CH₄ adsorbs dissociatively on the surface of the catalyst (R1), forming CH₃* surface species that further dehydrogenate towards CH₂* (R17). The latter reaction, as discussed in the previous section, was identified as the most kinetically relevant at these conditions. The dominant route proceeds *via* the dehydrogenation of CH₂* to form CH* surface species (R19) with a high contribution of 90.6%, followed by the exclusive dehydrogenation of CH* towards C* (R21). Similar findings were reported by Fan *et al.* [54], who presented a comprehensive microkinetic and DFT study of methane dry reforming over a Ni catalyst wherein the dominant pathway involved the exclusive dehydrogenation of CH₄ up to

the bare carbon atom. CO₂ following molecular adsorption on the catalyst surface (R15), decomposes directly to form CO* and O* (R57) with a high contribution percentage of 99.5%. The surface C* species react with formed O* to exclusively form CO* (R60), which desorbs molecularly (R14).

The other carbon containing species considered in the model are not involved in the primary conversion pathway but still influence the selectivity distribution. The formed CH₂* surface species also react with O* to form CHO* (R55) at a lesser contribution. CHO* dissociates primarily to CO* and H* (98%) *via* R43 and at a much smaller percentage to CH* and O* *via* R41. Adsorbed CO₂ also reacts with H* to form COOH* (R72) that exclusively converts to CO* (R69).

The main pathway discussed above is not altered by the co-feeding of H₂. Nonetheless, a change in the respective contributions of the CO₂ decomposition pathways is observed, with all H-mediated routes having a slightly increased relevance as also indicated in Figure 5.7.

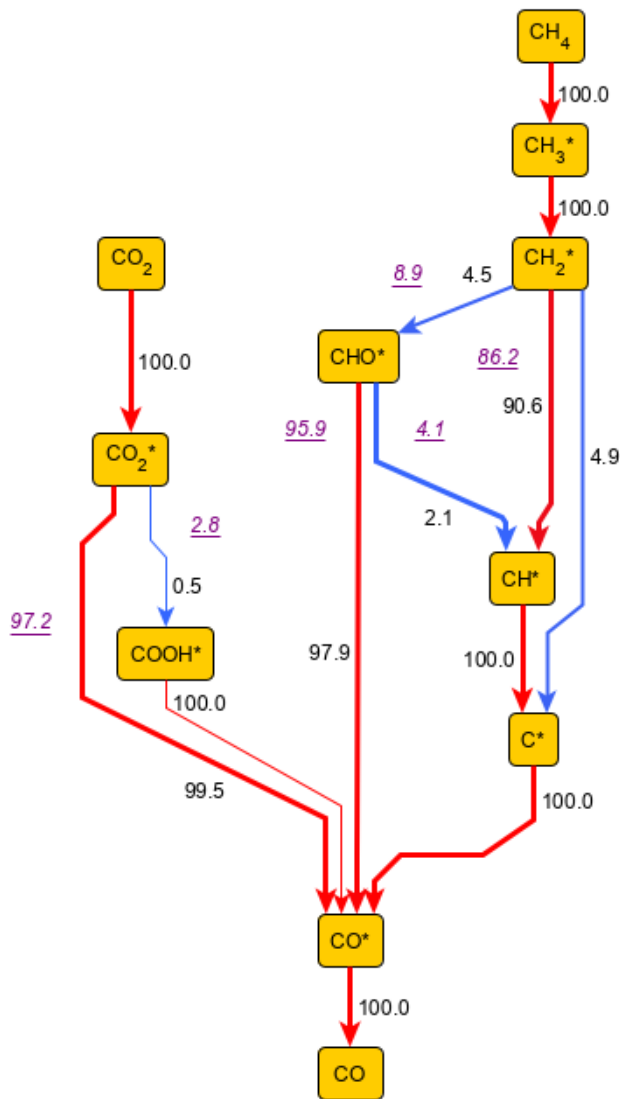


Figure 5-7: Contribution analysis at the end of the catalyst bed for pure DRM (regular black fonts) and for 20 % H_2 co-feeding DRM (underlined purple italics). Net production rates are considered in calculating contribution percentages of carbon containing species towards other species. Colour mapping from blue to red on lines indicates increasing contribution percentages. Line thickness indicates relative magnitude of the reaction rates. Conditions: 750°C , $\text{CH}_4/\text{CO}_2 = 1.35$, $\text{GHSV} = 700 \text{ NL CH}_4/\text{gcat}\cdot\text{h}$.

5.3.4.3 *Effect of products co-feeding*

The effect of H_2 co-feeding on surface coverage is analysed to further elaborate its intrinsic impact on the reaction mechanism. Changes in the partial coverages of H^* and CO^* at the start, middle and end of the catalyst bed, as the amount of H_2 in the feed stream is altered, are displayed in Table 5.3.

The model results reveal that the H₂ fed to the reactor adsorbs onto the catalyst surface and indeed further participates in surface reactions. As the H₂ concentration in the feed increases, the partial coverage of the H* species at the start of the catalyst bed is found to rise drastically. H* partial coverage values higher than 10% at the largest H₂ inlet fraction tested are reached, which are almost two orders of magnitude higher to the case of pure DRM. In all cases, across the catalyst bed, as also evidenced by the respective partial coverage decline, H* is consumed in surface reactions and associatively desorbs as molecular H₂. Concurrently, the addition of H₂ in the feed stream is also seen to cause a rise in the partial coverage of CO*. Under pure DRM conditions, the latter is found to rise gradually along the catalyst bed reaching maximum values of about 10%, while under co-feeding conditions it is seen to approximate values as high as 40% at the largest H₂ inlet fraction evaluated.

The increased availability of H* on the surface enhances the H-mediated CO₂ decomposition reactions, leading to higher CO* production, an effect equivalent to promoting rWGS activity, as discussed in Section 5.3.3.3. These decomposition pathways, involving COOH* and HCOO*, also enhance the production of O* and OH* species that further react with C* species originating from the dehydrogenation of CH₄. These model trends agree well with the experimentally observed increase in the conversion of both CH₄ and CO₂ reactants with H₂ co-feeding. Experimentally, the reactants conversion continues to rise with increasing H₂ co-feeding, until it reaches a maximum at about 20% of H₂ content in the feed. After this point, it is seen to plateau or slightly decrease, depending on temperature, with the drop in CH₄ conversion being more evident than that in CO₂. The modelling results attribute these experimental observations to the effect that H₂ co-feeding has on the coverage of CO*. At low H₂ inlet concentrations, the increase in CO* coverage is not high, hence the promoting effects on rWGS and SRM discussed above are obtained. At the highest H₂ inlet concentration tested of 33%, though, the coverage of CO* is high enough to negatively affect these pathways due to surface saturation. The H-mediated consumption of CH₄ is a secondary pathway in comparison to the H-mediated CO₂ consumption under H₂ co-feed conditions (for CH_x* species to react with O* or OH* formed by CO₂* decomposition, CO₂* react with H* has to precede). As a result, these secondary pathways are the first to be affected by any saturation effects, explaining further why experimentally CH₄ conversion is seen to be impacted more than that of CO₂.

Table 5.3: Partial surface coverages for H* and CO* at different locations of the catalyst bed. Conditions: 750°C, CH₄/CO₂ = 1.35, GHSV = 700 NL CH₄/gcat·h.

Location in catalyst bed	% H ₂ in feed	H* partial coverage	CO* partial coverage
Start of bed		3.70×10 ⁻³	3.27×10 ⁻³
Middle of bed	0	2.24×10 ⁻³	9.24×10 ⁻²
End of bed		1.17×10 ⁻³	0.1424
Start of bed		2.29×10 ⁻²	4.06×10 ⁻³
Middle of bed	10	6.91×10 ⁻³	0.1448
End of bed		4.54×10 ⁻³	0.2179
Start of bed		9.64×10 ⁻²	7.12×10 ⁻³
Middle of bed	20	4.64×10 ⁻²	0.2164
End of bed		8.97×10 ⁻³	0.3014
Start of bed		0.1106	1.25×10 ⁻²
Middle of bed	33	9.37×10 ⁻²	0.2626
End of bed		6.77×10 ⁻²	0.3806

In the case of CO co-feeding the experimental results show that there is an immediate negative impact on the conversion of CO₂ at all CO inlet concentrations studied, with the impact on CH₄ conversion being much milder. The changes in the partial surface coverage of CO* and H* with the varying CO co-feeding rates are displayed in Table 5.4. The partial coverage of CO* at the start of the bed shows a sharp increase of almost two orders of magnitude when the content of CO in the feed is increased from 0 to 9 %. The increased CO* coverage negatively affects the rWGS equilibrium, reducing the decomposition rate of CO₂ leading to the decay in CO₂ conversion. A slight decrease in CH₄ conversion noticeable can be attributed to the saturation effect of the surface CO* reducing the availability of sites for CH₄ dehydrogenation.

When the CO in feed is further increased to 19 %, a larger decay in CO₂ conversion coinciding with a larger partial coverage of CO* at all points on the bed was observed. This would lead to a larger negative effect on the rWGS thereby reducing the consumption of H₂. This explains the experimentally observed lower conversion of CO₂, higher selectivity for H₂ and the reduced yield of CO.

Table 5.4: Partial surface coverages for H* and CO* at different locations of the catalyst bed. Conditions: 750°C, CH₄/CO₂ = 1.35, GHSV = 700 NL CH₄/gcat·h.

Location in catalyst bed	% CO in feed	H* partial coverage	CO* partial coverage
Start of bed		3.70×10 ⁻³	3.27×10 ⁻³
Middle of bed	0	2.24×10 ⁻³	9.24×10 ⁻²
End of bed		1.17×10 ⁻³	0.1424
Start of bed		2.18×10 ⁻³	0.1068
Middle of bed	9	1.62×10 ⁻³	0.2581
End of bed		1.17×10 ⁻³	0.4136
Start of bed		1.67×10 ⁻³	0.2124
Middle of bed	19	9.42×10 ⁻⁴	0.3614
End of bed		7.17×10 ⁻⁴	0.4762

5.3.4.4 *Model parameters sensitivity*

A sensitivity analysis was also performed to identify the significance of the parameters of the microkinetic model, namely of the adsorption enthalpies. The normalised sensitivity coefficients calculated for the outlet molar fractions of the reactants when the model parameters are perturbed by 1 % of their base value (Table 5.5) are presented in Figure 5.8. From the analysis, it can be concluded that the adsorption enthalpy of CH₂ is the most sensitive model parameter, having a positive impact on the conversion of both reactants. This is in line with the earlier identified kinetically relevant step R17 producing CH₂*, and with UBI-QEP, which predicts an activation energy decrease for reactions whose products' adsorption enthalpies increase. In this regard, the increase in CH₂ adsorption enthalpy and the reduction of the barrier of step R17 enhances the conversion of the reactants. The adsorption enthalpy of CH₃ is also seen to have a positive effect on the conversion of both reactants, in this case due to the increase in the CH₃* surface coverage, which in turn enhances the rate of reactions the latter participates in as a reactant. Similar effects, but to a lesser extent, are observed for the chemisorption enthalpies of CH and C, with their increased adsorption enthalpy providing an overall enhancement of the dominant pathway.

The adsorption enthalpy of CO is identified to have a most significant negative influence on the conversion of reactants, particularly of CO₂, with the stronger binding of CO found to lead to the progressive saturation of the catalyst surface. This effect is analogous to the previously discussed

influence of CO co-feeding. Its increased impact on CO₂ versus CH₄ conversion is further in line with the experimental trends discussed in Section 5.3.3.4.

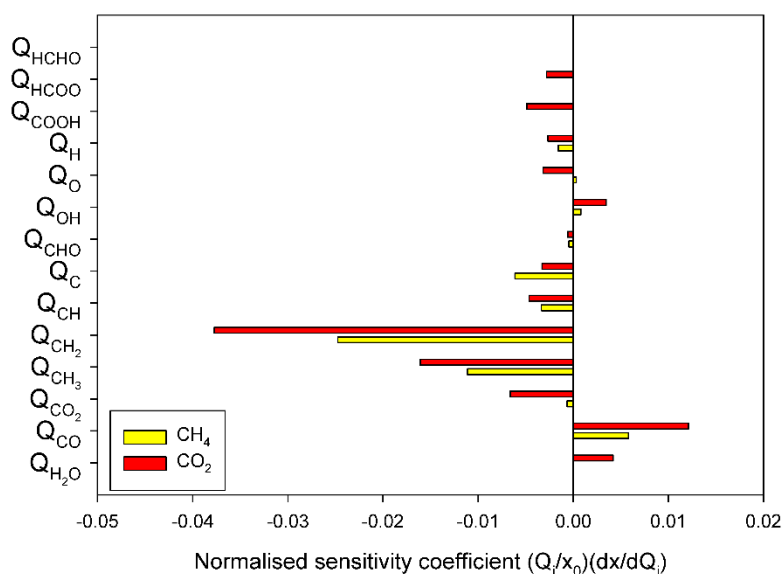


Figure 5-8: Model parameters sensitivity analysis for reactants outlet fractions. Base values for the parameters are shown in Table 5.5. Operating conditions: 750°C, CH₄/CO₂ = 1.35, GHSV = 700 NL CH₄/gcat·h.

5.3.4.5 Estimated model parameters evaluation

Table 5.5 shows the final estimated values for the parameters of the microkinetic model presented in Table 5.2 along with their 95 % confidence intervals. The initial values of the adsorption enthalpies of most of the species were obtained from the previous work on CH₄ steam reforming [13]. The values for HCOO and HCHO were obtained from DFT studies [55]. Based on the results of the sensitivity analysis the parameters that showed little or no sensitivity were fixed at literature values. The squared multiple correlation coefficient value obtained for the regression was close to unity ($R^2 = 0.964$), which coupled with the high F-value (346.08) for the global significance of regression (tabulated value = 3.01), confirms the model's good statistical performance.

The values of all model parameters used, including the chemisorption enthalpies and F_{loc} fitting factors, all conform to physically realistic values, providing confidence that the respective activation energies and overall rates of surface pathways are realistically represented. To further support the quality of the model predictions, the developed model was also used to simulate the CH₄ steam reforming over Rh catalyst experimental data from a previous study [13]. Only with minor changes to model parameter values, a good description of that data set was achieved. The

resulting parity diagram, found in the supplementary information, shows a satisfactory agreement between the model results and experimental data and further highlights the commonality of the reaction mechanism under steam and dry reforming conditions. The results of the present work further underline the ability of the model to be used for predicting the behaviour of this reaction under a variety of conditions that may occur during transient, recycle or feed variable operation.

Table 5.5: Estimated model parameters.

Species	Q (kJ/mol)	$F_{loc}(-)$
CH ₄	-	-
H ₂ O	61.10 [66]	1.0
H ₂	-	-
CO	122.94 ± 1.31	0.984 ± 0.008
CO ₂	22.68 ± 0.42	0.926 ± 0.014
CH ₃	205.30 ± 2.61	0.891 ± 0.086
CH ₂	387.44 ± 4.27	1.0
CH	558.07 [67–69]	1.0
C	759.07 ± 0.91	1.0
CHO	204.49 [67,69]	1.0
OH	252.10 [67]	1.0
O	453.68 [67]	1.0
H	251.25 [67]	1.0
COOH	253.57 [55]	0.926
HCOO	282.05 [55]	1.0
HCHO	92.21	1.0

5.4 Conclusions

A microkinetic model was developed for biogas dry reforming over a 0.5 wt. % Rh/Al₂O₃ catalyst in this work. The influence of operating parameters on biogas conversion and on selectivity to syngas was studied and evaluated with the microkinetic model developed, especially the effect of co-feeding H₂ or CO together with the biogas. In the reaction pathway predicted, CH₄ adsorbs dissociatively and further dehydrogenates. The dehydrogenation of CH₃* was identified as the most sensitive reaction step for both CH₄ and CO₂ conversion, as could be inferred from the positive impact on CH₂* and CH₃* adsorption enthalpies. Furthermore, CO₂ activation could follow three different paths, direct decomposition to CO and two H-mediated CO₂ decomposition reactions, the former being the main activation step, though the respective contribution of each one changes slightly when H₂ is co-fed.

Under H₂ co-feeding conditions, H₂ was adsorbed and consumed on several surface reactions, as was observed by the increase on the partial surface coverage of the H* species at the start of the catalyst bed, which later decreases as it progresses through the bed. Besides, H₂ addition enhances H-mediated CO₂ decomposition paths, thus causing a rise in the partial coverage of CO*, though it could lead to surface saturation at high H₂ inlet concentrations. All these effects were experimentally observed as an increase on biogas conversion and syngas yield and, therefore, as a promoting effect of rWGS and SRM reactions.

Experimental results showed a detrimental effect of increasing the CO content in the feed on CO₂ conversion, H₂ and CO yields. This effect was attributed to an increase on the partial coverage of CO* species at the start and throughout the catalyst bed, which negatively affects the rWGS equilibrium and saturates the catalyst surface.

The microkinetic model developed explained and satisfactorily predicted experimental results under a wide range of conditions, as reaction temperature, GHSV and gas feeding composition. In addition, the model could also be further validated using data on methane steam reforming over the Rh catalyst obtaining a good agreement with experimental results previously obtained [13]. Therefore, the validity of the microkinetic model developed in this work has been proven, which could have interesting applications in the design and modelling of biogas dry reforming reactors under different operation conditions, including recycle or variable feed compositions.

References

- [1] World Bioenergy Association, Steering committee, *Cold Reg. Sci. Technol.* 2 (1980) vii–xiv. [https://doi.org/10.1016/0165-232x\(80\)90063-4](https://doi.org/10.1016/0165-232x(80)90063-4).
- [2] A. Abdulrasheed, A.A. Jalil, Y. Gambo, M. Ibrahim, H.U. Hambali, M.Y. Shahul Hamid, A review on catalyst development for dry reforming of methane to syngas: Recent advances, *Renew. Sustain. Energy Rev.* 108 (2019) 175–193. <https://doi.org/10.1016/j.rser.2019.03.054>.
- [3] W.J. Jang, J.O. Shim, H.M. Kim, S.Y. Yoo, H.S. Roh, A review on dry reforming of methane in aspect of catalytic properties, *Catal. Today.* 324 (2019) 15–26. <https://doi.org/10.1016/j.cattod.2018.07.032>.
- [4] R. Singh, A. Dhir, S.K. Mohapatra, S.K. Mahla, Dry reforming of methane using various catalysts in the process: review, *Biomass Convers. Biorefinery.* (2019). <https://doi.org/10.1007/s13399-019-00417-1>.
- [5] Y. Wang, L. Yao, S. Wang, D. Mao, C. Hu, Low-temperature catalytic CO₂ dry reforming of methane on Ni-based catalysts: A review, *Fuel Process. Technol.* 169 (2018) 199–206. <https://doi.org/10.1016/j.fuproc.2017.10.007>.
- [6] N.A.K. Aramouni, J.G. Touma, B.A. Tarboush, J. Zeaiter, M.N. Ahmad, Catalyst design for dry reforming of methane: Analysis review, *Renew. Sustain. Energy Rev.* 82 (2018) 2570–2585. <https://doi.org/10.1016/j.rser.2017.09.076>.
- [7] Y. Gao, J. Jiang, Y. Meng, F. Yan, A. Aihemaiti, A review of recent developments in hydrogen production via biogas dry reforming, *Energy Convers. Manag.* 171 (2018) 133–155. <https://doi.org/10.1016/j.enconman.2018.05.083>.
- [8] A. Navarro-Puyuelo, I. Reyeró, A. Moral, F. Bimbela, L.M. Gandía, Rutas y retos para la valorización de biogás, *Av. Investig. En Ing.* 14 (2017) 211–224.
- [9] W.M. Budzianowski, A review of potential innovations for production, conditioning and utilization of biogas with multiple-criteria assessment, *Renew. Sustain. Energy Rev.* 54 (2016) 1148–1171. <https://doi.org/10.1016/j.rser.2015.10.054>.
- [10] A. Moral, I. Reyeró, C. Alfaro, F. Bimbela, L.M. Gandía, Syngas production by means of biogas catalytic partial oxidation and dry reforming using Rh-based catalysts, *Catal. Today.* 299 (2018) 280–288. <https://doi.org/10.1016/j.cattod.2017.03.049>.
- [11] W.-H. Chen, S.-C. Lin, Biogas partial oxidation in a heat recirculation reactor for syngas production and CO₂ utilization, *Appl. Energy.* 217 (2018) 113–125. <https://doi.org/10.1016/j.apenergy.2018.02.123>.
- [12] K.-H. Lin, H.-F. Chang, A.C.-C. Chang, Biogas reforming for hydrogen production over mesoporous Ni₂xCe_{1-x}O₂ catalysts, *Int. J. Hydrogen Energy.* 37 (2012) 15696–15703. <https://doi.org/10.1016/j.ijhydene.2012.03.130>.
- [13] P.N. Kechagiopoulos, S.D. Angeli, A.A. Lemonidou, Low temperature steam reforming of methane: A combined isotopic and microkinetic study, *Appl. Catal. B Environ.* 205 (2017) 238–253. <https://doi.org/10.1016/j.apcatb.2016.12.033>.
- [14] P.S. Roy, C.S. Park, A.S.K. Raju, K. Kim, Steam-biogas reforming over a metal-foam-coated (Pd – Rh)/(CeZrO₂ – Al₂O₃) catalyst compared with pellet type alumina-

- supported Ru and Ni catalysts, *Biochem. Pharmacol.* 12 (2015) 12–20. <https://doi.org/10.1016/j.jcou.2015.09.003>.
- [15] P. Durán, A. Sanz-Martínez, J. Soler, M. Menéndez, J. Herguido, Pure hydrogen from biogas: Intensified methane dry reforming in a two-zone fluidized bed reactor using permselective membranes, *Chem. Eng. J.* 370 (2019) 772–781. <https://doi.org/10.1016/j.cej.2019.03.199>.
- [16] U. Izquierdo, V.L. Barrio, K. Bizkarra, a. M. Gutierrez, J.R. Arraibi, L. Gartzia, J. Bañuelos, I. Lopez-Arbeloa, J.F. Cambra, Ni and RhNi catalysts supported on Zeolites L for hydrogen and syngas production by biogas reforming processes, *Chem. Eng. J.* 238 (2014) 178–188. <https://doi.org/10.1016/j.cej.2013.08.093>.
- [17] Y. Kathiraser, U. Oemar, E.T. Saw, Z. Li, S. Kawi, Kinetic and mechanistic aspects for CO₂ reforming of methane over Ni based catalysts, *Chem. Eng. J.* 278 (2015) 62–78. <https://doi.org/10.1016/j.cej.2014.11.143>.
- [18] S. Araki, N. Hino, T. Mori, S. Hikazudani, Autothermal reforming of biogas over a monolithic catalyst, *J. Nat. Gas Chem.* 19 (2010) 477–481. [https://doi.org/10.1016/S1003-9953\(09\)60102-X](https://doi.org/10.1016/S1003-9953(09)60102-X).
- [19] M. Luneau, E. Gianotti, F.C. Meunier, C. Mirodatos, E. Puzenat, Y. Schuurman, N. Guilhaume, Deactivation mechanism of Ni supported on Mg-Al spinel during autothermal reforming of model biogas, *Appl. Catal. B Environ.* 203 (2016) 289–299. <https://doi.org/10.1016/j.apcatb.2016.10.023>.
- [20] Q. Ha, U. Armbruster, H. Atia, M. Schneider, H. Lund, G. Agostini, J. Radnik, H. Vuong, A. Martin, Development of Active and Stable Low Nickel Content Catalysts for Dry Reforming of Methane, *Catalysts.* 7 (2017) 157. <https://doi.org/10.3390/catal7050157>.
- [21] Y. Kathiraser, Z. Wang, M.L. Ang, L. Mo, Z. Li, U. Oemar, S. Kawi, Highly active and coke resistant Ni/SiO₂ catalysts for oxidative reforming of model biogas: Effect of low ceria loading, *J. CO₂ Util.* 19 (2017) 284–295. <https://doi.org/10.1016/j.jcou.2017.03.018>.
- [22] N.D. Charisiou, G. Siakavelas, K.N. Papageridis, A. Baklavaridis, L. Tzounis, D.G. Avraam, M.A. Goula, Syngas production via the biogas dry reforming reaction over nickel supported on modified with CeO₂ and/or La₂O₃ alumina catalysts, *J. Nat. Gas Sci. Eng.* 31 (2016) 164–183. <https://doi.org/10.1016/j.jngse.2016.02.021>.
- [23] R. Balzarotti, C. Italiano, L. Pino, C. Cristiani, A. Vita, Ni/CeO₂-thin ceramic layer depositions on ceramic monoliths for syngas production by Oxy Steam Reforming of biogas, *Fuel Process. Technol.* 149 (2016) 40–48. <https://doi.org/10.1016/j.fuproc.2016.04.002>.
- [24] M.A. Goula, N.D. Charisiou, K.N. Papageridis, A. Delimitis, E. Pachatouridou, E.F. Iliopoulou, Nickel on alumina catalysts for the production of hydrogen rich mixtures via the biogas dry reforming reaction: Influence of the synthesis method, *Int. J. Hydrogen Energy.* 40 (2015) 9183–9200. <https://doi.org/10.1016/j.ijhydene.2015.05.129>.
- [25] N. Habibi, Y. Wang, H. Arandiyani, M. Rezaei, Effect of substitution by Ni in MgAl₂O₄ spinel for biogas dry reforming, *Int. J. Hydrogen Energy.* 42 (2017) 24159–24168. <https://doi.org/10.1016/j.ijhydene.2017.07.222>.

- [26] M. Zhang, J. Zhang, Z. Zhou, S. Chen, T. Zhang, F. Song, Q. Zhang, N. Tsubaki, Y. Tan, Y. Han, Effects of the surface adsorbed oxygen species tuned by rare-earth metal doping on dry reforming of methane over Ni/ZrO₂ catalyst, *Appl. Catal. B Environ.* 264 (2020) 118522. <https://doi.org/10.1016/j.apcatb.2019.118522>.
- [27] K. Li, C. Pei, X. Li, S. Chen, X. Zhang, R. Liu, J. Gong, Dry reforming of methane over La₂O₂CO₃-modified Ni/Al₂O₃ catalysts with moderate metal support interaction, *Appl. Catal. B Environ.* 264 (2020) 118448. <https://doi.org/10.1016/j.apcatb.2019.118448>.
- [28] N.D. Charisiou, L. Tzounis, V. Sebastian, S.J. Hinder, M.A. Baker, K. Polychronopoulou, M.A. Goula, Investigating the correlation between deactivation and the carbon deposited on the surface of Ni/Al₂O₃ and Ni/La₂O₃-Al₂O₃ catalysts during the biogas reforming reaction, *Appl. Surf. Sci.* 474 (2019) 42–56. <https://doi.org/10.1016/j.apsusc.2018.05.177>.
- [29] J. Phromprasit, J. Powell, S. Wongsakulphasatch, W. Kiatkittipong, P. Bumroongsakulsawat, S. Assabumrungrat, H₂ production from sorption enhanced steam reforming of biogas using multifunctional catalysts of Ni over Zr-, Ce- and La-modified CaO sorbents, *Chem. Eng. J.* 313 (2017) 1415–1425. <https://doi.org/10.1016/j.cej.2016.11.051>.
- [30] I. V. Yentekakis, G. Goula, M. Hatzisymeon, I. Betsi-Argyropoulou, G. Botzolaki, K. Kousi, D.I. Kondarides, M.J. Taylor, C.M.A. Parlett, A. Osatiashtiani, G. Kyriakou, J.P. Holgado, R.M. Lambert, Effect of support oxygen storage capacity on the catalytic performance of Rh nanoparticles for CO₂ reforming of methane, *Appl. Catal. B Environ.* 243 (2019) 490–501. <https://doi.org/10.1016/j.apcatb.2018.10.048>.
- [31] A. Navarro-puyuelo, I. Reyero, A. Moral, F. Bimbela, M.A. Bañares, L.M. Gandía, Effect of oxygen addition, reaction temperature and thermal treatments on syngas production from biogas combined reforming using Rh/alumina catalysts, *J. Ind. Eng. Chem.* 80 (2019) 217–226. <https://doi.org/10.1016/j.jiec.2019.07.051>.
- [32] F. Polo-Garzon, D. Pakhare, J.J. Spivey, D.A. Bruce, Dry Reforming of Methane on Rh-Doped Pyrochlore Catalysts: A Steady-State Isotopic Transient Kinetic Study, *ACS Catal.* 6 (2016) 3826–3833. <https://doi.org/10.1021/acscatal.6b00666>.
- [33] B. De Caprariis, P. De Filippis, V. Palma, A. Petrullo, A. Ricca, C. Ruocco, M. Scarsella, Rh, Ru and Pt ternary perovskites type oxides BaZr_(1-x)MexO₃ for methane dry reforming, *Appl. Catal. A Gen.* 517 (2016) 47–55. <https://doi.org/10.1016/j.apcata.2016.02.029>.
- [34] Y. Kathiraser, U. Oemar, E.T. Saw, Z. Li, S. Kawi, Kinetic and mechanistic aspects for CO₂ reforming of methane over Ni based catalysts, *Chem. Eng. J.* 278 (2015) 62–78. <https://doi.org/10.1016/j.cej.2014.11.143>.
- [35] J. Wei, E. Iglesia, Isotopic and kinetic assessment of the mechanism of reactions of CH₄ with CO₂ or H₂O to form synthesis gas and carbon on nickel catalysts, *J. Catal.* 224 (2004) 370–383. <https://doi.org/10.1016/j.jcat.2004.02.032>.
- [36] M.C.J. Bradford, M.A. Vannice, Catalytic reforming of methane with carbon dioxide over nickel catalysts II. Reaction kinetics, *Appl. Catal. A Gen.* 142 (1996) 97–122. [https://doi.org/10.1016/0926-860X\(96\)00066-X](https://doi.org/10.1016/0926-860X(96)00066-X).
- [37] J. Niu, S.E. Liland, J. Yang, K.R. Rout, J. Ran, D. Chen, Effect of oxide additives on the hydrotalcite derived Ni catalysts for CO₂ reforming of methane, *Chem. Eng. J.* 377 (2019)

119763. <https://doi.org/10.1016/j.cej.2018.08.149>.

- [38] X.E. Verykios, Catalytic dry reforming of natural gas for the production of chemicals and hydrogen, *Chem. Ind. Chem. Eng. Q.* 8 (2002) 238–255. <https://doi.org/10.2298/hemind0206238v>.
- [39] Z. Bao, Y. Lu, F. Yu, Kinetic study of methane reforming with carbon dioxide over NiCeMgAl bimodal pore catalyst, *AIChE J.* 63 (2017) 2019–2029. <https://doi.org/10.1002/aic.15579>.
- [40] B. V Ayodele, S.B. Abdullah, C.K. Cheng, Kinetics and mechanistic studies of CO-rich hydrogen production by CH₄/CO₂ reforming over Praseodymia supported cobalt catalysts, *Int. J. Hydrogen Energy.* 42 (2017) 28408–28424. <https://doi.org/10.1016/j.ijhydene.2017.09.037>.
- [41] A.I. Paksoy, C. Yassi Akdag, B. Selen Caglayan, A.E. Aksoylu, Kinetic and mechanistic features of carbon dioxide reforming of methane over Co–Ce/ZrO₂ catalysts, *Int. J. Chem. Kinet.* 51 (2019) 138–145. <https://doi.org/10.1002/kin.21237>.
- [42] B. Sawatmongkhon, K. Theinnoi, T. Wongchang, C. Haoharn, A. Tsolakis, Combination of Langmuir-Hinshelwood-Hougen-Watson and microkinetic approaches for simulation of biogas dry reforming over a platinum-rhodium alumina catalyst, *Int. J. Hydrogen Energy.* 42 (2017) 24697–24712. <https://doi.org/10.1016/j.ijhydene.2017.08.048>.
- [43] B. Nematollahi, M. Rezaei, M. Asghari, A. Fazeli, E.N. Lay, F. Nematollahi, A comparative study between modeling and experimental results over rhodium supported catalyst in dry reforming reaction, *Fuel.* 134 (2014) 565–572. <https://doi.org/10.1016/j.fuel.2014.05.093>.
- [44] A. Donazzi, A. Beretta, G. Groppi, P. Forzatti, Catalytic partial oxidation of methane over a 4% Rh/ α -Al₂O₃ catalyst Part II: Role of CO₂ reforming, *J. Catal.* 255 (2008) 259–268. <https://doi.org/10.1016/j.jcat.2008.02.010>.
- [45] J.F. Múnera, S. Irusta, L.M. Cornaglia, E.A. Lombardo, D. Vargas Cesar, M. Schmal, Kinetics and reaction pathway of the CO₂ reforming of methane on Rh supported on lanthanum-based solid, *J. Catal.* 245 (2007) 25–34. <https://doi.org/10.1016/j.jcat.2006.09.008>.
- [46] J. Wei, E. Iglesia, Structural requirements and reaction pathways in methane activation and chemical conversion catalyzed by rhodium, *J. Catal.* 225 (2004) 116–127. <https://doi.org/10.1016/j.jcat.2003.09.030>.
- [47] J.F. Múnera, L.M. Cornaglia, D.V. Cesar, M. Schmal, E.A. Lombardo, Kinetic studies of the dry reforming of methane over the Rh/La₂O₃-SiO₂ catalyst, *Ind. Eng. Chem. Res.* 46 (2007) 7543–7549. <https://doi.org/10.1021/ie061621p>.
- [48] A. Behroozsarand, A.N. Pour, Modeling of microreactor for methane dry reforming: Comparison of Langmuir-Hinshelwood kinetic and microkinetic models, *J. Nat. Gas Sci. Eng.* 20 (2014) 99–108. <https://doi.org/10.1016/j.jngse.2014.06.011>.
- [49] M. Maestri, D.G. Vlachos, A. Beretta, G. Groppi, E. Tronconi, A C₁ microkinetic model for methane conversion to syngas on Rh/Al₂O₃, *AIChE J.* 55 (2009) 993–1008. <https://doi.org/10.1002/aic.11767>.
- [50] K. Herrera Delgado, L. Maier, S. Tischer, A. Zellner, H. Stotz, O. Deutschmann, Surface

- reaction kinetics of steam- and CO₂-reforming as well as oxidation of methane over nickel-based catalysts, *Catalysts*. 5 (2015) 871–904. <https://doi.org/10.3390/catal5020871>.
- [51] Z. Xie, Q. Liao, M. Liu, Z. Yang, L. Zhang, Micro-kinetic modeling study of dry reforming of methane over the Ni-based catalyst, *Energy Convers. Manag.* 153 (2017) 526–537. <https://doi.org/10.1016/j.enconman.2017.10.022>.
- [52] a. K. Avetisov, J.R. Rostrup-Nielsen, V.L. Kuchaev, J.H. Bak Hansen, a. G. Zyskin, E.N. Shapatina, Steady-state kinetics and mechanism of methane reforming with steam and carbon dioxide over Ni catalyst, *J. Mol. Catal. A Chem.* 315 (2010) 155–162. <https://doi.org/10.1016/j.molcata.2009.06.013>.
- [53] L. Dehimi, Y. Benguerba, M. Virginie, H. Hijazi, Microkinetic modelling of methane dry reforming over Ni/Al₂O₃ catalyst, *Int. J. Hydrogen Energy*. 42 (2017) 18930–18940. <https://doi.org/10.1016/j.ijhydene.2017.05.231>.
- [54] C. Fan, Y.A. Zhu, M.L. Yang, Z.J. Sui, X.G. Zhou, D. Chen, Density Functional Theory-Assisted Microkinetic Analysis of Methane Dry Reforming on Ni Catalyst, *Ind. Eng. Chem. Res.* 54 (2015) 5901–5913. <https://doi.org/10.1021/acs.iecr.5b00563>.
- [55] A.B. Mhadeshwar, D.G. Vlachos, Hierarchical multiscale mechanism development for methane partial oxidation and reforming and for thermal decomposition of oxygenates on Rh, *J. Phys. Chem. B*. 109 (2005) 16819–16835. <https://doi.org/10.1021/jp052479t>.
- [56] M. Maestri, D.G. Vlachos, A. Beretta, G. Groppi, E. Tronconi, Steam and dry reforming of methane on Rh: Microkinetic analysis and hierarchy of kinetic models, *J. Catal.* 259 (2008) 211–222. <https://doi.org/10.1016/j.jcat.2008.08.008>.
- [57] N.E. McGuire, N.P. Sullivan, O. Deutschmann, H. Zhu, R.J. Kee, Dry reforming of methane in a stagnation-flow reactor using Rh supported on strontium-substituted hexaaluminate, *Appl. Catal. A Gen.* 394 (2011) 257–265. <https://doi.org/10.1016/j.apcata.2011.01.009>.
- [58] C. Karakaya, L. Maier, O. Deutschmann, Surface Reaction Kinetics of the Oxidation and Reforming of CH₄ over Rh/Al₂O₃ Catalysts, *Int. J. Chem. Kinet.* 48 (2016) 144–160. <https://doi.org/10.1002/kin.20980>.
- [59] F. Polo-Garzon, J.K. Scott, D.A. Bruce, Microkinetic model for the dry reforming of methane on Rh doped pyrochlore catalysts, *J. Catal.* 340 (2016) 196–204. <https://doi.org/10.1016/j.jcat.2016.05.019>.
- [60] A.B. Mhadeshwar, H. Wang, D.G. Vlachos, Thermodynamic Consistency in Microkinetic Development of Surface Reaction Mechanisms, (2003) 12721–12733.
- [61] L.C. Grabow, A.A. Gokhale, S.T. Evans, J.A. Dumesic, M. Mavrikakis, Mechanism of the water gas shift reaction on Pt: First principles, experiments, and microkinetic modeling, *J. Phys. Chem. C*. 112 (2008) 4608–4617. <https://doi.org/10.1021/jp7099702>.
- [62] A.T.F. Afolabi, C.Z. Li, P.N. Kechagiopoulos, Microkinetic modelling and reaction pathway analysis of the steam reforming of ethanol over Ni/SiO₂, *Int. J. Hydrogen Energy*. 44 (2019) 22816–22830. <https://doi.org/10.1016/j.ijhydene.2019.07.040>.
- [63] E. Shustorovich, H. Sellers, The UBI-QEP method: A practical theoretical approach to understanding chemistry on transition metal surfaces, *Surf. Sci. Rep.* 31 (1998) 1–119.

[https://doi.org/10.1016/s0167-5729\(97\)00016-2](https://doi.org/10.1016/s0167-5729(97)00016-2).

- [64] E. Shustorovich, The Bond-Order Conservation Approach to Chemisorption and Heterogeneous Catalysis: Applications and Implications, *Adv. Catal.* 37 (1990) 101–163. [https://doi.org/10.1016/S0360-0564\(08\)60364-8](https://doi.org/10.1016/S0360-0564(08)60364-8).
- [65] Z. Wang, X.M. Cao, J. Zhu, P. Hu, Activity and coke formation of nickel and nickel carbide in dry reforming: A deactivation scheme from density functional theory, *J. Catal.* 311 (2014) 469–480. <https://doi.org/10.1016/j.jcat.2013.12.015>.
- [66] J. Zhang, Z. Zhong, X.M. Cao, P. Hu, M.B. Sullivan, L. Chen, Ethanol steam reforming on rh catalysts: Theoretical and experimental understanding, *ACS Catal.* 4 (2014) 448–456. <https://doi.org/10.1021/cs400725k>.
- [67] J. Zhang, X.M. Cao, P. Hu, Z. Zhong, A. Borgna, P. Wu, Density functional theory studies of ethanol decomposition on Rh(211), *J. Phys. Chem. C* 115 (2011) 22429–22437. <https://doi.org/10.1021/jp206837z>.
- [68] M.M. Yang, X.H. Bao, W.X. Li, Density functional theory study of C H_x (x=1-3) adsorption on clean and CO precovered Rh(111) surfaces, *J. Chem. Phys.* 127 (2007). <https://doi.org/10.1063/1.2751155>.
- [69] Y. Choi, P. Liu, Mechanism of Ethanol Synthesis from Syngas on Rh (111), *J. Am. Chem. Soc.* 131 (2009) 13054–13061.

Supplementary information

To further ascertain the validity of this developed model and in turn the validity of the results of coverage effects and mechanism alterations caused by co-feeding H₂ and CO, the developed model was used to simulate previous methane steam reforming experiments over a Rh metal catalyst [13].

The parity plot showed great agreement between the model predicted results for reactant conversions and product selectivities, with minor changes to the model parameters. Thus instilling further confidence in the microkinetic model developed and results obtained above.

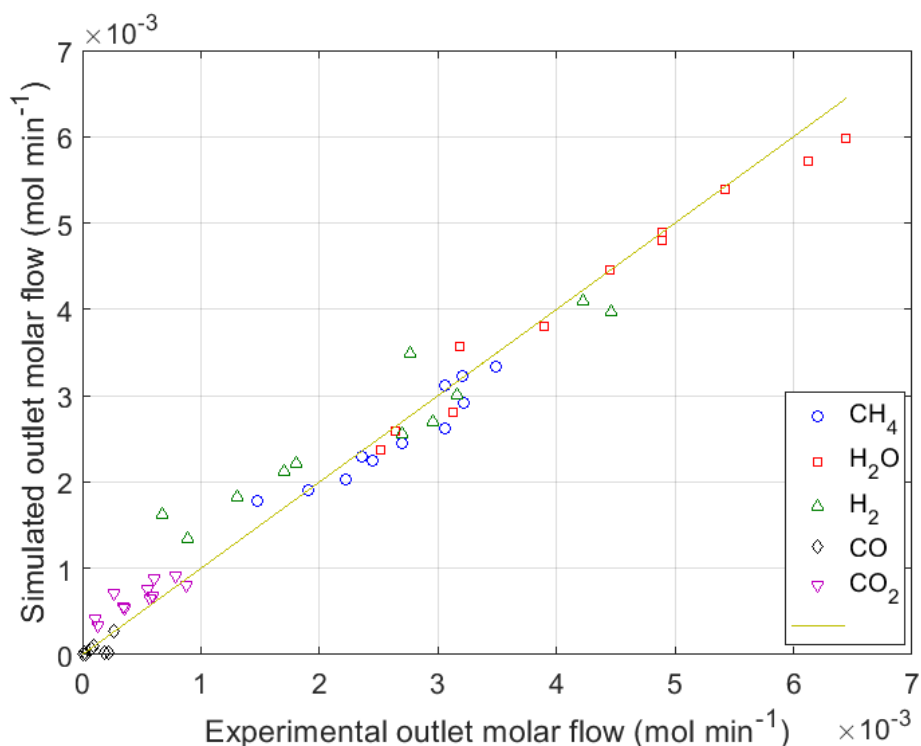


Figure 5-9: Parity diagram for CH₄, H₂O, H₂, CO and CO₂. Experimental conditions of steam reforming of methane are reported in previous work [13], while modelling results have been obtained with parameter values presented in Table 5.5.

Preface to Chapter 6

I was the lead investigator for the project located in this chapter. I was responsible for all major areas of concept formation, data collection and analysis, as well as manuscript composition. Kechagiopoulos P.N. was the main supervisory author on this project and was involved throughout the project in concept formation and manuscript composition.

The aim of this study was to investigate and provide an intrinsic kinetic and mechanistic understanding of the effect of support materials on the ethanol steam reforming mechanism, by

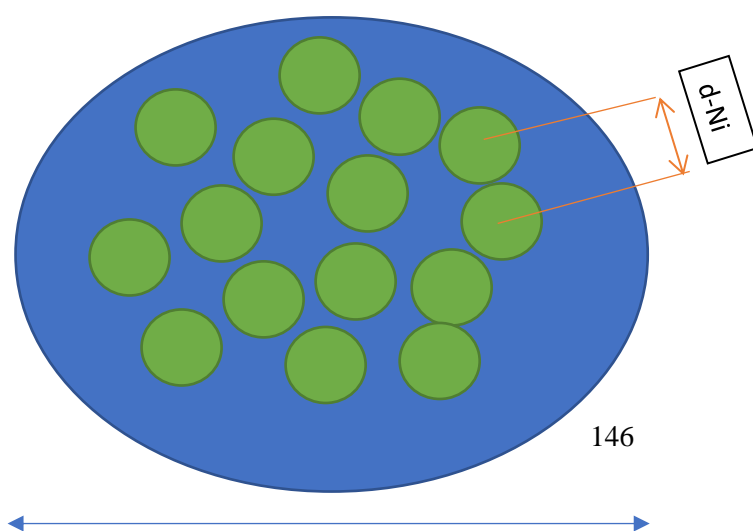
developing a microkinetic model capable of discerning the role of support activity and metal-support interactions on the reaction pathway and mechanism. This addresses the fourth objective of this thesis. The important role support materials play in the activity and stability of catalysts used for ethanol steam reforming was discussed in Chapter 2. Additionally, the importance of microkinetic modelling of bifunctional reaction mechanisms has been discussed in literature and was presented in Chapter 2.

The mean-field microkinetic model developed in Chapter 4 and improved in Chapter 5 was used as the basis for the formulation of this model. The model is expanded by implementing an additional catalytic site for adsorption/desorption and surface reactions of species. To initialise the DAE system, the initial values of surface partial coverages are obtained by evolving both clean catalytic sites towards steady state.

In the model a representative number of active sites for both surfaces have been included. The number of sites are estimated in such a way as to mimic the ratios of the number of metal and support sites in a real catalyst.

The active site density, surface area and the dispersion of the metal catalysts were experimentally determined just like in the case of the metal dominated model in Chapter 4. For the support site, geometrical calculations were performed assuming a hemispherical particle with optimal packing of Ni atoms. The known dispersion was used as the basis giving the ratio of Ni atoms in the surface to Ni atoms in the volume. The calculations below then give the ratio of support sites to metal sites based on the diameters of both. Similar geometric estimations were performed in the work of Kauppinen et al. [43].

Geometric estimation of support site density



D-Crystal

Figure 6.0: Top view of assumed geometry of catalyst

Assuming perfect spherical geometry for both Ni and Support

With a known dispersion correlating to the ratio of

$$1.2\% = \frac{Ni\ in\ surface}{Ni\ in\ volume} \quad (1)$$

$$Nickel_{surface} = \frac{0.5 * Area\ of\ support\ crystal\ sphere}{Area\ of\ Ni\ atom\ sphere} \quad (2)$$

$$Nickel_{volume} = \frac{0.5 * volume\ of\ support\ crystal\ sphere}{Volume\ of\ Ni\ atom\ sphere} \quad (3)$$

$$Area\ of\ Ni\ atom\ sphere = \pi d - Ni \quad (4)$$

$$Area\ of\ support\ crystal\ sphere = \pi D - Crystal \quad (5)$$

$$Area\ of\ Ni\ atom\ sphere = \frac{4}{3} \pi (d - Ni)^3 \quad (6)$$

$$Area\ of\ support\ crystal\ sphere = \frac{4}{3} \pi (D - Crystal)^3 \quad (7)$$

Solving the equations for the crystal and Ni diameters we find d-Ni = 1, D-Crystal = 325

The ratio of number of active sites on support to that of Ni can be estimated as 325:1.

However, the Ceria only constitutes 17% of the total support crystal sites, thus the number of support active sites is adjusted to:

$$Estimated\ Number\ of\ Ni\ active\ sites * 325 * 0.17 \quad (8)$$

The key assumption made to simplify the model development process is that the dominating catalytic effect of the mixed oxide support observed can be streamlined into the Ceria's ability to provide mobile surface oxygen and active sites for steam activation. The other oxides provide improved surface dispersion for the metal. Also, the zirconia tends to have a similar effect to ceria as the results of the experiments show, thus, to account for the possibility of the other oxides adding to the activity of the support, the active site density calculated for ceria is selected as a model parameter and a pre-emptive sensitivity analysis was done to determine how much of an impact the density of support sites has on the reactant conversion and product selectivities. It

was determined that the effect is negligible even when site density was doubled, this was mainly due to the fact that the transfer of surface oxygen to the metal site was non-activated and fast, so the effect of the support did not change much based on the support site density.

CHAPTER 6: MICROKINETIC EVALUATION OF THE BIFUNCTIONAL MECHANISM OF ETHANOL STEAM REFORMING OVER A Ni/CeZrLa

Ahmed Tijani F. Afolabi,^{a, b} Panagiotis N. Kechagiopoulos,^{a,*}

^a Chemical and Materials Engineering Group, School of Engineering, University of Aberdeen, Aberdeen, AB24 3UE, UK

^b Fuels and Energy Technology Institute, Curtin University, GPO Box U1987, Perth, WA 6845, Australia

* Corresponding author

E-mail addresses: p.kechagiopoulos@abdn.ac.uk (P.N. Kechagiopoulos).

Abstract

A bifunctional microkinetic model for ethanol steam reforming (ESR) over a Ni catalyst supported by a CeO₂ containing mixed oxide discerning the effects of the support material is presented for the first time and validated against experimental data. A single site microkinetic model based on the activity of the Ni metal alone provided a limited fit with the experimental kinetic data, revealing the need to consider the bifunctional mechanism of the reaction into the model. The thermodynamically consistent bifunctional model developed, considering two different adsorption sites, correctly described the experimental trends over a wide range of conditions. The kinetically relevant steps are found to be occurring in the ethanol dehydrogenation pathway with the initial dehydrogenation towards 1-hydroxyethyl taking prevalence. The analysis of oxidative and thermal dehydrogenation reaction classes showed that the former does not contribute to the relevant kinetic dehydrogenation step and only becomes relevant after the formation of acetyl intermediate. The abundance of O species on the metal, due to the support's activity, and the consequent increased contribution of oxidative dehydrogenation caused the C-C bond scission to occur later in the dehydrogenation pathway at the CCO intermediate *via* its reaction with surface O species towards CO. The model discerns the alterations to the overall reaction mechanism caused by the support activity, whilst correctly explaining the lack of participation of water derived species from the kinetically relevant reaction step.

6.1 Introduction

There has been a considerable amount of experimental research addressing the catalytic steam reforming of ethanol for the production of renewable hydrogen in the frame of a future sustainable hydrogen economy. Most of these works have focused on developing supported metal catalysts with high reforming activity and stability. To date, there are also ample mechanistic, kinetic and microkinetic analyses of the ethanol steam reforming process (ESR), mainly elucidating the effect of the metal catalyst on the reaction pathway. Akande et al. [1] developed a kinetic model for ESR over a Ni/Al₂O₃ catalyst assuming an Eley-Rideal mechanism at the low temperature range of 350-550°C. The dissociative adsorption of ethanol on the active metal sites was found as the rate determining step, however, the proposed model and reaction mechanism did not account for the formation of known primary products or intermediates such as acetaldehyde. The isotopic investigation of Gates et al. [2] on the decomposition of ethanol on a Ni(111) surface in the absence of water, as well as the periodic DFT calculations performed by Wang et al. [3] have elaborated on the decomposition pathways of ethanol over various metal (111) surfaces including Ni. It was shown that decomposition on Ni, proceeds *via* an initial O-H bond cleavage leaving an adsorbed ethoxy species (CH₃CH₂O*), followed by dehydrogenation to acetaldehyde and, eventually, a C-C cleavage, leading to the formation of CH_x and CO. Using DFT calculations and Brønsted-Evans-Polyani correlations for the decomposition of ethanol over Pt, Rh, Pd, Ru and Ir, Ferrin et al. [4] found the C-C cleavage in all active surfaces to occur at the ketenyl (CH₂CO*) intermediate. This was supported by the findings of Sutton et al. [5] during the combined DFT, microkinetic and experimental study of ethanol steam reforming over Pt, who found that the likely decomposition pathway occurred *via* an initial α-H abstraction leading to an adsorbed 1-hydroxyethyl (CH₃CHOH*) surface species. Further dehydrogenation steps occurred until C-C cleavage took place at the ketenyl (CH₂CO*) intermediate. The results from our previous works on the experimental and microkinetic analysis of ethanol steam reforming over Ni/SiO₂ catalyst [6,7], suggested the decomposition mechanism of ethanol over Ni during reforming to resemble the aforementioned pathway over Pt.

Very few kinetic modelling studies are available in literature focusing on the identification and elucidation of the effect of support materials on the adsorption and reaction mechanism of ESR. Grashinsky et al. [8] performed a kinetic study of ethanol steam reforming over Rh catalyst supported on a spinel structure MgAl₂O₄/Al₂O₃. Through their initial rate method analysis, they found that the rate determining step was a surface reaction involving two active sites of the same type. Nonetheless, the specific nature of the active sites was not identified. In the kinetic analysis of ethanol steam reforming over Ir/CeO₂ performed by Wang et al. [9], it was found that a model

based solely on the metal sites did not provide good agreement with the experimental results. A bifunctional model, following the Langmuir-Hinshelwood formalism, including both metal and support active sites and considering only reactions involving both sites provided satisfactory agreement with the experimental results. It was assumed that both reactants were initially adsorbed on the support surface and the Ir active sites were required for the formation and desorption of CO and H₂.

The nature and functionality of support materials can enhance activity in multiple ways, including enabling alternate reaction pathways or increasing stability against coke deposition on the metal [10,11]. It is, therefore, important to obtain an intrinsic mechanistic understanding of the role support materials in ESR. In this work, a comprehensive microkinetic model for ethanol steam reforming that incorporates the effect of the active sites on the support material and the possible reaction pathways and interactions between metal and support active sites is proposed and validated using kinetic data obtained over a Ni catalyst on a CeO₂ containing support. The work expands on the previous study on ethanol steam reforming over Ni/SiO₂, providing insight into the possible adsorption and reaction pathways on the support and the effect of these on the overall process reaction mechanism. A unified kinetic view on the ESR mechanism is obtained.

6.2 Procedures

6.2.1 Experimental details

The experimental data used in this study were obtained from the work of Zhurka et al. [12]. Experiments were carried out in a fixed bed reactor setup over a Ni/CeO₂-ZrO₂-La₂O₃ catalyst under explicit kinetic control. The kinetic dataset covers the effect of temperature and partial pressure of reactants across a wide range. The effect of the support material is attributed primarily to the presence of CeO₂ in the mixed oxide thanks to its oxygen mobility. This in line with the experimental results in [12], where the performance of a Ni/ZrO₂-La₂O₃ catalyst largely followed the trends observed over a Ni/SiO₂ catalyst, while critical selectivity and activity enhancements were obtained with the CeO₂ containing catalyst. A summary of the operating conditions and catalyst properties is provided in Table 6.1, with more details being available in the original publication.

Table 6.1: Experimental operating conditions and catalyst properties [12]

Catalyst	Ni/CeO ₂ (17%) - ZrO ₂ - La ₂ O ₃ (5%)
Ni loading (wt%)	10%
Ni dispersion (%)	1.2%
Specific surface area (m ² /g)	37.17
Catalyst weight per experiment (g)	0.08
Temperature (°C)	300-550
Partial pressure of ethanol (bara)	0.06-0.37
Partial pressure of water (bara)	0.26-1.56
W/F _{Eth,t0} (g _{cat} s g _{eth} ⁻¹)	91.88

6.2.2 Model formulation

The microkinetic model for ethanol steam reforming over Ni/CeO₂ containing mixed oxide support catalyst implemented in this work closely follows the procedures described in our previous work [7], hence only the main features and additions relating to the bifunctional aspect of the model are highlighted here. For all surface reactions, the reaction entropy and enthalpy are correlated to the corresponding gas phase reaction entropy and enthalpy in order to maintain thermodynamic consistency in line with the work of Kechagiopoulos et al. [13]. The enthalpy of surface species is obtained by deducting the chemisorption enthalpy of the species from the equivalent gas phase species enthalpy, with the chemisorption enthalpy being temperature dependent based on degrees of freedom lost or gained during adsorption or desorption as described in Mhadeshwar et al. [14]. The entropies for adsorbed species are estimated by deducting their standard three-dimensional translational entropy $S_{\text{trans,3D}}$ from the gas phase entropy. A fitting factor F_{loc} , which represents the fraction of rotational and vibrational entropy of the gas phase molecule that remains after adsorption, as described in Grabow et al. [15], is included in the estimation of surface species entropy. The fitting factor is part of the list of model parameters and is accounted for according to equation 5.8.

The rates of elementary reaction steps are calculated using the law of mass action and Arrhenius rate equation. Collision theory is used for the estimation of the pre-exponential factor values of forward adsorption steps, while transition state theory is used to estimate those of surface reactions [16]. The reverse reaction pre-exponential factors are calculated through the preservation of entropic thermodynamic consistency. The activation barriers for forward surface

reactions are calculated using the UBI-QEP method [17,18], while barriers of reverse reactions are calculated through enthalpic thermodynamic consistency. Adsorption reaction steps are considered non-activated.

In order to account for the support effect an additional type of active site is included in the microkinetic model. Adsorption/desorption and surface reaction steps may occur on these sites, similarly using the law of mass action, Arrhenius rate equation and thermodynamic consistency calculations described previously. The active site density and surface area of the Ni metal catalyst were experimentally determined [19]. The density of the support site was estimated using geometric assumptions with the known dispersion of 1.2% as a basis. The dispersion gives the ratio of Ni on the surface to Ni in the support crystal volume and from this an assumption of spherical crystal geometry is used to determine the ratio of Ni atoms support. For the 1.2% dispersion, the ratio of Ce sites to Ni sites was found as 55.25:1. A more detailed explanation is given in the preface to this chapter. The support site density calculated *via* this method was nonetheless subjected to a sensitivity analysis based on the reactions involving support sites, revealing a negligible effect on the conversion and product formation. The DDASPK solver [20] was used to integrate the differential and algebraic equations system that describes the evolution of molar flowrates of gas phase molecules, and partial coverages and respective balances on both types of active sites. Empty surfaces for both metal and support active sites are integrated towards steady state coverage at the inlet of the reactor in order to obtain the partial coverages for all surface species used to initialise the DAE system. The model parameters; chemisorption enthalpies and entropy fitting factor are estimated using Rosenbrock [21] and Levenberg-Marquardt [22] optimisation algorithms through regression of experimental data.

6.2.3 Surface reaction network description

A network of 82 elementary reaction steps occurring on two types of active sites with different active site densities, involving 26 surface species and 7 gaseous molecules, is considered for this model. The proposed bifunctional network the ESR over Ni/CeO₂ contains various possible reaction pathways (Table 6.2).

Table 6.2: Microkinetic model for ethanol steam reforming on Ni/CeO₂. Activation barriers are calculated using the model parameters shown in Table 3 via UBI-QEP and pre-exponential factors calculated via transition state theory as described in Section Model formulation and computational details. Arrhenius equation used of form $R_i^f = A_i * e^{-E_{a,i}/RT}$.

No.	Reaction	E_a (kJ mol ⁻¹)	A (s ⁻¹)
R1	CH ₃ CH ₂ OH + * → CH ₃ CH ₂ OH*	0.00	3.06 × 10 ⁺⁰⁴
R2	CH ₃ CH ₂ OH* → CH ₃ CH ₂ OH + *	43.49	3.55 × 10 ⁺¹³
R3	H ₂ O + * → H ₂ O*	0.00	5.32 × 10 ⁺⁰⁴
R4	H ₂ O* → H ₂ O + *	53.07	1.37 × 10 ⁺¹³
R5	H ₂ + 2* → H* + H*	30.92	1.47 × 10 ⁺⁰⁵
R6	H* + H* → H ₂ + 2*	97.58	4.41 × 10 ⁺¹²
R7	CH ₄ + 2* → CH ₃ * + H*	55.53	5.19 × 10 ⁺⁰⁴
R8	CH ₃ * + H* → CH ₄ + 2*	57.10	2.34 × 10 ⁺¹²
R9	CO + * → CO*	0.00	3.93 × 10 ⁺⁰⁴
R10	CO* → CO + *	98.74	2.16 × 10 ⁺¹³
R11	CO ₂ + * → CO ₂ *	0.00	3.14 × 10 ⁺⁰⁴
R12	CO ₂ * → CO ₂ + *	20.97	3.40 × 10 ⁺¹³
R13	CH ₃ CHO + * → CH ₃ CHO*	0.00	3.13 × 10 ⁺⁰⁴
R14	CH ₃ CHO* → CH ₃ CHO + *	74.52	3.36 × 10 ⁺¹³
R15	CH ₃ CH ₂ OH* + * → CH ₃ CHOH* + H*	58.92	7.83 × 10 ⁺¹²
R16	CH ₃ CHOH* + H* → CH ₃ CH ₂ OH* + *	42.61	1.51 × 10 ⁺¹³
R17	CH ₃ CH ₂ OH* + * → CH ₃ CH ₂ O* + H*	74.72	1.00 × 10 ⁺¹²
R18	CH ₃ CH ₂ O* + H* → CH ₃ CH ₂ OH* + *	36.81	1.93 × 10 ⁺¹³
R19	CH ₃ CHOH* + * → CH ₃ CHO* + H*	53.73	1.91 × 10 ⁺¹¹
R20	CH ₃ CHO* + H* → CH ₃ CHOH* + *	3.86	1.42 × 10 ⁺¹³
R21	CH ₃ CH ₂ O* + * → CH ₃ CHO* + H*	45.63	1.91 × 10 ⁺¹¹
R22	CH ₃ CHO* + H* → CH ₃ CH ₂ O* + *	17.28	1.42 × 10 ⁺¹³
R23	CH ₃ CHOH* + * → CH ₃ COH* + H*	46.07	1.91 × 10 ⁺¹¹
R24	CH ₃ COH* + H* → CH ₃ CHOH* + *	29.65	1.42 × 10 ⁺¹³
R25	CH ₃ COH* + * → CH ₃ CO* + H*	20.14	1.51 × 10 ⁺¹³
R26	CH ₃ CO* + H* → CH ₃ COH* + *	87.78	5.64 × 10 ⁺¹¹
R27	CH ₃ CHO* + * → CH ₃ CO* + H*	3.41	1.10 × 10 ⁺¹²
R28	CH ₃ CO* + H* → CH ₃ CHO* + *	104.50	3.38 × 10 ⁺¹³
R29	CH ₃ CO* + * → CH ₃ * + CO*	11.82	1.00 × 10 ⁺¹¹
R30	CH ₃ * + CO* → CH ₃ CO* + *	67.01	2.10 × 10 ⁺¹²
R31	CH ₃ CO* + * → CH ₂ CO* + H*	50.90	4.24 × 10 ⁺¹³
R32	CH ₂ CO* + H* → CH ₃ CO* + *	9.47	1.66 × 10 ⁺¹³

R33	$\text{CH}_2\text{CO}^* + ^*\text{H} \rightarrow \text{CH}_2^* + \text{CO}^*$	0.00	$7.43 \times 10^{+11}$
R34	$\text{CH}_2^* + \text{CO}^* \rightarrow \text{CH}_2\text{CO}^* + ^*\text{H}$	76.55	$1.93 \times 10^{+12}$
R35	$\text{CH}_2\text{CO}^* + ^*\text{H} \rightarrow \text{CHCO}^* + \text{H}^*$	81.57	$1.15 \times 10^{+13}$
R36	$\text{CHCO}^* + \text{H}^* \rightarrow \text{CH}_2\text{CO}^* + ^*\text{H}$	40.29	$1.65 \times 10^{+12}$
R37	$\text{CHCO}^* + ^*\text{H} \rightarrow \text{CH}^* + \text{CO}^*$	0.00	$5.18 \times 10^{+11}$
R38	$\text{CH}^* + \text{CO}^* \rightarrow \text{CHCO}^* + ^*\text{H}$	107.61	$3.74 \times 10^{+12}$
R39	$\text{CHCO}^* + ^*\text{H} \rightarrow \text{CCO}^* + \text{H}^*$	97.42	$2.18 \times 10^{+11}$
R40	$\text{CCO}^* + \text{H}^* \rightarrow \text{CHCO}^* + ^*\text{H}$	31.72	$1.34 \times 10^{+12}$
R41	$\text{CH}_3\text{CO}^* + \text{O}^* \rightarrow \text{CH}_2\text{CO}^* + \text{OH}^*$	52.01	$1.54 \times 10^{+13}$
R42	$\text{CH}_2\text{CO}^* + \text{OH}^* \rightarrow \text{CH}_3\text{CO}^* + \text{O}^*$	35.86	$3.88 \times 10^{+13}$
R43	$\text{CH}_2\text{CO}^* + \text{O}^* \rightarrow \text{CHCO}^* + \text{OH}^*$	76.16	$1.55 \times 10^{+13}$
R44	$\text{CHCO}^* + \text{OH}^* \rightarrow \text{CH}_2\text{CO}^* + \text{O}^*$	48.38	$1.45 \times 10^{+12}$
R45	$\text{CHCO}^* + \text{O}^* \rightarrow \text{CCO}^* + \text{OH}^*$	94.22	$5.06 \times 10^{+12}$
R46	$\text{CCO}^* + \text{OH}^* \rightarrow \text{CHCO}^* + \text{O}^*$	81.93	$5.22 \times 10^{+11}$
R47	$\text{CCO}^* + \text{O}^* \rightarrow \text{CO}^* + \text{CO}^*$	0.00	$4.47 \times 10^{+11}$
R48	$\text{CO}^* + \text{CO}^* \rightarrow \text{CCO}^* + \text{O}^*$	211.79	$5.32 \times 10^{+11}$
R49	$\text{COOH}^* + ^*\text{H} \rightarrow \text{CO}^* + \text{OH}^*$	44.88	$7.56 \times 10^{+10}$
R50	$\text{CO}^* + ^*\text{OH} \rightarrow \text{COOH}^* + ^*\text{H}$	24.87	$1.10 \times 10^{+12}$
R51	$\text{COOH}^* + ^*\text{H} \rightarrow \text{CO}_2^* + \text{H}^*$	0.79	$1.42 \times 10^{+11}$
R52	$\text{CO}_2^* + \text{H}^* \rightarrow \text{COOH}^* + ^*\text{H}$	18.58	$1.54 \times 10^{+13}$
R53	$\text{CO}_2^* + ^*\text{H} \rightarrow \text{CO}^* + \text{O}^*$	40.24	$1.93 \times 10^{+12}$
R54	$\text{CO}^* + \text{O}^* \rightarrow \text{CO}_2^* + ^*\text{H}$	55.93	$1.15 \times 10^{+13}$
R55	$\text{CH}_3^* + ^*\text{H} \rightarrow \text{CH}_2^* + \text{H}^*$	88.00	$1.03 \times 10^{+13}$
R56	$\text{CH}_2^* + \text{H}^* \rightarrow \text{CH}_3^* + ^*\text{H}$	64.97	$7.38 \times 10^{+12}$
R57	$\text{CH}_2^* + ^*\text{H} \rightarrow \text{CH}^* + \text{H}^*$	90.89	$8.03 \times 10^{+12}$
R58	$\text{CH}^* + \text{H}^* \rightarrow \text{CH}_2^* + ^*\text{H}$	82.75	$3.19 \times 10^{+13}$
R59	$\text{CH}_2^* + \text{O}^* \rightarrow \text{CHO}^* + \text{H}^*$	76.37	$3.58 \times 10^{+10}$
R60	$\text{CHO}^* + \text{H}^* \rightarrow \text{CH}_2^* + \text{O}^*$	27.08	$6.79 \times 10^{+12}$
R61	$\text{CHO}^* + ^*\text{H} \rightarrow \text{CO}^* + \text{H}^*$	0.00	$6.60 \times 10^{+11}$
R62	$\text{CO}^* + \text{H}^* \rightarrow \text{CHO}^* + ^*\text{H}$	81.97	$1.67 \times 10^{+13}$
R63	$\text{CH}_2^* + \text{O}^* \rightarrow \text{HCHO}^* + ^*\text{H}$	22.27	$2.35 \times 10^{+10}$
R64	$\text{HCHO}^* + ^*\text{H} \rightarrow \text{CH}_2^* + \text{O}^*$	7.80	$3.77 \times 10^{+11}$
R65	$\text{HCHO}^* + \text{O}^* \rightarrow \text{HCOOH}^* + ^*\text{H}$	0.00	$2.89 \times 10^{+12}$
R66	$\text{HCOOH}^* + ^*\text{H} \rightarrow \text{HCHO}^* + \text{O}^*$	94.28	$9.75 \times 10^{+12}$
R67	$\text{HCOOH}^* + ^*\text{H} \rightarrow \text{COOH}^* + \text{H}^*$	36.01	$1.70 \times 10^{+13}$
R68	$\text{COOH}^* + \text{H}^* \rightarrow \text{HCOOH}^* + ^*\text{H}$	88.65	$3.10 \times 10^{+12}$
R69	$\text{H}_2\text{O}^* + ^*\text{H} \rightarrow \text{OH}^* + \text{H}^*$	93.59	$1.44 \times 10^{+13}$

R70	$\text{OH}^* + \text{H}^* \rightarrow \text{H}_2\text{O}^* + *$	29.02	$2.00 \times 10^{+13}$
R71	$\text{OH}^* + * \rightarrow \text{O}^* + \text{H}^*$	63.92	$3.19 \times 10^{+13}$
R72	$\text{O}^* + \text{H}^* \rightarrow \text{OH}^* + *$	98.61	$4.90 \times 10^{+13}$
R73	$\text{H}_2\text{O} + \text{S} \rightarrow \text{H}_2\text{O-S}$	0.00 ^a	$4.91 \times 10^{+04}$
R74	$\text{H}_2\text{O-S} \rightarrow \text{H}_2\text{O} + \text{S}$	44.53	$1.39 \times 10^{+13}$
R75	$\text{H}_2\text{O-S} + \text{S} \rightarrow \text{OH-S} + \text{H-S}$	11.92 ^a	$1.44 \times 10^{+13}$
R76	$\text{OH-S} + \text{H-S} \rightarrow \text{H}_2\text{O-S} + \text{S}$	38.37	$2.00 \times 10^{+13}$
R77	$\text{OH-S} + \text{S} \rightarrow \text{O-S} + \text{H-S}$	0.00 ^a	$3.16 \times 10^{+13}$
R78	$\text{O-S} + \text{H-S} \rightarrow \text{OH-S} + \text{S}$	42.05	$4.90 \times 10^{+13}$
R79	$\text{H}_2 + 2\text{S} \rightarrow \text{H-S} + \text{H-S}$	54.86	$1.47 \times 10^{+05}$
R80	$\text{H-S} + \text{H-S} \rightarrow \text{H}_2 + 2\text{S}$	71.35	$4.41 \times 10^{+12}$
R81	$\text{O-S} + * \rightarrow \text{O}^* + \text{S}$	0.00	$1.00 \times 10^{+13}$
R82	$\text{O}^* + \text{S} \rightarrow \text{O-S} + *$	0.00	$1.00 \times 10^{+00}$

^a represents values obtained in the model using UBI-QEP method and verified as acceptable using values from theoretical and experimental publications [23–26].

Ethanol and water are proposed to molecularly adsorb on the Ni surface (R1-R2 and R3-4, respectively). The mode of adsorption of water on CeO₂ (stoichiometric or reduced) is a subject of enduring debate with varying views having been provided by relevant computational studies. Density functional calculations using the generalised gradient approximation (DFT-GGA+U) performed by Watkins et al. [25] concluded that water dissociatively adsorbs on stoichiometric CeO₂ surface and more rapidly dissociates on reduced CeO₂. On the other hand, Fronzi et al. [23] performed DFT implementing *ab initio* atomistic thermodynamics approach and concluded that the most stable configuration involves molecularly adsorbed water forming two O-H bonds on either ideal CeO₂ or reduced CeO₂ surface, with the latter having a stronger binding energy. Molinari et al. [27] using DFT-GGA+U concluded that the dissociative adsorption mode is coverage dependent as at higher coverages of water the molecular adsorption is favourable due to reduced interaction between the adsorbed molecules. In the current model, water is proposed to molecularly adsorb on the ceria surface (R73-74). The adsorbed water on either type of active site further dissociates to hydroxyl (OH-S) and hydrogen (H-S) on the support (R75-76) and OH* and H* on the metal (R69-70). The hydroxyl formed on the support (OH-S) further dissociates to form oxygen (O-S) and hydrogen (H-S), the latter of which associatively desorbs to produce gas phase hydrogen *via* R79-80. All the reactions on the support are made possible by the existence of oxygen vacancies that are replenished by these reactions. The mobile oxygen species from the support can transfer to the metal sites *via* a non-activated process R81-82. The

reaction barriers for the support site reactions are calculated using UBI-QEP method. This method is mostly used for metals and not metal oxides, therefore, the values obtained are compared to those obtained from theoretical and experimental studies of the adsorption and dissociation of water on ideal and reduced Ceria. The values were aggregable and acceptable. The possible dehydrogenation pathways of ethanol on Ni from our previous work [7] proceeding *via* the O-H abstraction or α -H abstraction forming ethoxy (R17-18) or 1-hydroxyethyl (R15-16) are included in the network. Both pathways further lead to the formation of acetyl *via* consecutive dehydrogenation steps described in R19-28. Following acetyl's formation, alternate pathways can take place, including dehydrogenation and oxidative dehydrogenation, and C-C cleavage at various stages of dehydrogenation, according to R29-46. The most dehydrogenated species CCO can react with O, leading to the production of adsorbed CO (R47-48). Water-gas shift (WGS) is described in the reaction of CO* with oxygen or hydroxyl surface species towards the formation of CO₂ in R49-R54. The hydrogenation/dehydrogenation and reforming reactions of CH_x* formed following C-C cleavage are finally accounted for in R55-R58. Methane and hydrogen dissociatively adsorb whilst acetaldehyde and the carbon oxides are adsorbed molecularly.

6.3 Results

6.3.1 Model validation

The microkinetic model developed in this work is fully defined on the basis of two sets of parameters: chemisorption enthalpies, Q_i , and fractions of local entropy, $F_{loc,i}$. Table 6.3 shows the final estimated values for the parameters of the microkinetic model after regression along with their 95% confidence intervals. The initial values of the adsorption enthalpies of most of the species were obtained from the previous work on ESR over Ni/SiO₂ [7] that in turn had been initialised based on and compared against literature DFT results. The adsorption enthalpies of H₂O and H on the CeO₂ surface, were obtained from literature DFT and experimental studies [23,24], whilst the others were initialized at physically realistic values. The fractions of local entropy were initialized at arbitrary values, again within physically realistic limits ($\lesssim 1$). Based on the results of the sensitivity analysis the parameters that showed little or no sensitivity were fixed at literature values. The squared multiple correlation coefficient value obtained for the regression was close to unity ($R^2 = 0.916$), which coupled with the high F-value (266.08) for the global significance of regression (tabulated value = 3.01), confirm the model's good performance. The values of all model parameters used, including the chemisorption enthalpies and F_{loc} fitting factors, all conform to physically realistic values, providing confidence that the

respective activation energies and overall rates of surface pathways are well represented. This section focuses on the model's description of the experimentally obtained results.

Table 6.3: Estimated model parameters with 95% confidence intervals. Chemisorption enthalpy values without confidence intervals were adopted from the literature sources shown and kept fixed, while those with confidence intervals were regressed using as initial values the respective literature values from the sources shown.

Species	Chemisorption enthalpy, Q (kJ/mol)	Source for initial or used value	Fraction of local entropy, F_{loc}
CH ₃ CH ₂ OH	45.84	[28]	1.0
H ₂ O	58.94	[29]	1.0
CO ₂	25.68	[13,29]	0.978 ± 0.0042
CH ₃ CHOH	181.4 ± 1.62	[28]	0.991 ± 0.001
CH ₃ CHO	71.04	[29]	1.0
CH ₃ CH ₂ O	171.54	[28]	1.0
OH	242.2	[29,30]	1.0
H	257.0	[29,31]	1.0
O	453.0	[13]	1.0
CH ₃ COH	214.2 ± 1.08	[29]	1.0
CH ₃ CO	192.4 ± 0.91	[29]	1.0
CH ₂ CO	84.6	[29]	1.0
CHCO	283.94 ± 0.62	[29]	1.0
COOH	250.01	[13]	1.0
CO	113.44	[13]	0.941 ± 0.012
CH ₃	200.48	[13,29]	1.0
CH ₂	391.73	[13]	1.0
CH	556.07	[13]	1.0
CCO	501.69	[29]	0.989 ± 0.0014
CHO	206.69	[13]	1.0

HCHO	23.68	[30]	1.0
HCOOH	65.01	[31]	1.0
H ₂ O-S	54.24	[23,24,32]	1.0
OH-S	358.6 ± 0.83	[26,33]	1.0
H-S	150.8	[24]	1.0
O-S	401.2 ± 2.13		1.0

To underline the need for the consideration of the support's role on the reaction mechanism, a single-site microkinetic model accounting only for the activity on the Ni metal was implemented following similar procedures as discussed above and previously [7]. Using this model to describe the ESR experimental data obtained over the CeO₂ containing Ni catalyst, an overall poor fit between the experimental and model results is obtained as evident from the parity plot shown in Figure 6-1. Strong quantitative deviations are particularly observed in the description of the products formation, reinforcing the necessity of explicitly considering the impact of the support on the kinetic pathways, in line with the experimental observations that identified major selectivity improvements due to the presence of CeO₂ [12].

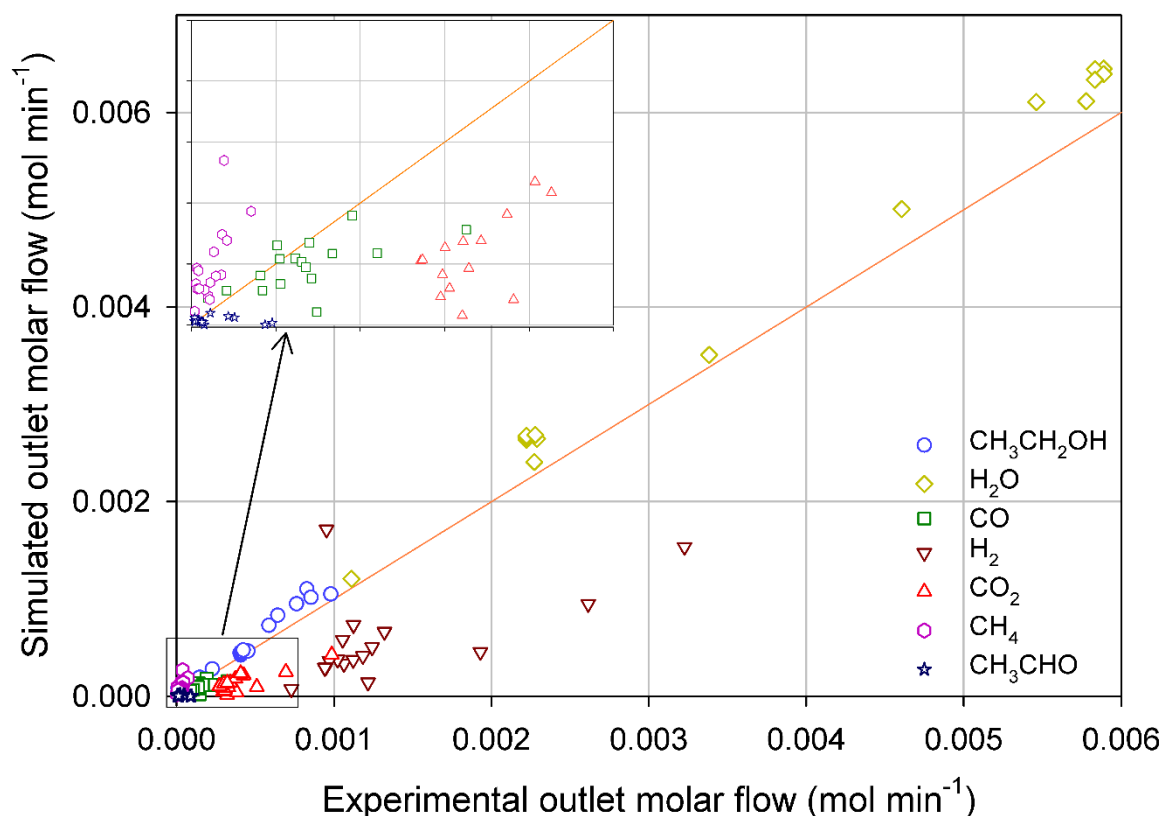


Figure 6-1: Parity plot comparing experimental product molar flow over Ni/CeO₂ with values obtained from model based on a single type of active site.

On the contrary, Figure 6-2, presenting the parity diagrams for the reactant and product species obtained using the bifunctional microkinetic model, shows an overall satisfactory agreement between the experimental results of the ESR over the CeO₂ containing Ni catalyst and the model predicted results. In order to confirm the consistency of the developed dual-site microkinetic model, experimental data over a Ni catalyst supported on inert SiO₂ obtained in a previous study [6] were also modelled. The same kinetic parameters for the reactions on the Ni metal were used in both cases, but for the Ni/SiO₂ simulations all reactions on the support were omitted. Again, a very good agreement between the experimental and model predicted data was achieved as seen in Figure 6-2. The correct description of the outlet molar fraction of the reactants in both cases, indicates the accurate consideration of activation and conversion pathways of the primary reactants over monofunctional or bifunctional Ni catalysts.

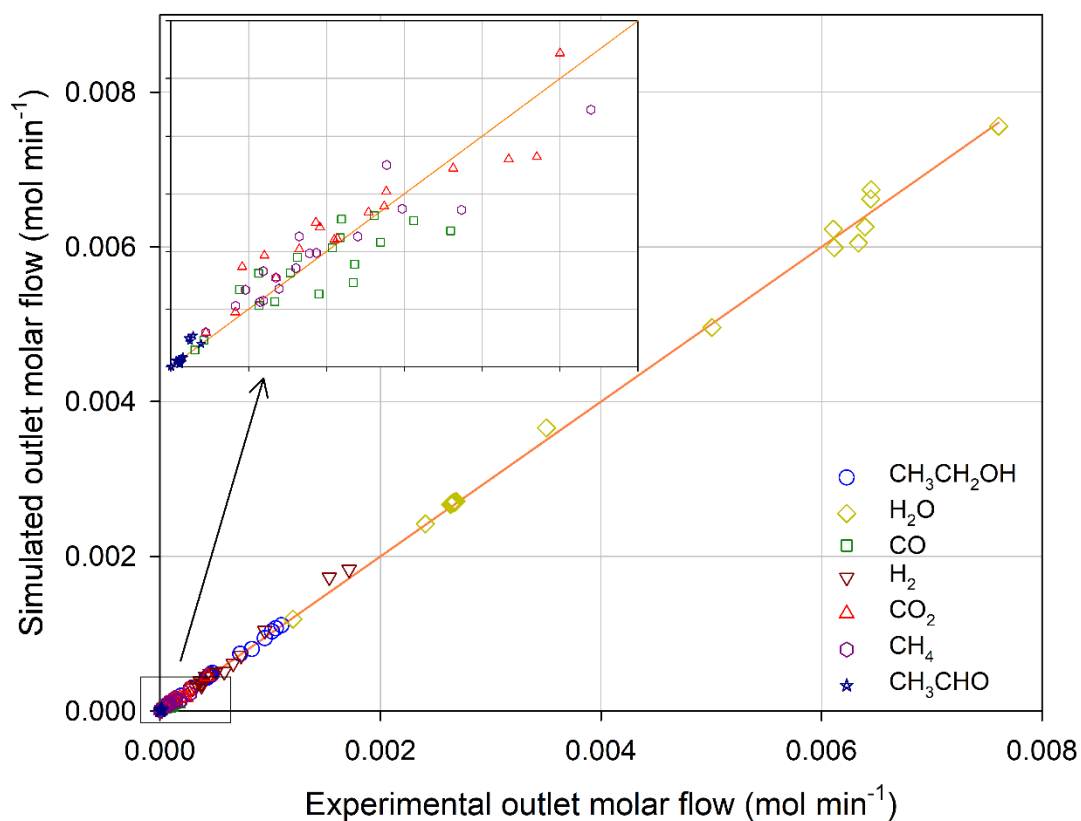
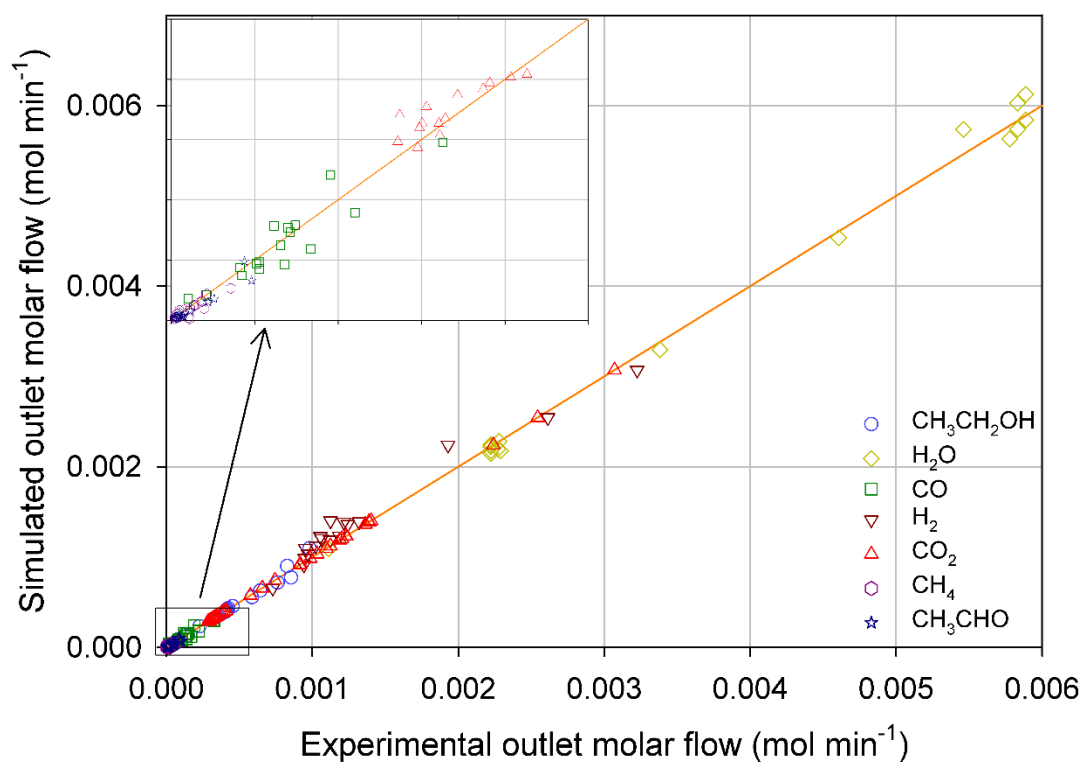


Figure 6-2: Parity plot comparing experimental outlet molar flow over Ni/CeO₂ (top) and Ni/SiO₂ (bottom) with values calculated from the bifunctional microkinetic model.

Performance curves presenting the effect of temperature and the partial pressure of ethanol and water on the conversion of ethanol and water, as well as the carbon selectivities towards CO, CO₂, CH₄ and CH₃CHO, are displayed in Figure 6-3. It is clear that the bifunctional microkinetic model developed is able to reproduce well all experimental trends using the parameters reported in Table 6.3, improving significantly on the predictions of the metal only, single site, model. Of particular attention in the experimental results was the CO₂ carbon selectivity being dominant even at low temperatures and further increasing with temperature (Figure 6-3a). Concurrently, a decrease in the selectivity of CO and a very low production of CH₄ and CH₃CHO throughout the temperature range studied were noted [12]. These selectivity trends clearly differed from those obtained over Ni/SiO₂ [6], where at low temperatures the carbon selectivity towards CO, CH₄ and CH₃CHO significantly outweighed that of CO₂. The experimental results indicated that, even at low temperatures, the activity of CeO₂ and particularly its well-recognised Oxygen Storage Capacity (OSC) and associated high oxygen mobility promoted the secondary WGS and methane steam reforming (MSR) reaction pathways. CH₃CHO is reported to mostly be a primary product in the reaction mechanism [6,34–37], therefore improved conversion and the promotion of secondary reactions further led to a much lower affinity for CH₃CHO production. These kinetic behaviours against temperature are all accurately reproduced by the model in Figure 6-3a, indicating that the surface pathways leading to product formation are accurately described.

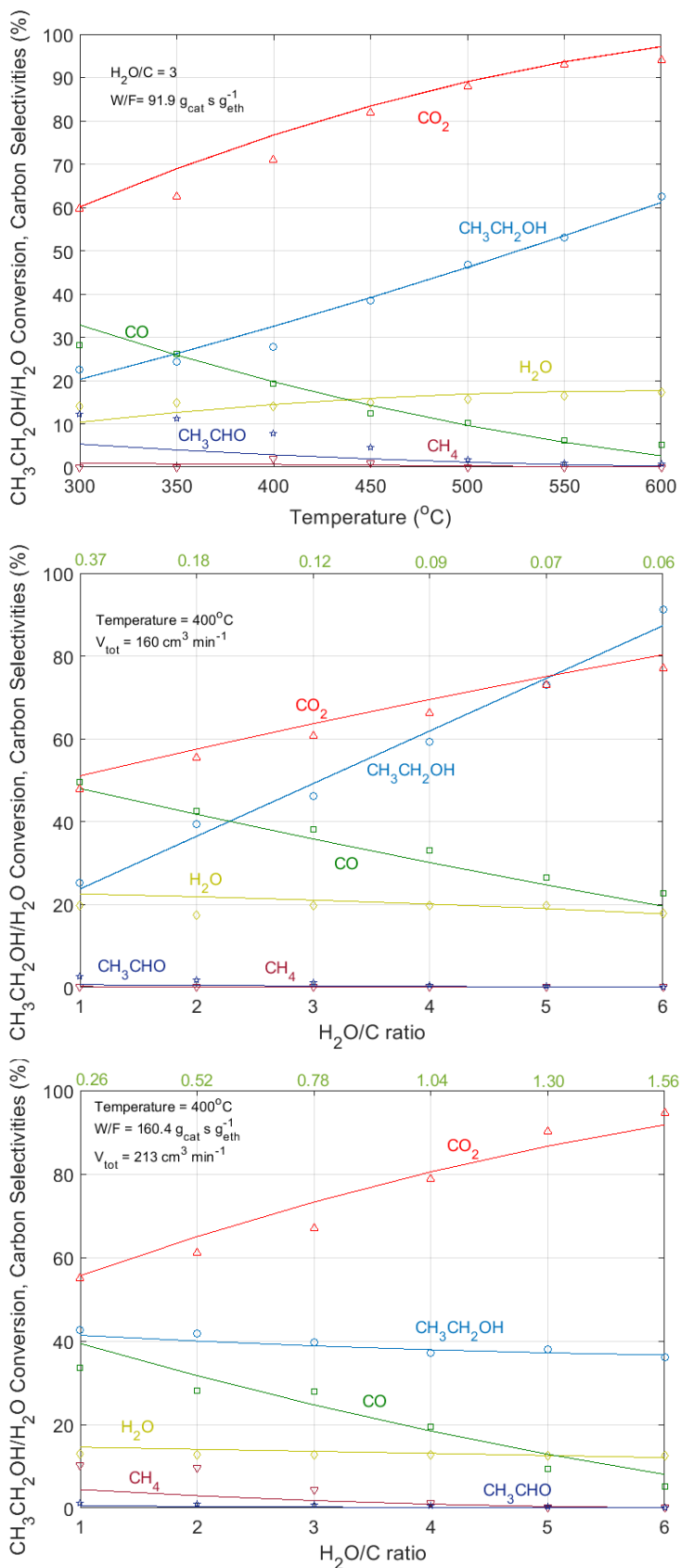


Figure 6-3: Comparison of model predicted conversions and selectivities over Ni/CeO₂ catalyst (lines) with experimental results (symbols). Operating conditions are indicated on the respective panels.

Figure 6-3b presents the effect of ethanol partial pressure at constant water partial pressure and total pressure, while in Figure 6-3c the effect of water partial pressure at constant ethanol partial pressure and total pressure is shown. When the ethanol partial pressure is varied the model correctly predicts an increase in the conversion of ethanol and selectivity towards CO₂, concurrent to a decrease in CO selectivity, in line with experimental observations. The water partial pressure variation, again in close agreement with experimental trends, shows a mild decrease in the conversion of ethanol, however the selectivity towards CO₂ increases whilst that of CO declines. In both cases there is minimal production of CH₄ and CH₃CHO. The observed selectivity trends are consistent with the promotion of secondary reaction pathways resulting from the enhanced presence of water derived surface species. The conversion profiles suggest a positive and slightly negative partial reaction order for ethanol and water, respectively, and are in overall agreement to those obtained over the Ni/SiO₂ catalyst too. However, the substantial production of CO₂ even at the very low H₂O/C of 1 clearly evidences the role of the CeO₂ support and the correct accounting of this effect by the model.

Given the overall good agreement between the model and experimental results across a wide range of conditions, the kinetic relevance of reaction steps of the bifunctional mechanism is further evaluated in the following section.

6.3.2 Kinetic relevance of reaction steps

The pre-exponential factors of each individual surface reaction pair, which were calculated by transition state theory, were varied by a small fraction of their base value. The effect of this perturbation on the conversion of the reactants was quantified by calculating normalised sensitivity coefficients. Figure 6-4 shows the results of the pre-exponential factors sensitivity analysis on the outlet molar flow of ethanol at 400°C and 450°C and at H₂O/C = 3. The most important reaction steps identified by the model all occur in the ethanol dehydrogenation pathway in agreement with previous studies [5,38,39]. The two most prominent steps are seen to be the dehydrogenation of CH₃CHOH* to CH₃COH* and the subsequent dehydrogenation of the latter to CH₃CO*, according to R23-24 and R25-26, respectively. These reactions were also identified as having the largest kinetic relevance when the experimental data over the Ni/SiO₂ were modelled with the bifunctional model but omitting support site reactions. The findings agree with the experimental observations [12] and the discussion in the previous section on the positive order of ethanol, suggesting that the activity of CeO₂ in the support does not alter the overall reaction mechanism.

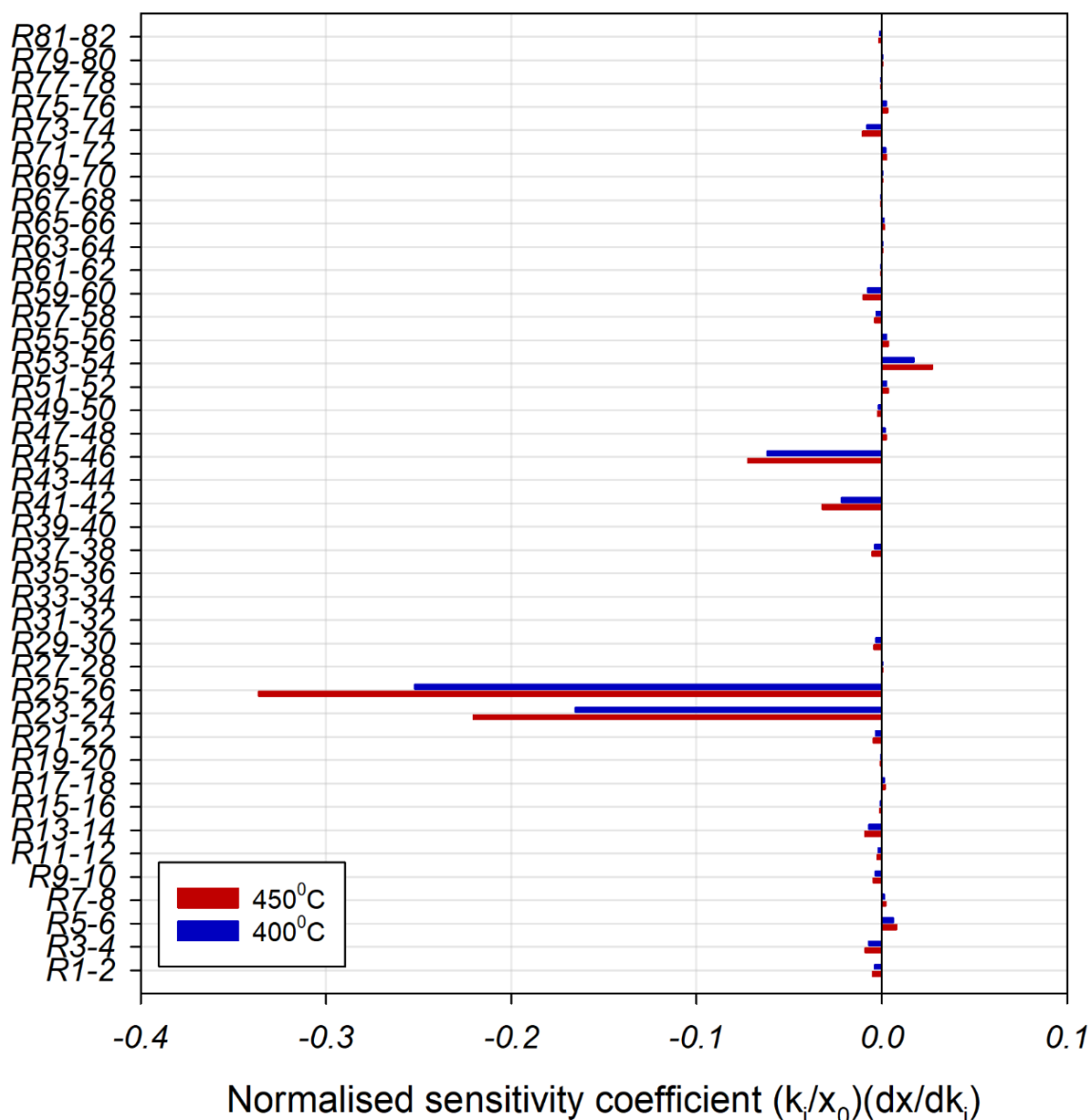


Figure 6-4: Sensitivity analysis of pre-exponential factors of microkinetic model reactions shown in Table 6.2, at 400°C & 450°C and $H_2O/C = 3$ for ethanol outlet molar fraction. Base values for pre-exponential factors are calculated as described in Section Model formulation and computational details.

A positive effect on the conversion of ethanol is also identified for the oxidative dehydrogenation of CH_3CO^* to CH_2CO^* and the oxidative dehydrogenation of $CHCO^*$ to CCO^* according to reactions R41-42 and R45-46, respectively. Importantly, these reactions show no kinetic relevance in the modelled ESR data over Ni/SiO₂ as can be seen in the sensitivity analysis figure in the supplementary information. The C-C cleavage in the ethanol decomposition pathway has been reported to occur at intermediates of different degree of dehydrogenation, namely

CH₃CHO* [2], CH₃CO* [40], CH₂CO* [4] or CHCO* [5,41]. The observed increased relevance of the oxidative dehydrogenation reactions in this case, indicates that the enhanced presence of surface O from the support impacts on the energetics of the dehydrogenation pathway and consequently the intermediate at which C-C cleavage occurs.

The effect of the pre-exponentials perturbation on the outlet molar fractions of CO and CO₂ and H₂ are completely in line with the results of the ethanol sensitivity analysis. R23-24, R25-26, R41-42 and R45-46 are the major kinetically relevant steps for the formation of these species, all positively affecting their production. For CH₄, R41-42 and R45-46 do not display any kinetic relevance. As previously discussed, oxidative dehydrogenation reactions were identified to promote the dehydrogenation of ethanol and cause the C-C cleavage to occur at the fully dehydrogenated CCO* intermediate. This reduces the amount of CH_x* present on the surface and the likelihood of methane desorbing. The figures of the sensitivity analysis for the outlet fractions of all gaseous products can be found in the Supplementary Information. To summarise, the sensitivity analysis revealed steps R23-24, R25-26, R41-42 and R45-46 to be the kinetically important steps under the simulated conditions. This conclusion will be elaborated in the next section, where the reaction steps involved in the overall reaction pathways are probed *via* a contribution analysis.

6.3.3 Reaction pathway analysis

To elucidate the significance and kinetic relevance of the various reaction pathways, a differential contribution analysis at the outlet of the catalyst bed was conducted at the same conditions as those in the previous section. The net formation rates of all carbon containing species are utilised in estimating their conversion percentages to other compounds. Results of the analysis are presented in Figure 6-5 and are discussed below.

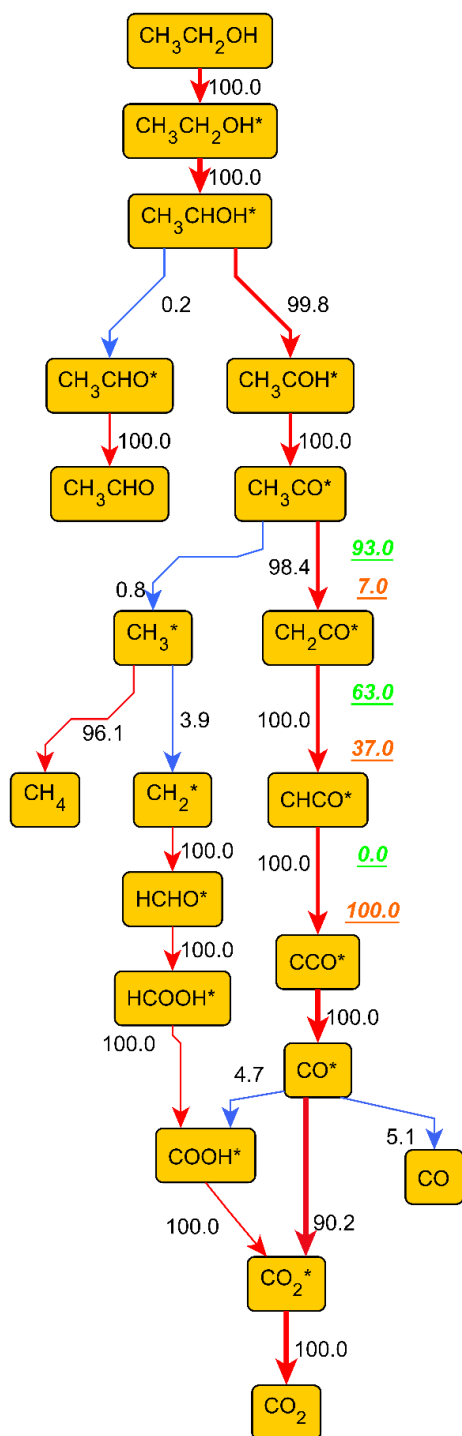


Figure 6-5: Reaction pathway analysis for ethanol steam reforming over Ni/CeO₂ at 400°C and H₂O/C = 3. Net production rates are considered in calculating contribution percentages of carbon containing species towards other species. Colour mapping from blue to red indicates increasing contribution percentages. Line thickness indicates the relative magnitude of the rates of the reaction. The respective contributions of the thermal and oxidative dehydrogenation reaction classes to the dehydrogenation pathway are presented as underlined values in green (top) and orange (bottom), respectively, for instances where the contribution is split.

Note: the cleavage of CH_3CO^* also produces CO^* with a contribution of 0.8% this arrow was removed to keep the figure clean and clear however the minor contribution is accounted for in the results.

According to the model predictions, ethanol adsorbs molecularly *via* R1, and then exclusively converts *via* an α -dehydrogenation to CH_3CHOH^* . After the initial dehydrogenation, CH_3CHOH^* continues dehydrogenating forming CH_3CHO^* and CH_3COH^* *via* R19 and R23, respectively. The latter is the dominant route, with a predicted contribution of 99.8% to ethanol's conversion. This is in line with the discussion in the previous section which identified R23 as a major kinetically relevant reaction step. The formed CH_3COH^* further dehydrogenates towards CH_3CO^* with a 100% conversion contribution *via* R25, which was identified in the previous section as the step with the highest kinetic relevance. The formed CH_3CO^* preferentially dehydrogenates towards CH_2CO^* at a high overall conversion contribution of 99.2%, either directly *via* R31 or oxidatively *via* R41 at respective contributions of 93% and 7%. The decomposition of CH_3CO^* towards CH_3^* and CO^* *via* R29 is a minor pathway at a 0.8% contribution. The CH_3^* formed predominantly desorbs associatively as CH_4 *via* R8, while a small percentage takes part a pathway equivalent to methane steam reforming, forming COOH^* and ultimately CO_2 .

The formed CH_2CO^* exclusively dehydrogenates towards CHCO^* again either directly or oxidatively *via* R35 and R43, respectively. Notably, for this conversion the respective contribution of the oxidative step becomes significant at 37%. Simulating ESR over Ni/SiO₂, the C-C cleavage was predicted to occur at the CH_2CO^* intermediate, with minimal formation of CHCO^* . These results indicate that the abundance of O-species induced by the support activity impacts on the dehydrogenation pathways by the promotion of oxidative steps. This will be further elaborated in the following section.

The formed CHCO^* dehydrogenates to CCO^* , however, interestingly, and in line with previous discussion, this exclusively takes place oxidatively *via* step R45. Reaction of CCO^* with O^* forms CO^* , the latter reacting at a high contribution of ~80% with O^* towards CO_2^* (R54) or with OH^* towards COOH^* *via* R50, also leading to CO_2^* formation. Desorption as gas phase CO accounts only for 5% of the conversion contribution of CO^* .

Regarding the steam-derived surface species, the water is predicted to preferentially adsorb molecularly on the support sites, decomposing further towards H-S and OH-S and eventually O-S and H-S. These series adsorption and dissociation reactions on the support surface are equivalent to the replenishment of oxygen vacancies on ceria by water derivatives. The mobile surface O species on the support easily migrate to the metal according the R81, which is assumed

to be a non-activated process, allowing for an abundance of O* species to build on the metal sites and further react.

6.3.4 Oxidative dehydrogenation of ethanol derivatives

An in-depth analysis of the reaction pathways of ethanol derivatives and the associated surface coverages was carried out to identify the contribution of the support on the overall observed reaction mechanism. Two reaction classes, namely direct and oxidative dehydrogenation, are considered and the contribution of each to the reaction mechanism is assessed.

The first three intermediates along ethanol's main dehydrogenation pathway as presented in the previous section, CH₃CH₂OH*, CH₃CHOH* and CH₃COH*, are initially considered, assessing the activation energies and contribution of the two reaction classes towards the consumption of these species. Three cases are analysed to quantify the impact of the support on the favoured pathway. The first involves the ESR reaction at 400°C and H₂O/C = 3, occurring only on Ni sites. The second accounts for the effect of an increased abundance of steam derivatives by assuming a H₂O/C = 6 again only on Ni sites. The third includes the activity of the support at a H₂O/C = 3.

Table 6.4 shows the contribution of the two reaction classes to the consumption of these ethanol derivatives in the dehydrogenation pathway. Clearly, the direct dehydrogenation is almost exclusively favoured over the oxidative route, with the consumption contribution approaching almost 100% in all scenarios considered, regardless of the H₂O/C ratio or the participation of the support. This result agrees with discussions in the previous sections of the observed partial reaction orders of ethanol (positive) and H₂O (almost zero), as well as the kinetically relevant steps identified not involving any steam derivatives and all occurring in the direct dehydrogenation pathway. The oxidative reactions of these species were therefore not included in the final formulation of the kinetic model.

Table 6.4: Contributions of thermal and oxidative dehydrogenation reaction classes to the consumption of the first 3 dehydrogenation reactants for three different catalytic scenarios at 400°C.

Surface intermediate	Reaction class	Consumption contribution for different catalytic systems during ESR at 400°C		
		H ₂ O/C =3 on Ni sites	H ₂ O/C =6 on Ni sites	H ₂ O/C =3 on Ni/CeO ₂ sites
CH ₃ CH ₂ OH*	Direct dehydrogenation CH ₃ CH ₂ OH* + * → CH ₃ CHOH* + H*	100	100	99.99
	Oxidative dehydrogenation CH ₃ CH ₂ OH* + O* → CH ₃ CHOH* + OH*	0	0	0.01
CH ₃ CHOH*	Direct dehydrogenation CH ₃ CHOH* + * → CH ₃ COH* + H*	100	100	99.96
	Oxidative dehydrogenation CH ₃ CHOH* + O* → CH ₃ COH* + OH*	0	0	0.04
CH ₃ COH*	Direct dehydrogenation CH ₃ COH* + * → CH ₃ CO* + H*	100	100	99.98
	Oxidative dehydrogenation CH ₃ COH* + O* → CH ₃ CO* + OH*	0	0	0.02

Once formed, CH₃CO* may undergo consecutive β-C dehydrogenation steps towards CH₂CO*, CHCO* and CCO*. According to the reaction pathway analysis, C-C scission may also occur at each of these intermediates. These direct and oxidative dehydrogenation reaction classes along with the C-C scission are assessed for the aforementioned three scenarios. Respective results can be seen in Table 6.5.

Table 6.5: Contributions of thermal and oxidative reaction classes as well as C-C scission to the consumption of the other dehydrogenation reactants for three different catalytic scenarios at 400°C.

	Reaction class	Consumption contribution for different catalytic systems during ESR at 400°C			Net reaction rate $Rate_{for} - Rate_{rev}$		
		H ₂ O/C =3 on Ni sites	H ₂ O/C =6 on Ni sites	H ₂ O/C =3 on Ni/CeO ₂ sites	H ₂ O/C =3 on Ni sites	H ₂ O/C =6 on Ni sites	H ₂ O/C =3 on Ni/CeO ₂ sites
CH ₃ CO	Surface intermediate						
	Direct dehydrogenation CH ₃ CO* + * → CH ₂ CO* + H*	100	99.98	92.26	8.98E-05	3.79E-05	3.26E-03
	Oxidative dehydrogenation CH ₃ CO* + O* → CH ₂ CO* + OH*	0	0.02	6.94	6.40E-10	7.33E-07	2.92E-05
	C-C scission CH ₃ CO* + * → CH ₃ * + CO*	0	0	0.8	4.95E-07	2.86E-07	7.95E-07
CH ₂ CO	Direct dehydrogenation CH ₂ CO* + * → CHCO* + H*	0.02	0.01	62.97	7.68E-09	6.32E-09	1.99E-03
	Oxidative dehydrogenation CH ₂ CO* + O* → CHCO* + OH*	0	0	37.03	7.34E-11	8.95E-10	3.06E-04
	C-C scission CH ₂ CO* + * → CH ₂ * + CO*	99.98	99.99	0	8.98E-05	3.79E-05	8.84E-07
CHCO	Direct dehydrogenation	0	0	0	3.16E-11	1.77E-11	2.68E-05

	$\text{CHCO}^* + * \rightarrow$ $\text{CCO}^* + \text{H}^*$						
	Oxidative dehydrogenation $\text{CHCO}^* + \text{O}^* \rightarrow$ $\text{CCO}^* + \text{OH}^*$	0	0	100	6.27E-13	8.22E-12	3.45E-03
	C-C scission $\text{CHCO}^* + * \rightarrow$ $\text{CH}^* + \text{CO}^*$	100	100	0	8.36E-10	2.08E-09	2.29E-06

For the CH_3CO^* intermediate and the scenarios where reactions occur only on Ni, the direct dehydrogenation is favoured over both the oxidative dehydrogenation and the C-C scission reactions both for $\text{H}_2\text{O}/\text{C}$ ratio of 3 and 6 at 100% and 99.98% contribution, respectively. The forward activation barrier of the C-C scission is the lowest at 11.82 kJ/mol, however the net reaction rates calculated as the difference between the forward and reverse reaction rates of CH_3CO^* C-C scission (4.95×10^{-7} , 2.86×10^{-7} , 7.95×10^{-7}) are over 2 orders of magnitude lower than that of direct dehydrogenation for all catalytic scenarios. In the scenario where H_2O activation on the support is possible, there is an abundance of surface O^* species on the metal, while no steam-derived H^* is present on the metal. This significantly alters the surface species coverage, which in turn affects the net rates of all reactions. An improvement in the net reaction rate of the oxidative dehydrogenation is observed, which can be attributed to the increased surface coverage of O^* in turn leading to an increased forward reaction rate for the oxidative dehydrogenation based on the rate equation $r = k[\text{CH}_3\text{CO}^*][\text{O}^*]$, therefore contributing more to the consumption of CH_3CO^* (6.94%). The direct dehydrogenation remains the path with highest contribution at 92.26%, with C-C cleavage to CH_3^* and CO^* comprising the remainder 0.8%.

For the CH_2CO^* intermediate, in the cases considering only the activity of Ni, the C-C cleavage is the dominant pathway accounting for almost 100% of the consumption of CH_2CO^* for both $\text{H}_2\text{O}/\text{C}$ ratios studied with the forward reaction being non-activated. In these cases, the net reaction rate for the C-C cleavage is much higher than that of both dehydrogenation reactions. When the support is active, the direct dehydrogenation is favoured with a 62.97% contribution to the consumption of CH_2CO^* , with the oxidative dehydrogenation accounting for the remaining 37.03% and the C-C cleavage not occurring at all. The net reaction rate for the C-C scission in this case is lower than that of the dehydrogenation reactions. This is attributed to the increased coverage of CO^* causing the reverse reaction rate of the C-C scission to have a higher value, thereby reducing the net reaction rate.

The final dehydrogenation step involves CHCO^* . The C-C cleavage of CHCO^* is estimated again to be non-activated resulting in the species exclusively reacting towards CH^* and CO^* when only Ni is active, for either $\text{H}_2\text{O}/\text{C}$. When the support is accounted for, the oxidative dehydrogenation accounts for 100% of the consumption of CHCO^* . The net rate of the oxidative dehydrogenation (3.45×10^{-3}) is two orders of magnitude higher than that of the direct dehydrogenation (2.68×10^{-5}). This is as a result of the slightly lower forward reaction barrier but significantly higher reverse reaction barrier when compared to the direct dehydrogenation. The oxidative dehydrogenation reaction also has a larger forward pre-exponential than both direct dehydrogenation and C-C scission. When the increased O^* and CO^* coverage is also taken into consideration, with the former positively affecting the oxidative dehydrogenation forward reaction while the latter negatively affects the C-C scission net reaction rate, the resulting exclusive oxidative dehydrogenation of CHCO^* is explained. The formed CCO^* from the oxidative dehydrogenation in this model undergoes a C-C scission with the aid of surface O^* forming two CO^* species in a non-activated forward reaction step.

The changes in surface coverages of CH_x^* , H_2O^* , O^* and OH^* along the catalyst bed for the three scenarios described above is presented in Figure 6-6. When reactions take place only on Ni active sites at a $\text{H}_2\text{O}/\text{C} = 3$, the partial coverage of CH_2^* is the highest amongst the CH_x^* species along the catalyst bed reaching values of 10^{-2} . The CH_3^* and CH^* partial coverages are approximately, one and four orders of magnitude lower than that of CH_2^* . These coverages agree with CH_2^* being formed from the C-C scission of CH_2CO^* as discussed above and then partly undergoing hydrogenation to CH_3^* and eventually CH_4 . The adsorbed H_2O^* dominates the surface with a partial coverage that varies from 0.61 to 0.58 across the bed, while the O^* and OH^* species have much smaller coverages below 10^{-2} values. As a result, the oxidative dehydrogenation of ethanol derivatives is not favoured. Increasing the $\text{H}_2\text{O}/\text{C}$ to 6, the partial coverage of H_2O^* rises to values of 0.74 to 0.72 across the bed, while those of O^* and OH^* species only slightly increase compared to the previous scenario, reaching values of 10^{-2} . The CH_2^* and CH_3^* partial coverages decrease slightly, indicating a more pronounced competition for active sites at the increased H_2O^* presence. The CH^* partial coverage is again the lowest, in agreement with the dehydrogenation pathway terminating at the CH_2CO^* intermediate.

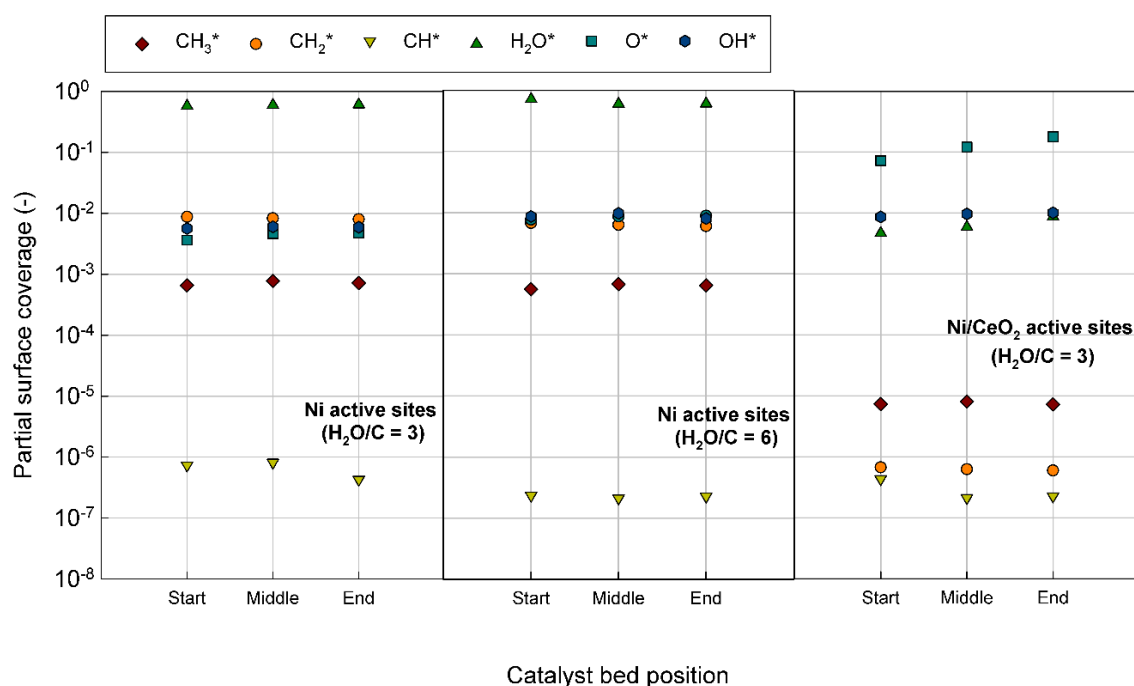


Figure 6-6: Surface coverage of specific species for three different catalytic scenarios at 400°C.

For the case that the support participates in the adsorption and dissociation of water, the partial coverage of H₂O* on the metal is significantly lower (below 10⁻²) as a result of the abundance of active sites on the support available for the adsorption and activation of water. The mobile oxygen species from the support transferring easily to the metal sites causes the partial coverage of O* on the metal to be significantly increased along the bed to values ranging from 0.07 to 0.18. This leads to the oxidative dehydrogenation reactions being more favourable and results in the promotion of the respective pathway as discussed earlier. The partial coverages of all CH_x* species in this scenario are very low, indicating that the C-C scission occurs primarily after the dehydrogenation of CHCO* at the CCO* intermediate. The CH₃* partial coverage appears to be the highest amongst the CH_x* species, explained by the minor C-C scission occurring at the CH₃CO* intermediate.

6.3.5 Model parameter sensitivity

A sensitivity analysis was also performed to identify the significance of the parameters of the microkinetic model, focusing on the adsorption enthalpies. The normalised sensitivity coefficients calculated for the outlet molar fractions of the ethanol and CH₄ when the model parameters are perturbed by 1% of their base value shown in Table 6.3, are presented in Figure 6-7. The adsorption enthalpy of CH₃CHOH is observed to be the one of the most sensitive parameters having a positive impact on the conversion of ethanol. The increase of $Q_{\text{CH}_3\text{CHOH}}$ leads to a reduction of the barrier of the initial dehydrogenation step, a rise in the coverage of CH₃CHOH due to its stronger binding, and an increase of the barrier of the second

dehydrogenation step, overall resulting in a net increase of ethanol's reaction rate. Higher adsorption enthalpies of CH_3COH , CH_3CO , CH_2CO and CHCO have a positive impact on the conversion of ethanol for similar reasons. Kinetically their production reactions are promoted by the reduction of their activation barriers, while their consumption reactions are favoured on account of higher reactant species coverages. The O and OH adsorption enthalpies on the support also impact positively the conversion of ethanol, reducing the dissociation barrier of H_2O and enhancing the supply of O species to Ni. Lastly, the observed negative impact of the adsorption enthalpy of H on ethanol conversion is due to the metal surface saturating by H^* species.

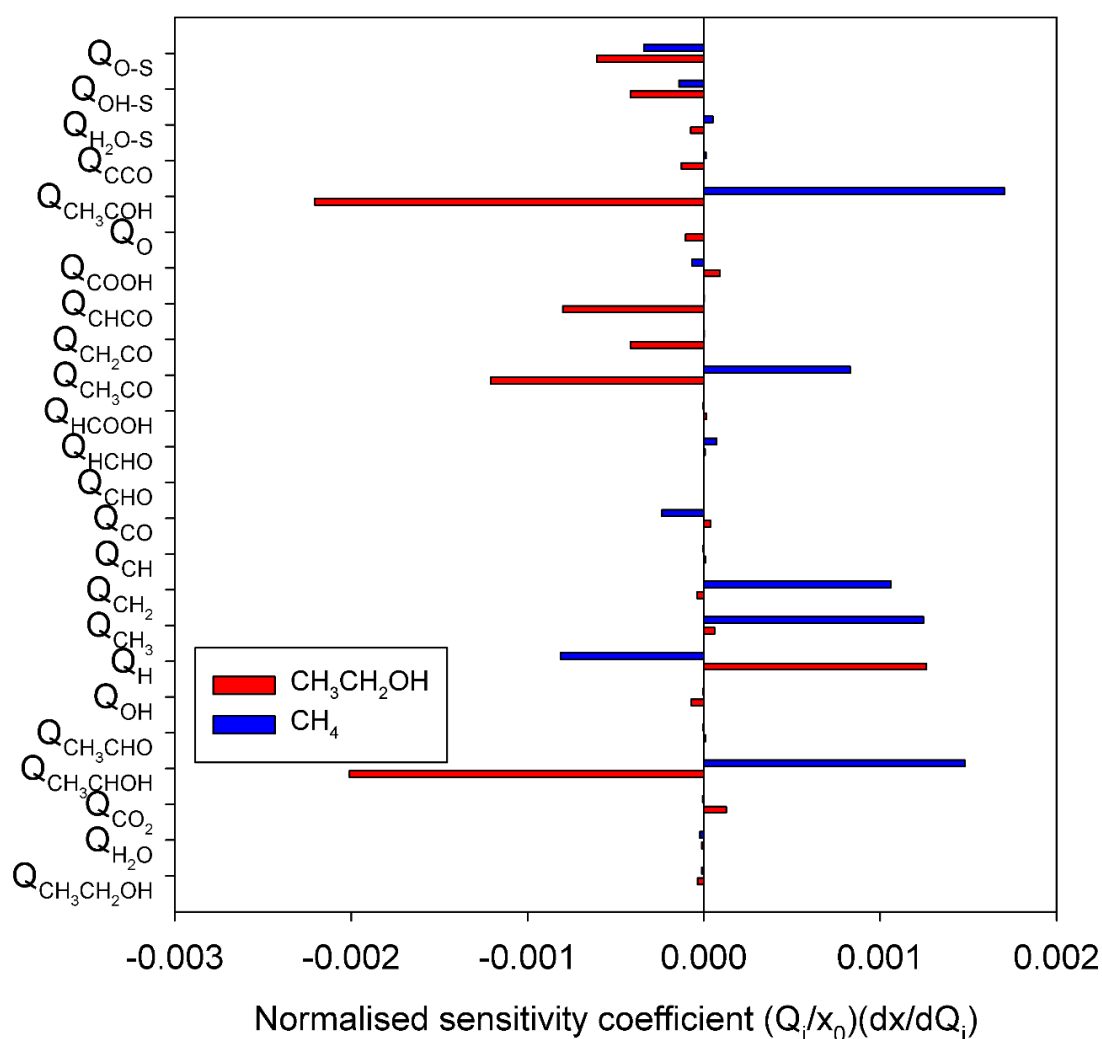


Figure 6-7: Model parameter sensitivity analysis for ethanol and CH_4 outlet molar flow at 400°C and $\text{H}_2\text{O}/\text{C} = 3$. Base values for the parameters are shown in Table 6.3.

The results of the analysis on H_2O and CO , CO_2 and H_2 all show the same qualitative trends, with a positive effect on ethanol outlet molar fraction (reduced conversion) leading to a negative effect on the products molar fractions (lower production) and a positive effect on H_2O (reduced

conversion) and are hence not presented here for brevity. For CH₄, the adsorption enthalpies of CH₂CO and CHCO do not influence the production unlike for the other products, indicating that these species do not participate significantly in the formation pathway of CH₄. Increased CH₃ and CH₂ adsorption enthalpies reduce the activation barriers of C-C cleavage reactions forming them and promote their hydrogenation to CH₄. Finally, the slightly negative impact O and OH adsorption enthalpies on the support have on the production of CH₄ is due to the enhancement of methane steam reforming pathways caused by the increased presence of O* and OH* on the metal surface.

6.4 Conclusions

In the current work a microkinetic model is presented for the ethanol steam reforming over a Ni metal with ceria containing support catalyst and served as a tool for exploring the bifunctional mechanism of the reaction process. The model is used to simulate a wide range of kinetic experimental data. A simple model based on a single active site proved inadequate in describing the obtained kinetic data, whereas a bifunctional model with two distinct types of sites provided satisfactory agreement with the data. The model considers the adsorption of ethanol and its dehydrogenation to various derivatives, to be occurring on the metal sites, whilst the activation and dissociation of water occurs on the ceria support with the O* species migrating freely to the metal sites. The dehydrogenation of ethanol on the metal surface towards 1-hydroxyethyl and subsequently towards CH₃COH* and CH₃CO* were found to be the kinetically relevant steps explaining the experimentally observed positive reaction order for ethanol. The abundance of O* species on the metal, propagated by the support site activity was found to lead to the increased relevance of the oxidative dehydrogenation reaction pathway. The latter caused the C-C scission to occur much later in the dehydrogenation pathway negatively affecting the formation of CH₄. However, the oxidative dehydrogenation was found to only be relevant after the formation of acetyl, up until when the thermal dehydrogenation dominates meaning the kinetically determining formation of 1-hydroxyethyl involves no water-derived species.

References

- [1] A. Akande, A. Aboudheir, R. Idem, A. Dalai, Kinetic modeling of hydrogen production by the catalytic reforming of crude ethanol over a co-precipitated Ni-Al₂O₃ catalyst in a packed bed tubular reactor, *Int. J. Hydrogen Energy*. 31 (2006) 1707–1715. <https://doi.org/10.1016/j.ijhydene.2006.01.001>.
- [2] S.M. Gates, J.N. Russell Jr., J.T. Yates Jr., Bond activation sequence observed in the chemisorption and surface reaction of ethanol on Ni(111), *Surf. Sci.* 171 (1986) 111–134.
- [3] J.H. Wang, C.S. Lee, M.C. Lin, Mechanism of ethanol reforming: Theoretical foundations, *J. Phys. Chem. C*. 113 (2009) 6681–6688.

- <https://doi.org/10.1021/jp810307h>.
- [4] P. Ferrin, D. Simonetti, S. Kandoi, E. Kunkes, J.A. Dumesic, J.K. Nørskov, M. Mavrikakis, Modeling ethanol decomposition on transition metals: A combined application of scaling and brønsted-evans-polanyi relations, *J. Am. Chem. Soc.* 131 (2009) 5809–5815. <https://doi.org/10.1021/ja8099322>.
- [5] J.E. Sutton, P. Panagiotopoulou, X.E. Verykios, D.G. Vlachos, Combined DFT, microkinetic, and experimental study of ethanol steam reforming on Pt, *J. Phys. Chem. C.* 117 (2013) 4691–4706. <https://doi.org/10.1021/jp312593u>.
- [6] M.D. Zhurka, A.A. Lemonidou, J.A. Anderson, P.N. Kechagiopoulos, Kinetic analysis of the steam reforming of ethanol over Ni/SiO₂ for the elucidation of metal-dominated reaction pathways, *React. Chem. Eng.* 3 (2018) 883–897. <https://doi.org/10.1039/c8re00145f>.
- [7] A.T.F. Afolabi, C.Z. Li, P.N. Kechagiopoulos, Microkinetic modelling and reaction pathway analysis of the steam reforming of ethanol over Ni/SiO₂, *Int. J. Hydrogen Energy.* 44 (2019) 22816–22830. <https://doi.org/10.1016/j.ijhydene.2019.07.040>.
- [8] C. Grashinsky, M. Laborde, N. Amadeo, A. Le Valant, N. Bion, F. Epron, D. Duprez, Ethanol steam reforming over Rh(1%)MgAl₂O₄/Al₂O₃: A kinetic study, *Ind. Eng. Chem. Res.* 49 (2010) 12383–12389. <https://doi.org/10.1021/ie101284k>.
- [9] F. Wang, W. Cai, C. Descorme, H. Provendier, W. Shen, C. Mirodatos, Y. Schuurman, From mechanistic to kinetic analyses of ethanol steam reforming over Ir/CeO₂ catalyst, *Int. J. Hydrogen Energy.* 39 (2014) 18005–18015. <https://doi.org/10.1016/j.ijhydene.2014.06.121>.
- [10] L. V Mattos, G. Jacobs, B.H. Davis, F.B. Noronha, Production of hydrogen from ethanol: Review of reaction mechanism and catalyst deactivation, *Chem. Rev.* 112 (2012) 4094–4123. <https://doi.org/10.1021/cr2000114>.
- [11] Y.C. Sharma, A. Kumar, R. Prasad, S.N. Upadhyay, Ethanol steam reforming for hydrogen production: Latest and effective catalyst modification strategies to minimize carbonaceous deactivation, *Renew. Sustain. Energy Rev.* 74 (2017) 89–103. <https://doi.org/10.1016/j.rser.2017.02.049>.
- [12] M.D. Zhurka, A.A. Lemonidou, P.N. Kechagiopoulos, Elucidation of metal and support effects during ethanol steam reforming over Ni and Rh based catalysts supported on (CeO₂)-ZrO₂-La₂O₃, *Catal. Today.* (2020) 1–12. <https://doi.org/10.1016/j.cattod.2020.03.020>.
- [13] P.N. Kechagiopoulos, S.D. Angeli, A.A. Lemonidou, Low temperature steam reforming of methane: A combined isotopic and microkinetic study, *Appl. Catal. B Environ.* 205 (2017) 238–253. <https://doi.org/10.1016/j.apcatb.2016.12.033>.
- [14] A.B. Mhadeshwar, H. Wang, D.G. Vlachos, Thermodynamic Consistency in Microkinetic Development of Surface Reaction Mechanisms, *J. Phys. Chem. B.* 107 (2003) 12721–12733. <https://doi.org/10.1021/jp034954y>.
- [15] L.C. Grabow, A.A. Gokhale, S.T. Evans, J.A. Dumesic, M. Mavrikakis, Mechanism of the water gas shift reaction on Pt: First principles, experiments, and microkinetic modeling, *J. Phys. Chem. C.* 112 (2008) 4608–4617. <https://doi.org/10.1021/jp7099702>.
- [16] J.A. Dumesic, D.F. Rudd, L.M. Aparicio, J.E. Rekoske, A.A. Treviño, *The Microkinetics of Heterogeneous Catalysis*, 1993.
- [17] E. Shustorovich, H. Sellers, The UBI-QEP method: A practical theoretical approach to understanding chemistry on transition metal surfaces, *Surf. Sci. Rep.* 31 (1998) 1–119. [https://doi.org/10.1016/s0167-5729\(97\)00016-2](https://doi.org/10.1016/s0167-5729(97)00016-2).
- [18] E. Shustorovich, *The Bond-Order Conservation Approach to Chemisorption and Heterogeneous Catalysis: Applications and Implications*, *Adv. Catal.* 37 (1990) 101–163. [https://doi.org/10.1016/S0360-0564\(08\)60364-8](https://doi.org/10.1016/S0360-0564(08)60364-8).
- [19] S.D. Angeli, L. Turchetti, G. Monteleone, A.A. Lemonidou, Catalyst development for

- steam reforming of methane and model biogas at low temperature, *Appl. Catal. B Environ.* 181 (2016) 34–46. <https://doi.org/10.1016/j.apcatb.2015.07.039>.
- [20] P.N. Brown, A.C. Hindmarsh, L.R. Petzold, Using Krylov methods in the solution of large-scale differential-algebraic systems, *SIAM J. Sci. Comput.* 15 (1994) 1467–1488.
- [21] H.H. Rosenbrock, An Automatic Method for Finding the Greatest or Least Value of a Function, *Comput. J.* 3 (1960) 175–184. <https://doi.org/10.1093/comjnl/3.3.175>.
- [22] D.W. Marquardt, An algorithm for least-squares estimation of nonlinear parameters, *J. Soc. Ind. Appl. Math.* 11 (1963) 431–441.
- [23] M. Fronzi, S. Piccinin, B. Delley, E. Traversa, C. Stampfl, Water adsorption on the stoichiometric and reduced CeO₂(111) surface: A first-principles investigation, *Phys. Chem. Chem. Phys.* 11 (2009) 9188–9199. <https://doi.org/10.1039/b901831j>.
- [24] G. Vicario, G. Balducci, S. Fabris, S. De Gironcoli, S. Baroni, Interaction of hydrogen with cerium oxide surfaces: A quantum mechanical computational study, *J. Phys. Chem. B.* 110 (2006) 19380–19385. <https://doi.org/10.1021/jp061375v>.
- [25] M.B. Watkins, A.S. Foster, A.L. Shluger, Hydrogen cycle on CeO₂ (111) surfaces: Density functional theory calculations, *J. Phys. Chem. C.* 111 (2007) 15337–15341. <https://doi.org/10.1021/jp071715s>.
- [26] J. Carrasco, D. L opez-Dur an, Z. Liu, T. Ducho n, J. Evans, S.D. Senanayake, E.J. Crumlin, V. Matol n, J.A. Rodr guez, M.V. Ganduglia-Pirovano, In situ and theoretical studies for the dissociation of water on an active Ni/CeO₂ Catalyst: Importance of strong metal-support interactions for the cleavage of O-H bonds, *Angew. Chemie - Int. Ed.* 54 (2015) 3917–3921. <https://doi.org/10.1002/anie.201410697>.
- [27] M. Molinari, S.C. Parker, D.C. Sayle, M.S. Islam, Water adsorption and its effect on the stability of low index stoichiometric and reduced surfaces of ceria, *J. Phys. Chem. C.* 116 (2012) 7073–7082. <https://doi.org/10.1021/jp300576b>.
- [28] O. Skoplyak, M.A. Barteau, J.G. Chen, Ethanol and ethylene glycol on Ni/Pt(1 1 1) bimetallic surfaces: A DFT and HREELS study, *Surf. Sci.* 602 (2008) 3578–3587. <https://doi.org/10.1016/j.susc.2008.09.040>.
- [29] Y.X. Ran, Z.Y. Du, Y.P. Guo, J. Feng, W.Y. Li, Density functional theory study of acetic acid steam reforming on Ni(111), *Appl. Surf. Sci.* 400 (2017) 97–109. <https://doi.org/10.1016/j.apsusc.2016.12.148>.
- [30] I.N. Remediakis, F. Abild-Pedersen, J.K. N rskov, DFT study of formaldehyde and methanol synthesis from CO and H₂ on Ni(111), *J. Phys. Chem. B.* 108 (2004) 14535–14540. <https://doi.org/10.1021/jp0493374>.
- [31] W. Zhao, S.J. Carey, S.E. Morgan, C.T. Campbell, Energetics of adsorbed formate and formic acid on Ni(111) by calorimetry, *J. Catal.* 352 (2017) 300–304. <https://doi.org/10.1016/j.jcat.2017.05.023>.
- [32] Z. Yang, Q. Wang, S. Wei, D. Ma, Q. Sun, The effect of environment on the reaction of water on the ceria(111) surface: A DFT+U study, *J. Phys. Chem. C.* 114 (2010) 14891–14899. <https://doi.org/10.1021/jp101057a>.
- [33] M.R. Li, Y.Y. Song, G.C. Wang, The Mechanism of Steam-Ethanol Reforming on Co₁₃/CeO₂-x: A DFT Study, *ACS Catal.* 9 (2019) 2355–2367. <https://doi.org/10.1021/acscatal.8b03765>.
- [34] J. Sun, X.P. Qiu, F. Wu, W.T. Zhu, H₂ from steam reforming of ethanol at low temperature over Ni/Y₂O₃ and Ni/La₂O₃ catalysts for fuel-cell application, *Int. J. Hydrogen Energy.* 30 (2005) 437–445. <https://doi.org/10.1016/j.ijhydene.2004.11.005>.
- [35] P. Biswas, D. Kunzru, Steam reforming of ethanol for production of hydrogen over Ni/CeO₂ - ZrO₂, *Int. J. Hydrogen Energy.* 32 (2007) 969–980. <https://doi.org/10.1016/j.ijhydene.2006.09.031>.
- [36] T.K. Phung, T.L.M. Pham, A.N.T. Nguyen, K.B. Vu, H.N. Giang, T.A. Nguyen, T.C. Huynh, H.D. Pham, Effect of Supports and Promoters on the Performance of Ni-Based

- Catalysts in Ethanol Steam Reforming, *Chem. Eng. Technol.* 43 (2020) 672–688. <https://doi.org/10.1002/ceat.201900445>.
- [37] A.N. Fatsikostas, X.E. Verykios, Reaction network of steam reforming of ethanol over Ni-based catalysts, *J. Catal.* 225 (2004) 439–452. <https://doi.org/10.1016/j.jcat.2004.04.034>.
- [38] M. Li, W. Guo, R. Jiang, L. Zhao, X. Lu, H. Zhu, D. Fu, H. Shan, Density functional study of ethanol decomposition on Rh(111), *J. Phys. Chem. C* 114 (2010) 21493–21503. <https://doi.org/10.1021/jp106856n>.
- [39] M. Koehle, A. Mhadeshwar, Microkinetic modeling and analysis of ethanol partial oxidation and reforming reaction pathways on platinum at short contact times, *Chem. Eng. Sci.* 78 (2012) 209–225. <https://doi.org/10.1016/j.ces.2012.05.017>.
- [40] J. Zhang, Z. Zhong, X.M. Cao, P. Hu, M.B. Sullivan, L. Chen, Ethanol steam reforming on rh catalysts: Theoretical and experimental understanding, *ACS Catal.* 4 (2014) 448–456. <https://doi.org/10.1021/cs400725k>.
- [41] D. Zanchet, J.B.O. Santos, S. Damyanova, J.M.R. Gallo, J.M.C. Bueno, Toward understanding metal-catalyzed ethanol reforming, *ACS Catal.* 5 (2015) 3841–3863. <https://doi.org/10.1021/cs5020755>.
- [42] M.D. Zhurka, A.A. Lemonidou, J.A. Anderson, P.N. Kechagiopoulos, Kinetic analysis of the steam reforming of ethanol over Ni/SiO₂ for the elucidation of metal-dominated reaction pathways, *React. Chem. Eng.* 3 (2018) 883–897. <https://doi.org/10.1039/C8RE00145F>.
- [43] M.M. Kauppinen, M.M. Melander, A.S. Bazhenov, K. Honkala, Unraveling the Role of the Rh-ZrO₂ Interface in the Water-Gas-Shift Reaction via a First-Principles Microkinetic Study, *ACS Catal.* 8 (2018) 11633–11647. <https://doi.org/10.1021/acscatal.8b02596>.

Supplementary Information

The ethanol steam reforming experimental data over Ni/SiO₂ obtained from the work of Zhurka et al. [42], initially modelled in Chapter 4, was modelled again using the newly designed bifunctional microkinetic model. This was done not only to accentuate the impact the

implementation of support active sites in the microkinetic model makes in the reaction mechanism and pathway, but also to instil confidence regarding the validity and consistency of the newly developed model.

The reactions occurring on the support sites were discarded and only metal site reactions were included in the model. The parity presented below showed great agreement between the model predicted and experimental results. The sensitivity analysis results also presented below showed that the kinetically relevant reaction steps and the important surface species were the same as those observed in the initial metal dominated model in Chapter 4.

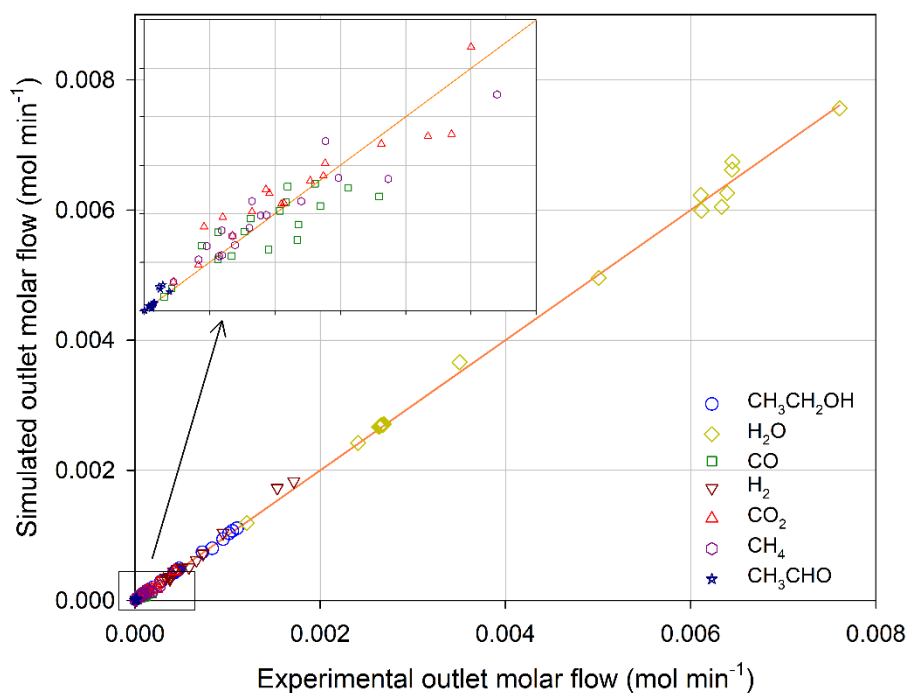


Figure 6-8: Parity plot comparing experimental outlet molar flow over Ni/SiO₂ with values calculated from the bifunctional microkinetic model.

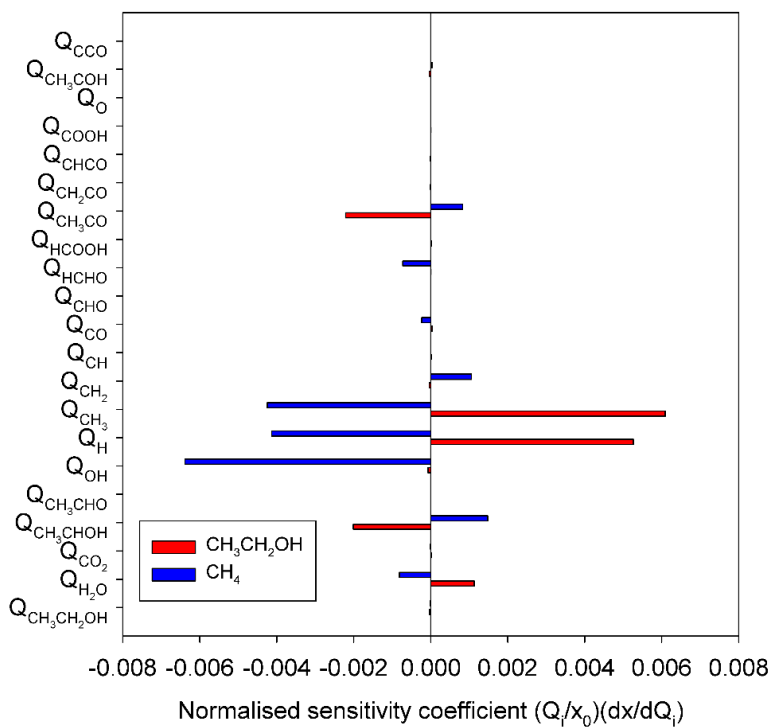
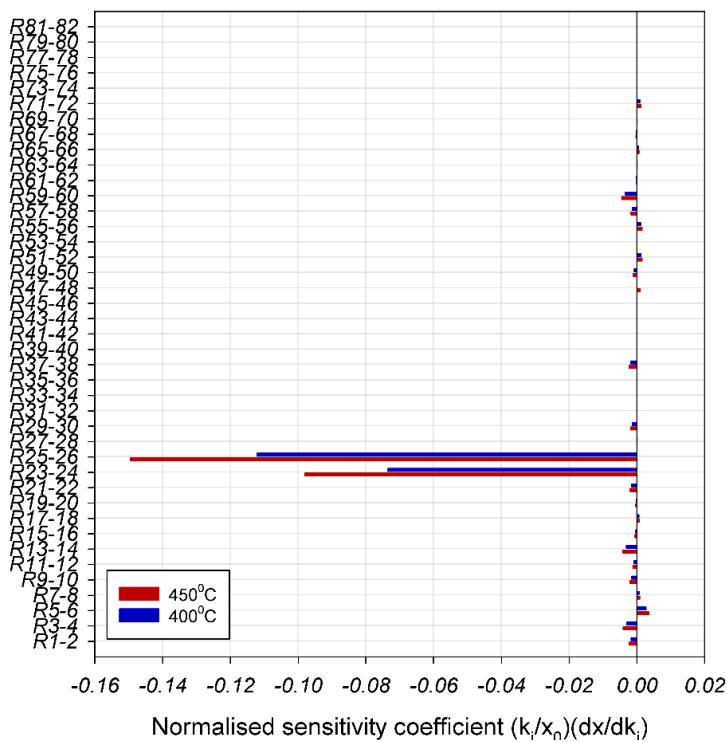
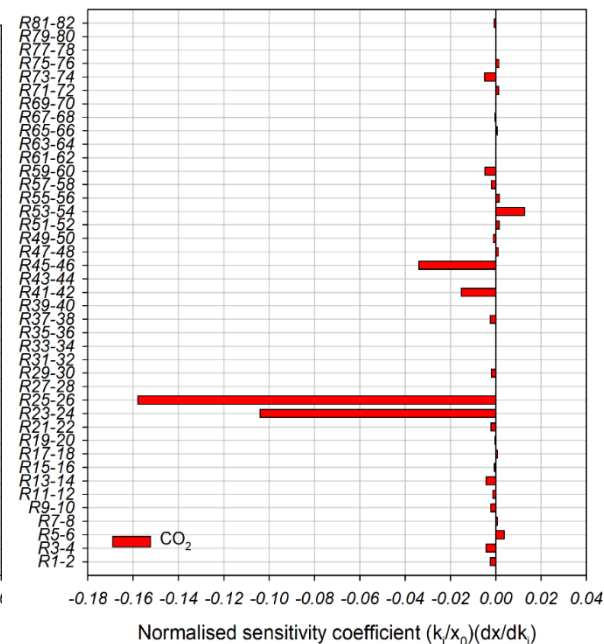
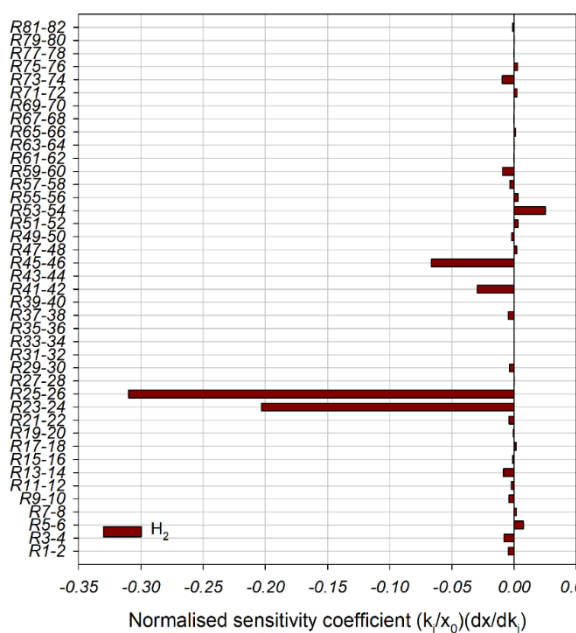
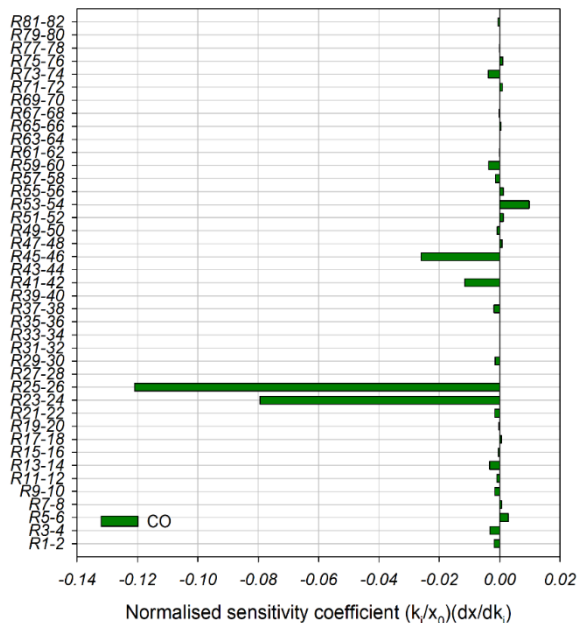
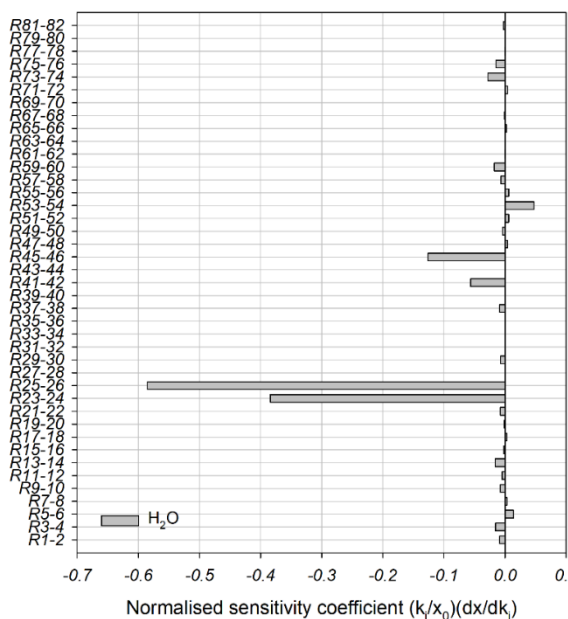


Figure 6-9: Sensitivity analysis of pre-exponential factors of Ni/SiO₂ microkinetic shown in *Error! Reference source not found.* excluding support site reactions, at 400°C & 450°C (H₂O/C = 3) for ethanol outlet molar fraction and model parameters sensitivity analysis for ethanol and CH₄ outlet molar flow at 400°C (H₂O/C = 3).

The results of the sensitivity analysis of the pre-exponential factors displaying the kinetically relevant reaction steps for the production of other gaseous products not presented in the paper are seen below.



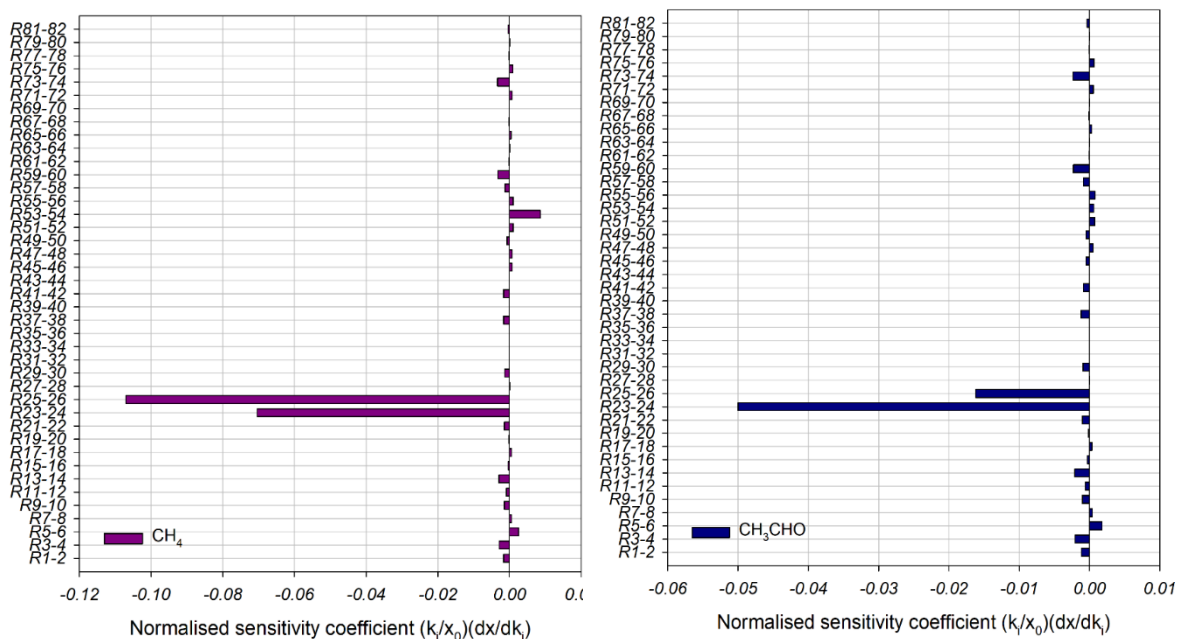


Figure 6-10: Sensitivity analysis of pre-exponential factors of microkinetic model reactions shown in Table 6.2, at 450°C and H₂O/C = 3 for gas product outlet molar fraction. Base values for pre-exponential factors are calculated as described in Section Model formulation and computational details.

Preface to Chapter 7

A version of this chapter has been published in the Fuel Processing Technology Journal (A.T.F. Afolabi, P.N. Kechagiopoulos, Y. Liu, C.Z. Li, Kinetic features of ethanol steam reforming and decomposition using a biochar-supported Ni catalyst, Fuel Processing Technology. 212 (2021) 106622. <https://doi.org/10.1016/j.fuproc.2020.106622>). I was the lead investigator, responsible for all major areas of concept formation, data collection and analysis, as well as manuscript composition. Liu Y. contributed to data collection. Kechagiopoulos P.N. was the secondary supervisory author and was mainly involved in the early stages of concept formation and majority of the manuscript review. Li C.Z. was the main supervisory author on this project and was involved in concept formation and manuscript composition.

The aim of this study was to investigate the reaction mechanism of ethanol steam reforming and ethanol decomposition over a biochar supported Ni catalyst. Proposing biochar as a sustainable alternative to the popular but cost-inefficient metal oxide supports, due to its intrinsic content of surface O-containing functional groups and alkali and alkaline earth metals. The methodology of the kinetic experiments undertaken in this study are presented in the paper as well as in Chapter 3.

CHAPTER 7: KINETIC FEATURES OF ETHANOL STEAM REFORMING AND DECOMPOSITION USING A BIOCHAR-SUPPORTED Ni CATALYST

Ahmed Tijani F. Afolabi,^{a, b} Panagiotis N. Kechagiopoulos,^{b,*} Yurong Liu,^a Chun-Zhu Li^{a,*}

^a Fuels and Energy Technology Institute, Curtin University, GPO Box U1987, Perth, WA 6845, Australia

^b Chemical and Materials Engineering Group, School of Engineering, University of Aberdeen, Aberdeen, AB24 3UE, UK

* Corresponding authors

E-mail addresses: czlicurtin@gmail.com (C.-Z. Li).

p.kechagiopoulos@abdn.ac.uk (P.N. Kechagiopoulos).

Abstract

The catalytic steam reforming of bio-ethanol will provide a sustainable route for renewable hydrogen production in a future hydrogen economy. Ni catalysts will be an economically attractive alternative to noble metals. Biochar is a promising reforming catalyst or catalyst support, having shown already good activity for tar reforming. The structure of biochar, its inherent alkali and alkaline earth metallic species and the content of O-containing functional groups are factors affecting its catalytic performance. A kinetic study of ethanol steam reforming and decomposition over a biochar-supported Ni catalyst is presented in this study in order to elucidate the role of biochar in the reaction mechanism. The effects of temperature, space velocity and reactant partial pressure were investigated over a range of conditions. The chemical structural features of used biochar samples were characterized with Raman spectroscopy. Biochar itself was found to be catalytically active and participating in ethanol reforming and decomposition. It was established that the reactions on Ni and biochar active sites were not independent. Analysis of kinetic compensation effects showed commonality on biochar and suggested that the rate-limiting step occurs in the dehydrogenation pathway on the biochar surface. O-containing functional groups in biochar were observed to reduce with reforming/decomposition time.

Keywords: Ethanol steam reforming; Nickel; Biochar; O-containing functional groups; Reaction mechanism

7.1 Introduction

Hydrogen is considered a clean and sustainable alternative energy carrier as it can be derived from renewable biomass [1–4]. Hydrogen has traditionally been produced from the reforming of natural gas or the gasification of coal. This however leads to high CO₂ emissions. Replacing natural gas and coal with renewable biomass-derived feedstock can contribute substantially in nullifying the environmental impact of the hydrogen production process. As such, oxygenated compounds derived from biomass have become increasingly economically appealing due to their abundance and availability. Bio-ethanol as a feedstock for the catalytic steam reforming has been researched considerably due to its attainability from diverse renewable feedstock through fermentation [5–8].

The kinetics and mechanisms of ethanol steam reforming (ESR) has been the subject of various experimental and theoretical studies, with recent reviews having discussed the current mechanistic understanding [9,10]. A common finding is that the metal catalyst promotes the scission of the C-H and C-C bonds, thus the primary mechanism is dependent on the selected metal as the catalyst.

Various metal catalysts have been investigated including Ni [11–14], Co [11], Pt [15,16], Rh [11,17,18] and Pd [19]. The consensus is that ethanol dehydrogenates, possibly forming acetaldehyde as a primary product, before C-C cleavage occurs leaving CO and CH_x precursors, which would then participate in secondary reactions; water-gas shift (WGS) and methane steam reforming (MSR). The specific dehydrogenation pathway and the level of dehydrogenation prior to C-C cleavage differs based on the metal catalyst used [20]. With minimal trade-off in activity and much higher economic feasibility, Ni has garnered attention and preference over noble metal catalysts for ESR. Early on, the isotopic work of Gates et al. [21], as well as, more recently, the periodic density functional theory (DFT) calculations of Wang et al. [11], describe the decomposition pathway on Ni as proceeding *via* initial dehydrogenation towards ethoxy and further dehydrogenation towards CH₃CHO which is a primary product. The C-C cleavage is likely to occur at the CH₃CHO or CH₃CO intermediates [20].

Recent reviews presenting the progress and advances in ESR on non-noble transition metals [22] and Ni specifically [23] have all highlighted the importance of promoters and support materials on improving the catalyst stability and performance. Nonetheless, high-performance catalysts, particularly if not noble metal based, rely many times on complex formulations [24], e.g. core-shell structures, or are supported on mixed oxides, using a variety of dopants, that unavoidably would increase the cost of catalyst production and the process in a commercial framework.

Biochar is the solid product of biomass pyrolysis and/or partial gasification. Due to its low cost and high porosity, it has garnered significant attention recently as a catalyst or metal catalyst support for various reactions, including reforming, (trans)esterification and hydrolysis [25]. The study of catalytic cracking and steam reforming of tar and its model compounds using biochar-based catalysts has been a major literature focus [26], demonstrating the high reforming and tar destruction activity of biochar-based catalysts [27–30]. In addition, the energy value of the spent biochar can be recovered by combustion or gasification further reducing energy loss and disposal cost [31–33]. Various studies have further shown that the properties of intrinsic alkali and alkaline earth metallic (AAEM) species in biochar contribute to its catalytic activity [33–35]. Biochar produced from pyrolysis and subsequent gasification usually has a high concentration of O-containing functional groups [36]. Previous studies have shown the importance of the O-containing functional groups to the activity of biochar [33,37].

Therefore, utilising biochar as a support material for Ni would allow the further reduction of the overall cost of the reforming process and enhance its sustainability. It can further increase the number of available sites and the available functionalities on the catalyst through the inherent content of surface oxygen containing groups and alkali and alkaline earth metals, potentially enhancing the catalyst stability. There is, however, an evident scarcity in literature with regards to the use of biochar as a catalyst or support for the steam reforming of small, non-aromatic biomass derived oxygenates and the investigation of kinetics for such reaction processes. The steam reforming of acetic acid has been studied recently on Ni/biochar [27,38], however no similar works exist for ethanol. The intrinsic kinetic effect a biochar support would possibly have on the adsorption and reaction pathway in the ethanol reforming process remains unclear.

In this work a comprehensive experimental kinetic study of ESR and ethanol decomposition over a biochar-supported Ni catalyst is presented over a range of experimental conditions in a fixed-bed reactor. Ethanol is selected as the simplest biomass-derived fuel that can allow the study of the simultaneous reactions involving hydroxyl groups and C-C bonds. The activity of biochar support during reforming was investigated and the roles of the carbon structure of biochar, inorganic AAEM species in biochar and Ni are distinguished. Unique reaction features are reported for the first time for this reaction system, including the preferential adsorption and decomposition pathways of ethanol and water on the different types of biochar sites. The possibility of interactions between the Ni and biochar active sites was also investigated. Finally, kinetic compensation effect of the reaction system is studied for the first time detailing the wide range of energies on the Ni/biochar sites, not typically observed on traditional ESR catalysts.

7.2 Experimental

7.2.1 Sample preparation

The samples of biochar utilised were acquired from the Renergi gasification demonstration plant at Curtin University, Australia [39]. The sample was prepared from the pyrolysis and subsequent partial gasification of Mallee wood biomass. The gasification of the sample took place for a duration of 5-10 minutes at temperature of 750-850°C ensuring increased O-containing functional group concentration and in turn increased catalytic activity [31,37]. The presence of surface O-containing functional groups on these samples, specifically of aromatic C – O and C = O structures, was confirmed *via* X-Ray Photoelectron Spectroscopy in previous work [36]. The biochar sample was sieved to obtain two samples of particle size, ranges 106-250 µm and 55-106 µm, respectively. The elemental composition of the biochar (dry and ash-free basis) was 91.5% carbon, 1.0% hydrogen, 0.7% nitrogen and 6.8% oxygen (by difference).

The Ni/biochar catalyst with 10 wt.% Ni was prepared by the commonly applied incipient wetness impregnation method [26,27,38] using Ni(NO₃)₂·6H₂O obtained from Merck as the precursor. The water saturation volume of biochar was determined and then an aqueous solution of precursor was prepared with the same volume of water. The aqueous solution was added to the biochar sample and stirred for 4 hours before being dried in an oven at 105°C overnight. The collected catalyst sample was calcined in Ar flow (100 ml min⁻¹) with a ramp rate of 15°C min⁻¹ to 600°C for 3 hours.

7.2.2 Reactor set up

A quartz tubular fixed-bed reactor of internal diameter 10 mm was used for the catalytic reforming and decomposition of ethanol. The catalyst bed was made up of two layers supported on a porous plate, including a layer of quartz wool to support the bed and then the Ni/biochar catalyst bed mixed with quartz sand to maintain bed height and smooth gas flow through the bed. A thermocouple was placed directly above the catalyst bed to ensure accurate temperature readings. The reactant mixture was fed by an HPLC pump. The feed was preheated using a heating tape set at 150°C prior to reactor inlet. Mass flow controllers (MFC) were used to control the flowrates of nitrogen and hydrogen gas, the former used as the carrier gas and the latter used for catalyst reduction prior to the experimental run. Connected pressure gauges were used to monitor the pressures of the gas flows.

The outlet of the reactor is connected to a three-way valve. The first outlet was connected to a HP Agilent 6890 capillary column GC equipped with pre-column backflush, a flame ionization detector (FID) and a thermal conductivity detector (TCD) for the analysis of total gaseous

product range at regular intervals. The second outlet was connected to three cold traps filled with 50, 40 and 30ml of HPLC-grade CHCl₃/CH₃OH mixture (4:1 volume ratio) in series [40]. The traps are cooled by an ice-water bath (0°C) and two dry-ice baths (-78°C) respectively to collect liquid effluent, which was then analysed in a Agilent 6850 GC/5975B MS.

7.2.3 Experimental conditions and parameters

Prior to experiments the catalyst was reduced at 500°C with a stream of 5% H₂ in N₂ flow of 1 L min⁻¹ for 1 h. To ensure explicit kinetic control, external mass transfer was investigated by varying the carrier gas flow rate from 0.1 to 2.5 L min⁻¹ of N₂ (at 450°C and atmospheric pressure) and observing the changes in the observed reaction rate. Internal mass transfer was investigated by varying the catalyst particle size range of the catalyst and likewise observing the changes in reaction rate. Reaction conditions were chosen to ensure that the observed reaction rates were controlled by the reaction kinetics. This necessitated conversion to be low (typically below 20%) and the operating temperature to be limited up to 450°C.

Reaction temperature was varied in the range of 300-450°C with a fixed reactant H₂O/C (C in feed) of 3 mol_{H₂O}/mol_C and N₂ flow of 2 L min⁻¹ at atmospheric pressure. It is important to note that initial runs were performed with no catalyst in the bed, in order to ascertain the impact of the gas phase reactions. Negligible conversion and no discernible peaks were observed from the gas phase reactions in the temperature range of 300°C to 450°C at H₂O/C ratio of 3.

The partial pressure of water was varied from 15.94 to 88.59 mbar with the partial pressure of ethanol kept at 7.91 mbar. The partial pressure variation experiments were performed at 400°C. The contact time effect was investigated by varying the reactant feed flow from 0.5 to 3.0 ml min⁻¹, corresponding to a catalyst wt./flowrate of ethanol (W/F_{0,ethanol}) of 58 to 349 g_{cat} s g_{eth}⁻¹ (fixed catalyst weight) at 400°C with a fixed H₂O/C ratio of 3 and at atmospheric pressure. All experiments were carried out with a catalyst mass of approximately 0.1000 g.

Thermodynamic equilibrium data were obtained *via* the simulation of a Gibbs reactor (Gibbs free energy minimisation) in Aspen Plus software using the Peng-Robinson equation of state. The data were collected in terms of the parameters: conversion, selectivity and yield. The experimental equivalents of these parameters were calculated as shown below:

$$\text{Conversion: } X_C = \frac{F_{Eth}^{In} - F_{Eth}^{Out}}{F_{Eth}^{In}} \times 100\%$$

$$\text{Carbon selectivity of } y \text{ compound: } S_c(y) = \frac{F_y^{out}}{\sum F_{Carbon\ products}^{out}} \times 100\%$$

$$\text{Hydrogen yield: } Y_{H_2} = \frac{F_{H_2}^{out}}{n \times F_{Eth}^{in}} \times 100\%$$

where F^{in} and F^{out} represent inlet and outlet flowrates, respectively. n equals 6 and 3 for steam reforming and decomposition experiments, respectively.

Measured ethanol consumption rates were used to construct Arrhenius plots through the assumption of a pseudo-first-order reaction rate in ethanol partial pressure for both reforming and decomposition experiments:

$$r = kP_{Eth}; \quad k = Ae^{\frac{-E_a}{RT}}$$

7.2.4 Biochar characterization

Raman spectroscopy has been extensively implemented in characterising the chemical structure of biochar [41–44]. The structural features of the aromatic ring systems as well as the O-containing functional groups of the biochar samples obtained in this study were analysed using a Perkin-Elmer Spectrum GX FT-IR/Raman spectrometer. The procedure was adopted from the work of Li et al. [41] and has been described in detail in a previous study [42]. Briefly, 0.25 wt.% biochar sample was mixed with KBr and then ground and scanned. A baseline-corrected Raman spectrum in the range of 800-1800 cm^{-1} was fitted with 10 Gaussian bands [41]. Large aromatic ring systems with 6 or more fused benzene rings were represented by the assigned D band at 1300 cm^{-1} , while the G_R (1540 cm^{-1}), V_L (1465 cm^{-1}) and V_R (1380 cm^{-1}) bands represented the smaller aromatic ring systems containing 3-5 fused benzene rings. The total Raman peak area in the spectral range of 800-1800 cm^{-1} was used to reflect the relative content of O-containing functional groups that generate a resonance effect together with their attached aromatic ring systems.

7.3 Results and discussion

7.3.1 Ethanol steam reforming catalysed by biochar supported Ni.

Figure 7-1a depicts the effect of reaction temperature on ESR catalysed by Ni/biochar. The conversion of ethanol increases from 1.8% to 30% with increasing temperature from 300°C to 450°C. The hydrogen yield observed increases concurrently with conversion, with a yield of 21% obtained at 450°C. The observed selectivity trends in Figure 7-1b & c, are qualitatively similar to the common trends in literature for ESR catalysed by Ni [14,45–47]. The selectivity of CH_3CHO decreased while those of CO and CH_4 increased with temperature, these trends being consistent with the promotion of dehydrogenation of ethanol and decomposition of CH_3CHO as

temperature increases. The selectivity of CO₂ also increased with temperature, which is consistent with the presence of some water-gas shift activity. However, when the ratio of CO/CO₂ across the temperature range is considered, the values, though decreasing with temperature, stay consistently above 1. Additionally, the observed CO/CH₄ ratio is seen to be almost constant through the temperature range at about 1.2, indicating the lack of strong secondary reaction activity to affect the decomposition products distribution. Ni is typically known to promote the water-gas shift reaction at temperatures of 400°C and above, with CO/CO₂ ratios approaching equilibrium values (0 to 0.2) at 450°C and higher, as is evidenced in the results by Zhurka et al. [14] and Vicente et al. [45] of ESR catalysed by Ni supported on inert SiO₂. It can therefore be inferred that the presence of biochar has in some way altered the reaction mechanism commonly exhibited on Ni.

The Arrhenius plot for this temperature range is shown in Figure 7-2, from which an apparent activation energy of about 70 kJ mol⁻¹ is calculated.

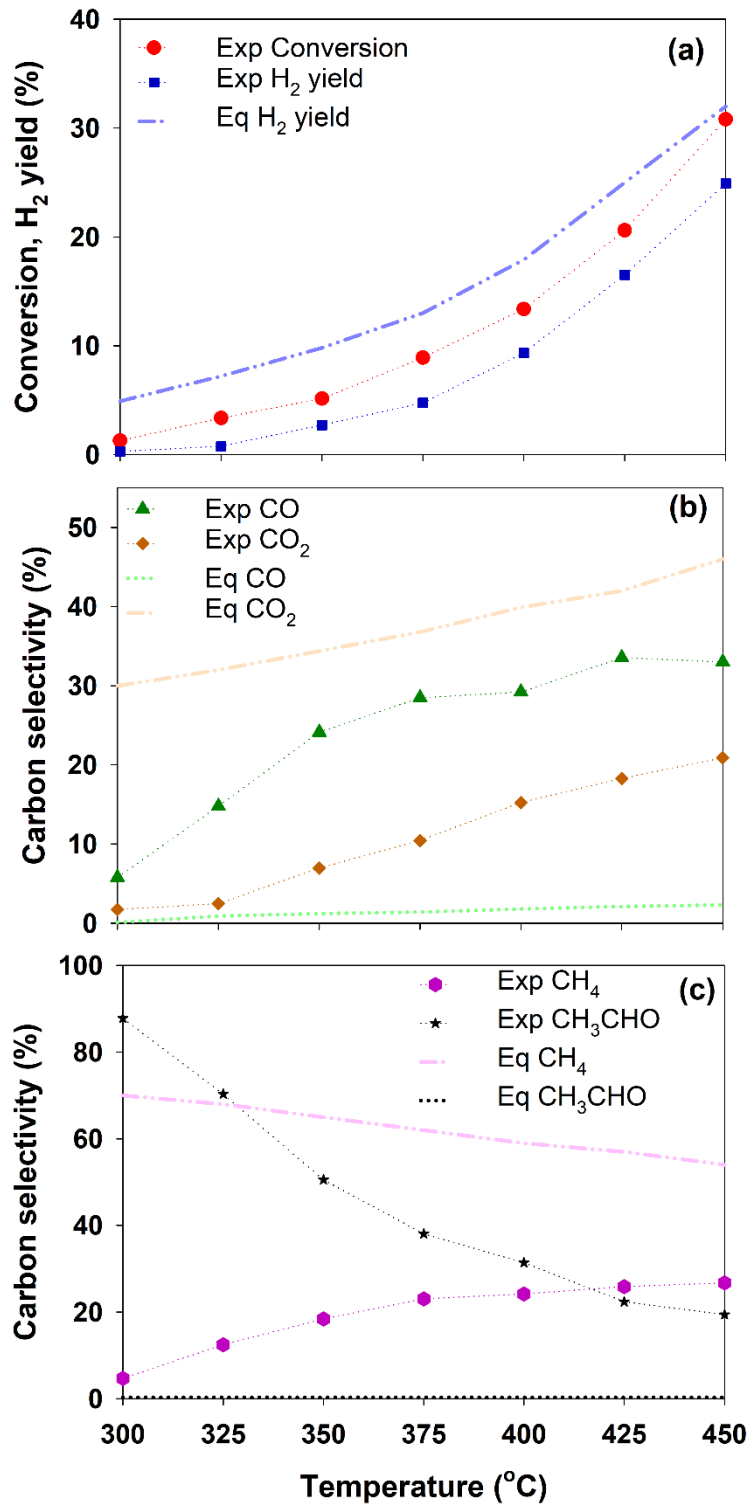


Figure 7-1: Effect of temperature on conversion and H₂ yield (a), carbon selectivities of CO & CO₂ (b) and CH₄ & CH₃CHO (c) during ESR catalysed by Ni/biochar compared with equilibrium (Exp = experimental, Eq = equilibrium) ($S/C = 3$, $W/F_{Eth} = 90.9 \text{ g}_{cat} \text{ s}^{-1} \text{ g}_{Eth}^{-1}$).

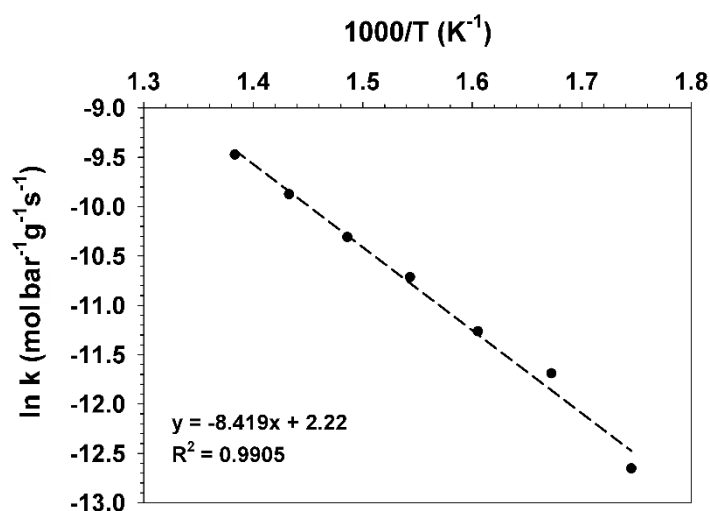


Figure 7-2: Arrhenius plot of ESR catalysed by Ni/biochar (S/C = 3, W/F_{Eth} = 90.9 g_{cat} s⁻¹ g_{Eth}⁻¹).

Typically, during ethanol reforming over Ni catalyst [9,14,21], CO and CH₄ are formed from the decomposition of ethanol. The surface adsorbed precursors of CO and CH₄ undergo WGS and MSR to produce CO₂ and increase H₂ yield. In previous studies on Ni [14,45] where there exists only one type of active site and both the ethanol-derived species and the steam-derived species adsorb on the same type of site, the active species of both ethanol and steam are close enough in proximity to readily react. In this study, besides Ni, there exists two or more different types of active sites for the, possibly preferential, adsorption of ethanol-derived species and steam-derived species, including AAEM and, more importantly, O-containing functional groups on the biochar surface. Depending on reaction intermediate type, the strength of adsorption on Ni/biochar during acetic acid reforming has been seen to vary with the amount/type of O-containing functional groups [38]. H radicals on the biochar surface interacting with O-containing functional groups have been suggested to affect (reduce) tar reforming reactivity [36].

It follows then that a possible strong binding of ethanol-derived species at sites different or not in proximity to those occupied by steam-derived species would allow ethanol derivatives to undergo dehydrogenation to CH₃CHO and decomposition towards CO and CH₄ with limited probability of further reforming and performing WGS or MSR. Another explanation could be the occurrence of a H-rich catalyst surface as a result of the dehydrogenation and decomposition reactions. This could alter the working state of the biochar surface or lead to a partial occupation of active sites through the consumption or modification of O-containing functional groups, disrupting the dynamic equilibrium of all surface species and affecting product distribution. This could also inhibit the dissociative adsorption of H₂O, leading to a scarcity of oxygen required

for the promotion of secondary reactions on the surface. An abundance of surface H-species could also affect the WGS equilibrium and cause formed CO_2 to be consumed by other reactions.

The effects of varying the partial pressure of water on ethanol conversion and H_2 yield were investigated and are presented in Figure 7-3. The experiments were conducted at a constant overall pressure, a constant partial pressure of ethanol and a constant total volumetric flow maintained by controlling the N_2 gas flow. The conversion of ethanol is relatively constant with the observed decrease from 15.2% to 14.6% with increase in partial pressure of water being almost within acceptable error range. Figure 7-3 also presents the carbon selectivity of products with corresponding equilibrium selectivity data for this experiment. At high partial pressures of water, the water-gas shift reaction appears to be more promoted, with CO/CO_2 ratios below 1 and CO/CH_4 ratio decreasing as the partial pressure of water increases.

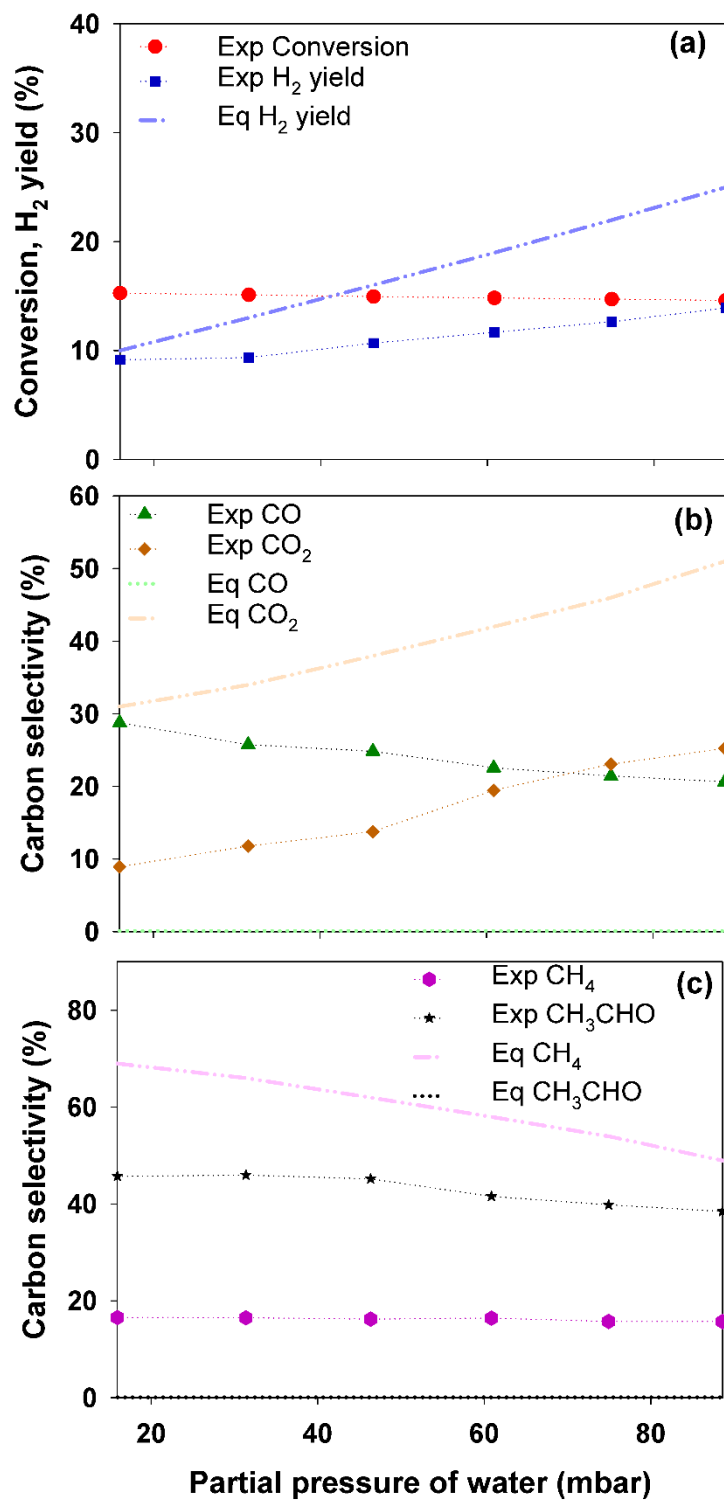


Figure 7-3: Effect of partial pressure of water on ethanol conversion and H₂ yield (a), carbon selectivities of CO & CO₂ (b), CH₄ & CH₃CHO (c) during ESR catalysed by Ni/biochar compared with equilibrium at 400°C.

It follows from our initial explanation that increasing the abundance of available steam-derived surface species relative to ethanol-derived species would cause the possible spill-over and interactions to be more achievable, leading to improved WGS activity. The increased steam-derived species relative to ethanol-derived species would also mean less surface-H from dehydrogenation and decomposition reactions. Therefore, the adsorption and dissociation of H₂O on the surface would not be as hindered causing more oxygen to be available for secondary WGS reaction.

Figure 7-4 presents the effects of space time, depicted in terms of the W/F ratio ($\text{g}_{\text{cat}} \text{ s } \text{g}_{\text{Eth}}^{-1}$), on the conversion of ethanol and H₂ yield at 400°C and a S/C ratio of 3. The ethanol conversion and H₂ yield as expected increased with increased contact time. A mild slope of increase was observed, likely related to the very low partial pressure of ethanol (8 mbar) resulting in low observed reaction rates. Figure 7-4 also shows how the selectivity towards carbon-based products evolved with changing ethanol conversion at a fixed temperature, pressure and S/C ratio with only the W/F ratio ($\text{g}_{\text{cat}} \text{ s } \text{g}_{\text{Eth}}^{-1}$) varied. The results show that with increased contact time and conversion, there are small changes to the selectivities of the products.

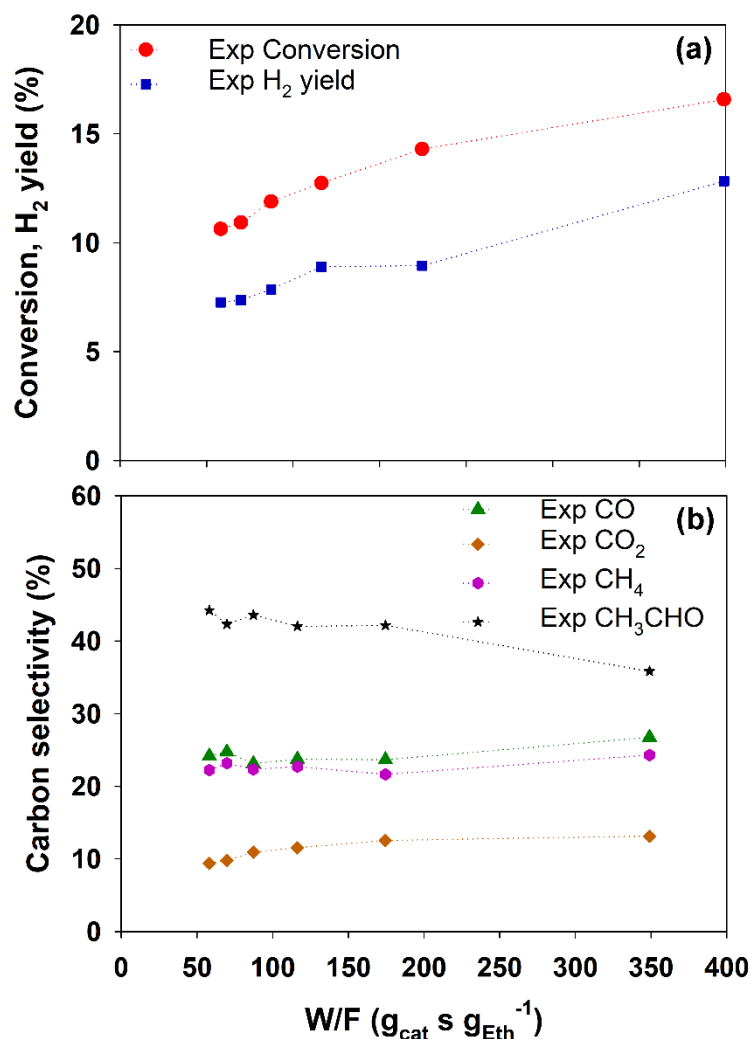


Figure 7-4: Effect of W/F on ethanol conversion and H_2 yield (a) and carbon selectivities of CO , CO_2 , CH_4 and CH_3CHO (b) during ESR catalysed by Ni/biochar at $400^\circ C$ ($S/C = 3$).

The observed conversion and product distribution could be due to the Ni active sites, the AAEM in biochar and/or the carbon structure of biochar. The following sections discuss results of experiments designed to distinguish the individual roles of these possible reaction sites.

7.3.2 Ethanol steam reforming catalysed by acid-washed biochar

To further understand the role of biochar and investigate the effects of the presence of alkali and alkaline earth metals in biochar, the effect of temperature was investigated for the ESR reaction over a sample of biochar that was acid-washed in an aqueous solution of 1M HNO_3 and then filtered and dried in a furnace overnight at $110^\circ C$. The acid-washing process has been shown to lead to an effective removal of AAEM species K, Mg and Ca, reaching 90% for K content reduction for similar biochar samples from mallee wood [34].

Figure 7-5 shows the effect of reaction temperature on ESR catalysed by the acid-washed biochar. The conversion in this case increased from 1.1% at 300°C to 4.1% at 450°C with the H₂ yield increasing from 0.2% to 2.1%. The selectivity trend shows CH₃CHO selectivity reduced as temperature increased and concurrently the selectivities of CO and CH₄ increased. This indicates that the dehydrogenation pathway on biochar goes through CH₃CHO, which decomposed as temperature increased to form CO and CH₄. The lack of CO₂ as stated previously could be attributed to the possible presence of different active sites for the ethanol derivatives and the steam derivatives as well as the occurrence of H-rich surface. The Arrhenius plot for the acid-washed biochar catalysed reaction in this temperature range is also shown in Figure 7-6, from which the apparent activation energy observed is about 30 kJ mol⁻¹. A more noticeable deviation from a linear fit is observed in this case, possibly due to the very low conversion values and reaction rates of these experiments, however still an acceptable R² value of 0.92 is obtained. The scatter in Figure 7-6 may also reflect true changes in the reaction system, which are manifested in the changes in the slope of the Arrhenius plot. The analytical equipment used in this study did not allow for a more accurate quantification of conversion (as low as 1%) and reaction rate at the lowest temperature investigated. Further investigation is warranted in the future.

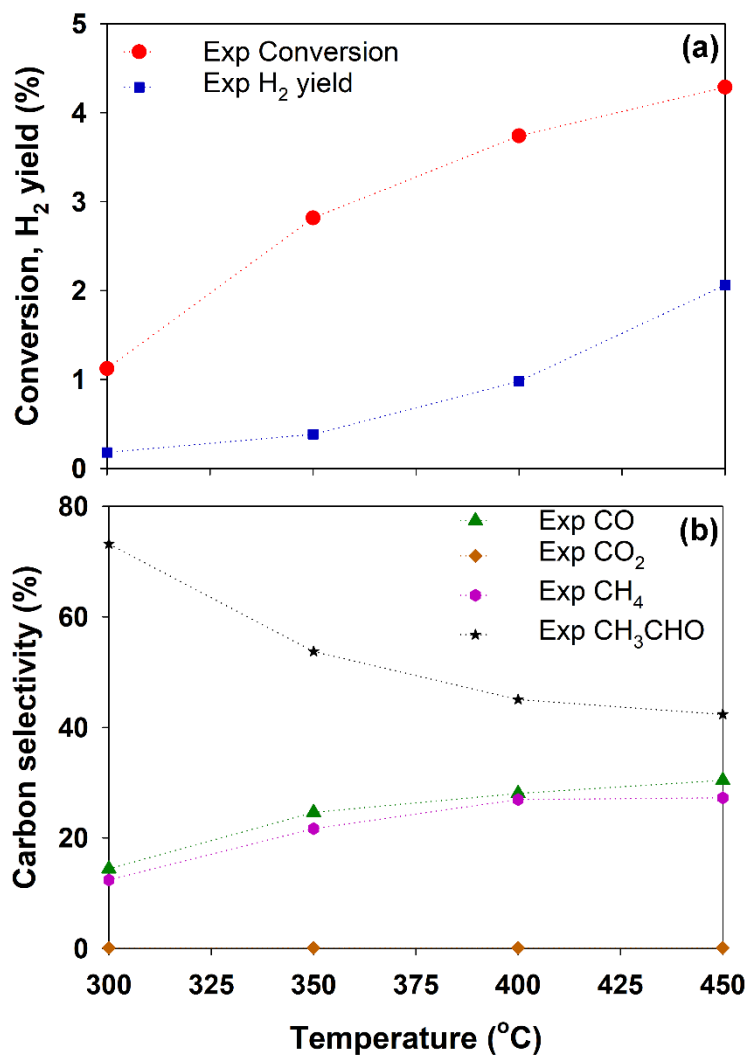


Figure 7-5: Effect of temperature on conversion, H₂ yield (a) and carbon selectivities of CO, CO₂, CH₄ & CH₃CHO (b) during ESR catalysed by acid-washed biochar (S/C = 3, W/F_{Eth} = 90.9 g_{cat} s⁻¹ g_{Eth}⁻¹).

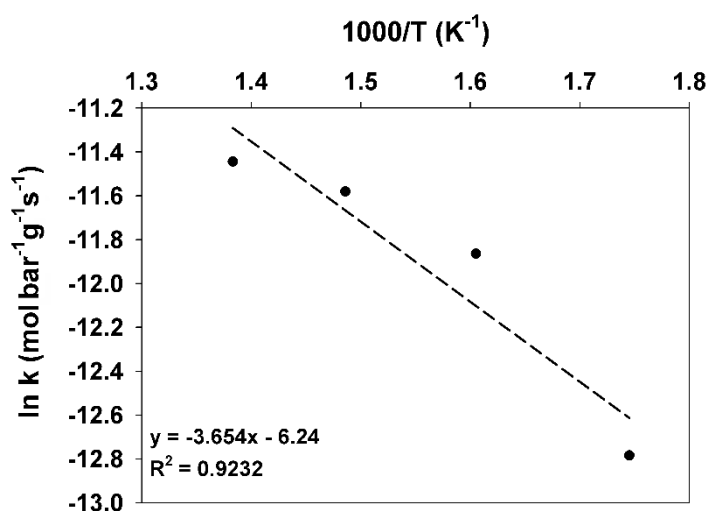


Figure 7-6: Arrhenius plot of ESR catalysed by acid-washed biochar (S/C = 3, $W/F_{\text{Eth}} = 90.9 \text{ g}_{\text{cat}} \text{ s}^{-1} \text{ g}_{\text{Eth}}^{-1}$).

7.3.3 Ethanol steam reforming catalysed by biochar

The effect of temperature was also investigated for the ESR reaction over biochar alone as a catalyst with results shown in Figure 7-7. The conversion increased with temperature from 1.5% to 8.3% with H_2 yield also increasing with temperature. It is observed that at similar conversions the H_2 yield of the ESR catalysed by acid-washed biochar is less than that of the biochar catalysed reaction. The observed conversion at 300°C for both biochar and acid-washed biochar catalysts, as well as the fact that there is negligible gas phase reaction at these conditions are indicative of biochar exhibiting catalytic behaviour for ESR. The selectivity towards CH_3CHO , CH_4 and CO are all much higher than that of CO_2 , and the decomposition pathway is promoted more with temperature increase as selectivity towards CH_4 and CO increase whilst that of CH_3CHO decreases.

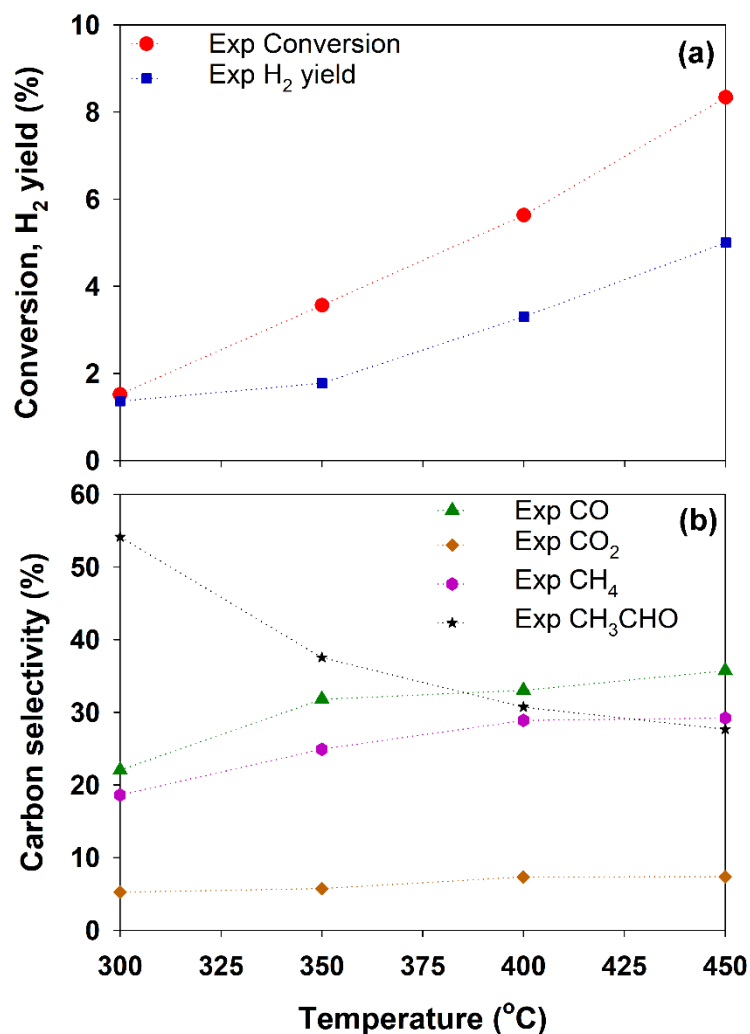


Figure 7-7: Effect of temperature on conversion and H₂ yield (top) and carbon selectivities of CO, CO₂, CH₄ & CH₃CHO (bottom) during ESR catalysed by biochar (S/C = 3, W/F_{Eth} = 90.9 g_{cat} s⁻¹ g_{Eth}⁻¹).

More CO₂ formation relative to the acid-washed-biochar-catalysed reaction products is observed. The decomposition products CH₄ and CO are also more promoted over biochar, therefore it could be implied that the AAEM species in biochar have additional catalytic effects. The results suggest that the presence of AAEM to some extent promotes the decomposition pathway leading to better conversion whilst also possibly providing additional sites for the adsorption of steam derived species and consequently better WGS activity. The Arrhenius plot for the biochar catalysed reaction in this temperature range is shown in Figure 7-8 from which the apparent activation energy observed is about 39 kJ mol⁻¹.

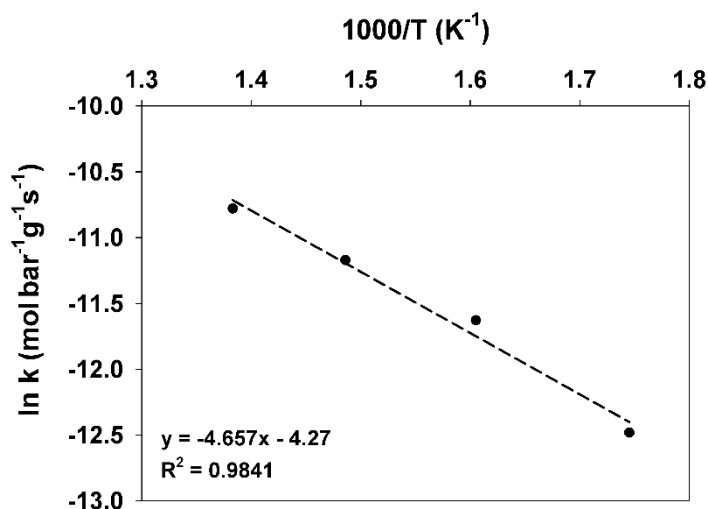


Figure 7-8: Arrhenius plot of ESR catalysed by biochar ($S/C = 3$, $W/F_{\text{Eth}} = 90.9 \text{ g}_{\text{cat}} \text{ s}^{-1} \text{ g}_{\text{Eth}}^{-1}$).

7.3.4 Water-gas shift reaction catalysed by Ni/biochar

To elucidate the reason for the lack of WGS activity observed during the ESR catalysed by Ni/biochar and gain more insight into the effects of the interactions between the different active sites, WGS reaction catalysed by Ni/biochar was performed in the same temperature range 300°C to 450°C and at the same $\text{H}_2\text{O}/\text{C}$ (C in CO) ratio of 3. The results presented in Figure 7-9 show that the CO conversion to CO_2 and H_2 increased from 5.4% to 72.7% as temperature increased. It is therefore evident that the Ni/biochar catalyst does not inhibit WGS reaction.

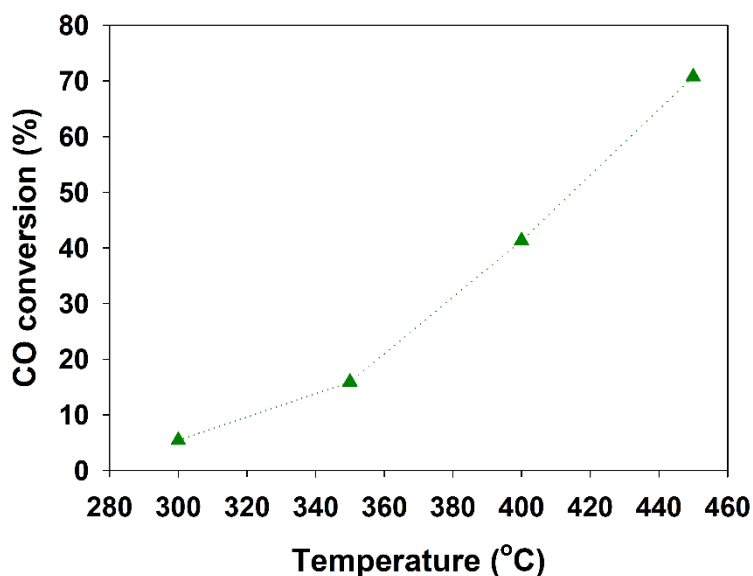


Figure 7-9: Effect of temperature on the conversion of CO during WGS reaction catalysed by Ni/biochar ($S/C = 3$, $W/F_{\text{CO}} = 45.6 \text{ g}_{\text{cat}} \text{ s}^{-1} \text{ g}_{\text{CO}}^{-1}$).

This result supports the explanation in Section 7.3.1, as, in the absence of ethanol as is the case in these experiments, the catalyst surface would be significantly less H-rich. This would allow H₂O adsorption and dissociation to proceed more easily. Also, the spill-over of steam-derived species would be much easier as there are no ethanol-derived species on the catalyst surface.

7.3.5 Ethanol decomposition

In an attempt to gain further insight into the main reaction pathways on Ni and biochar, two temperature scan experiments were carried out to investigate the decomposition of ethanol on Ni/biochar and just biochar. Figure 7-10a presents the effect of temperature on the decomposition of ethanol over Ni/biochar. The carbon selectivity distribution as temperature changes is presented in Figure 7-10b. With no CO₂ formation whatsoever, the CH₃CHO selectivity is seen to decrease as CH₄ and CO selectivity increases steadily with increasing temperature. The carbon balance is completed by a minimal formation of C₂H₆.

The conversion/H₂ yield and carbon selectivity results of the similar experiments over a biochar catalyst are presented in Figure 7-10c & d respectively. The selectivity evolution shows no CO₂ once again, CO selectivity was low and decreased with temperature and CH₄ selectivity decreased in tandem with increase in C₂H₆ selectivity. As temperature increased, the formation of C₂H₆ is seen to dominate with no CH₃CHO production.

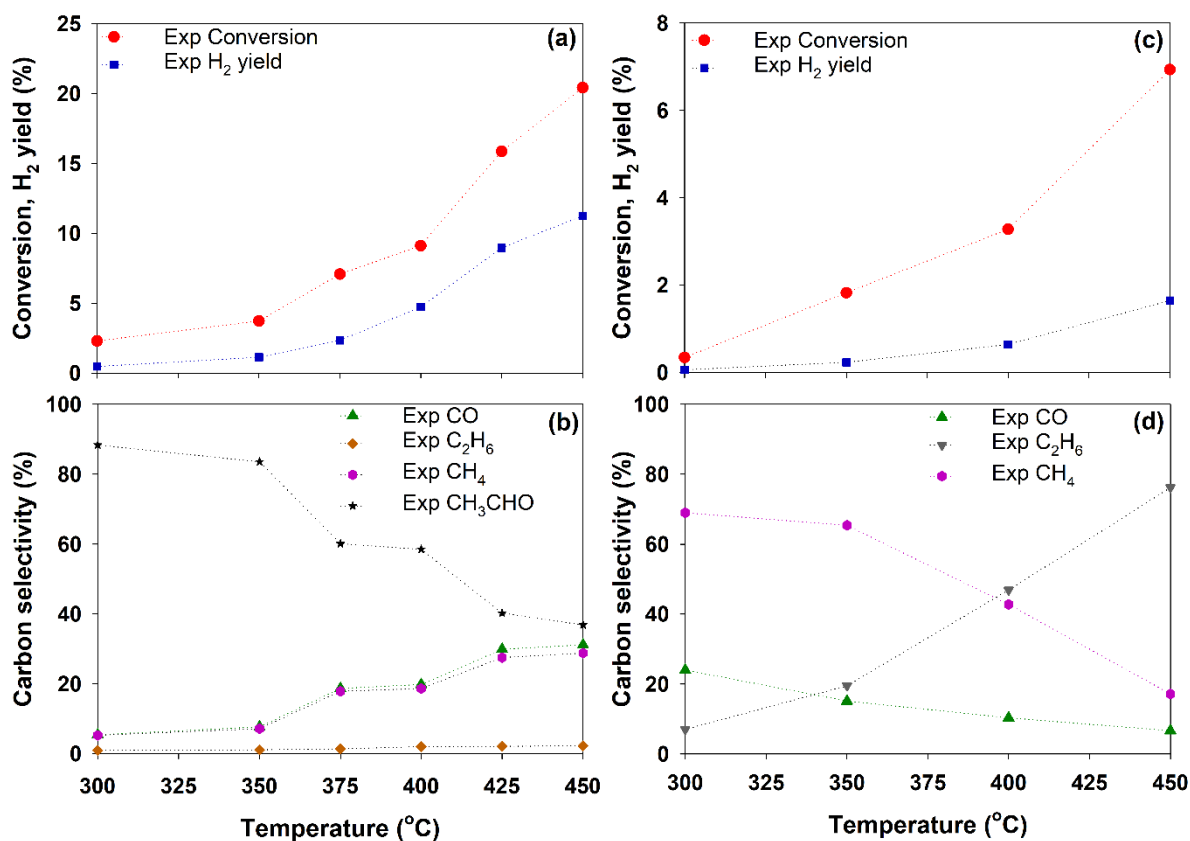


Figure 7-10: Ethanol decomposition conversion and H₂ yield over Ni/biochar (a), carbon selectivities of CO, C₂H₆, CH₄ and CH₃CHO over Ni/biochar (b), ethanol decomposition conversion and H₂ yield over biochar (c), carbon selectivities of CO, C₂H₆ and CH₄ over biochar (d) ($S/C = 0$, $W/F_{\text{Eth}} = 90.9 \text{ g}_{\text{cat}} \text{ s}^{-1} \text{ g}_{\text{Eth}}^{-1}$).

A likely explanation for the C₂H₆ presence, which is not commonly encountered in ESR literature, is that a possible reaction pathway exists on biochar wherein upon adsorption the OH is cleaved from the absorbed ethanol leaving a CH₃CH₂ adsorbed ethanol derived species, which could then associatively desorb with available surface hydrogen forming C₂H₆. Alternatively, in the absence of enough hydrogen, the CH₃ produced from decomposition may tend to recombine to give C₂H₆ rather than react with hydrogen to form CH₄. The Arrhenius plots of the decomposition reactions on Ni/biochar and biochar are presented in Figure 7-11.

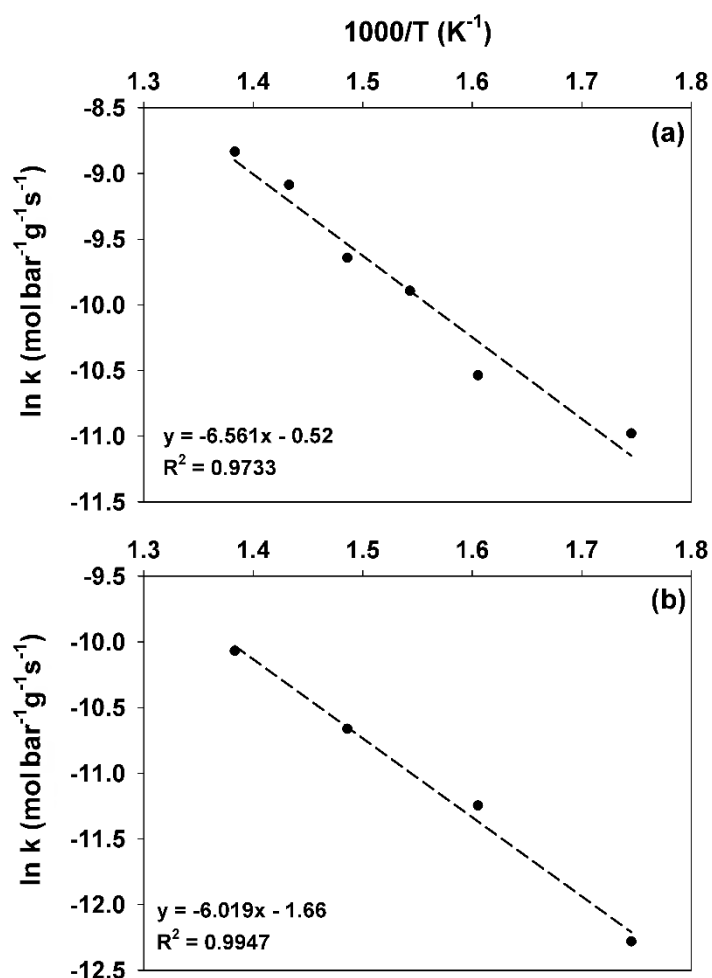


Figure 7-11: Arrhenius plots of ethanol decomposition catalysed by Ni/biochar (a) and biochar (b) ($S/C = 0$, $W/F_{\text{Eth}} = 90.9 \text{ g}_{\text{cat}} \text{ s}^{-1} \text{ g}_{\text{Eth}}^{-1}$).

Table 7.1 presents a brief summary of the results of the reforming and decomposition over the different catalysts. The table shows the obtained apparent activation energies and pre-exponential factors from the Arrhenius plots, as well as the conversion and selectivity towards CH_3CHO at the minimum and maximum temperature limit examined. From the data it is conclusive that biochar is not inert and has a different reaction mechanism to that of Ni, as we observe different activation energy from the Arrhenius plots of both biochar and acid-washed biochar. If the effect of biochar alone is subtracted from the data of Ni/biochar, the resulting data does not match trends observed over Ni on inert supports. We can therefore conclude that the reactions on biochar and Ni active sites are not independent.

Table 7.1: Summary of ethanol steam reforming/decomposition results over the various catalytic systems studied.

Catalyst	Conversion at 300°C (Selectivity to CH ₃ CHO)	Conversion at 450°C (Selectivity to CH ₃ CHO)	E _a (kJ mol ⁻¹)	ln A (mol bar ⁻¹ g ⁻¹ s ⁻¹)
No catalyst (Gas phase reaction)	Not detected	Not detected	-	-
Ni/SiO ₂ [14]	3% (17%)	30% (7%)	48.0	7.2
Ni/biochar	1.8% (87.8%)	30.8% (19.6%)	69.9	2.2
Biochar	1.5% (54.2%)	8.3% (27.6%)	38.7	-4.3
Acid-washed biochar	1.1% (73.2%)	4.3% (42.4%)	30.4	-6.2
Ni/biochar catalysed decomposition	2.3% (88.4%)	20.4% (36.9%)	54.6	-0.5
Biochar catalysed decomposition	0.3% (-)	6.9% (-)	50.0	-1.7

7.3.6 Analysis of kinetic compensation effect

Figure 7-12 presents a graph of the reaction activation energies vs pre-exponential factors for ethanol consumption and product formation in the experiments (steam reforming and decomposition) over the different catalysts: Ni/biochar, biochar and acid-washed biochar. The resulting straight-line points to evidence of the presence of some kinetic compensation effect (KCE) [48].

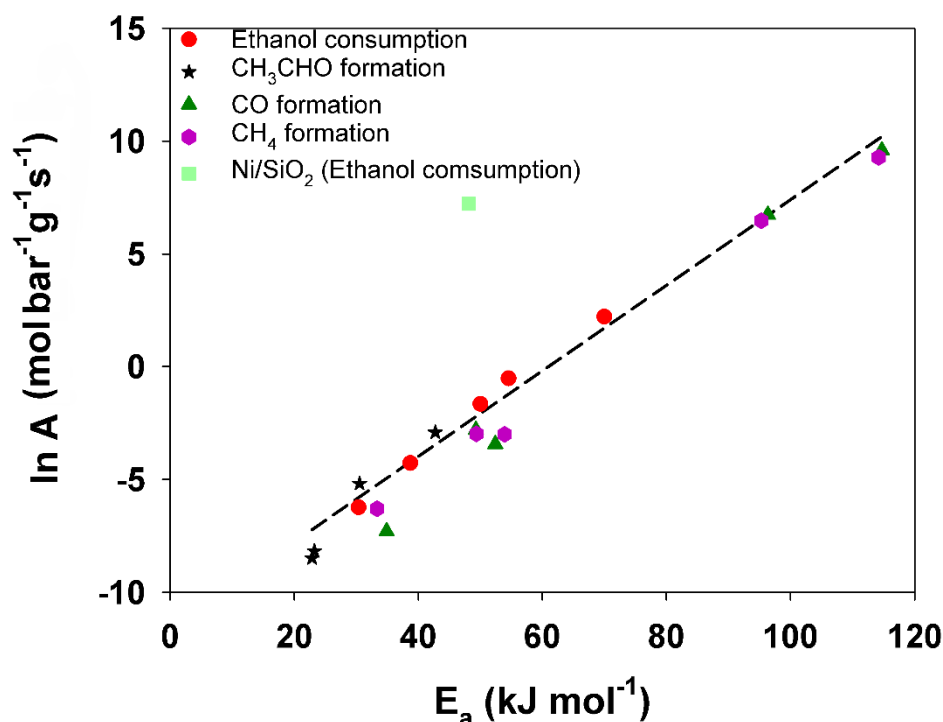


Figure 7-12: Reaction barriers vs pre-exponential factors for ethanol consumption and product formation in the experiments over the different catalysts showing the presence of a kinetic compensation effect. Ni/SiO₂ data obtained from [14].

To explain the existence of KCE we can consider there exists a continuum distribution of active sites on a catalyst surface, some of which are more reactive than others at a given temperature. With an increase in temperature the sites with high barrier for the reaction may become active. Therefore, at lower temperatures the measured rate is affected mainly by sites with low reaction energy barriers. At higher temperatures the measured rate is now affected by both type of sites leading to a concurrent increase in the number of sites (higher reaction pre-exponential factor) and the reaction barrier as both high and low energy sites contribute to the measured rate (higher activation energy). In our case we have two different types of sites; Ni on biochar and biochar itself. Biochar surface has a wide range of different structures which would have a distribution of sites with different energies and affect the Ni-biochar interactions. Therefore, Ni/biochar would also have different structures and sites with different energies. The presence of kinetic compensation effect means that within the set of reactions a common feature is shared which could be the reactants or the catalyst [48]. In this case the commonality most likely lies in the catalyst, specifically biochar.

Understandably, the interactions of reactants, adsorbates and reaction intermediates with biochar supported metal catalysts are particularly complex and would require further

investigation *via* advanced in situ characterisation methods in conjunction with theoretical studies to fully elucidate them. Nonetheless, given the observed trends and kinetic compensation effect it can be postulated that the reaction mechanism most logically involves ethanol and steam adsorbing on the biochar surface as illustrated in Figure 7-13. The organic nature of biochar allows it to offer sites with better affinity for ethanol relative to Ni [25,36,38]. In particular, the O-containing structure may be similar to those on ethanol and/or acetaldehyde, making the transition from ethanol to acetaldehyde easier. The dehydrogenation and decomposition reactions may occur on biochar sites or on sites around the Ni/biochar interface. As previously noted, typically during reforming process ethanol will first go through dehydrogenation and decomposition steps. From the KCE analysis, the decomposition and reforming reactions share the same commonality and it can be extrapolated that the rate limiting step occurs on biochar within the dehydrogenation pathway.

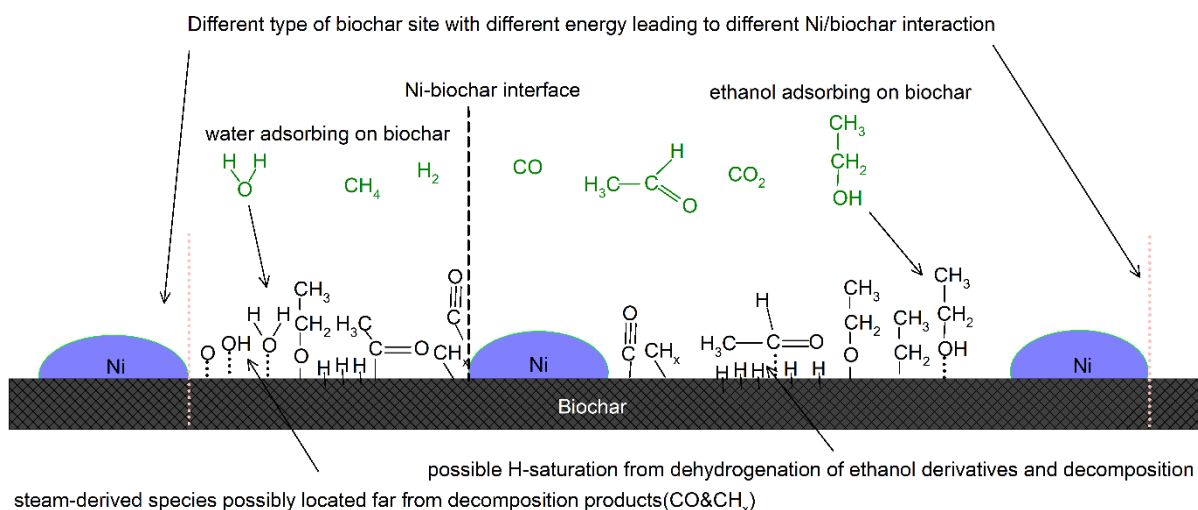


Figure 7-13: Schematic view of postulated distribution of ethanol and steam derived species on various active sites on Ni/biochar during the reforming reaction.

7.3.7 Raman spectroscopic characterization of biochar

Samples from the ESR process over Ni/biochar and just biochar at S/C ratio of 3 and 450°C, as well as samples from the ethanol decomposition experiments over Ni/biochar and biochar at S/C ratio of 0 and 450°C were characterized *via* Raman spectroscopy. For each experiment, two different reaction times were used, namely 30 mins and 60 mins, noting that there was little to no discernible change in the reaction rate for both reaction times. Spectra from raw biochar as well as fresh Ni/biochar catalyst after reduction in H₂ were also collected for comparison. The Raman spectra of all biochar samples in the range of 800-1800 cm⁻¹ are presented in Figure 7.15

in the Supplementary Information. These spectra were curve fitted by 10 Gaussian peaks, as described in the work of Li et al. [41,42]. An example Raman spectrum deconvolution is shown in Figure 7.16 in the Supplementary Information, evidencing the successful spectrum curve-fitting with these bands. The total Raman peak areas for these biochar samples are shown in Figure 7-14.

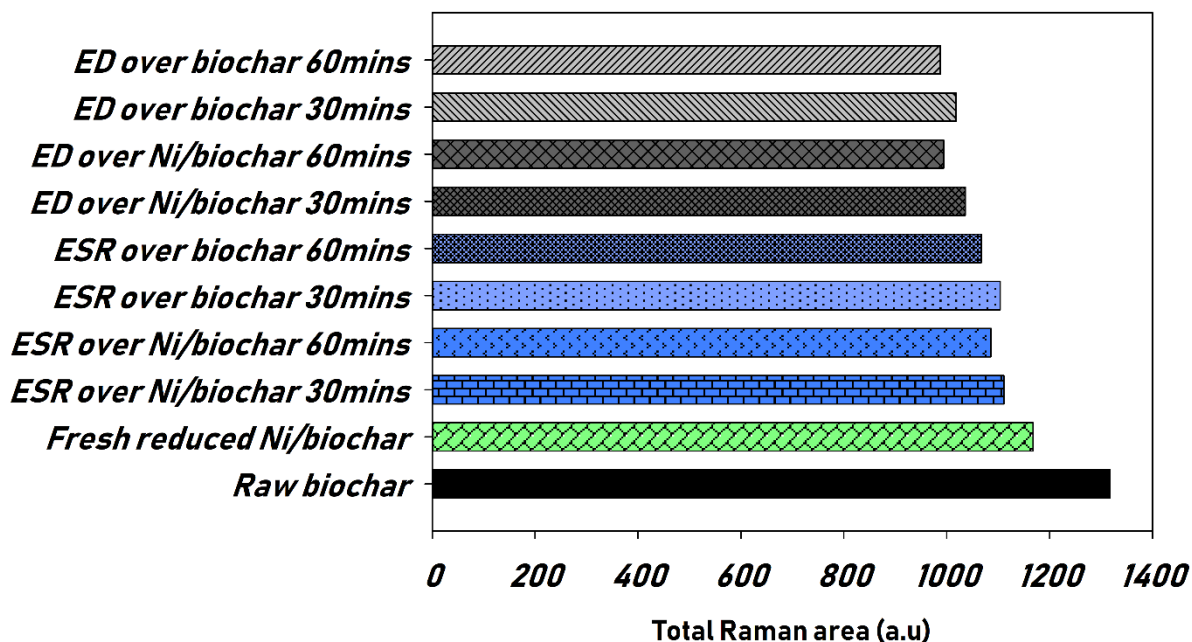


Figure 7-14: Raman spectroscopic data showing total Raman peak area ($800 - 1800 \text{ cm}^{-1}$) of biochar samples obtained from ESR (ethanol steam reforming) and ED (ethanol decomposition) experiments at 450°C at different reaction times, in comparison to that of raw biochar and fresh reduced Ni/biochar.

After reforming and decomposition reactions the total Raman peak area in all biochar samples decreased, indicating the consumption of the O-containing functional groups when biochar is used as a catalyst. When comparing the Ni/biochar catalysed and biochar catalysed ESR samples, the depletion of O-containing functional groups content with reaction time is found to be similar at approximately 8.5% over the 30-60 min reaction interval. This could be implying that the biochar is similarly active even when used as a support and the ethanol and steam preferentially adsorb on biochar active sites. In addition, when comparing the samples from the ethanol decomposition experiments over Ni/biochar and biochar, the Raman area depletion values are also similar at roughly 15% over the 30-60 min reaction interval. Again, this possibly implies that even in the case where only ethanol and ethanol derived species are present, they preferentially adsorb on biochar active sites.

It is further noted in the previous data that Raman peak area reduction during decomposition is larger than during ESR. This is further elaborated in Table 7.2 showing the reduction of total Raman peak area as the S/C ratio is increased at 400°C over Ni/biochar, and the respective H₂ yield and CO and CO₂ selectivities for these experiments. The total Raman peak area which relates to the content of O-containing functional groups is observed to reduce at a lower rate with increasing abundance of H₂O, indicating that the presence of steam facilitates the replenishment or maintenance of the O-containing functional groups on the biochar surface. These findings are in good agreement with previous studies where steam has been used to activate biochar and increase the surface-O functionality [25,36,49], and suggest that the catalytic activity of Ni/biochar is linked with and can be enhanced by the presence of O-containing functional groups, as also evidenced by the increasing H₂ yield and CO₂ selectivity values in Table 7.2.

Table 7.2: Relative change in total Raman peak area (800 - 1800 cm⁻¹) over the 30-60 min reaction interval of biochar samples obtained from experiments varying S/C ratio at 400°C over Ni/biochar and respective products formation.

Reaction conditions	Total Raman peak area change (%)	CO ₂ selectivity (%)	CO selectivity (%)	H ₂ yield (%)
Ethanol decomposition	-14.69	0	20.81	4.72
ESR at S/C = 1	-13.23	8.89	28.78	9.14
ESR at S/C = 3	-8.33	13.76	24.61	10.67
ESR at S/C = 6	-3.45	25.35	20.12	14.11

7.4 Conclusions

Ethanol steam reforming and decomposition experiments over a wide range of conditions were carried out over Ni/biochar, biochar and acid-washed biochar catalysts in an attempt to ascertain the overall reaction mechanism and the effect of the biochar support on the latter.

The observed results show that biochar is catalytically active during reforming and decomposition and follows a different mechanism from that of Ni. The AAEM in biochar contribute to the observed catalytic effect of biochar. The reactions on the active sites of biochar and Ni are not independent. Low CO₂ formation was observed during the ESR over all catalysts. This was not the case during independent WGS kinetic experiments over Ni/biochar, suggesting that, during ESR, WGS is hindered possibly by coverage effects or changes in the working state of the catalyst surface induced from the adsorption and dehydrogenation of ethanol.

The decomposition of ethanol on biochar in the absence of steam interestingly showed the formation of C₂H₆ species, which could be a result of the abstraction of the OH group forming an ethyl CH₃CH₂ surface species which would associatively desorb with available hydrogen. It could also be as a result of the CH₃ species formed from decomposition recombining to C₂H₆ due to lack of sufficient hydrogen to form CH₄. Kinetic compensation effect was observed with a possible rate limiting step on biochar being common to all reactions. The Raman spectroscopy results show similar reduction in O-containing functional groups when biochar is used alone or as a support to Ni, while the presence of H₂O in both cases helps maintain the population of these groups.

References

- [1] P. Nikolaidis, A. Poullikkas, A comparative overview of hydrogen production processes, *Renew. Sustain. Energy Rev.* 67 (2017) 597–611.
- [2] M. Ni, D.Y.C. Leung, M.K.H. Leung, A review on reforming bio-ethanol for hydrogen production, *Int. J. Hydrogen Energy.* 32 (2007) 3238–3247.
- [3] N. Sanchez, R.Y. Ruiz, B. Cifuentes, M. Cobo, Hydrogen from glucose: A combined study of glucose fermentation, bioethanol purification, and catalytic steam reforming, *Int. J. Hydrogen Energy.* 41 (2016) 5640–5651.
- [4] P.D. Vaidya, A.E. Rodrigues, Insight into steam reforming of ethanol to produce hydrogen for fuel cells, *Chem. Eng. J.* 117 (2006) 39–49.
- [5] C.. Rioche, S.. Kulkarni, M.. Meunier, J.. Breen, R.. Burch, Steam reforming of model compounds and fast pyrolysis bio-oil on supported noble metal catalysts, *Appl. Catal. B Environ.* 61 (2005) 130–139.
- [6] R. González-Gil, I. Chamorro-Burgos, C. Herrera, M.A. Larrubia, M. Laborde, F. Mariño, L.J. Alemany, Production of hydrogen by catalytic steam reforming of oxygenated model compounds on Ni-modified supported catalysts. Simulation and experimental study, *Int. J. Hydrogen Energy.* 40 (2015) 11217–11227.
- [7] R. Trane, S. Dahl, M.S. Skjøth-Rasmussen, A.D. Jensen, Catalytic steam reforming of bio-oil, *Int. J. Hydrogen Energy.* 37 (2012) 6447–6472.
- [8] L. V Mattos, G. Jacobs, B.H. Davis, F.B. Noronha, Production of hydrogen from ethanol: Review of reaction mechanism and catalyst deactivation, *Chem. Rev.* 112 (2012) 4094–4123.
- [9] D. Zanchet, J.B.O. Santos, S. Damyanova, J.M.R. Gallo, J.M.C. Bueno, Toward understanding metal-catalyzed ethanol reforming, *ACS Catal.* 5 (2015) 3841–3863.
- [10] K.D. Punase, N. Rao, P. Vijay, A review on mechanistic kinetic models of ethanol steam reforming for hydrogen production using a fixed bed reactor, *Chem. Pap.* 73 (2019) 1027–1042.
- [11] J.H. Wang, C.S. Lee, M.C. Lin, Mechanism of ethanol reforming: Theoretical foundations, *J. Phys. Chem. C.* 113 (2009) 6681–6688.
- [12] I. Llera, V. Mas, M.L. Bergamini, M. Laborde, N. Amadeo, Bio-ethanol steam reforming on Ni based catalyst. Kinetic study, *Chem. Eng. Sci.* 71 (2012) 356–366.
- [13] A. Akande, A. Aboudheir, R. Idem, A. Dalai, Kinetic modeling of hydrogen production by the catalytic reforming of crude ethanol over a co-precipitated Ni-Al₂O₃ catalyst in a packed bed tubular reactor, *Int. J. Hydrogen Energy.* 31 (2006) 1707–1715.
- [14] M.D. Zhurka, A.A. Lemonidou, J.A. Anderson, P.N. Kechagiopoulos, Kinetic analysis of the steam reforming of ethanol over Ni/SiO₂ for the elucidation of metal-dominated reaction pathways, *React. Chem. Eng.* 3 (2018) 883–897.

- [15] R. Alcalá, M. Mavrikakis, J.A. Dumesic, DFT studies for cleavage of C-C and C-O bonds in surface species derived from ethanol on Pt(111), *J. Catal.* 218 (2003) 178–190.
- [16] F. Soyol-Baltacioğlu, A.E. Aksoylu, Z.I. Önsan, Steam reforming of ethanol over Pt-Ni Catalysts, *Catal. Today.* 138 (2008) 183–186.
- [17] S. Cavallaro, Ethanol Steam Reforming on Rh/Al₂O₃ Catalysts, *Energy and Fuels.* 14 (2000) 1195–1199.
- [18] J. Zhang, Z. Zhong, X.M. Cao, P. Hu, M.B. Sullivan, L. Chen, Ethanol steam reforming on rh catalysts: Theoretical and experimental understanding, *ACS Catal.* 4 (2014) 448–456.
- [19] M. Li, W. Guo, R. Jiangs, L. Zhao, H. Shan, Decomposition of ethanol on Pd(111): A density functional theory study, *Langmuir.* 26 (2010) 1879–1888.
- [20] J.E. Sutton, D.G. Vlachos, Ethanol activation on closed-packed surfaces, *Ind. Eng. Chem. Res.* 54 (2015) 4213–4225.
- [21] S.M. Gates, J.N. Russell Jr., J.T. Yates Jr., Bond activation sequence observed in the chemisorption and surface reaction of ethanol on Ni(111), *Surf. Sci.* 171 (1986) 111–134.
- [22] S. Ogo, Y. Sekine, Recent progress in ethanol steam reforming using non-noble transition metal catalysts: A review, *Fuel Process. Technol.* 199 (2020) 106238.
- [23] T.K. Phung, T.L.M. Pham, A.N.T. Nguyen, K.B. Vu, H.N. Giang, T.A. Nguyen, T.C. Huynh, H.D. Pham, Effect of Supports and Promoters on the Performance of Ni-Based Catalysts in Ethanol Steam Reforming, *Chem. Eng. Technol.* 43 (2020) 672–688.
- [24] V. Palma, C. Ruocco, M. Cortese, M. Martino, Bioalcohol Reforming: An Overview of the Recent Advances for the Enhancement of Catalyst Stability, *Catalysts.* 10 (2020).
- [25] R. Shan, J. Han, J. Gu, H. Yuan, B. Luo, Y. Chen, A review of recent developments in catalytic applications of biochar-based materials, *Resour. Conserv. Recycl.* 162 (2020) 105036.
- [26] J. Ashok, N. Dewangan, S. Das, P. Hongmanorom, M.H. Wai, K. Tomishige, S. Kawi, Recent progress in the development of catalysts for steam reforming of biomass tar model reaction, *Fuel Process. Technol.* 199 (2020) 106252.
- [27] J. Chen, M. Wang, S. Wang, X. Li, Hydrogen production via steam reforming of acetic acid over biochar-supported nickel catalysts, *Int. J. Hydrogen Energy.* 43 (2018) 18160–18168.
- [28] D. Buentello-Montoya, X. Zhang, J. Li, V. Ranade, S. Marques, M. Geron, Performance of biochar as a catalyst for tar steam reforming: Effect of the porous structure, *Appl. Energy.* 259 (2020) 114176.
- [29] L. Ren, L.J. Yan, Y.H. Bai, Y. Liu, P. Lv, Y.X. Wang, F. Li, Effects of loading methods and oxidation degree of support on the tar reforming activity of char-supported Ni catalyst using toluene as a model compound, *Fuel Process. Technol.* 201 (2020) 106347.
- [30] C. Quan, H. Wang, N. Gao, Development of activated biochar supported Ni catalyst for enhancing toluene steam reforming, *Int. J. Energy Res.* 44 (2020) 5749–5764.
- [31] Z. Min, P. Yimsiri, M. Asadullah, S. Zhang, C.Z. Li, Catalytic reforming of tar during gasification. Part II. Char as a catalyst or as a catalyst support for tar reforming, *Fuel.* 90 (2011) 2545–2552.
- [32] Y. Song, Y. Zhao, X. Hu, L. Zhang, S. Sun, C.Z. Li, Destruction of tar during volatile-char interactions at low temperature, *Fuel Process. Technol.* 171 (2018) 215–222.
- [33] Y. Song, Y. Wang, X. Hu, S. Hu, J. Xiang, L. Zhang, S. Zhang, Z. Min, C.Z. Li, Effects of volatile-char interactions on in situ destruction of nascent tar during the pyrolysis and gasification of biomass. Part I. Roles of nascent char, *Fuel.* 122 (2014) 60–66.
- [34] S. Zhang, Y. Song, Y.C. Song, Q. Yi, L. Dong, T.T. Li, L. Zhang, J. Feng, W.Y. Li, C.Z. Li, An advanced biomass gasification technology with integrated catalytic hot gas cleaning. Part III: Effects of inorganic species in char on the reforming of tars from wood and agricultural wastes, *Fuel.* 183 (2016) 177–184.

- [35] C. Xu, Z.-Y. Du, S.-Q. Yang, H.-D. Ma, J. Feng, Effects of Inherent Potassium on the Catalytic Performance of Ni/Biochar for Steam Reforming of Toluene as a Tar Model Compound, *Chinese J. Chem. Eng.* (2020) 108653.
- [36] Y. Liu, M. Paskevicius, H. Wang, G. Parkinson, J.P. Veder, X. Hu, C.Z. Li, Role of O-containing functional groups in biochar during the catalytic steam reforming of tar using the biochar as a catalyst, *Fuel*. 253 (2019) 441–448.
- [37] Z. Min, S. Zhang, P. Yimsiri, Y. Wang, M. Asadullah, C.Z. Li, Catalytic reforming of tar during gasification. Part IV. Changes in the structure of char in the char-supported iron catalyst during reforming, *Fuel*. 106 (2013) 858–863.
- [38] Y. Wang, Z. Zhang, S. Zhang, Y. Wang, S. Hu, J. Xiang, X. Hu, Steam reforming of acetic acid over Ni/biochar catalyst treated with HNO₃: Impacts of the treatment on surface properties and catalytic behaviors, *Fuel*. 278 (2020) 118341.
- [39] Advanced biomass gasification technology, Australian Renewable Energy Agency. <https://arena.gov.au/projects/advanced-biomass-gasification-technology/>. (accessed October 28, 2019), (2018) 1–13.
- [40] Z. Min, M. Asadullah, P. Yimsiri, S. Zhang, H. Wu, C.Z. Li, Catalytic reforming of tar during gasification. Part I. Steam reforming of biomass tar using ilmenite as a catalyst, *Fuel*. 90 (2011) 1847–1854.
- [41] X. Li, J. Hayashi, C.Z. Li, FT-Raman spectroscopic study of the evolution of char structure during the pyrolysis of a Victorian brown coal, *Fuel*. 85 (2006) 1700–1707.
- [42] X. Li, J. Hayashi, C.Z. Li, Volatilisation and catalytic effects of alkali and alkaline earth metallic species during the pyrolysis and gasification of Victorian brown coal. Part VII. Raman spectroscopic study on the changes in char structure during the catalytic gasification in air, *Fuel*. 85 (2006) 1509–1517.
- [43] H.L. Tay, S. Kajitani, S. Zhang, C.Z. Li, Inhibiting and other effects of hydrogen during gasification: Further insights from FT-Raman spectroscopy, *Fuel*. 116 (2014) 1–6.
- [44] H.L. Tay, S. Kajitani, S. Zhang, C.Z. Li, Effects of gasifying agent on the evolution of char structure during the gasification of Victorian brown coal, in: *Fuel*, Elsevier Ltd, 2013: pp. 22–28.
- [45] J. Vicente, J. Ereña, C. Montero, M.J. Azkoiti, J. Bilbao, A.G. Gayubo, Reaction pathway for ethanol steam reforming on a Ni/SiO₂ catalyst including coke formation, *Int. J. Hydrogen Energy*. 39 (2014) 18820–18834.
- [46] J. Comas, F. Marino, M. Laborde, N. Amadeo, Bio-ethanol steam reforming on Ni/Al₂O₃ catalyst, *Chem. Eng. J.* 98 (2004) 61–68.
- [47] P. Biswas, D. Kunzru, Steam reforming of ethanol for production of hydrogen over Ni/CeO₂ - ZrO₂, *Int. J. Hydrogen Energy*. 32 (2007) 969–980.
- [48] B. V. L'vov, A.K. Galwey, Interpretation of the kinetic compensation effect in heterogeneous reactions: Thermochemical approach, *Int. Rev. Phys. Chem.* 32 (2013) 515–557.
- [49] Y. Liu, M. Paskevicius, H. Wang, C. Fushimi, G. Parkinson, C.Z. Li, Difference in tar reforming activities between biochar catalysts activated in H₂O and CO₂, *Fuel*. 271 (2020) 117636.

Supplementary Information

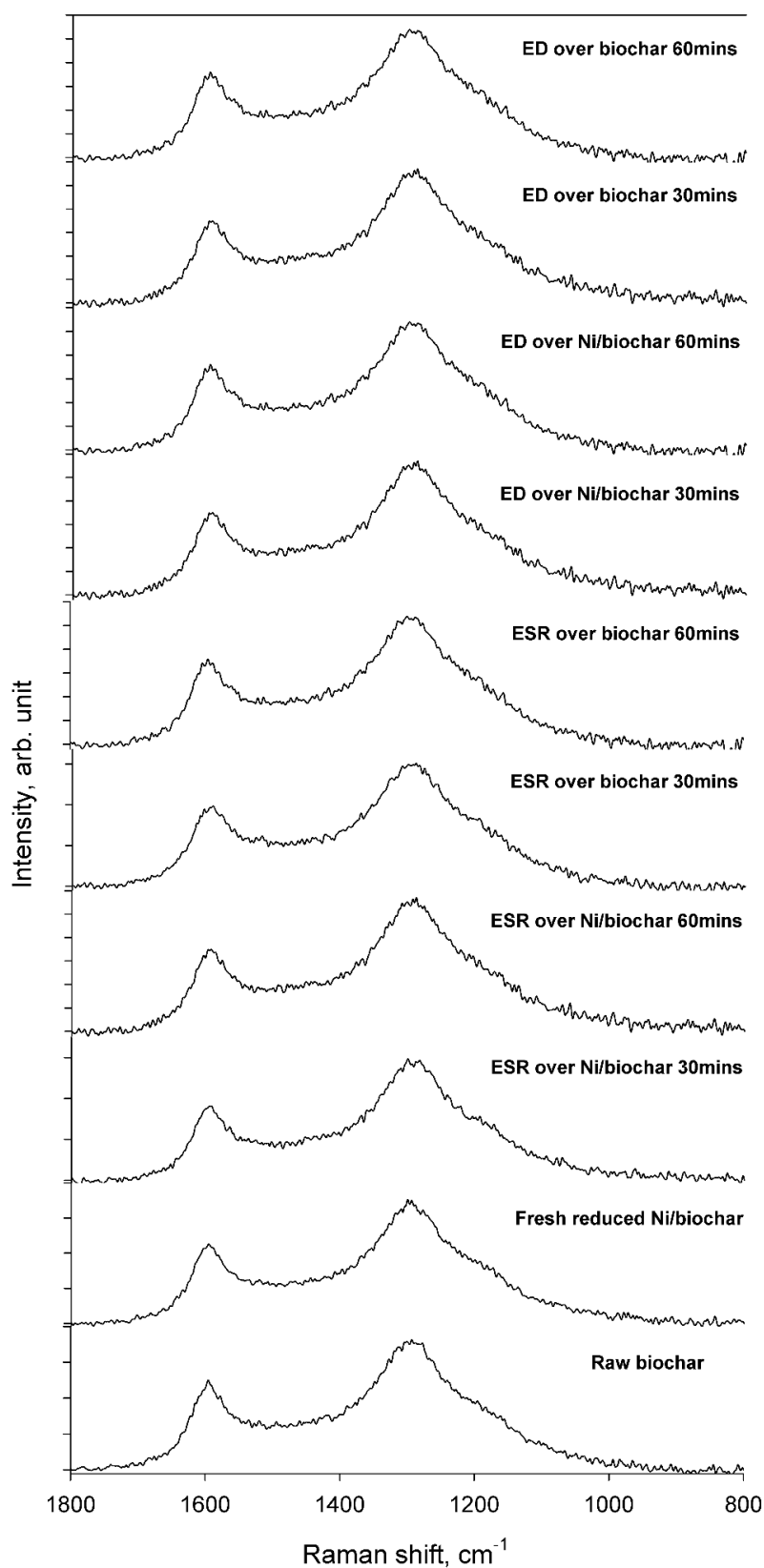


Figure 7-15: Normalised Raman spectra of biochar samples obtained from ESR (ethanol steam reforming) and ED (ethanol decomposition) experiments at different reaction times, in comparison to that of raw biochar and fresh reduced Ni/biochar.

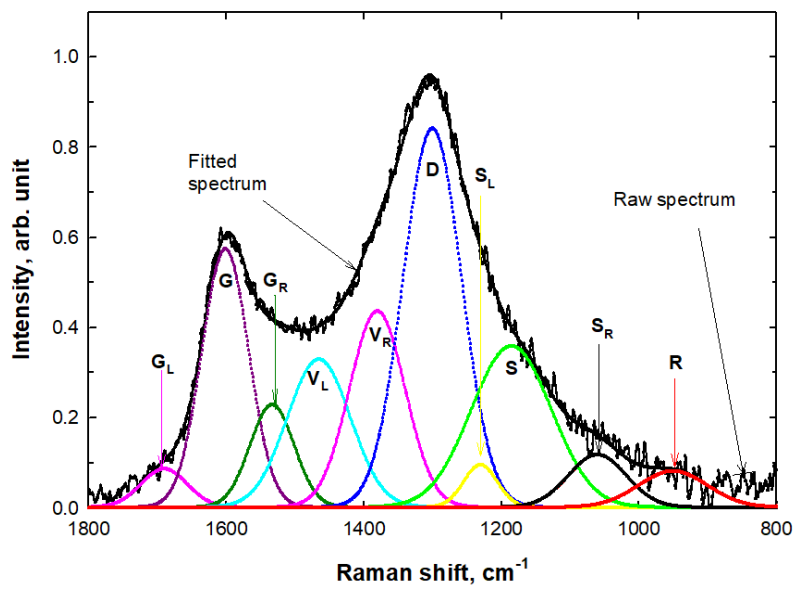


Figure 7-16: Deconvolution example of a Raman spectrum using 10 bands for a biochar sample.

CHAPTER 8: CONCLUSION

In this study, the role of support materials in the mechanism and kinetics of the ethanol steam reforming process was investigated computationally through microkinetic modelling and experimentally *via* kinetic experiments. Additionally, the industrially relevant, effect of product co-feeding on the mechanism and kinetics of the dry reforming of biogas was also computationally investigated.

First, a microkinetic model for the ethanol steam reforming process over a metal dominated catalyst with inert support was developed. Ni metal was selected of the relatively cheaper non-noble metal catalysts, due to its high activity and hydrogen yield potential. The mean-field microkinetic model developed used semi-empirical rate constant estimation methods: Transition state theory for pre-exponential factors and unit bond index-quadratic exponential potential (UBI-QEP) for activation energy estimations. Thermodynamic consistency was conserved by constraining the surface reaction thermodynamic properties and correlating them to gas-phase properties using the adsorption properties. The adsorption energies of surface adsorbate species were initially obtained from experimental and DFT studies and then set as model parameters.

The model was able to correctly describe and replicate a wide range of experimentally obtained results and provide insight on the reaction pathway and kinetically relevant reaction steps and adsorbate species. The observed kinetically relevant dehydrogenation of 1-hydroxyethyl towards CH_3COH^* and CH_3CO^* confirmed the experimental observation of a positive partial reaction order for ethanol, while the gradual surface saturation of the catalyst surface by adsorbed steam was the reason behind the experimentally observed slightly negative partial reaction order. The influence of the secondary water-gas shift mechanism and methane steam reforming mechanism was pronounced and observed to be vital to describing the experimentally observed product distribution. The model proposed a decomposition pathway similar to those observed over noble metal catalysts. The C-C cleavage point which is important in understanding the selectivities of products was proposed to be occurring at the ketenyl intermediate. This validated model served as the basis for the development of a more comprehensive kinetic system capable of describing the bifunctional mechanism and thus disseminating the effect of support materials on the ethanol steam reforming mechanism.

Subsequently, the developed microkinetic model was improved upon and expanded to include and describe multiple active sites. Thus, serving as a tool for examining the bifunctional mechanism of reaction processes in which the support materials play an active role. The model was developed for the ethanol steam reforming process, this time catalysed by a Ni metal with a

Ceria containing support mixed oxide. An initial assumption made for simplification of the developed model was that the overwhelming effect of the support mixed oxides could be approximated to the effects of the Ceria active sites. The number of sites attributed to ceria was then varied in order to account for the probable effect of the other oxide sites, however, the change in the number of sites yielded no serious alteration to the mechanism. The number of active sites of the support material was estimated using hemispherical geometry assumption as well as assumed optimal packing of Ni atoms. The number of active sites of the metal was again experimentally determined and the dispersion of the Ni sites on the support surface was experimentally determined. The knowledge of the metal dispersion served as a basis for the geometric calculation of ratio of support sites to metal sites. The bifunctional mean-field microkinetic model developed utilised the same semi-empirical rate estimation methods of the first model.

The model was used to simulate a wide range of kinetic experimental data over the bifunctional catalyst. Initially, a model based on a single active site was used to simulate the data and provided inadequate description and agreement with the kinetic data especially in terms of product distribution. This confirmed the requirement of a model capable of incorporating a bifunctional mechanism. The bifunctional microkinetic model on the other hand, provided satisfactory agreement with the data. The proposed model saw the adsorption of ethanol and its derivative adsorbates to be adsorbed on the Ni metal active sites whilst, the activation of steam occurred on the ceria support sites with the mobile oxygen surface species migrating freely from the support to the metal sites. The dehydrogenation of ethanol derivatives 1-hydroxyethyl and CH_3COH^* were determined to be the most kinetically relevant steps, justifying the observed positive partial reaction order for ethanol in the experiments. The oxidative dehydrogenation pathway was observed to have been promoted by the increased abundance of surface O^* species on the metal sites. This increased relevance of the oxidative dehydrogenation pathway pushed the scission of the C-C bond to occur later in the dehydrogenation pathway of ethanol, affecting the product distribution and limiting the production of CH_4 . The oxidative dehydrogenation was however only relevant in the reaction mechanism after the formation of acetyl, before which the thermal dehydrogenation dominated the pathway. The kinetically relevant reaction step therefore did not involve any steam-derived species. This model was therefore able to provide more intrinsic and comprehensive insight into the effects and roles played by active support material specifically ceria in our case in the overall reaction mechanism and product distribution for the ethanol steam reforming (ESR) process.

Furthermore, the industrially relevant effect of co-feeding CO and H₂ during the dry reforming of biogas process was investigated. A microkinetic model was developed for the biogas dry reforming process a Rh/Al₂O₃ catalyst using the first developed model as a basis. The influence of various operating parameters on the conversion of biogas and the syngas selectivity were evaluated using the developed microkinetic model. The effect of co-feeding H₂ and CO with biogas were specifically targeted. The developed model provided ample agreement with the experimental kinetic data. The dehydrogenation of adsorbed CH₃* species was observed as the most kinetically relevant reaction step. The activation of CO₂ on the catalyst surface was proposed to follow three paths which included: the direct decomposition towards CO*, the H-mediated decomposition towards COOH* and the H-mediated decomposition towards HCOO*. The direct decomposition to CO* was observed as the main activation step for CO₂, however, the contributions of the H-mediated steps changed slightly with the addition of a H₂ co-feed.

During the co-feeding of H₂, an increase in the partial surface coverage of H* species was observed at the start of the catalyst bed and later decreased across the bed, meaning the co-fed H₂ was adsorbed and participated in surface reactions. The increase in the surface H* abundance led to an increased relevance H-mediated CO₂ activation steps, improving the overall conversion and syngas formation. However, this also led to an increased partial surface coverage of CO* which at high values of H₂ co-feeding inlet concentrations led to the saturation of the surface. This explained the experimentally observed maxima of conversion and yield with increasing H₂ inlet concentrations. The experimental results indicated a negative impact of increased CO co-feeding concentration of the conversion of CO₂. This was explained by the model to be as a result of an increased partial coverage of CO* and the start of the bed, which negatively affects the reverse water-gas shift equilibrium and saturates the surface of the catalyst.

The developed microkinetic model was able to provide much needed comprehensive insight into the impact of industrially relevant product co-feeding on the reaction mechanism and product distribution of the biogas dry reforming process which could have interesting applications in reactor modelling and catalyst design for this process.

Finally, kinetic experiments of ethanol steam reforming and decomposition processes were carried out over a sustainable and relative to acidic and basic oxides, cheap biochar supported Ni catalyst. The experiments were performed over a wide range of condition over a Ni/biochar catalyst, a biochar catalyst and an acid-washed biochar catalyst, in order to determine the overall reaction mechanism and the effect of biochar support on the reaction mechanism. The results indicated that biochar displayed catalytic activity for the reforming and decomposition of

ethanol, while following a different mechanism to that observed over Ni. The present alkali and alkaline earth metals in biochar contributed to its catalytic activity. The reactions on the active sites of Ni and biochar were found to not be independent. During the ethanol steam reforming experiments, the formation of CO₂ was observed to be low, however when independent water-gas shift experiments were performed, the CO₂ formation was high. This indicated that the water-gas shift reaction sub-mechanism during the ethanol steam reforming process was hampered either by the effect of surface species coverages or by the changes in the working state of the catalyst surface induced from the adsorption and dehydrogenation of ethanol.

The decomposition of ethanol on biochar in the absence of steam interestingly showed the formation of C₂H₆ species, which could have been as a result of the abstraction of the OH group forming an ethyl CH₃CH₂ surface species which would associatively desorb with available hydrogen. It could also have been as a result of the CH₃ species formed from decomposition recombining to C₂H₆ due to lack of sufficient hydrogen to form CH₄. Kinetic compensation effect was observed with a possible rate limiting step on biochar being common to all reactions. The Raman spectroscopy results show similar reduction in O-containing functional groups when biochar is used alone or as a support to Ni, while the presence of H₂O in both cases helps maintain the population of these groups.

Future recommendations

Some suggestions presented below would provide further scientific contributions to the areas of focus in this study.

Firstly, with the foundation provided by the developed models in this work, it is recommended that expansion and investigation into the reforming of higher oxygenated hydrocarbons be undertaken. As was expressed in this work, it is of vital importance to obtain intrinsic kinetic understanding of the reforming processes in order to improve efficiency and make the technology more feasible and viable. Microkinetic modelling provides a tool for accomplishing this goal, therefore other oxygenated hydrocarbons like glycerol, phenol, and on a larger scale bio-oil should be investigated in-depth.

Additionally, more advanced methods of rate constant estimation (quantum mechanical methods i.e., DFT) able to provide even better accuracy in terms of prediction of reaction mechanisms and intrinsic kinetics can be incorporated and used in the microkinetic modelling of these processes to provide even better comprehensive understanding of the processes.

Secondly, the bifunctional mean-field microkinetic model proposed in this work can stand as a tool for performing process optimisation and catalyst selection. Therefore, it is recommended that for the ethanol steam reforming process a bifunctional microkinetic Sabatier analysis be performed to provide insight into the optimal catalytic metal-support systems for the ESR process. It is also recommended that the knowledge obtained from the bifunctional model mechanism descriptions be used to determine the desired roles and effects of a support material that benefit the ESR process and use this to propose cheaper and more sustainable catalytic systems.